Contribution to multi-physical studies of small synchronous-reluctance machine for automotive equipment

by

Mohd Azri Hizami RASID

presented to

The Doctoral School
Université de Technologie de Compiègne

in partial fulfillment of the requirements
for the degree of
Doctor of Philosophy
in the subject of

Information and System Technologies

Presented on 11 February 2016 in front of the jury panel:

Guy FRIEDRICH	Université de Technologie de Compiègne	President
Xavier MININGER	Université Paris Sud	Referee
Abdelmounaïm TOUNZI	Université de Lille	Referee
Daniel DEPERNET	Université de Technologie de Belfort-Montbeliard	Examiner
Caroline DOC	Renault	Examiner
Vincent LANFRANCHI	Université de Technologie de Compiègne	Director
Alejandro OSPINA	Université de Technologie de Compiègne	Co-Director

Laboratoire d'Electromécanique de Compiègne
Université de Technologie de Compiègne
Sorbonne Universités

UMP

Abstract

Due to environmental concern related to CO_2 emissions, automobile manufacturers has been increasingly engaging in electrifying multiples on-board applications. Functions that are being electrified involve crucial and complex applications such as clutches, power steering, assisted brakes and others. Furthermore, these functions are often placed in a particularly challenging environment in terms of spaces, thermal, vibration and acoustic. As results, research on electrical motors to find the most suitable motor to a given applications has been intensified.

In this environment, machines optimal design requires simultaneous consideration of numerous physical phenomena ; both in terms of expected performance and constraints to be respected. The physics that can be affected includes the electromagnetic / electromechanical performance, thermal behavior and vibro-acoustic behavior. Among a large choice of machine, with the manufacturer cost and manufacturing concern taken into account, the synchronous reluctance machine with segmented rotor has been found to be particularly interesting for application with severe ambient temperature and encumbrance limitation.

This study has therefore as objectives to evaluate the capacity of the synchronous reluctance machine in all physics mentioned and eventually shows the interaction between these physics, thus performance alteration of the machine operated in automobile equipment environment. Multi-physics model were developed and confronted to experimental validations using a prototype machine that was designed for an electrical clutch. Using the validated model, different performance figures of synchronous reluctance machines with different rotor topologies were compared.

Resulting from the study, valid electromagnetic, electromechanical, thermal and vibro-acoustic models are now available to be used as tools in future machine design. The synchronous reluctance with segmented rotor prototype machine has been shown to be capable to be used in the electrical clutch application studied in particular. Following performance evaluations in different physics, suggestions of improvements have also been proposed.

Acknowledgements

Firstly, I would like to express my sincere gratitude to my advisors Prof. Vincent Lanfranchi and Dr. Alejandro Ospina for the continuous support of my Ph.D study and related research, for their patience, motivation, and immense knowledge. Their guidance helped me in all the time of research and writing of this thesis. The casual conversations that we had were the most precious, where both of them have shown me how to be a good teacher, how to give chance to students to learn and grow wiser and how to see the academic and scientific works in a wider perspectives. I could not have imagined having a better advisor and mentor for my Ph.D study.

Besides my advisor, I would like to thank the rest of my thesis committee: Prof. Abdelmounaïm Tounzi, Prof. Xavier Mininger, Prof. Guy Friedrich, Dr. Daniel Depernet and Dr. Caroline Doc, for their insightful comments and encouragement, but also for the hard questions which incented me to widen my research from various perspectives.

My sincere thanks also goes to the director of L. E. C. who provided me an opportunity to be among respected researchers, and who gave access to the laboratory and research facilities. Special thanks to the engineers and technician of the laboratory, Dr. Kadija Benkara and Loïc Charbonnier. Without their support it would not be possible to conduct this research.

I thank my fellow labmates for the stimulating discussions that we had, either scientific disscussion or others. Special thought to my officemates through the nearly 4 years of my study, Jaafar Hallal, Paul Gning and Sebastian Pinto who have helped me a lot.

Last but not the least, the most important people to whom I owe a lot, I would like to thank my family: My beloved and supportive wife Aainaa and my two heart-soothing sons Ouwaïss and Thufayl, my precious parents who have always prayed for me, my brother and two sisters, extended families and my friends.

Thank you. “Que dieu vous préserve tous.”

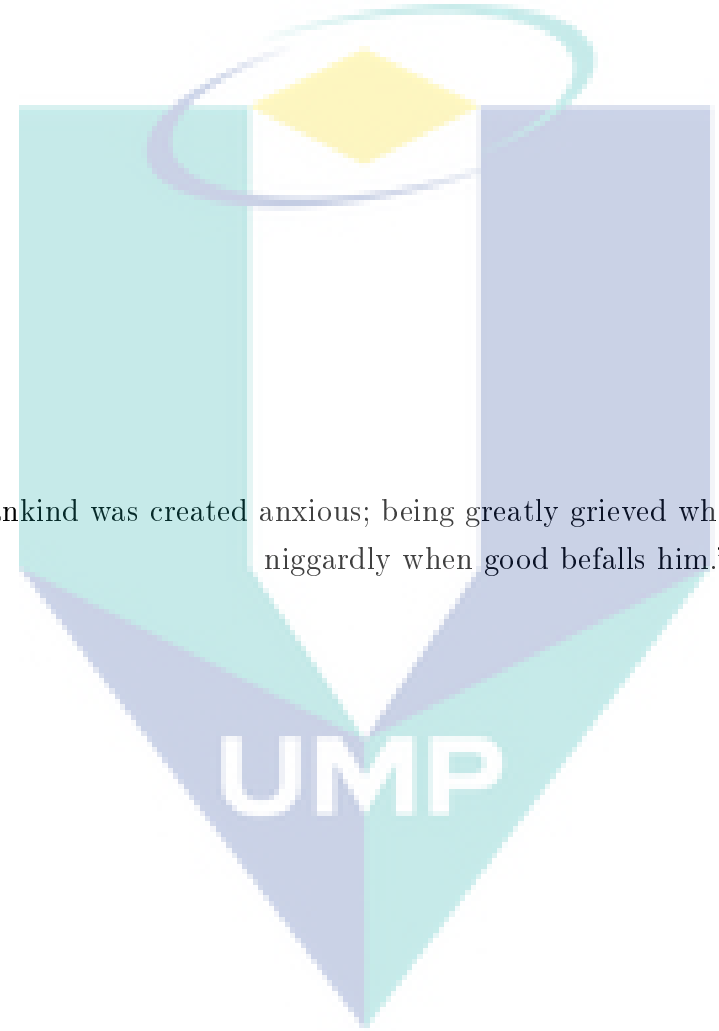

"Indeed, mankind was created anxious; being greatly grieved when evil afflicts him, and niggardly when good befalls him." (al-Quran 70 : 19-21)

Contents

Abstract ii

Acknowledgements iii

Introduction 1

Electrification of automotive equipments . . . 1

General requirements for automotive equipment . . . 2

Automotive environment . . . 4

Different motor choice for automotive application . . . 5

Aim of the work . . . 6

1 State of the Art on Synchronous Reluctance Motor 8

1.1 Historical context . . . 8

1.2 Syncrel rotor's topology . . . 11

1.3 Study case: Syncrel for e-Clutch . . . 14

1.3.1 Context of application . . . 14

1.3.2 Design process and final motor design . . . 16

1.3.3 Prototype motor assembly . . . 17

2 Electro-mechanical performance 23

2.1 Principle of operations . . . 24

2.2 Description of the test bench . . . 26

2.3 Torque-speed characteristics computation . . . 28

2.3.1 Application on Syncrel prototype motor . . . 31

2.3.2 Validation test . . . 33

2.3.2.1 Friction torque identification . . . 34

2.3.2.2 Torque-speed area validation . . . 35

2.3.2.3 Conclusion . . . 38

2.3.3 Robustness of linear analytical input . . . 39

2.3.3.1 Inductance L_d and L_q . . . 39
2.3.3.2 Maximum-torque-load angle β . . . 43
2.4 Power factor . . . 47
2.4.1 Computation tool . . . 48
2.4.1.1 Experimental validation . . . 49
2.4.2 Influence of speed on $cos(\varphi)$ . . . 51
2.4.3 Influence of load angle β on $cos(\varphi)$ . . . 51
2.4.4 $cos(\varphi)$ variation due to winding's temperature variation. . . . 52
2.5 Interaction between different parameters . . . 53
2.5.1 Influence of load angle on power factor and torque . . . 53
2.5.2 Degradation of speed limit in function of winding resistance and its effect on power factor . . . 55
2.6 Efficiency . . . 57
2.6.1 Copper losses . . . 59
2.6.2 Iron losses . . . 61
2.6.2.1 Generalities: iron losses modeling . . . 61
2.6.2.2 Application on Syncrel prototype machine . . . 63
2.6.2.3 Determination of magnetic losses coefficients K_h and K_{exc} . . . 66
2.6.3 Power balance check . . . 68
2.7 Comparison with other motor . . . 69
2.8 Conclusion . . . 72

3 Thermal behavior **76**
3.1 Modeling method . . . 77
3.2 LP model: generalities . . . 79
3.2.1 Heat transfer mechanisms . . . 80
3.2.2 Thermal parameters calculation . . . 82
3.2.2.1 Thermal resistances . . . 82
3.2.2.2 Thermal capacitance . . . 83
3.3 Thermal model of the Syncrel motor . . . 84
3.3.1 Slot equivalent thermal resistance . . . 85
3.3.2 End winding thermal resistance . . . 91
3.3.3 Stacked iron sheet thermal resistance . . . 93
3.3.4 Surface contact thermal resistance . . . 94
3.3.5 Experiments . . . 96
3.3.5.1 Identification of external surface thermal resistance R_{ext} . . . 96

3.3.5.2 Validation of the complete LP model . . . 97
3.4 Sensitivity study of the thermal model . . . 99
3.4.1 Influence of exterior surface thermal resistance, R_{ext} . . . 101
3.4.2 Influence of slot equivalent thermal resistance, R_{slot} . . . 104
3.4.3 Conclusion on sensitivity study . . . 107
3.5 Simulation on different duty cycle . . . 108
3.5.1 Model accuracy on short time range . . . 108
3.5.2 Standard duty cycle . . . 114
3.5.3 E-Clutch duty cycle. . . . 116
3.6 Conclusion . . . 123

4 Torque ripple and vibro-acoustic behavior 130
4.1 Torque ripple of segmented-rotor Syncrel . . . 130
4.1.1 Torque ripple characteristics evaluation using FE analysis . . . 132
4.1.1.1 Torque ripple in function of current I_s, at fixed load angle β 132
4.1.1.2 Torque ripple in function of load angle β, at fixed current I_s 134
4.1.2 Experimental observation . . . 138
4.1.3 Comparison with other rotor topologies . . . 141
4.1.4 Perspective on torque ripple reduction . . . 145
4.2 Vibro-acoustic behavior . . . 146
4.2.1 Vibro-acoustic of electric machine: generalities . . . 147
4.2.1.1 Electromagnetic forces modeling . . . 148
4.2.1.2 Vibration modeling . . . 151
4.2.2 Vibro-acoustic evaluation of the Syncrel motor . . . 155
4.2.2.1 Magnetic pressure computation . . . 156
4.2.2.2 Modal analysis . . . 162
4.2.2.3 Response in operational condition . . . 163
4.2.2.4 Experimental validations and discussion . . . 165
4.2.3 Conclusion and perspectives . . . 170

Conclusion and perspectives 174

Publications 178

Appendix 180

Introduction

Electrification of automotive equipments

The need to address global energy issues is more urgent than ever. Economies face threats to their energy security, and the evolution of climate change requires urgent government action. As a result, G8 leaders at Gleneagles in July 2005 and in St. Petersburg in July 2006 called on the International Energy Agency (IEA) for "advice on alternative energy scenarios and strategies aimed at a clean, clever and competitive energy future". Their recent report in 2010 shows that transportation contributes up to quarter of CO_2 emissions worlwide (left Figure 1) and road vehicles are a major part of the energy-use puzzle.

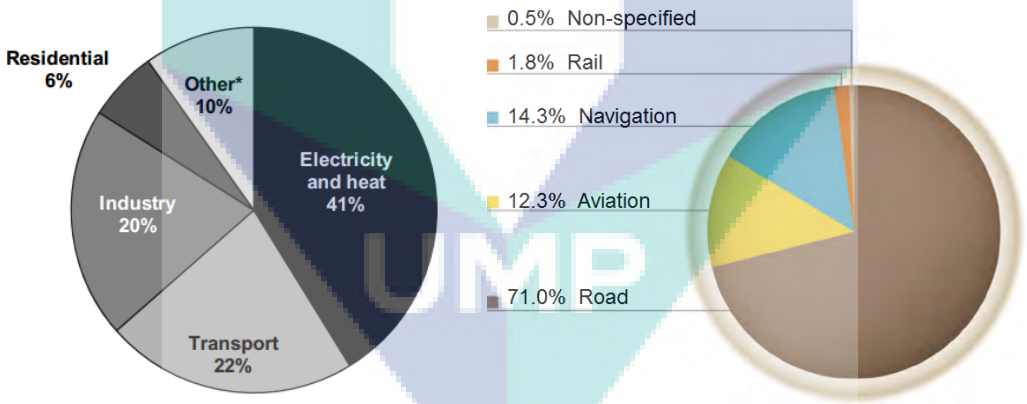

Figure 1: World CO_2 emissions by sector and transport modal split in 2010. Source: "CO_2 emissions from fuel combustions 2010." by IEA.

Road vehicles dominate global CO_2 emissions, emitting as much as 70% (right: Figure 1) of transport emissions and are one of the fastest growing energy end-uses. As a result, transport sector's share of oil consumption has been increasing steadily at around 0.5% per year. Transport energy demand will continue on this path unless more action is taken urgently. Following these worrying observations, automakers are intensifying vehicles electrification that they have already opted since several past years with aids and incentives from governments and regional authorities.

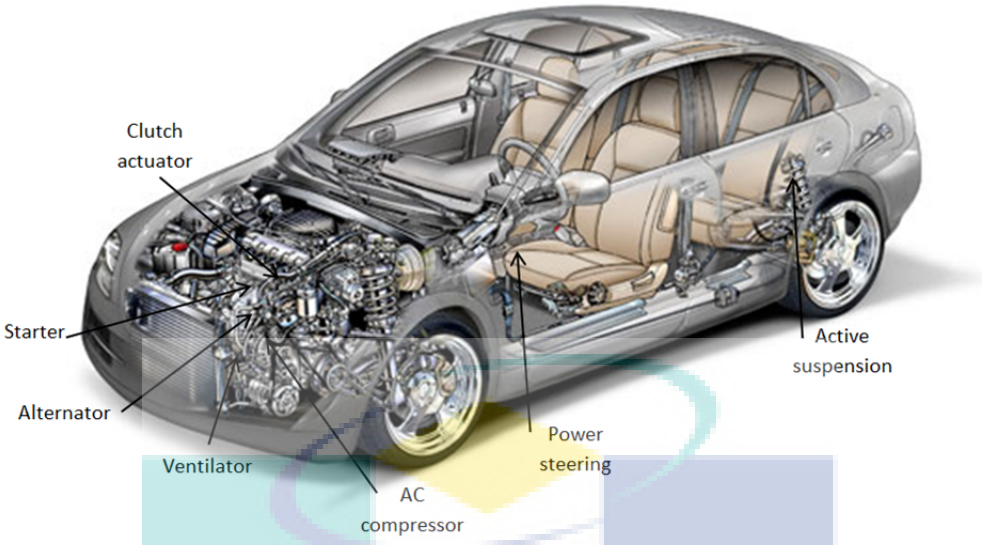

Figure 2: Utilization of electric motor for different on-board automotive application.

The automotive sector have been using electrical machine as actuators both for traction and its on-board equipments (Figure 2). The electrification increased considerably and the trend should continue in the coming years. Prior to year 2000, rotating electrical motors are used for simple applications such as windscreen wipers, windscreen washer pumps, fan and windows. The main technology used is the dc motor. In recent years, many research and development have been done aiming electronically commutated motors technology for more complex type of applications, which can be categorized as 'drive by wire' applications (clutches, brakes, power steering etc.). These include induction motor, permanent magnet synchronous motor, variable reluctance motor and a lot more.

The key criteria in designing electrical motors for automotive equipments has long been economic solely. Automaker's main objective was mostly cost minimization without any real interest and consideration on efficiency, performance and different multiphysics criterias (thermal, vibration, acoustic, etc.). However, as a consequence of the ever increasing use of electrical motor for various equipments and their integration into more critical and complexes applications, we are currently witnessing a shift in this industry where design criteria takes more and more multiphysics performance into consideration.

General requirements for automotive equipment

Different sectors have different requirements and constraints. In automotive equipment sector, these requirements and constraints are determined by both automakers and equipments manufacturer. They depend on the functions to be assured by the application. A thoroughout functional analysis on the application will let manufacturer takes into consideration

multiple aspects of usage (user, environment, legislation and standard) in designing the equipment. Main requirements that are common to many application can be divided into three categories: machine performance, volume and weight, and cost (Figure 3).

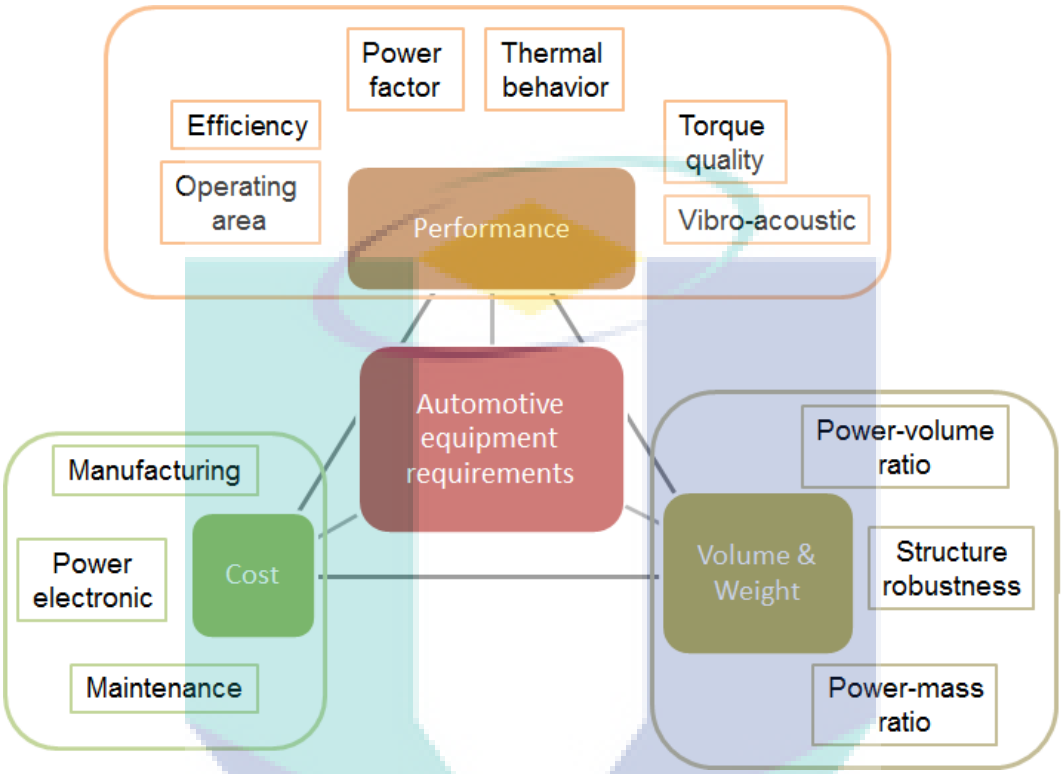

Figure 3: Requirements related to automotive equipment actuator.

The performance area includes operating area, efficiency, power factor, thermal behavior, torque quality, vibration and noise level. In the category of volume and weight, a motor need to fit in a given encumbrance and weight limit thus, achieve certain power to volume ratio, power to mass ratio while maintaining a sufficient structural strength and robustness. As for the cost, the mass production characteristic of the automotive industry means that the manufacturing, the power electronic and the maintenance of the motor need to be as cheap as possible. In summary, concerning the three requirements area, the motor needs to have an optimum compromise between high performance while maintaining small volume and weight at a lowest cost possible.

In our study, we will concentrate on the evaluation of the performance of the motor, which includes electro-mechanical performance, thermal performance and vibro-acoutic. To do so, it is necessary to have an overview of the environment constraints related to automotive application beforehand.

Automotive environment

The functions in automotive that are being electrified are getting more and more complex. They involve crucial applications such as clutches, power steering, assisted brakes and others. These crucial functions are often placed in a particularly challenging environment in terms of spaces, thermal, vibration and acoustic (Figure 4).

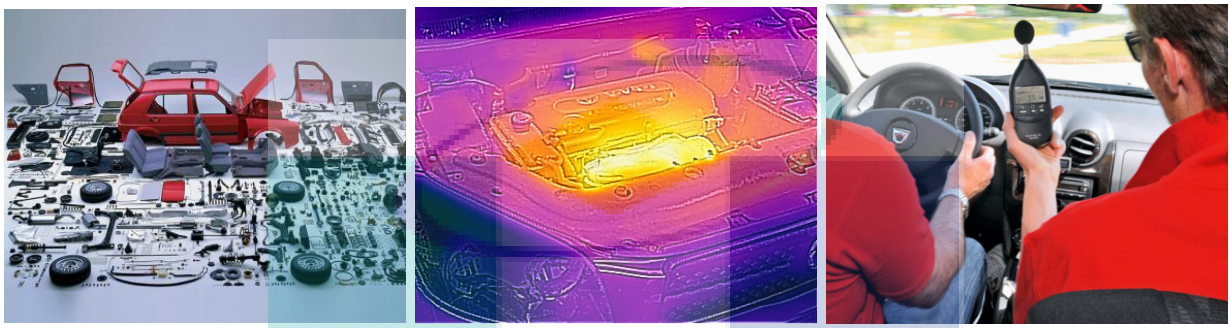

Figure 4: Limited space (left), high temperature (middle) and vibro-acoustic regulation (right) are the major challenges in motor design for automotive application.

In terms of space and encumbrance, with increasing concern in road safety, more and more spaces are dedicated to vehicle security features and protecting structures leaving automakers with very few options to place their motors. The usual places available are either under the car chasis, in the boot compartment or the engine compartement. These are especially constraining area for various reasons. For exemple, component integration under the chasis are avoided in order to reduce the car height which affects the car stability and handling significantly. As for the boot, this space is either left for car user to maximise the car ergonomics or even in some case, it has been already used for energy storage (batteries for electric cars and gaz tanks for NGV[1] cars). Finally, for the engine compartement, spaces are very limited with different important mechanical components creating a whole complex environment. As to summarize, no matter where the location is, a motor for automotive equipment has to be small in size in order to be integrated easily into the car. Thus, a criteria that has to be included in the motor specification related to space limitation is a motor with high power and torque to volume ratio.

For thermal aspects, a vehicle environment is particularly demanding. Most of the location where the motor can be placed are subjected to high temperature especially the engine compartement where the environment temperature exceeds 120°C. Combined with limited space as mentioned before, every little elevation of temperature is risky as the heat will be

[1]Natural Gas Vehicle that uses compressed natural gas (CNG) or liquefied natural gas (LNG) as a cleaner alternative to other fossil fuels.

rapidly concentrated. As already known, electrical motor are at risk of total destruction in this situation regarding to several thermal sensitive components. It could be magnets for permanent magnet type of motor and winding insulator for others. So as to avoid the Curie temperature of the magnetic material used and the maximum bearable temperature of the insulator, the motor should be designed in order to evacuate the heat generated efficiently. A thermally efficient designed machine is then necessary for automotive applications.

Finally, from a psycho acoustic point of view, electric machines generate relatively high frequencies acoustic noises that could be particularly unpleasant for users compared to internal combustion engines ones. Its high frequencies take origine from the mechanical vibration of ferromagnetic parts such as the stator or the rotor structure. The magnetic originated force or mostly known as Maxwell force are to be monitored closely as it can be amplified consequently at different eigen frequencies of the machine. A proper studies on the eigen frequencies and frequential response function (FRF) has then to be made on a machine that is designed for automotive equipment so that the noise will be bearable for users. Besides, vibration can also affects the mechanical structure, for example by fatigue mechanism which can reduce the motor or the neighboring components life span.

Different motor choice for automotive application

Following the constraints of the environments viewed in previous section, a range of motor choice can suit more or less a given application. In general, direct current motors are not suitable due to its drawbacks that get worst with limited volume : inertia, brushes-armature contact, friction, and lifespan. Hence, motors that are usually considered in different comparison focus exclusively on alternating current motor, which are : Permanent Magnet Synchronous Motor (PMSM), Synchronous Reluctance Motor (Syncrel), Switched Reluctance Motor (SRM) and Induction motor. Without going into details, different comparison can be summarized in Table 1.

We can see that syncrel motor emerges as an interesting solution. A motor without winding and mechanical friction on the rotor helps to reduce the elevation of temperature. Its passive rotor just like the SRM. make its major losses (copper loss and iron loss) located on the stator. Thus, it is easier to evacuate the heat produced using a simple cooling system.

A permanent magnet motor such as the PMSM could work with an efficient magnet like samarium cobalt (SmCo). However, the high cost of this material can be unacceptable for automotive applications working in a mass scale industry. On the other hand, less expensive thus less efficient magnet is is temperature-sensitive. The magnet's flux density can significantly decreases once subjected to high temperature.

Table 1: Summary of advantages and disadvantages of different machines

machine	**advantages**	**inconvenients**
PMSM	- high torque to mass ratio - high efficiency - possibility to be in overspeed (under certain magnet conditions)	- performance affected by temperature rise - risk of demagnetization (temperature, current peak, overspeed...) - magnets assembly - cost
SRM	- easy winding, high filling factor - low cost material - easy manufacturing - no rotor Joule losses - low cost machine	- iron have to be saturated (losses by circulation in iron) - lower power factor compared to PMSM - small air gap needed - high torque ripple, vibration and acoustic noise
Syncrel	- robust - low cost material - no rotor Joule losses	- low power factor - small air gap needed - manufactirung difficulties (depends on rotor topoloy) - lower efficiency compared to PMSM
IM	- robust - low manufacturing cost - no torque ripple	- low torque to volume ratio - poor global efficiency - poor power factor - rotor Joule losses diffcult to evacuate

With all these arguments, we are then left with the choice between SRM and syncrel motor which are very similar. However, as a synchronous motor, syncrel machine comes with more possibilities to reduce the torque ripple problem. Syncrel can then be seen as the intermediate solution between the SRM and the PMSM.

Aim of the work

We have seen that electrical machines optimal design requires simultaneous consideration of numerous physical phenomena as mentioned before; both in terms of expected performance or in terms of constraints to be respected. For example, an optimum electromagnetic alone is often a non-thermal sense and vice versa, not yet mentioning the vibration and acoustic. It is therefore necessary to use a multi-physical model in order to achieve an optimized design of the machine that takes into account all the physical phenomena involved. For the specific application of clutch actuator, following the choice made regarding the syncrel machine and

its topology which will be presented in next chapter, our studies propose consequently a multiphysical evaluation of the machine. It will be first treated in separate chapter: electro-mechanical performance, thermal behavior and vibro-acoustic behavior. With the evaluation results, we hope to provide the electrotechnical community with a base for comparison and positioning of the Syncrel motor among other motors. In the process, the study will eventually results in several models, tools and improvement propositions that could serve for an optimum designing process in the future.

Chapter 1

State of the Art on Synchronous Reluctance Motor

1.1 Historical context

The foundation for building electric motors was laid thanks to three main discoveries and inventions: continuous electrical power, magnetic fields and electromagnet [1].

In chronological order many consider that all the development started following the possibility of producing electricity voluntarily. In 1800, using a stack of silver and zinc plates, a continuous electrical power production (as opposed to a spark or static electricity) was invented by Allessandro Volta.

Later in 1820, Hans Christian Oersted found the generation of magnetic field from electric current after an observation of the deflection of a compass needle. Nearly at the same time, in 1821, Micheal Faraday demonstrated the electromagnatic rotation using a vertically suspended wire, magnets and mercury (Figure 1.1)[1].

Finally in 1825, William Sturgeon invented the electromagnet using a coil of wires with an iron core to enhance the magnetic field (Figure 1.1)[2]. The cylindrical coil, called solenoid itself was an earlier invention by André-Marie Ampère in 1820.

[1] Photo courtesy of Division of Work & Industry, National Museum of American History, Smithsonian Institution

[2] Photo courtesy of Transactions of the Society for the Encouragement of the Arts, Manufacturers and Commerce

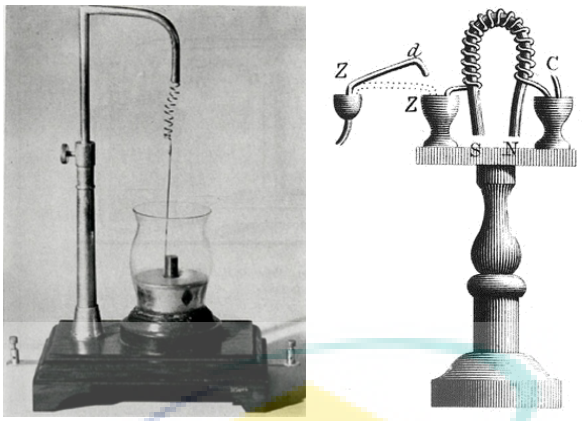

Figure 1.1: Left: Rotating wire by Faraday, 1821 ; Right: First electromagnet by Sturgeon, 1825.

In terms of motor, the first rotating device driven by electromagnetism was built in 1822 by Peter Barlow, called the Barlow wheel Figure 1.2. With the usage of a thin copper wheel, magnets and mercury, it can be considered a simple and primitive system that helps to prove the effect of Lorentz force continuously. Therefore, it is not usually consedered as a real electirc motor.

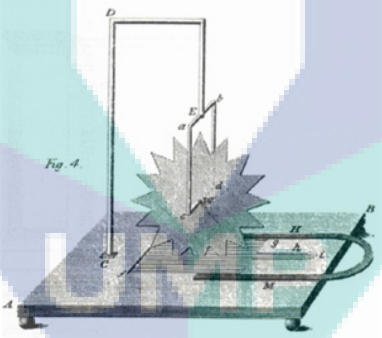

Figure 1.2: Barlow's wheel, as published in Philosophical Magazine, 1822, vol. 59.

In 1838, the first form of switched reluctance motor was patented by W. H. Taylor [2]. The machine was composed of a wooden wheel on the surface, on which was mounted seven pieces of soft iron equally spaced around the periphery. The wheel rotated freely in the framework in which four electromagnets were mounted. These magnets were connected to a battery through a mechanical switching arrangement on the shaft of the wheel such that excitation of an electromagnet would attract the nearest piece of soft iron, turning the wheel and energizing the next electromagnet in the sequence to continue the motion.

The invention of AC multiphase initiated by Nikola Tesla in 1882 has eventually led to an induction motor patent in 1887 [3] after the discovery of rotating magnetic field principle.

A rotating magnetic field generated by two phase alternating current was used in his first AC motor. Slightly before Tesla, Galileo Ferraris has also build independantly a similar two phase induction motor in 1885. Both motors are illustrated in Figure 1.3. After this point, polyphases AC motors started to take important place in industries in various forms.

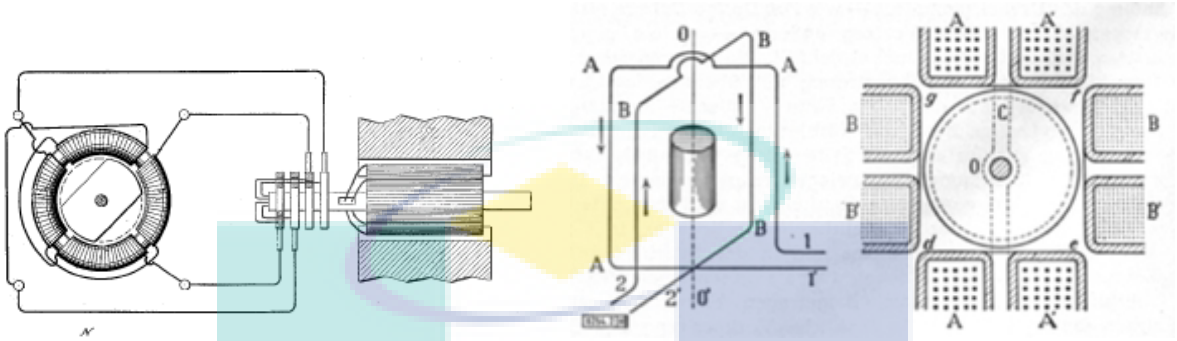

Figure 1.3: Right: Illustration of Tesla's alternating current induction motor from U.S. Patent 381,968 ; Left: Schematic drawing of Ferraris' first induction motor.

While squirrel cage induction motor has always been a popular choice in a very large industrial fields due to its low cost, simple structure and overall performance, it has been shown that synchronous reluctance (Syncrel) machine in the form of simple salient pole is one of the oldest type of electric motors, antedating the induction motors by many years. Kotsko in [4] initiated the revival of reluctance motor in the 30's[3]. He believed that the less advantageous opinion on the Syncrel motor at that moment is due to the faulty form of the rotor non-optimized design. He came up with the notion of optimizing the $\frac{L_d}{L_q}$ ratio (which he called k) in order to get a maximum torque and concluded his proposition with a theoretical rotor design as shown in Figure 1.4. The industrial manufacturing technique at that time did not allow construction of such complex and precise structure.

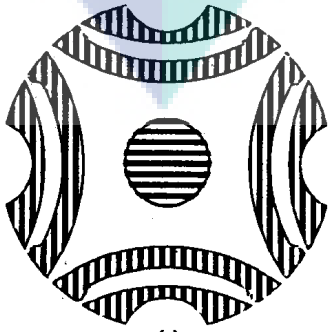

Figure 1.4: Kotsko's theoretical rotor design in 1930's.

[3]Kostko called the machine the Salient-Pole-Rotor Reaction Synchronous Motor without field coils [4]

Furthermore, without a vector control, syncrel motor structure with cage was used largely as line start motor just like induction motor. The primary reason of their usage is to attain synchronism of a number of shafts after the starting, such as in fiber spinning industry [5]. The performance of the machine at the moment was very low. Early examples of this kinds of machines are the "Permasyn" by General Electric [6, 7]. For a long time, the Syncrel motor has been used as such and not evolved towards a high performance machine until late 20th century.

The improvement on Syncrel performance was due to two main reasons. On one hand, with the advancement in manufacturing process, the search for high anisotropy rotor emerged in the 60's. This periods have seen many works on rotor topologies such as [8, 9, 10]. On the other hand, later in the 80's, the development of closed-loop control, powered by inverter was first applied on brushless dc motor. It gave a new push to research on high performance syncrel motor and drives devoid of cage that can be clearly seen in example such as [11, 12, 13]. Since then, more studies to improve the performance, topology wise and control wise to make it comparable to more performance type of machine has flourished.

1.2 Syncrel rotor's topology

A syncrel motor consists of a wound stator and a magnetically anisotropic (salient) rotor. The stator structure is similar to that of any ac motor. In general, three-phase windings are used. The spatial conductor distribution is supposed to be sinusoidal, in principle. The rotor is mainly passive where the torque produced originates solely from reluctance torque due to the rotor magnetic anisotropy. In a simple explanation, reluctance torque is produced as consequence of the rotor tendancy to line up along a minimum reluctance position [14].

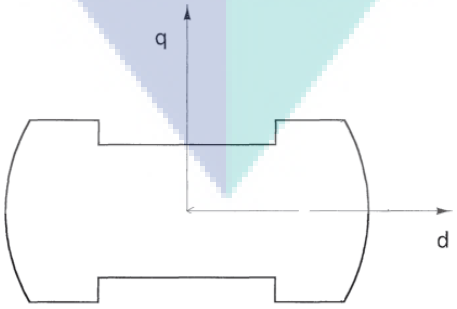

Figure 1.5: Simple two pole salient rotor.

The rotor magnetic anisotropy can be achieved by different topology. Basicly, reference can be made to a two pole, simply salient structure as in Figure 1.5. A *dq* frame synchronous to the rotor is considered where the d-axis is in the direction of maximum permeance and

q-axis in the direction of minimum permeance. The researches on the syncrel topology that look to optimize this saliency ratio (L_d/L_q) is very diverse. We categorize the syncrel rotor topology into four major groups schematically presented in Figure 1.6.

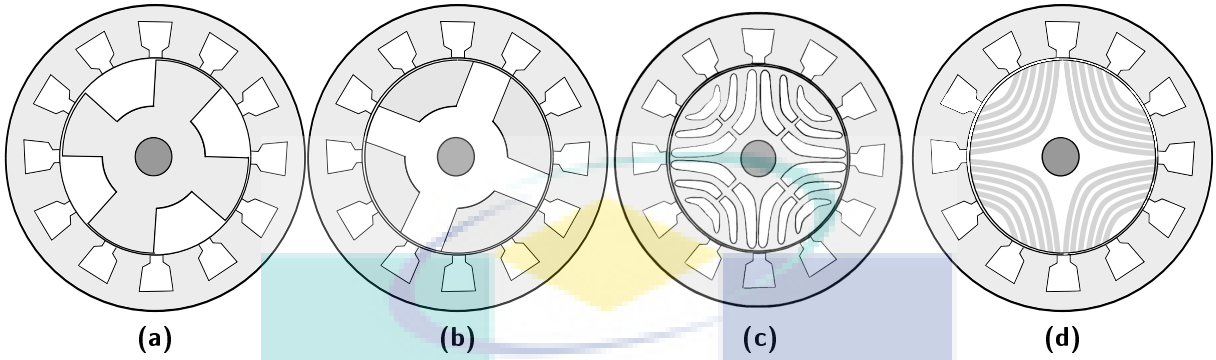

Figure 1.6: Different syncrel rotor topology: a) simple salient pole rotor; b) segmented rotor; c) flux barrier rotor; d) axially laminated rotor.

Before going into details on each rotor topology, it needs to be noted that the saliency ratio of a given rotor topology increases in general with the motor's size. Therefore, comparison of the saliency ratio on different rotor topology from different studies is only reliable for the same size motors.

a) Solid rotor

Solid rotor is a simple salient pole rotor. It is the most elementary form of variable reluctance rotor. It is usually constructed as a solid massive piece, hold by shaft. Its design has a simple and rigid structure but a low saliency ratio especially for a small size motor and consequently poor performance due to a high quadrature permeance. However, the rigid structure creates the possibility of using it in high-speed [15] and extremely high-speed machines [16]. Different variations of construction to maximize the saliency ratio while retaining its structural advantage can be found [17]: classic solid, drilled and slitted are among them[18].

As for saliency ratio, Chiba in [19] has reported a saliency ratio of about 2.5 for a two pole motor while Hassan has reported a higher saliency ratio, but not more than 3.8 in [20].

b) Segmented rotor

The segmented rotor is characterized by an assembly of ferromagnetic rotor segment on a non-magnetic holder that is connected to the shaft. It is capable of having a high saliency

ratio due to lack of ferromagnetic material on the rotor shaft [19, 20]. A relatively simple rotor assembly can also be achieved using dovetail structure connecting the shaft and the segments, as done in [21]. Besides being used for syncrel, segmented rotor structure is also being actively studied in recent years for switched reluctance motor (SRM) [22, 23]. Interestingly for SRM, it has been proven that it would increase the torque density compared to a conventional rotor structure.

For saliency ratio, Miller in [24] has used an interior permanent magnet rotor devoided of its magnet that made it resembles to a segmented rotor and resulted in a saliency ratio of 4.7. A far smaller motor built by Doc in [21] has found a saliency ratio around 2.5.

c) Flux-barrier rotor

Flux-barrier rotor is the most studied syncrel rotor topology. A higher saliency ratio compared to previous two rotors can be easily attained using specific forms of flux barrier and saturated bridges. There are commonly two sub-categories of this rotor: passive and magnet assisted. Adding small amount of permanent magnet, positioned at specific place can improve the saliency ratio [25, 26]. However, the presence of magnet made the syncrel less robust thermally and more costly. Therefore, research on flux barrier optimization without magnet assistant continues to interest many [27, 28, 29, 30].

Despite the high saliency ratio, it is very important to note that flux-barrier is more complex to design and manufacture especially for small motor. It cannot be designed simply with analytical tool as the flux leakage and saturation in the structure is very complex compared to two previous rotor [29]. As for manufacturing, the flux-barrier can be punched on metal sheet, however, more sotisphicated and expensive cutting process than a simple punch press may be needed for small motor.

d) Axially-laminated rotor

The axially laminated rotor design has a good saliency ratio and performance, but the eddy current losses as a result of the axial lamination are larger [28]. The mechanical design has also been studied since a long time. Cruickshank [31] and Roa [32] has reported a saliency ratio of 5.2 and 6.8 respectively. This rotor is extremely complex for industrial manufacturing, at least for four-pole machines, where the sheets have to be bent and connected with bolts [33]. It is therefore not suitable for mass production.

1.3 Study case: Syncrel for e-Clutch

The motor studied in this thesis is a Syncrel motor with segmented rotor that was designed in a previous Ph.D thesis [21]. One prototype motors was handed to the laboratory for validation tests. All the study and experiments in this thesis are based on this motor. Therefore, it is necessary to explain the application and context in which the motor was designed, the design process and finally presents the resulting geometrical dimensions of the motor.

1.3.1 Context of application

The motor studied is the result of a project named "e-Clutch", which consists of selecting and designing a machine intended for clutch actuator. The objectif was to replace the existing automated electrical clutch actuator which is widely used in automotive industry, called 'clutch actuator by compensation' which is a 'semi-electrical' system. This existing system already make use of an electrical actuator, which is more advantageous than the classic hydraulic system. However, the clutch is actuated using a system combining a DC motor force and helical spring force as can be seen in Figure 1.7.

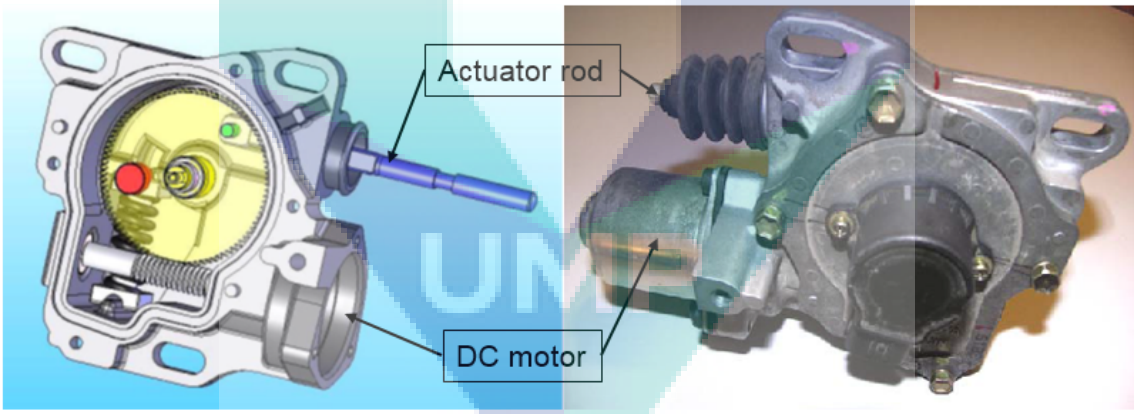

Figure 1.7: The clutch actuator by compensation system, which can be found for example in the Toyota Aygo MMT. The whole system is then mounted onto the transmission system housing.

The motor torque is transmitted to the actuator rod using a worm gear with a large diameter gear which enables a reduction of torque required from the motor at the expense of two major inconveniences: space (and mounting solution) and motor lifespan.

In perspective of improvements, a new compact system with a more direct and simpler power transmission to the clutch diaphragm was required by the manufacturer. A preliminary design is shown in Figure 1.8.

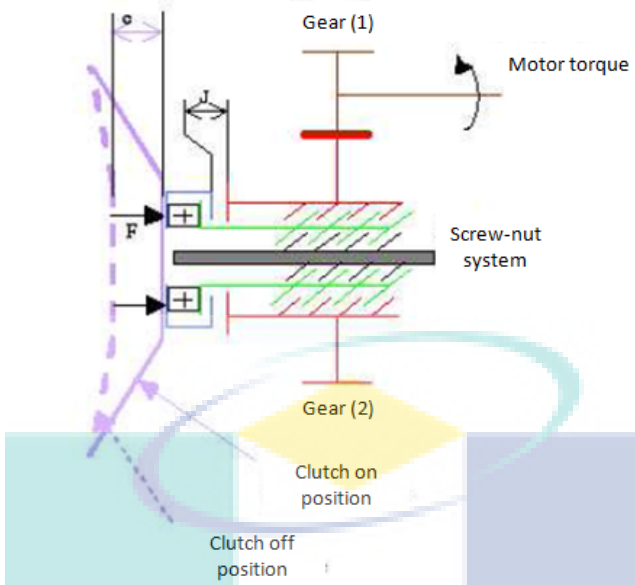

Figure 1.8: Kinetic diagram of the new clutch actuator mechanism.

In this design, the motor will actuate the actuator rod through a screw-nut system without helps of other mechanism such as spring. The motor need to be small in order to be integrated directly into the transmission housing, and not as a separate assembly as before. The details of the system can be found in [21].

As consequence of the system chosen, the motor is subjected to several constraints and they were specified by the manufacturer as following:

1. The torque and speed characteristics: The motor needs to satisfy operating points specified in Table 1.1.

Operating mode	Engaging clutch			Disengaging clutch		
	time (ms)	speed (rot/min)	torque (N.m)	time (ms)	speed (rot/min)	torque (N.m)
		critical points			critical points	
assisted	160	7290	0.18	400	1800	0.28
non-assisted	385	2050	0.54	400	1800	0.28
		at maximum torque			at maximum torque	
assisted	160	3990	0.33	400	1800	0.28
non-assisted	385	2050	0.54	400	1800	0.28

Table 1.1: Torque and operating time specifications for e-Clutch application.

2. Encumbrance: The maximum diameter (including the casing) is limited to 45.25mm. This is the amount of space available between the clutch diaphragm and its housing.

The maximum length is 150mm including the space that need to be reserved for a speed sensor. A further estimation on the sensor and end-winding size lead to the choice of having an active length of 70mm.

3. Thermal: The maximal temperature subjected to hydraulic actuator is 140°C. The motor has to be able to resists the high temperature considering that the most fragile part is the winding (the maximum admissable temperature is at 220°C for a thermal class H conductor). Furthermore, being installed in the transmission housing, the motor has to be sealed to protect the moving parts from being damaged by dust, oil and eventual used clutch lining. Being sealed, the heat can be easily accumulated in the motor, thus, a low losses motor and thermally robust motor is required.

1.3.2 Design process and final motor design

After looking into different motor options, the Syncrel motor with segmented rotor was chosen mainly due to its thermal and mechanical robustness, the cost and manufacturing feasibility.

The design process was divided in two stages. The first step was to choose discret parameters of the motor such as number of slots per phase and poles pairs $\{N_{spp}, p\}$ in order to have a preliminary design. In the process, an important goemetrical parameter which is the length of the non-magnetic part of the rotor, $l_{non\,mag}$ was highlighted, and therefore fixed following an optimization. The second design step was the determination of the resting continuous geometrical parameters and computation of the resulting inductances L_d and L_q using reluctance network models (Figure 1.9).

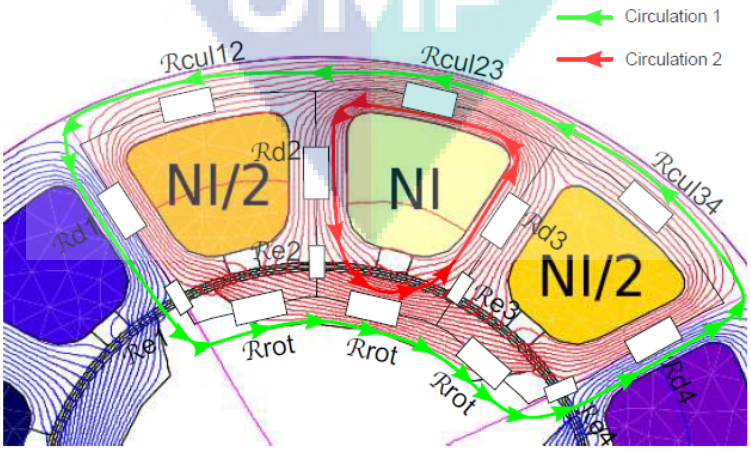

Figure 1.9: A reluctance network used by Doc in [21] to compute L_d and L_q analytically.

The material was chosen thereafter and the L_d and L_q calculated were validated using

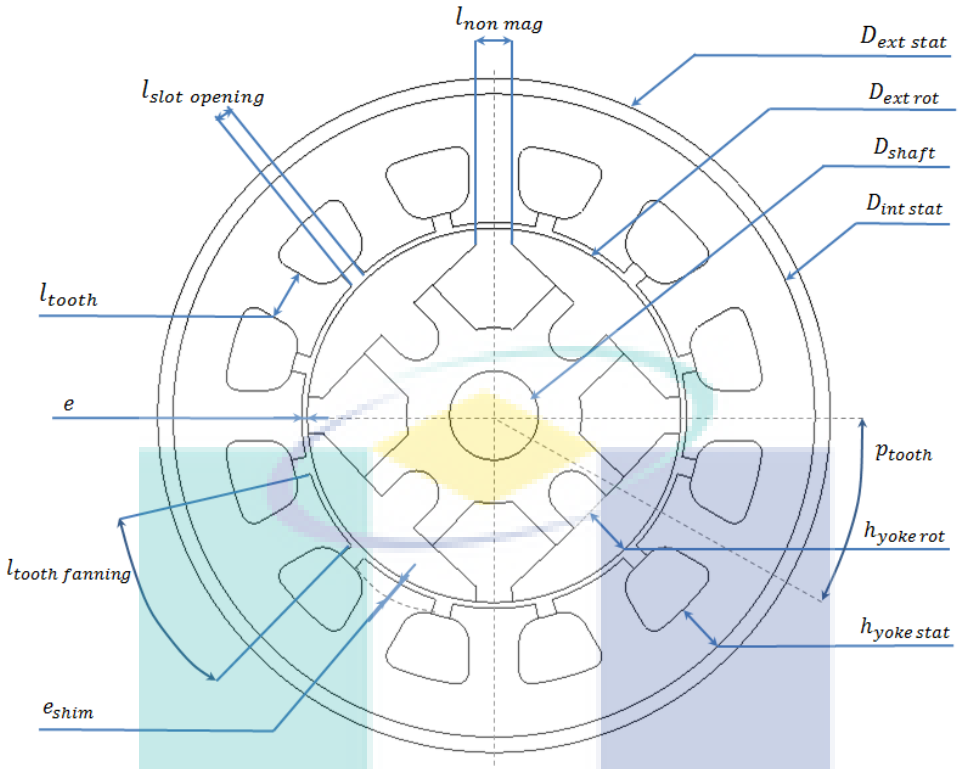

Figure 1.10: Syncrel machine dimensions.

FE analysis. After finishing the design phase, the aspect of system including the relation between different mechanical transmission components and the optimum speed profile choice were carefully taken into account to deduce the critical operating point that the motor needs to reach in order to satisfy the application. The designed motor ability to attain the critical operating points found was verified.

The definitive machine design is shown in Figure 1.10 with thier parameters values can be found in Appendix A.

1.3.3 Prototype motor assembly

A prototype motor was built and handed to the lab to be tested. The construction took into account the manufacturing and assembly feasibility. For example, the stator yoke and the teeth are separated in order to simplify the winding mounting on teeth.

In assembly, firstly, the magnetic rotor segments which are made using stacked iron sheet are mounted together by slotting them into a lightweight aluminum profile with a dovetail assembly (1.11a). Iron sheet is used as to minimize iron loss efficiently, thus helps us decrease furthermore the heat produced. The bearing is then mounted on the rotor assembly. Later, the bearing housing is mounted. The bearing has slots on which the stator teeth are fixed

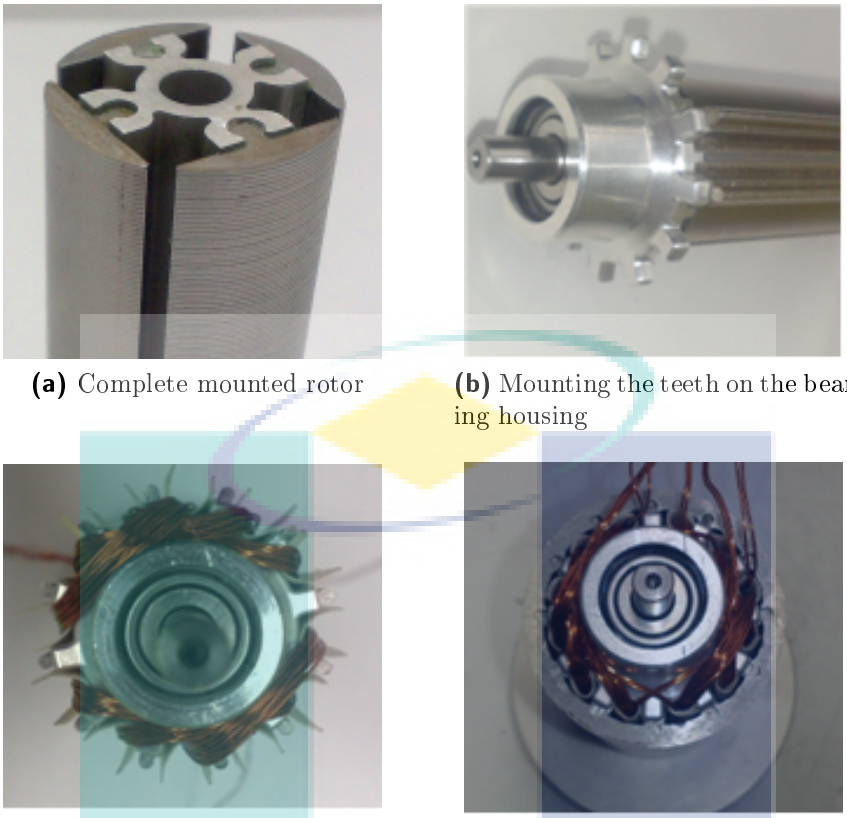

(a) Complete mounted rotor

(b) Mounting the teeth on the bearing housing

(c) Complete winding on the already mounted teeth.

(d) Completed Syncrel motor assembly.

Figure 1.11: The assembly of the Syncrel machine prototype.

(1.11b). Then the 3 winding phases are wounded on the mounted teeth (1.11c). This method allows us to avoid inserting the winding into slots through small slot opening. The rotor-bearing-teeth-winding assembly is then slotted into the stator yoke (1.11d).

The stator winding is mounted in a distributed full-pitch configuration[4] with star connection between the 3 phases are done inside the machine. The 3 phases and the neutral point are connected to a socket which are accessible on the test bench.

The speed control[5] is used as it is more adapted to the e-Clutch application where a certain speed profile was required to actuate the clutch plate. By consequence the current will be regulated in function of the resistance torque and acceleration torque that has to be overcame in order to satisfy the speed profile.

[4]The winding diagram of the machine can be seen in Appendix C

[5]Control diagram can be found in Appendix B

Bibliography

[1] Doppelbauer M., A short history of electric motors, The Institute of Electrical Engineering, Karlsruhe Institute of Technology 8

[2] W.H.Taylor, "Obtaining Motive Power", Patent No.8255, England, 2nd May 1840 9

[3] Tesla, N. A New System of Alternate Current Motors and Transformers American Institute of Electrical Engineers, Transactions of the, 1888, V, 308-327 9

[4] Kostko, J. Polyphase reaction synchronous motors American Institute of Electrical Engineers, Journal of the, 1923, 42, 1162-1168 10

[5] Toliyat H. A., Handbook of Electric Motors, CRC Press 2004, Chapter 2, 142 11

[6] Merrill, F.W., "Permanent-magnet excited synchronous motors", Trans. A.I.E.E., 1955, 74, Part II, pp. 1754–1760 11

[7] Merill F.W., "Dynamoelectric machine magnetic core member" (GE Permasyn motor), U.S. Patent 2,735,952, January 4, 1954 11

[8] J.F.H.Douglas: "The theory of anisotropic field structures in synchronous machines", Trans. American Institute Electric Engineers, 1956, Vol. 75, PT. III, pp. 84–86 11

[9] V.B.Honsinger: "The inductance Ld and Lq of reluctance machines", IEEE Transaction on Power Apparatus and Systems, Vol. PAS- 90, Jan-Feb. 1971, pp. 298–304 11

[10] A.J.O.Cruichshank, A.F.Anderson and R.W.Menzies: "Theory and performance of reluctance motors with axially laminated anisotropic rotors", IEE Proceedings, Vol. 118, No. 7, July 1971, pp. 887–893 11

[11] A.Fratta and A.Vagati: "A reluctance motor drive for high dynamic performances applications", IEEE Trans. On Industry Applications, July-Aug. 1992, Vol. 28, n. 4, pp. 873–879 11

[12] T.J.E.Miller, C.Cossar, A.J.Hutton and D.A.Staton: "Design of a synchronous reluctance motor drive", IEEE Transactions on Industry Applications, Volume: 27 Issue: 4, July-Aug. 1991, pp. 741–749 11

[13] L.Xu, X.Xu, T.A.Lipo and D.W.Novotny: "Control of a synchronous reluctance motor including saturation and iron loss", IEEE Trans, on Industry Applications, Vol. IA-27, No. 5, 1991, pp. 977–985 11

[14] Matsuo, T.; Lipo, T.A., "Rotor design optimization of synchronous reluctance machine," in Energy Conversion, IEEE Transactions on , vol.9, no.2, pp.359-365, Jun 1994 11

[15] Lamghari-Jamal M.-I., Fouladgar J., Zaim E.-H., Trichet D. 2006. A magnetothermal study of a high speed synchronous reluctance machine. IEEE Transactions on Magnetics, Vol. 42, No. 4, April 2006, pp. 1271-1274 12

[16] Fukao T., Chiba A., Matsui M. 1989. Test results on a super-high-speed amorphous-iron reluctance motor. IEEE Transactions on Industry Applications, Vol. 25, No. 1, January/February 1989, pp. 119-125 12

[17] Laporte, B.; Chabane, M.; Sargos, F.M., "Application of a boundary integral method to the optimization of solid rotor machines," in Energy Conversion, IEEE Transactions on , vol.9, no.3, pp.604-612, Sep 1994 12

[18] El Hadi Zaim, M., "High-Speed Solid Rotor Synchronous Reluctance Machine Design and Optimization," in Magnetics, IEEE Transactions on , vol.45, no.3, pp.1796-1799, March 2009 12

[19] Fukao, T., Chiba, A., and Matsui, M.: 'Test results on a super high-speed amorphous-iron reluctance motor', IEEE Trans., 1989, IA-25, (l), pp. 119-125 12

[20] Hassan, S.A., Osheiba, A.M.F., and Mhamadein, A.L.: 'Performance of different types of reluctance motors: experimental comparative study', Elect. Mach. Elerrromech., 1980, 5, pp. 225-236 12

[19] Lawrenson, P.J.; Agu, L.A., "A new unexcited synchronous machine," in Electrical Engineers, Proceedings of the Institution of , vol.110, no.7, pp.1275-, July 1963 13

[20] Lawrenson, P.J.; Gupta, S.K., "Developments in the performance and theory of segmental-rotor reluctance motors," in Electrical Engineers, Proceedings of the Institution of , vol.114, no.5, pp.645-653, May 1967 13

[21] Doc C., “Contribution à la Conception et au Dimensionnement d’un Actionneur d’Embrayage”, Ph.D. Thesis, Université de Technologie de Compiègne, 2010. 13, 14, 15, 16

[22] Mecrow, B.; El-Kharashi, E.; Finch, J. & Jack, A. Segmental rotor switched reluctance motors with single-tooth windings Electric Power Applications, IEE Proceedings -, 2003, 150, 591-599 13

[23] Widmer, J. & Mecrow, B. Optimized Segmental Rotor Switched Reluctance Machines With a Greater Number of Rotor Segments Than Stator Slots Industry Applications, IEEE Transactions on, 2013, 49, 1491-1498 13

[24] Miller, T.J.E., Staton, D.A., and Wood, S.E.: ‘Optimisation of the synchronous reluctance motor geometry’. IEE Conference on Electrical Machines and Drives, London, 1991, UK 13

[25] Niazi, P.; Toliyat, H.A.; Dal-Ho Cheong; Jung-Chul Kim, "A Low-Cost and Efficient Permanent-Magnet-Assisted Synchronous Reluctance Motor Drive," in Industry Applications, IEEE Transactions on , vol.43, no.2, pp.542-550, March-april 2007 13

[26] Obata, M.; Morimoto, S.; Sanada, M.; Inoue, Y., "Performance of PMASynRM With Ferrite Magnets for EV/HEV Applications Considering Productivity," in Industry Applications, IEEE Transactions on , vol.50, no.4, pp.2427-2435, July-Aug. 2014 13

[27] Miller, T.; Hutton, A.; Cossar, C. & Staton, D. Design of a synchronous reluctance motor drive Industry Applications, IEEE Transactions on, 1991, 27, 741-749 13

[28] Matsuo, T. & Lipo, T. Rotor design optimization of synchronous reluctance machine Energy Conversion, IEEE Transactions on, 1994, 9, 359-365 13

[29] Kim, K.-C.; Ahn, J. S.; Won, S. H.; Hong, J.-P. & Lee, J. A Study on the Optimal Design of SynRM for the High Torque and Power Factor Magnetics, IEEE Transactions on, 2007, 43, 2543-2545 13

[30] Moghaddam, R.-R.; Magnussen, F. & Sadarangani, C. Novel rotor design optimization of Synchronous Reluctance Machine for low torque ripple Electrical Machines (ICEM), 2012 XXth International Conference on, 2012, 720-724 13

[31] Cruickshank, A.J.O.; Anderson, A.F.; Menzies, R.W., "Theory and performance of reluctance motors with axially laminated anisotropic rotors," in Electrical Engineers, Proceedings of the Institution of , vol.118, no.7, pp.887-894, July 1971 13

[32] Chandrasekhara Rao, S., "Dynamic performance of reluctance motors with magnetically anisotropic rotors," in Power Apparatus and Systems, IEEE Transactions on , vol.95, no.4, pp.1369-1376, July 1976 13

[33] Chalmers, B.J.; Musaba, L., "Design and field-weakening performance of a synchronous reluctance motor with axially laminated rotor," Industry Applications, IEEE Transactions on , vol.34, no.5, pp.1035,1041, Sep/Oct 1998

13

Chapter 2

Electro-mechanical performance

Overview

In this chapter, the electro-mechanical performance of the segmented rotor Syncrel motor will be studied. The chapter is divided into seven sections.

The chapter starts with a section of a brief presentation on principle of operations of the Syncrel machine.

All the following studies are based on the prototype motor exposed in section 1.3. Therefore, in the second section, the test bench is presented and the conditions and limitations of the test benchare is detailed so as to justify the operating points chosen in different experiments.

The study begins in the third section where the torque-speed area analytical computation tool is presented: the algorithms, input parameters and analytical equations used. The tool is later applied to the Syncrel prototype motor, giving the theoretical torque-speed area of the prototype motor. Validation test done on several operating points is later presented. A subsection treats the robustness of two input parameters of the computation tool which are usually considered as linear and fixed at a theoretical values: direct and quadrature inductance, and the optimum load angle.

The fourth section deals with the power factor of the motor. It starts with the construction of an analytical computation tool and its validation. Subsequently, the computation tool is used to look into influences of different parameters on the power factor.

The fifth section takes advantages of the second and third section to establish interactions between different electro-mechanical parameters. It also proposes two abacus that can help user to navigate between different parameters and understand their influence on each other.

In the last section, the efficiency of the motor was studied by investigating each losses in the motor.

Finally, a comparison between the segmented rotor with two other Syncrel rotor architectures was done. Advantages and inconveniences of Syncrel motor with segmented rotor in different area will be highlighted.

2.1 Principle of operations

From its structure, a Syncrel machine can be seen as a salient-pole synchronous motor without excitation. Just as in a synchronous machine, the Syncrel stator winding is most frequently a three-phase winding with p poles pair which are fed by a balanced three-phase, alternating current at ω_{elec} angular frequency. The three-phase winding create then a magnetomotive force (MMF) rotating at an angular speed of $\omega_{mecha} = \frac{\omega_{elec}}{p}$. The electromagnetic torque are produced by the salient torque exclusively. The energy conversion is done by variations of inductances (self inductance and mutual inductance). These variations are due to the rotation of the rotor which is magnetically asymmetric, between the direct axis (minimum reluctance) and the the quadrature axis (maximum reluctance) (Figure 2.1).

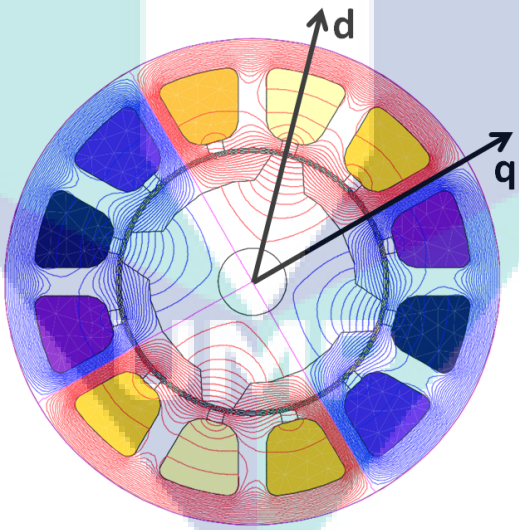

Figure 2.1: Direct axis and quadrature axis of a Syncrel machine with $2p$ poles segmented rotor (in quadrature position).

With an asymmetry between the direct axis and the quadrature axis, the rotor positioned itself accordingly to the rotating MMF. in such a way that the magnetic flux crossing in the airgap presents as minimum reluctance as possible while pulling its load. By rotating, the MMF drag the rotor at the same speed of ω_{mecha}. The angle between the flux axis and the direct axis of the rotor is called load angle, β.

In a steady state, by neglecting the iron losses as generally admitted for stacked core

Syncrel motor [2], the electromagnetic energy can be as Equation 2.1 [2]:

$$W = \frac{1}{2}(L_d i_d^2 - L_q i_q^2) = \frac{3}{8} I_s^2 (L_d - L_q)\cos 2\beta + \frac{3}{8} I_{dq}(L_d - L_q) \tag{2.1}$$

L_d and L_q are direct and quadrature inductances, i_d and i_q are direct and quadrature current, I_s is the RMS current in 3 phases, β is the electrical load angle and I_{dq} is the RMS current of a two-phase equivalent motor in a Park coordinate.

It can be noticed that the energy equation has two part. One part which is independent from β cannot be converted to torque ; it is the magnetizing energy. The other part with $cos2\beta$ which its amplitude is proportional to the difference $L_d - L_q$ can be converted to electromagnetic torque. The torque is obtained by deriving the energy in function of the rotor position $\frac{\beta}{p}$:

$$\Gamma = \frac{\partial W}{\partial(\frac{\beta}{p})} \tag{2.2}$$

Thus,

$$\Gamma = \frac{3}{2} p(L_d - L_q) I_d I_q = \frac{3}{4} p(L_d - L_q) I_s^2 \sin 2\beta \tag{2.3}$$

It can be seen that the maximum torque is attained when $\beta = 45°$.In this particular case, the torque can then be written as:

$$\Gamma_{max} = \frac{3}{2} p(L_d - L_q) I_s^2 \tag{2.4}$$

From Equation 2.4, it is shown that the torque depends directly to the $L_d - L_q$ difference. It reflects the fact that the torque production takes origin from the asymmetry between the direct and quadrature axis of the machine; also called the saliency of the machine. In order to maximize the torque of the Syncrel machine, it is then necessary to have a rotor structure leading us to the highest $L_d - L_q$, or in other words, maximizing L_d and minimizing L_q.

The saliency ratio $^{L_d}/_{Lq}$ has also been shown to play major role on power factor. It is defined by Equation 2.5 [2].

$$cos(\varphi)_{max} = \frac{X_d^2 - X_q^2 + 4R_s\sqrt{X_d X_q + R_s^2}}{(X_d + X_q)^2 + 4R_s^2} \tag{2.5}$$

By neglecting the winding resistance, an approximation of the power factor in function of the ratio saliency as in Equation 2.6 can also be found in litterateurs [2, 5]:

$$cos(\varphi)_{max} = \frac{\frac{L_d}{L_q} - 1}{\frac{L_d}{L_q} + 1} \tag{2.6}$$

2.2 Description of the test bench

After having presented the principles of operations of a Syncrel motor, different electro-mechanical characteristics of our prototype motor will be evaluated theoretically and then validated experimentally. Before going through each electro-mechanical characteristics and their validation, it is necessary to present the prototype motor test bench and clarify the validation test that can be done and their limitations.

Various devices (power, control, measurement and real-time observation) were fitted to the prototype machine in order to make evaluation on various aspects of the motor. The test bench configuration can be seen in Figure 2.2.

The motor is equipped with an incremental encoder with 500 points of resolution and the signal is treated by a Microautobox digital signal processor system with multiples other signals. Other signals tha are processed include the currents in the three phases of the winding, the winding and the casing temperature and the speed. All of the parameters can be observed in real time using the Dspace Control Desk environment Figure 2.3 and registered for later data exploitation. Some of control parameters such as the speed (in speed control mode), and other correctors can also be modified in real time. The power electronic is assured by the Rapid Pro power unit.

Despite having the advantage of a compact and fast prototyping system for in-vehicle applications, there is however an inconvenient: the current in the Rapid-Pro switches is limited to 30A in transient phase whereas the motor was designed for a maximum current of 50A. For further security, the peak current attainable is limited to 20A by software. Not all operating points of the motor can therefore be tested. The resistance of the connection between the output of the Rapid-Pro power unit and the motor winding is around 30mΩ and the resistance of each switch is around 15mΩ. This allows us to take into account the voltage drop and deduce the real voltage at the winding terminal.

To make a load test possible, a hysteresis brake is used (Figure 2.2). The main criteria that lead to its selection instead of a motor (used in generator mode) is the lack of mechanical friction. Knowing that our motor has a low torque capacity (maximum of 0.58 theoretically), small variation of torque need then to be tested. A high mechanical friction in the load machine will make this impossible. Besides, there are several other advantages: the simplicity of the control (the braking force is in function of the current supply), and the torque smoothness and independence of speed in a very large speed range.

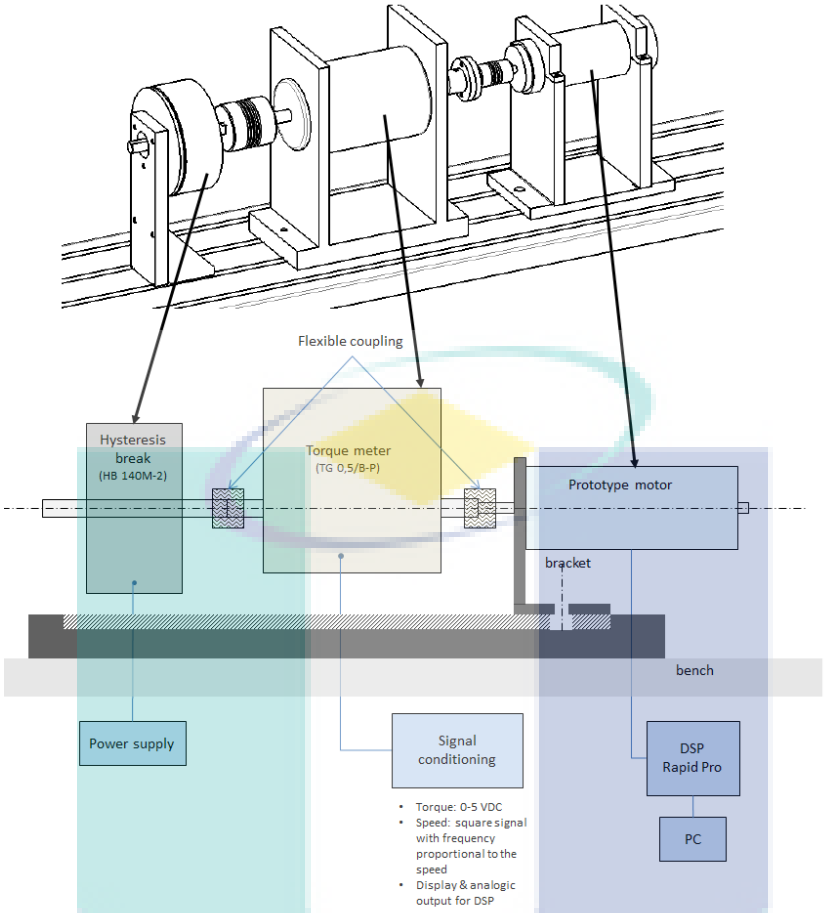

(a) The test bench configuration.

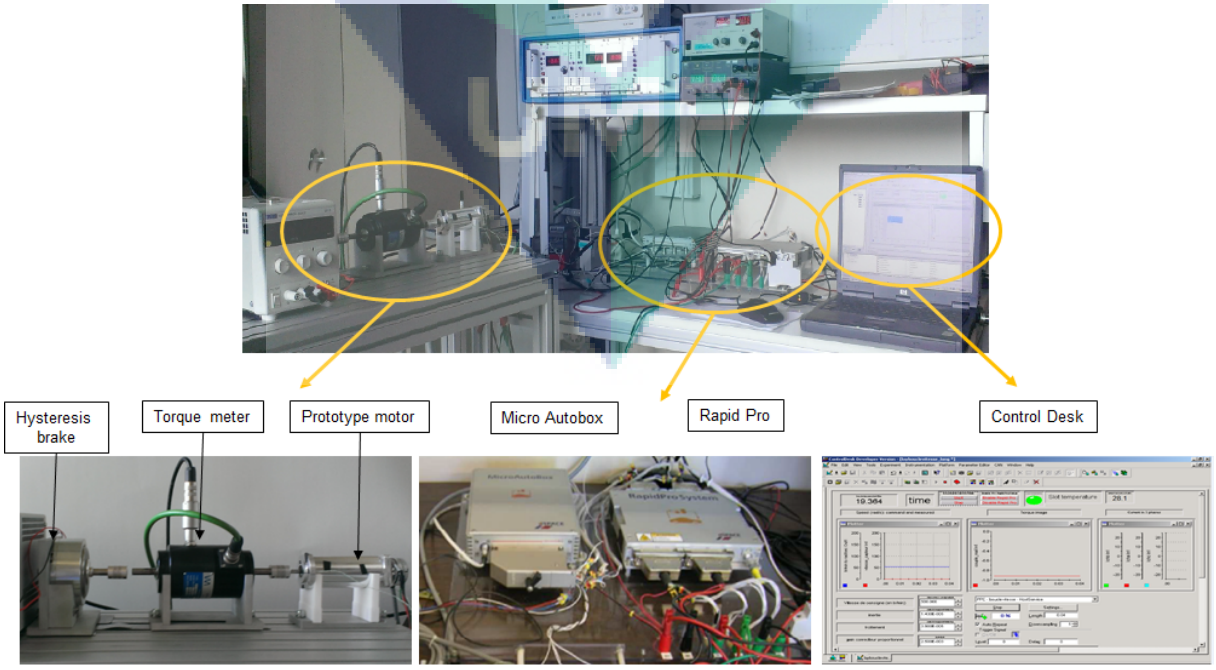

(b) The completely mounted test bench .

Figure 2.2: The prototype motor test bench.

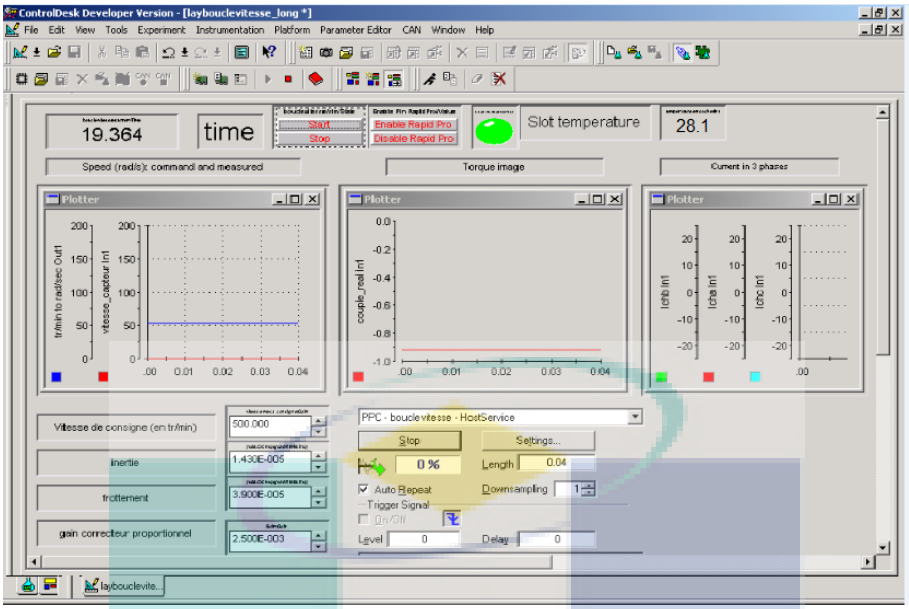

Figure 2.3: The Dspace Control Desk environment: showing the real-time observation on current, speed, torque image and winding temperature.

The torque measurement is assured by a torquemeter with a precision of ±0.01N.m. The torque displayed on the device is compared with the torque image calculated by Microautobox in real-time using the current information. This helps to verify that the theoretical torque corresponds to the real torque delivered by the motor shaft.

Two thermocouples were installed in a slot and on the motor's casing surface to observe the temperature and prevent any over-heating, thus the destruction of the prototype. The insulation used in the motor's conductor was rated at a temperature index of 220°C.

2.3 Torque-speed characteristics computation

In this section, the development of an analytical tool allowing the mapping of torque-speed operating area of a Syncrel motor will be explained. The main objective of the tool is to be able to establish the torque-speed $(N;\Gamma)$ performance of a Syncrel motor in function of its topology (L_d, L_q R_s), the control (load angle β) and the power supply limitation (I_{max} and U_{max}, which depends on the application). The tool will be tested and validated using the parameters of our Syncrel prototype motor. A valid tool will make it possible to Syncrel motor designer to optimize their operating area in function of options that they have regarding motor topology, the control and power supply (Equation 2.7).

$$(N,\Gamma) = f(L_d, L_q R_s, \beta, I_{max}, U_{max}) \tag{2.7}$$

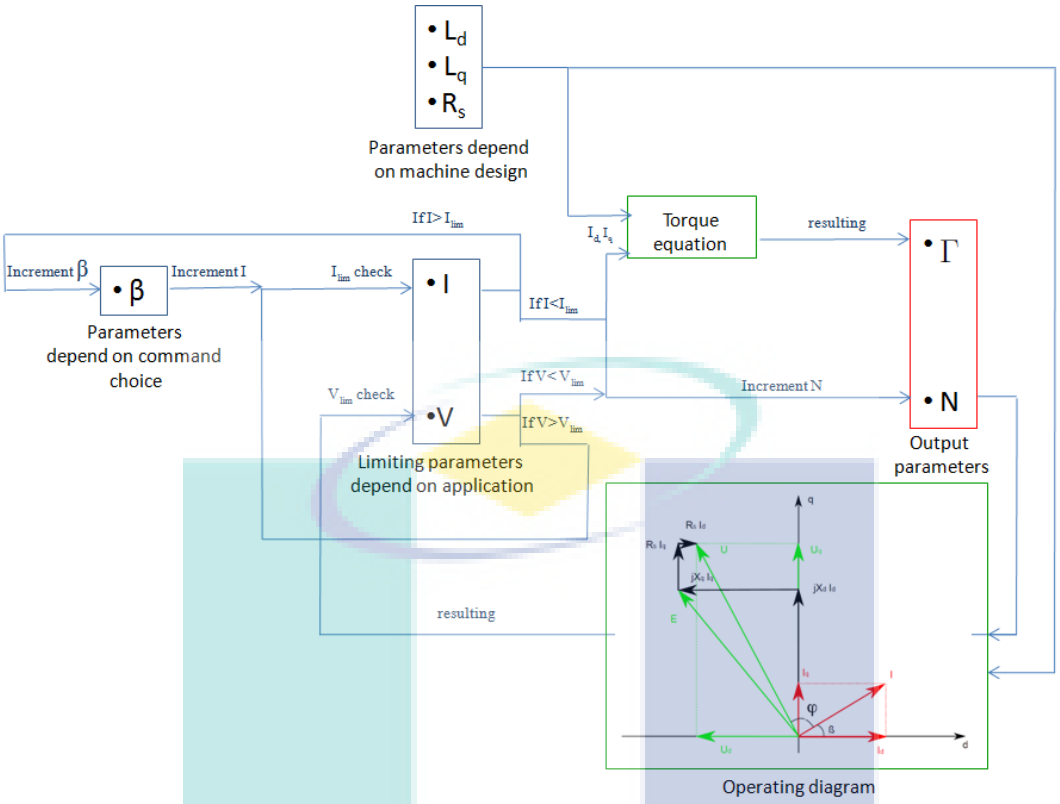

Figure 2.4: The algorithm used for the construction of the torque speed area of the machine.

The computation algorithm of the tool can be explained by the diagram presented in Figure 2.4. The operating points which are pairs of speed-torque (N, Γ) (presented in red boxes in Figure 2.4) can be obtained using two main analytical tools which are the torque analytical equation (Equation 2.8) and equations extracted from the operating diagram of a Syncrel machine (Figure 2.5) .

$$\Gamma = \frac{3}{2} p (L_d - L_q) I_d I_q \tag{2.8}$$

This operating diagram takes into account only copper losses considering that it is generally admitted that copper losses tend to dominate iron losses in an AC machine . Both of these analytical sets of equations are presented in green box in Figure 2.4.

The input parameters of the computation tool are presented in blue boxes. They are the determining parameters that will shape the torque-speed characteristics of a given Syncrel motor. They can be divided into 3 categories as following:

1. Parameters that depend on the machine design: the direct and quadrature inductance (L_d and L_q), and the stator winding resistance (R_s).

2. Parameters that depend on the control of the machine: the load angle (β).

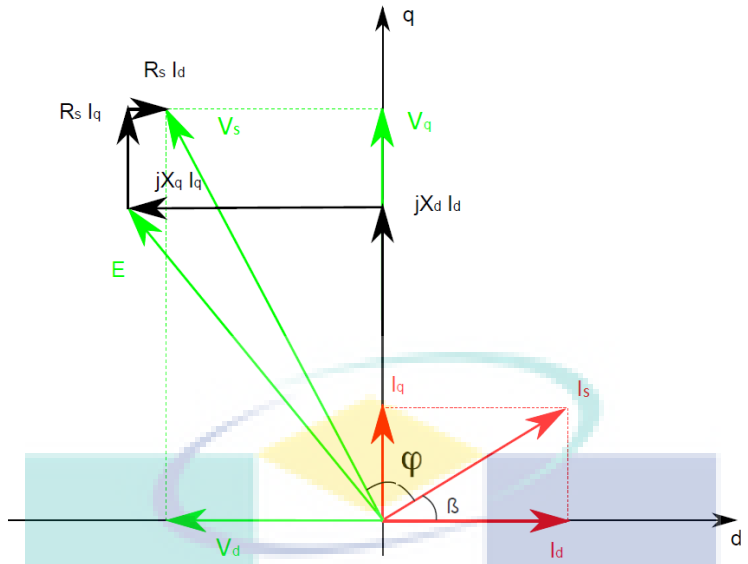

Figure 2.5: The Syncrel motor operating diagram [1].

3. Parameters that depend on the application environment: power supply limitation (I and V).

With all the input and analytical tools in place, the computation of (N;Γ) pairs will be done through three nested loops: the load angle loop, the current-torque loop and the voltage-speed loop. The computation will begin with the initialization of the load angle β. At the given load angle, the supply current $\hat{I}$ is incremented and checked if it surpass the $\hat{I}_{lim}$. If it is under the maximum value, then the corresponding I_d and I_q are calculated (Equation 2.9 with $I_s = \hat{I}$).

$$\begin{aligned} I_d &= I_s cos(\beta) \\ I_q &= I_s sin(\beta) \end{aligned} \tag{2.9}$$

Next, using the calculated I_d and I_q, the torque produced at this current level can be calculated using Equation 2.10.

$$\Gamma = \frac{3}{2} p(L_d - L_q) I_d I_q \tag{2.10}$$

For this torque level, the speed of the motor will be incremented until it attain the voltage supply limit. This is done by incrementing the speed ω in Equation 2.11 which was deduced from the operating diagram.

$$V_s = \sqrt{(R_s.I_d - \omega.L_{q.}I_q)^2 + (R_s.I_q + \omega.L_{d.}I_d)^2} \tag{2.11}$$

The loop will be repeated until the voltage $\hat{V}$ reaches $\hat{V}_{lim}$ (with with $V_s = \hat{V}$). With this being done, the speed loop reach its end. All the speed attainable within the voltage limitation at the first torque incrementation level is now traced (Figure 2.6a).

The algorithm will now go back to the current-torque loop and continue the current incrementation, calculate the corresponding torque before going again into the voltage-speed loop to retrace all the speed attainable within the voltage limitation (Figure 2.6b). The current-torque loop incrementation will be terminated once the maximum current is reached. At this point, a complete torque-speed area at a given load angle is fully traced (Figure 2.6c). Other torque-speed area in function of different load angles can be traced by incrementing the load angles.

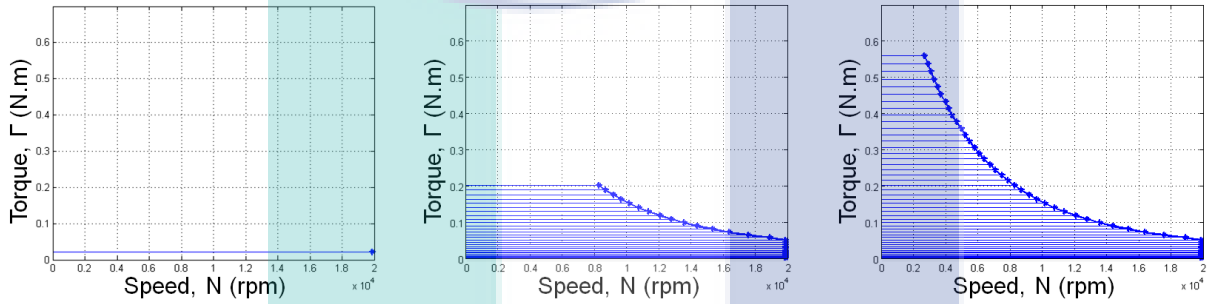

(a) First incrementation of the current-torque loop followed by incrementation of speed-voltage loop until the voltage limit reached.

(b) Incrementation of current-torque loop followed by incrementation of speed-voltage loop in progress as long as the current limit is not reached.

(c) All the operating points traced once the current limit is reached.

Figure 2.6: At $\beta = 45°$, the execution of the calculation algorithm would give the sequence (a) (b) and (c).

2.3.1 Application on Syncrel prototype motor

With the operating area computation tool being programmed, the operating area of our prototype motor for e-Clutch application can now be evaluated. As for the input parameters, they are determined as following:

1. Motor-design dependent parameters: L_d and L_q was found using reluctance network model with linearity hypothesis, as explained in subsection 1.3.2 ($L_d = 0.255$mH, $L_q = 0.110$mH). As for R_s, it was measured on the prototype motor ($R_s = 0.22\Omega$).

2. Control dependent parameters: the load angle β will be tested at different values: $25°, 35°, 45°, 55°, 65°, 75°, 85°$

3. Application environment dependent parameters: $\hat{I}_{lim}$ and $\hat{V}_{lim}$ is set at the automotive battery power supply limitation ($\hat{I}_{lim}$=50A, $\hat{V}_{lim}$ = 14V).

As results, the following torque-speed operating areas are obtained (Figure 2.7).

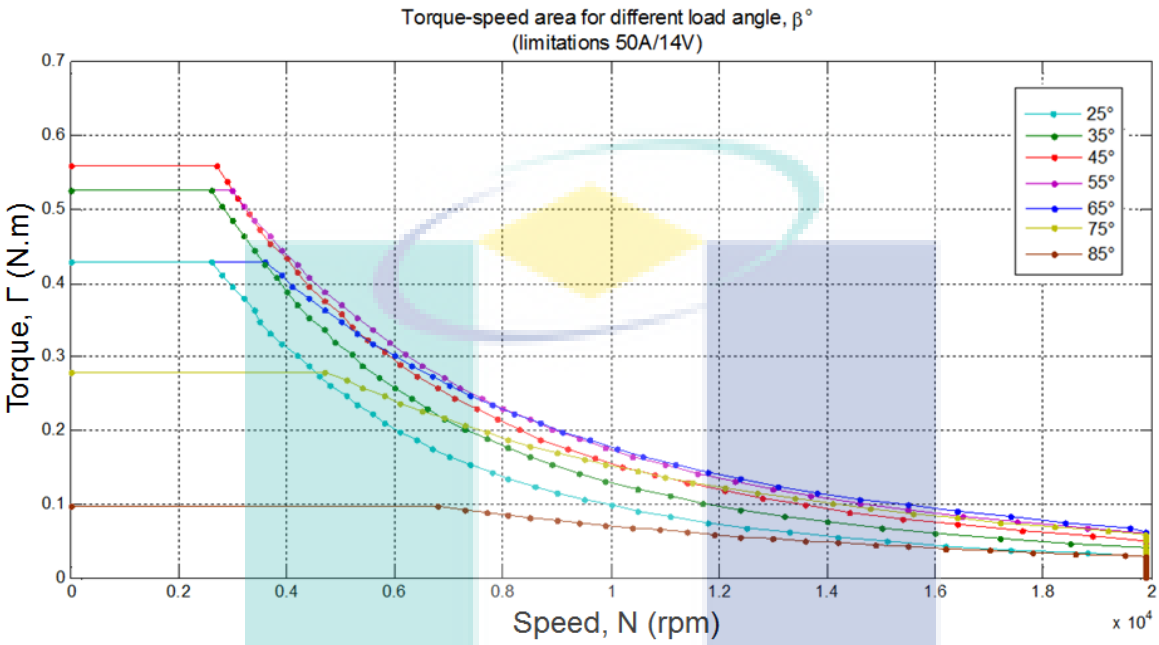

Figure 2.7: Computed torque-speed area of the prototype Syncrel machine.

Three operating area limits can be identified:

1. Current limitation area: the torque plateau that can be found in low speed range. These area can only be extended into a higher torque level by increasing the current.

2. Current and voltage limitation area: These are the tipping points between the plateau and the curvature in the torque-speed area. These are points where the maximum power is developed by the motor at a given load angle.

3. Voltage limitation area: These are the curvature lines limiting the speed of the motor. In order to go to a higher speed (extension of the curve to the right), the option is either to make available a higher voltage supply, or to change the load angle to the one that can give a higher speed. The later is at the cost of having a higher current, thus a higher copper losses.

Regarding the simulation results on our Syncrel prototype motor, it can be seen that for a speed less than 2700 rpm, at an equal current input, the maximum torque can only be

achieved at $\beta = 45°$[1]. This is expected as it is the theoretical optimum load angle that can be deduced from Equation 2.10, without taking into account the voltage limitation. Thus, it is the optimum load angle for the lower speed range that will give the highest range of torque and generate the less copper losses. The computed maximum torque is 0.58N.m.

At speed higher than 2700 rpm, the torque-speed characteristic is less predictable than a rotor-excited motor. In rotor-excited motor such as PMSM, it is a usual practice to reach a higher speed by changing the load angle β to generate a direct current in such a way that the rotor flux will be weaken. However, for Syncrel motor, reaching higher speed does not necessarily means that the load angle need to be changed. It does not behave like a permanent magnet machine by reducing the direct current I_d because the torque produced in the motor is a pure reluctance torque and not produced by rotor field reaction. It can clearly be seen in Figure 2.7, that by increasing I_q (increasing the load angle β), the machine can not necessarily attain a higher speed (e.g: $\beta = 35°$). Most of the operating points attainable by the motor can be attained at the same load angle, $\beta = 45°$.

2.3.2 Validation test

The analytical tools shows that the Syncrel motor is theoretically capable of going into high speed and have a relatively high torque at its optimum load angle which is $\beta = 45°$. In this section, the analytical model as well as the tool used to establish the torque-speed operating area of the prototype motor will be validated. At the same time the performance of the prototype Syncrel motor can be evaluated exhaustively. In order to do so, several operating points in the theoretical torque-speed area will be tested relating (I, V) and (Γ, N).

Taking into account the test bench limitation as explained in section 2.2, the area that will be tested is going to be limited in torque by the maximum current deliverable by the test bench system which is 20A. The speed tested is also limited to 5000rpm because the mechanical strength of the dovetail-rotor structure regarding centrifugal force has never been tested for high speed.

The validation test was done with the motor operating at a constant speed using a speed profile as shown in an example illustrated in the left of Figure 2.8. The speed profile is subjected to the machine using a speed control command[2]. During the long steady speed phase, the brake was actuated step by step, demanding different levels of torque in increasing order (right side of Figure 2.8) until the maximum torque deliverable by the motor in the test bench set up is reached. The theoretical maximum torque deliverable due to the test bench

[1]The limit of load stability is also situated at this angle. For a load angle exceeding 45°, the rotor will become unstable. The computed load angle of 55°, 65°, 75° and 85° will never be used.

[2]The control diagram can be found in Appendix B

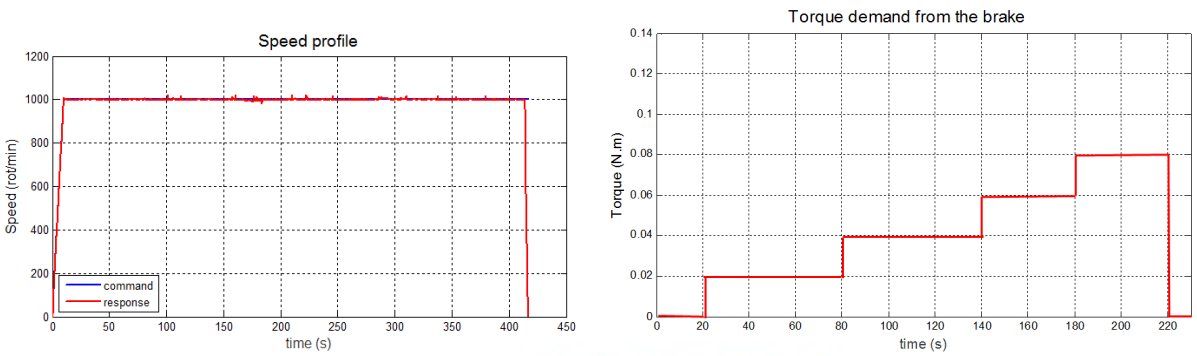

Figure 2.8: Left: The speed profile used to validate the motor operating points. Right: Torque demand from the brake.

current limitation (20A) was found to be at 0.09N.m. With the test speed limited to 5000rpm, the validation operating area has been reduced to $(\Gamma_{max}, N_{max}) = (0.09\text{N.m}, 5000\text{rpm})$. We will see later in subsection 2.3.3 that the limited validation points are not problematic as they will be double-checked and validated using FE analysis. The validation can then be extrapolated to a larger (Γ, N) range provided the linearity hypothesis is considered valid.

2.3.2.1 Friction torque identification

As mentioned in section 2.2, there are two means of torque measurement: the torquemeter which measure the torque directly on the shaft, and the torque image which is calculated on the PC using the current information treated in Microautobox. Knowing that the electromagnetic torque will have to overcome the friction torque and the demanded mechanical output torque ($P_{emag} = P_{output} + P_{friction}$), identification of the friction torque will allow a correct comparison, thus validation. To estimate the motor and the test bench set up friction, a no-load test was carried out in two configurations: with the brake and torquemeter connected and with the motor alone. The torque is deduced using the torque image calculated from the current information.

The results in Figure 2.9 shows the torque image, with the load system connected (red) and not connected (blue). It can be seen that the motor alone has some resistance torque. It appears to be relatively linear in function of speed, leading to a conclusion that the friction is predominantly dry friction. The dry friction observed could come from imbalance due to the positioning of the speed sensor which is on the overhang side of the motor. Compared to the maximum theoretical torque deliverable by the motor which is at 0.58N.m, the resistance torque at around 0.01N.m can be considered low (1.8% of the maximum torque). This also means that torque precision less than ±0.01N.m cannot be attained with the prototype motor.

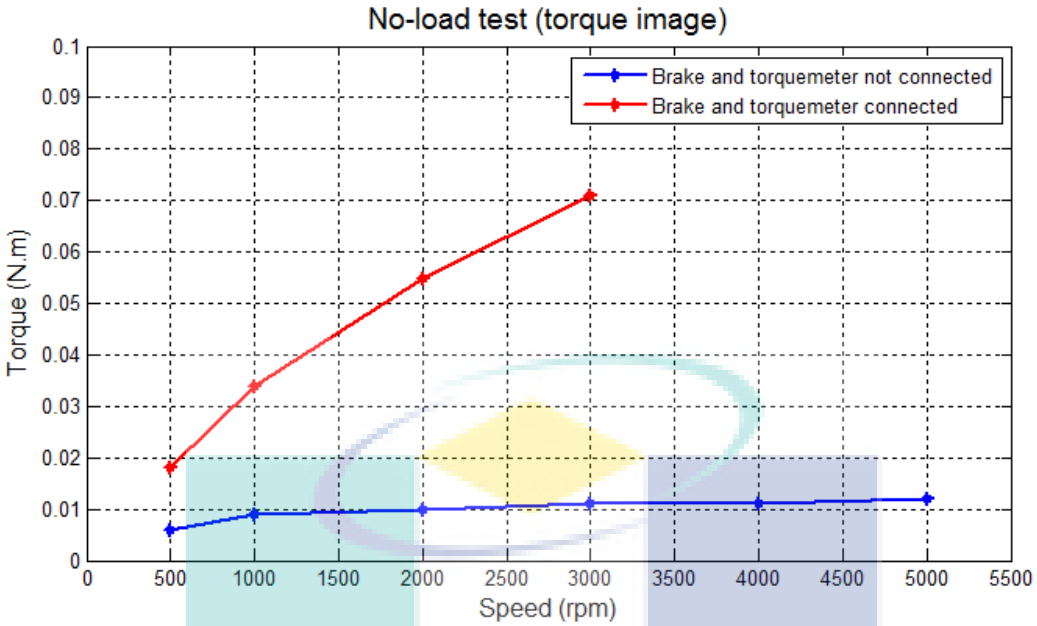

Figure 2.9: No-load tests show resistance torque due to friction in the motor (blue) and in the complete brake-connected test bench (red).

For the complete test bench where the torquemeter and the brake are connected to the motor shaft, the resistance torque is higher and increase in function of speed. It is also relatively linear except with a higher friction increase rate in function of speed. The hysteresis brake itself has near-zero friction while the torquemeter has some friction. The main cause might come from the misalignment of the motor, torquemeter and the brake shafts in the setup. For the validation test, the source of the friction is unnecessary to be determined as long as the resistance torque of the test bench in function of speed is now known.

2.3.2.2 Torque-speed area validation

With the friction of the test bench determined, torque-current relation computed can now be validated by comparing the torque image and the measured torque at different torque levels. Figure 2.10 shows an example of comparison between magnetic torque image in blue (calculated from the current) and measured mechanical output torque in green (measured using torquemeter) at N=500rpm. Two observations were made:

1. At a given speed, the average magnetic torque and the measured output torque has a constant difference $\triangle\Gamma = \Gamma_{c_i} - \Gamma_{m_i}$ at all torque levels. This has been predicted using the no-load test presented in subsubsection 2.3.2.1 where $\triangle\Gamma$ can be attributed to the friction in the test bench set-up. In this example at N=500rpm, $\Gamma_{c_i} - \Gamma_{m_i}$ is

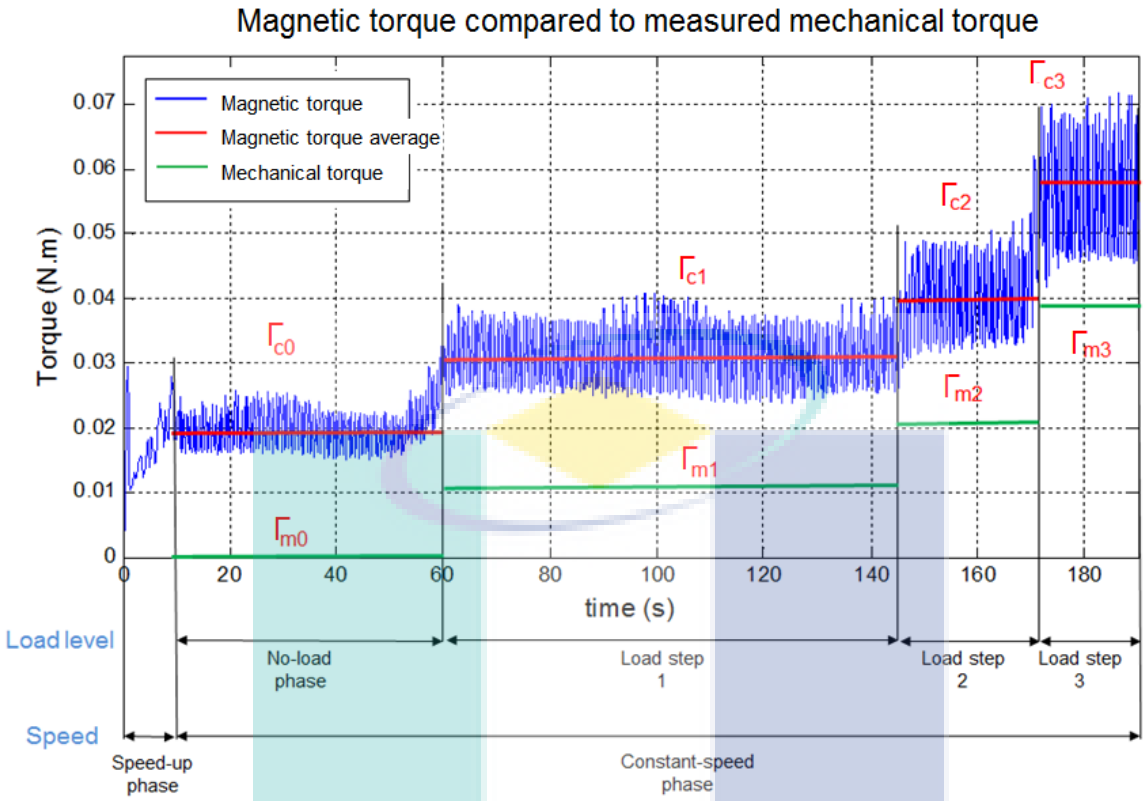

Figure 2.10: Demand in torque at N=500rpm (mechanical torque T_{m_i} measured using the torquemeter and electromagnetic torque T_{c_i}calculated from the current image).

equal to 0.02N.m which correspond to the friction torque found in Figure 2.9 (red line). With the friction torque taken into account, we find that $\Gamma_{c_i} - \Gamma_{m_i}$. All the current points tested for validation are shown in Figure 2.11a and all the measures match the torque image calculated. Following the results, torque-current relation was validated on different operating points and therefore robust.

2. As for voltage-speed relation, it is validated by comparing the measured and computed voltage fed to the machine at different operating points. These operating points are attained using the same speed control in Figure 2.8. Knowing the voltage drop between power electronic stages and the motor, the voltage measured on a phase of the motor should be equal to the voltage commanded by the speed control. At a given speed, the voltage commanded by the speed control is then used as the measured voltage V_m. The computed voltage V_c on the other hand was deduced from the computation tools used to deduce the torque-speed operating area. For a given operating point $(\Gamma_i : N_i)$, by entering the corresponding current (giving Γ_i), resistance and limiting the speed to N_i, V_c can then be computed. The resistance need to be remeasured at

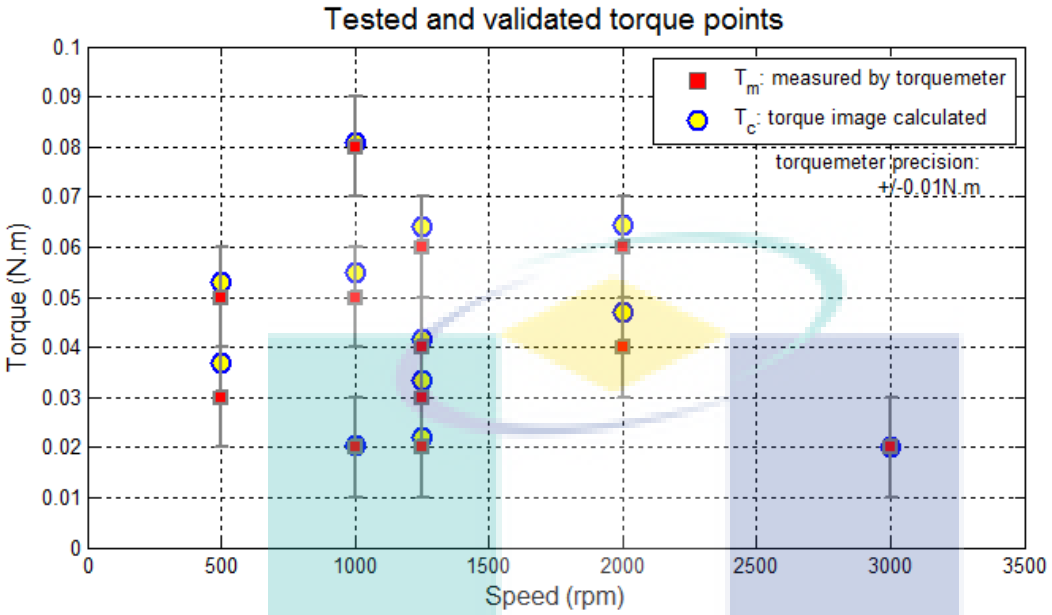

(a) Torque points validated in dynamic test. Remark: the current points tested is limited to 3000rpm due to the test bench friction torque that is superior to the maximum torque deliverable for higher speed.

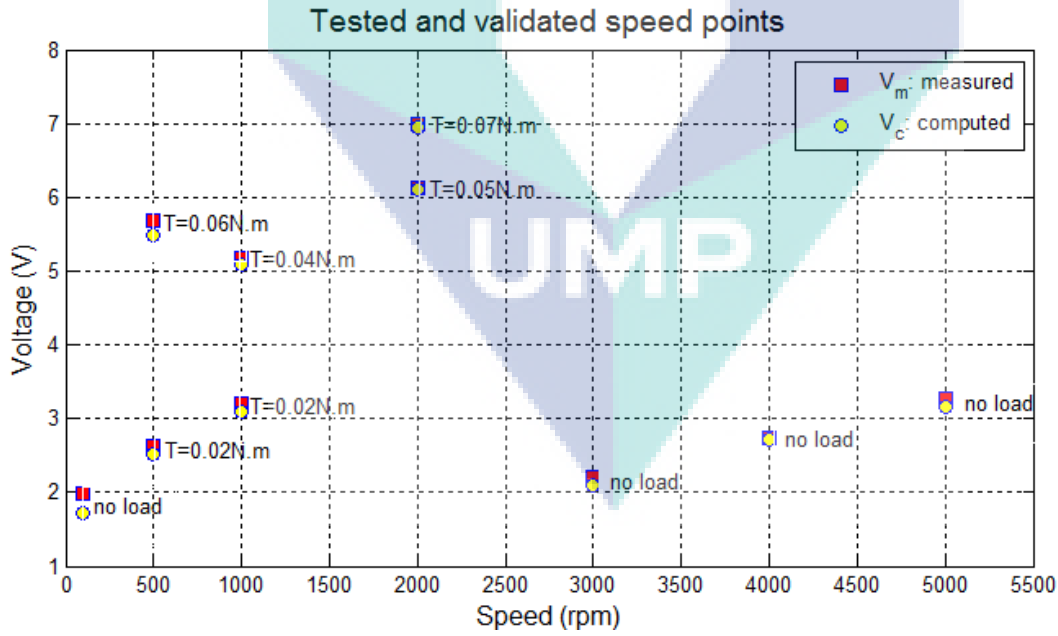

(b) Speed points validated in dynamic test.

Figure 2.11: The torque-speed area experimental validation.

each operating points as its values rises in function of temperature due to the speed profile and different load level demanded. The results obtained are reported in Figure 2.11b. It can be seen that the measured voltages match the computed voltages thus, the voltage-speed relation can be validated.

2.3.2.3 Conclusion

The torque-speed characteristic computation tool has been validated on different operating points despite the limited operating area. The validation can be extrapolated to a larger operating area with two conditions:

1. The winding resistance during operation can be measured: The increase of winding resistance due to heat generated from copper losses will increase the voltage demand in order to attain a speed point. Therefore, in function of utilization cycle, the maximum speed attainable with the available voltage supply can decrease. The variation of the winding resistance in function of temperature as well as its effect on the speed range will be treated in subsection 2.6.1. The operating area presented in Figure 2.7 represents then an approximation in hypothetical case where the winding resistance is constant. A more precise operating area can only be achieved by knowing the torque-current profile subjected to the motor in order to compute the temperature rise due to copper losses. Once the torque-current profile is known, the winding resistance variation can be injected into the computation tool to obtain the precise operating area.

2. L_d and L_q are constant: It is important to make sure that no generalized saturation occurs, especially in the high end torque. In case of important saturation, the variation of inductance, especially L_d need to be taken into account in the computation (L_q does not usually vary much as it is in non-magnetic direction). If a motor is designed in the limit of linearity, minor local saturation that could still occurs in certain geometry will not affect the attainable predicted torque. A further validation test in the high torque end can be necessary if the critical point in the pre-design process happens to be in that area.

With the computation tool validated for this prototype machine, it can then be used to evaluate the operating areas of different Syncrel motors with other power supply limitation.

As for our prototype Syncrel motor, it has been shown to be capable to satisfy the electric clutch application requirement (speed of 7000rpm at 0.2N.m of torque)

2.3.3 Robustness of linear analytical input

In the computation tool exposed and validated in the previous section, it has been shown that there are three input parameters that influence directly the operating area range of the Syncrel motor. This section will treat the difficulties on determining two of the three[3] input parameters: L_d and L_q, and the optimum load angle β regarding their precision and the error that they could generate on the torque prediction. Each parameter will be deduced using FE analysis and later compared to the ones found analytically (used in previous computation presented in subsection 2.3.1).

2.3.3.1 Inductance L_d and L_q

L_d and L_q are the torque defining parameters for a Syncrel motor. In subsection 1.3.2, it was mentioned that L_d and L_q used in the computation of torque-speed area were found using a reluctance network model done by [1]. In this study, the reluctance network model is based on hypothesis that the material is linear. Using the $B = f(H)$ magnetization curve (Figure 2.12) of the steel sheet, we are comparing the resulting inductances of linear and non-linear material. The comparison is detailed in Table 2.1.

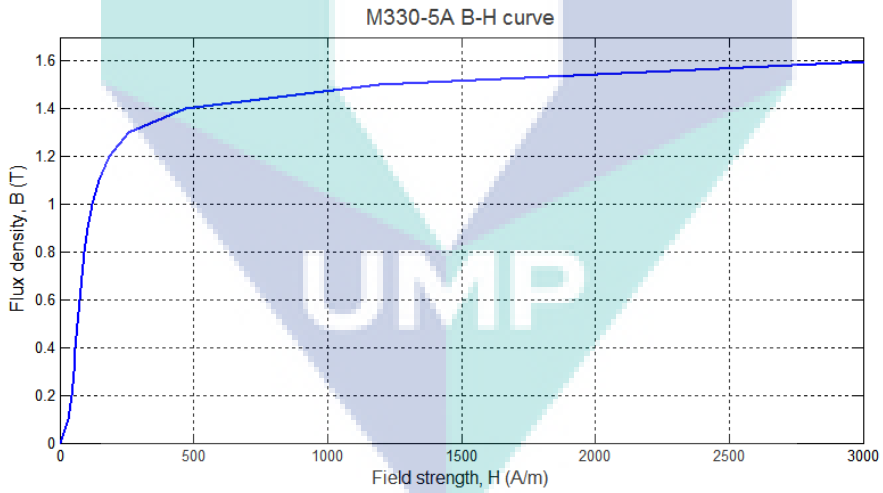

Figure 2.12: $B = f(H)$ curve of the material M330-50A provided by manufacturer (Surahammarsbruk).

The comparison shows that L_d and L_q found thanks to FE analysis using linear material match the ones found using analytical model with a good precision. Whereas in non-linear material, non-negligible difference on L_d can be observed starting from a current between 20A and 30A. L_q matches at all points. For linear material, there will be simply no saturation,

[3]The power supply (I and V) will not be treated as their precision depends on the power source options.

Inductance	Analytical model [2]	FEM					
		linear material	non-linear material				
			Current, I_s (A)				
			10	20	30	40	50
L_d (mH)	0.2590	0.2544	0.2544	0.2544	0.2496	0.2492	0.2485
L_q (mH)	0.0994	0.1015	0.1015	0.1015	0.1015	0.1015	0.1015

Table 2.1: Direct and quadrature inductance in different model found using FE analysis. The method used to deduce the inductances using FE analysis are described in [6].

thus leading to continuous increase of flux density in function of current, resulting to a higher inductance in direct direction. For non-linear material, minor saturation occurs starting from at a current between 20A and 30A (Figure 2.13), affecting the global flux density, thus reducing L_d.

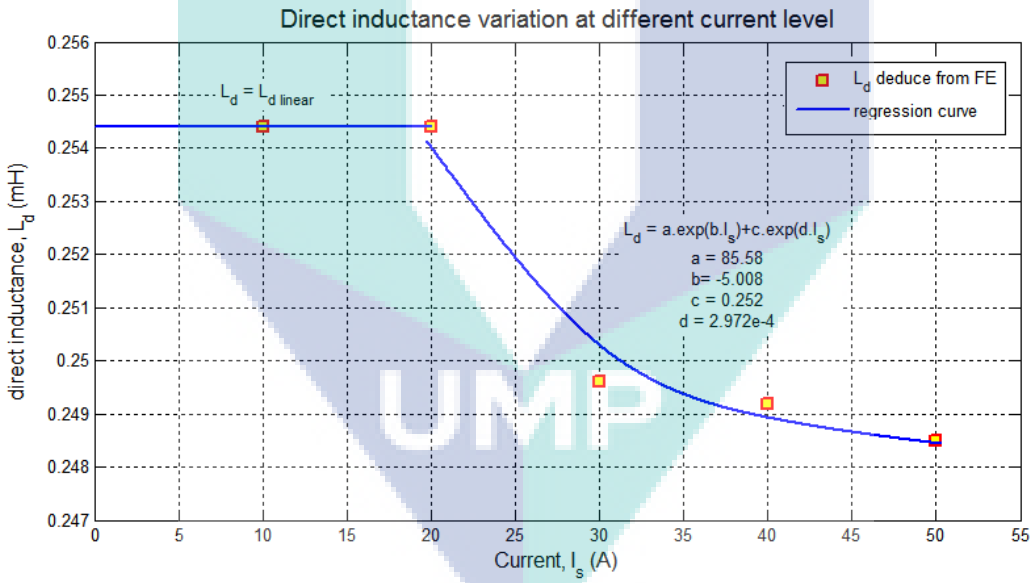

Figure 2.13: Direct inductance variation deduced from FE analysis showing the effect of material saturation. Minor local saturation affects direct inductance starting from a current between 20A and 30A.

The error is however very small as the motor was designed to be at the limit of saturation when it is in the maximum torque position at maximum current (2.37% of induction error at maximum current). In quadrature direction, the same L_q was found because most of the flux pass through the air where the non-linearity of the material does not have any impact. It can be summarized that the simplification on non-linearity of the material can directly

affect L_d starting from a certain current level. L_d will then decrease in a pattern shown in Figure 2.13, thus decreasing the torque proportionally.

The effect of direct inductance error on the torque computation at different current level is illustrated in Figure 2.14. Having computed the resulting torque for both linear and non-linear material, the proportionality between direct inductance error and torque error for the prototype motor can be established (Figure 2.15).

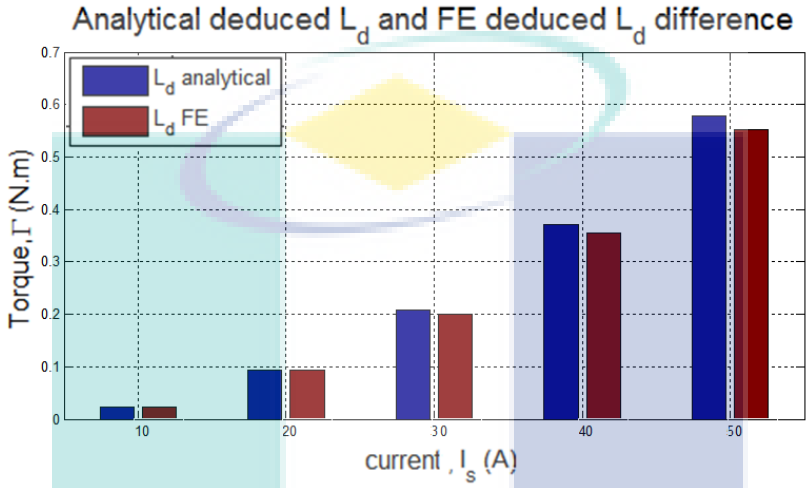

Figure 2.14: Torque in function of L_d and I_s for linear and non-linear material.

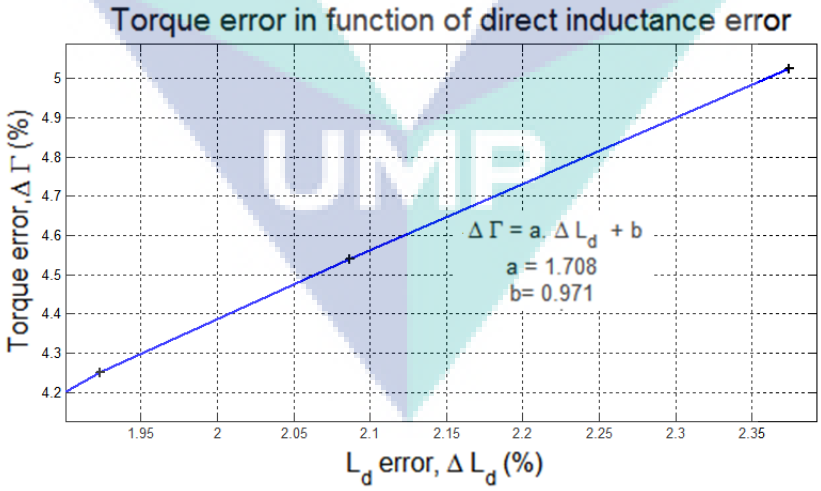

Figure 2.15: The proportionality between torque computation error and the direct inductance error.

With the direct inductance variation curve (Figure 2.13) and the proportionality between direct inductance error and torque error curve (Figure 2.15), a tool relating the current and the torque error can therefore be provided (Figure 2.16).

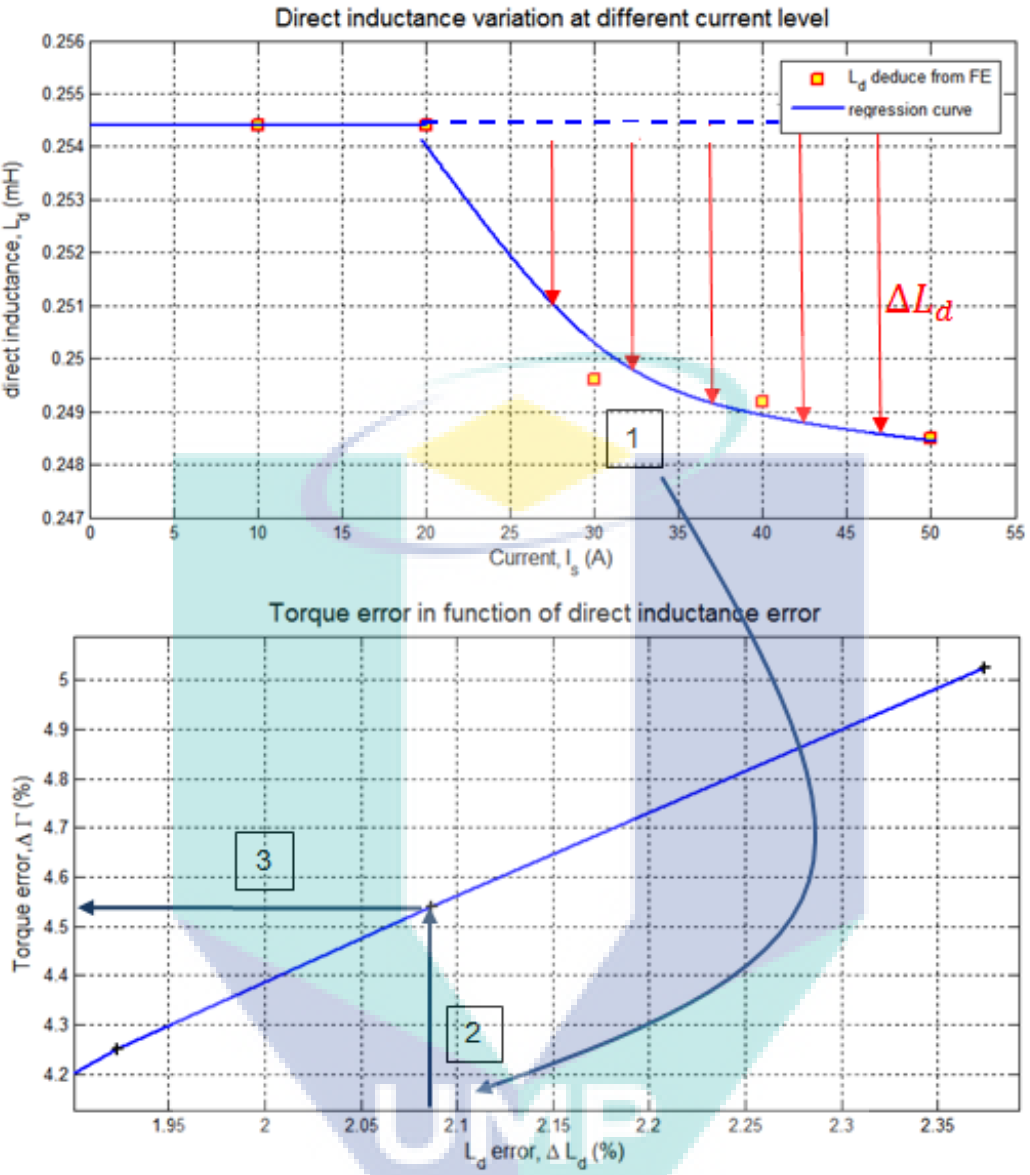

Figure 2.16: Tool helping the deduction of torque computation error in function of current due to linearity hypothesis. The tool functions through 3 steps.

In function of current, the tool will first compute the direct inductance error $\triangle L_d$ using the top graph (step 1), then it will calculate the percentage of error compared to the inductance in non-linear material (step 2), and finally find the torque error using the bottom graph (step 3). Using the updated tool integrating the material non-linearity, the torque-speed area with non-linearity considered can be traced Figure 2.17.

Each point in the torque-speed operating area with material non-linearity taken into account can now be found thanks to a fast analytical tool. Regarding the Syncrel prototype motor, it can be seen that the maximum torque difference is merely at 4.1% and the maximum

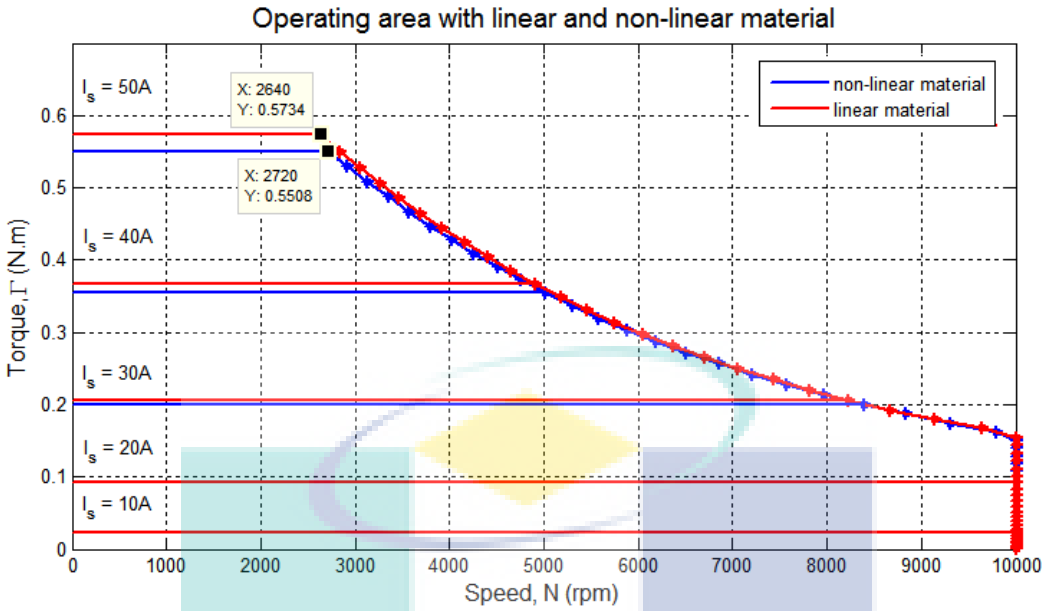

Figure 2.17: Computed operating area comparison between linear and non-linear material for a load angle $\beta = 45°$ and power supply of 14V/50A.

difference in speed is 90rpm.

In conclusion, regarding the requirement, the linearity hypothesis made by [1] during the pre-design phase is acceptable for the application operating area range. However, the updated tool shows that a better torque prediction can be achieved thanks to FE analysis using non-linear material. Therefore, the tool is now more robust in an unlimited operating area range.

The experimental validation in subsubsection 2.3.2.2 was made on operating points where non-linearity cannot be observed, leading to an easy validation. In perspective, an integration of a more capable power electronics is therefore needed to make a validation of the non-linear torque-speed area possible.

2.3.3.2 Maximum-torque-load angle β

The load angle β is another input parameter used in torque-speed area computation[4]. It is the control parameter that sets the values of I_d and I_q,influencing directly the torque Equation 2.12.

$$\Gamma = \frac{3}{2} p (L_d - L_q) I_d I_q \tag{2.12}$$

In steady state, it is theoretically proved that the electrical load angle that maximize the

[4]Reminder on the load angle can be found in Appendix D

torque at a given current I_s is $\beta = \pi/4$. We wanted to know the maximum torque position if the machine is operated in static. In terms of application, it can be useful to know the static torque behavior of the machine in case the machine need to be used in such condition. Instead of leaving the load angle to $\beta = \pi/4$, the load angle can then be chosen correctly so as to maintain a high static torque and produces as low copper losses as possible at the same time.

Therefore, the previously validated FE model was used to simulate an operating machine rotating at constant speed, with a constant current of $I_s = 50$A, and on different load angle β ranging at $\beta \in [\pi/4, 5\pi/4]$. Figure 2.18 shows the torque surface result.

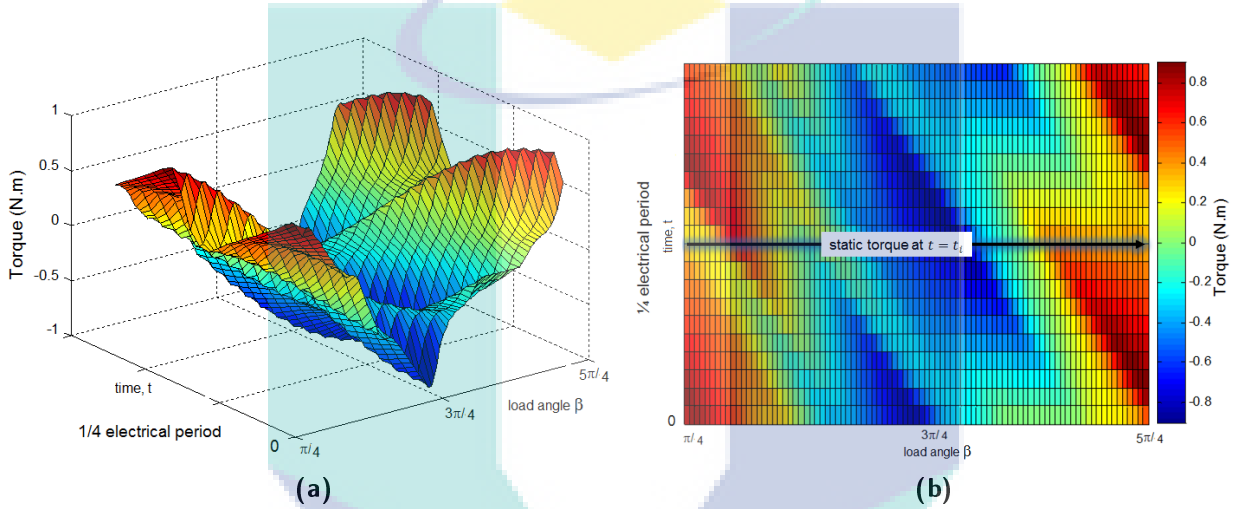

Figure 2.18: Torque surface in function of mechanical load angle and magnetic field position for 1/8 rotation at N=1500rpm, I_s=50A.

Figure 2.18a shows the torque surface in three dimension while Figure 2.18b is the two dimensional view of the surface on the time-load angle plane. In order to look for the static torque waveform, we need to look the torque variation along the load angle axis at a given time. By fixing a time point $t = t_i$ and sweeping through the load angle (horizontal black arrow in 2.18b), it is in fact equivalent to rotating the rotor in a static stator magnetic field[5]. Therefore different static torque waveforms can be observed in function of time. Moreover, as the rotor rotates synchronously with the stator magnetic field, these different static waveforms are related to a given stator magnetic field position[6].

For example, at two different magnetic field positions θ_1 and θ_2, the static torque waveforms are as presented in Figure 2.19.

[5]Remark: On the other axis (vertically), sweeping the time at a given load angle will give us the torque pulsation.

[6]The convention chosen on the magnetic field or flux axis can be found in Appendix D

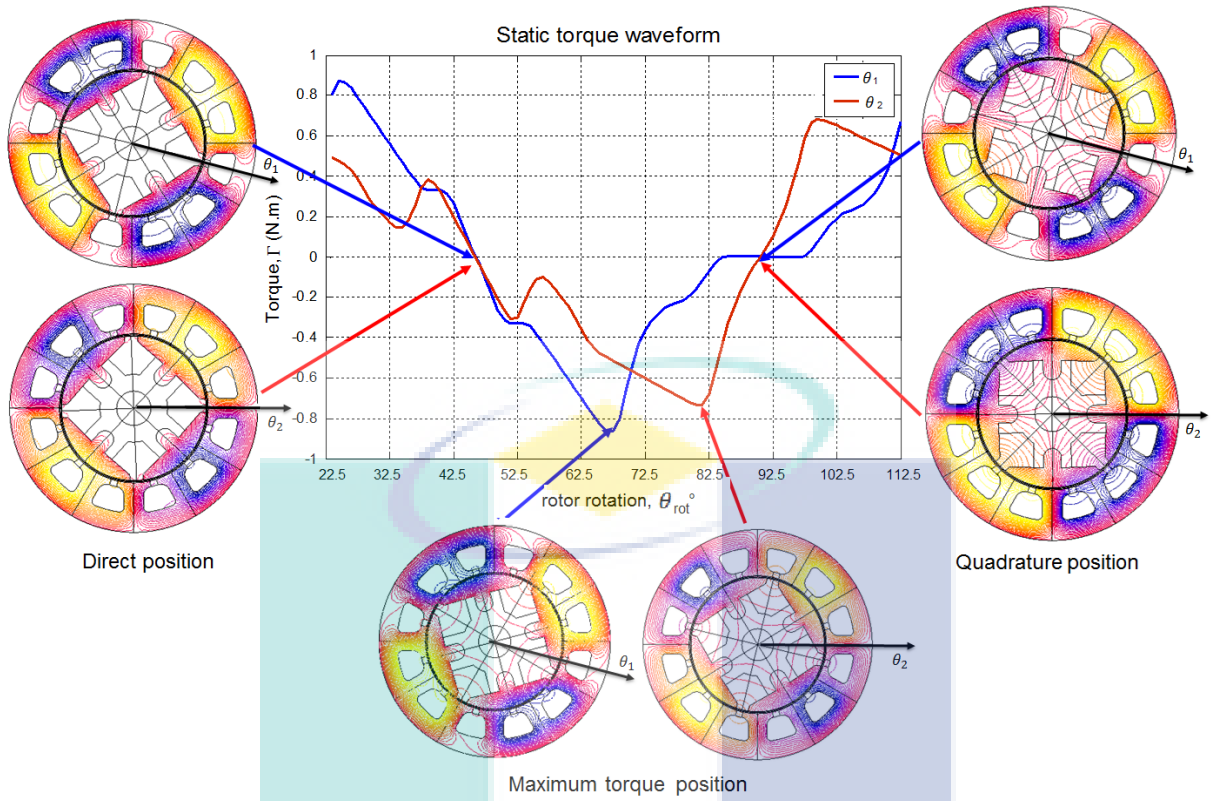

Figure 2.19: Static torque waveforms at two different static stator magnetic field position θ in function of rotor rotating through angle θ_{rot}. Flux linkage for direct position, quadrature position and maximum-torque position in each case are also shown.

As we are now referring to a rotating rotor in a static stator magnetic field, instead of using load angle, the position of the rotor will be referred as θ_{rot}. With a four poles machine, a single period of the static torque waveform can be observed as the load angle rotor rotates up to 90°. During the rotation, the rotor passes through direct position, maximum torque position and quadrature position. We observed that the static torque is not sinusoidal. This is mainly caused by the variation of reluctance along the airgap due to existence of slots opening and the non-magnetic parts on the rotor segments. This results in flux linkage variation as the rotor rotates, thus distorted static torque waveforms [12].

In the two magnetic fields positions shown in Figure 2.19, the direct and quadrature position can be found at nearly the same rotor position θ_{rot}. They are positions in which the static torque on the rotor shaft is zero. The direct and quadrature position can be seen to be 45° away from each other. However, the maximum static torques are attained at different rotor position and most importantly, they are not located in the middle between the direct and quadrature positions. Maximum static torque varies in amplitude and it is attained at different rotor position in function of the magnetic field position, not always in between the

direct and quadrature position as in normal operating machine ($\beta = \pi/4$ condition for torque delivered in rotation).

The difference can be explained by the fact that, the maximum-torque-load angle of $\beta = \pi/4$ deduced from the torque equation Equation 2.12 is applicable with the assumption that the motor rotates in steady state and the given torque is an average torque. However, if we look to an any given instant, L_d and L_q depends on the magnetic field position θ which affect flux linkage variation due to slots opening and non-magnetic segments of the rotor. Rather than having a single value for each L_d and L_q, the inductance matrix Equation 2.13 depends on the rotation angle θ [12].

$$\begin{bmatrix} \lambda_d \\ \lambda_q \end{bmatrix} = \begin{bmatrix} L_d(\theta) & L_{dq}(\theta) \\ L_{dq}(\theta) & L_q(\theta) \end{bmatrix} \begin{bmatrix} i_d \\ i_q \end{bmatrix} \tag{2.13}$$

If we are interested in the average of the static torque, the green curve in Figure 2.20 which is the average torque for all magnetic field position θ_i, calculated from Figure 2.18b shows that the maximum magnitude average torque is attained at $\beta = \pi/4$, as deduced from the torque equation Equation 2.12.

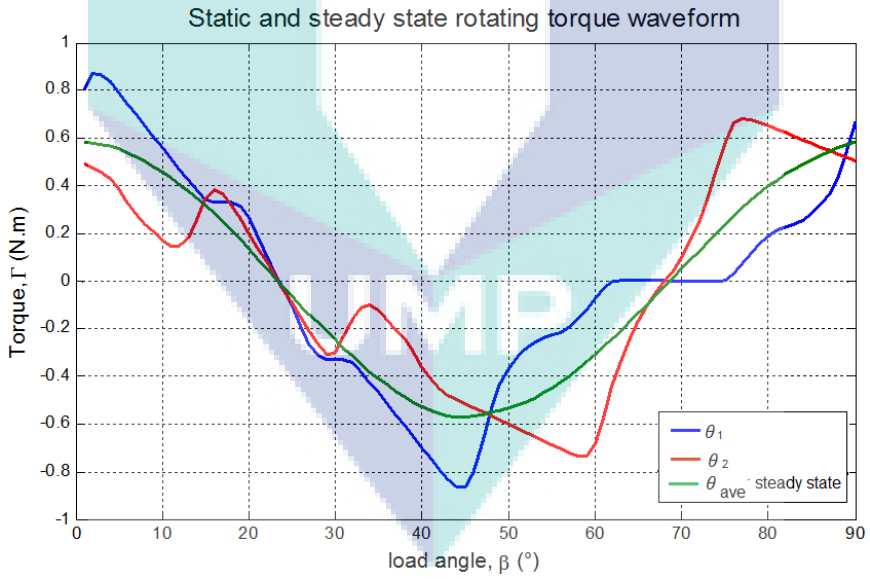

Figure 2.20: The average torque in function of load angle.

In comparison to static torques, two static torque at two different magnetic field positions as shown in Figure 2.19 previously (blue and red curve) show a totally different rotor position to attain the maximum torque and their maximum torque are not of the same amplitude.

Following the observation, a graphic tool allowing user to choose the best rotor position in reference to the magnetic field position such as in Figure 2.21 can be proposed.

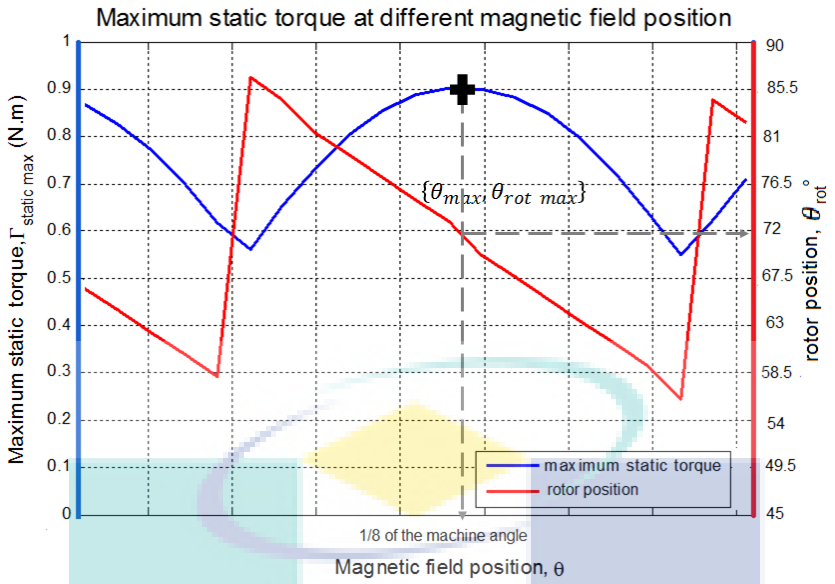

Figure 2.21: The maximum static torque in function of the stator magnetic field position θ, and the corresponding load angle β to attain them.

We can see that the maximum static torque in function of magnetic field position varies ranging from $\Gamma_{static\,max} \in [0.56N.m\,,\,0.90N.m]$ and they are attained at load angles in between the direct and quadrature position. In this part of the machine (over 1/8 of the machine), the maximum static torque regardless in any magnetic field position can be localized, for example at the point $\{\theta_{max}, \theta_{rot\,max}\}$ shown in. This pattern is of course periodic over the circumference of the machine.

In conclusion, while the steady state rotating machine will attain the maximum average torque at a load angle of $\beta = \pi/4$, the static torque can however be attained at different rotor positions. As the notion of static torque is instantaneous, it is highly related to the magnetic field position in the stator. Graphic in Figure 2.21 can helps choosing the optimum magnetic field position and load angle and rotor position $\{\theta, \theta_{rot}\}$ that gives the maximum static torque. Thanks to an optimum choice of $\{\theta, \theta_{rot}\}$, the maximum static torque can be attained with a minimum current, thus a lower copper losses.

2.4 Power factor

The goal of many applications, especially embedded is to have the power factor, $cos\varphi$ as close as possible to 1 which means that the necessary power to be supplied is very close

to the actual consumed power, reducing losses and the size and weight of power electronic components.

The power factor of the Syncrel motor has been a major inconvenient compared to other motors [9, 10, 11].

With a low winding resistance compared to the reactance, it is a common practice in literature to simplify the power factor formulation by neglecting the winding resistance[4]. With this simplification, a practical approximation of the power factor in function of the ratio saliency is usually done [2, 5] (Equation 2.14):

$$cos(\varphi)_{max} = \frac{\frac{L_d}{L_q} - 1}{\frac{L_d}{L_q} + 1} \tag{2.14}$$

The maximum saliency ratio in Syncrel motors are usually too low to achieve a comparable power factor to permanent magnet motor with an identical stator. This affirmation is justified with the condition that the winding resistance is negligible in comparison to the reactances.

However, in our prototype motor, the resistance is unusually high[7]. More importantly, the resistance plays a major role in our multiphysical approach, specially, considering the evolution of its values with temperature. Furthermore, in automotive application where the initial environment temperature is already high, the winding resistance cannot be neglected.

Therefore, the power factor of the motor will be evaluated using the operating diagram of the Syncrel machine with the winding resistance taken into account.

2.4.1 Computation tool

The first objective in this section is to evaluate the $cos\varphi$ of the prototype Syncrel machine. In order to do so, the operating diagram (Figure 2.22) has been computed and can be simulated so as to calculate the power factor $cos\varphi$. The input parameter needed for $cos\varphi$ computation are:

1. L_d and L_q, and R_s: the inductances and the resistance of the machine which depend on the machine architecture. The resistance is also variable depending on the temperature.

2. β, I_s(or V_s) and ω: the load angle, the current (or the voltage) supply, and the machine speed which depend on the command choice and operating points. The power supply will be limited to 14V/50A.

Following the diagram, the vectors relating different parameters are (Table 2.2):

[7] related to small conductors necessary to have the necessary Ampere.turn (N.I) in small machines

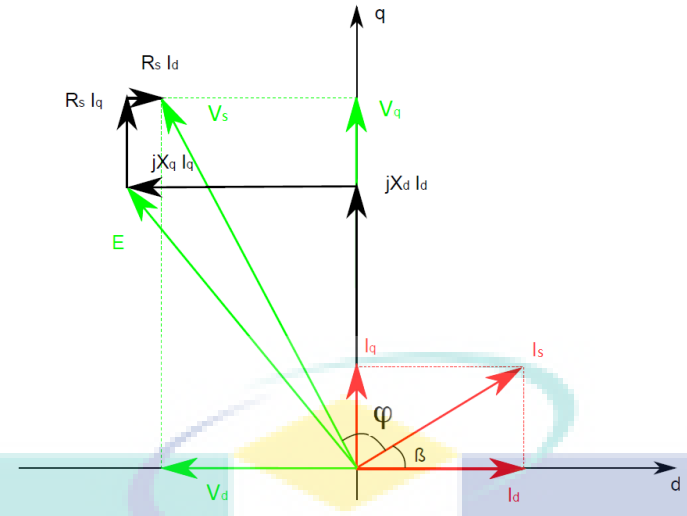

Figure 2.22: The Syncrel machine operating diagram.

Following $\vec{d}$ axis	Following $\vec{q}$ axis
$I_d = I_s cos(\beta)$	$I_q = I_s sin(\beta)$
$\omega.L_{q.}I_q$	$\omega.L_{d.}I_d$
$R_s.I_d$	$R_s.I_q$
$V_d = V_s cos(\beta + \varphi - \pi/2)$	$V_d = V_s sin(\beta + \varphi - \pi/2)$

Table 2.2: The vectors constructing the operating diagram of a Syncrel machine.

with:
$V_s = \sqrt{(R_s.I_d - \omega.L_{q.}I_q)^2 + (R_s.I_q + \omega.L_{d.}I_d)^2}$
$E = \sqrt{(\omega.L_{q.}I_q)^2 + (\omega.L_{d.}I_d)^2}$

The vectors list above shows that in function of current, all other parameters (L_d,L_q, R_s, β, and ω) can influence the power factor. However, L_d variation (due to saturation in higher current) has been found to be having negligible effect on power factor. The following subsections will then treat the influence of other parameters on power factor. Beforehand, the power factor computation tools has to be validated.

2.4.1.1 Experimental validation

Power factor computation tool was validated using the test bench. The motor was operated at no-load using the same speed profile and speed control as in Figure 2.8 so as to maintain a constant speed during a certain time. At steady-state speed, the current and voltage on a winding phase was recorded, and the phase shift was later calculated. Figure 2.23 shows two examples of the current-voltage phase shift recorded and the corresponding computed operating diagram.

Table 2.3 shows the comparison between experimental and computed $cos(\varphi)$. The com-

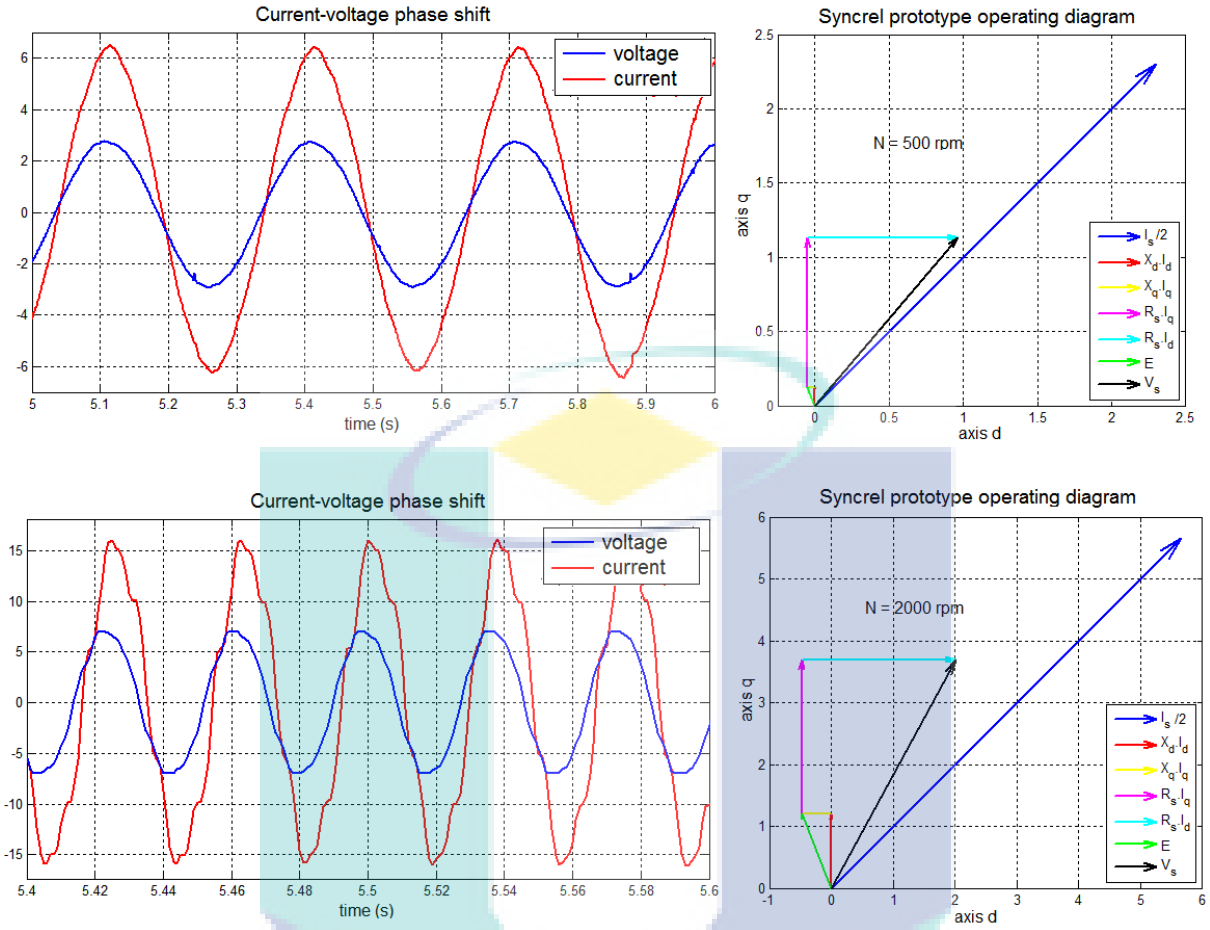

Figure 2.23: Top: Experimental current-voltage phase shift observed at N=500rpm and the corresponding computed operating diagram. Bottom: Experimental current-voltage phase shift observed at N=2000rpm and the corresponding computed operating diagram. φ is the angle between the current (blue vector) and the voltage (black vector).

putation can be considered valid after observing a maximum difference less than 0.1.

N (rpm)	experimental $cos(\varphi)$	computed $cos(\varphi)$	difference
500	0.97	>0.99	0.03
1000	0.95	0.98	0.03
2000	0.91	0.95	0.04
3000	0.87	0.91	0.04

Table 2.3: $cos(\varphi)$ comparison between computation and experimental results.

Following the validation of the power factor computation tool, the influence of different parameters on the power factor will be studied in next subsections.

2.4.2 Influence of speed on $cos(\varphi)$

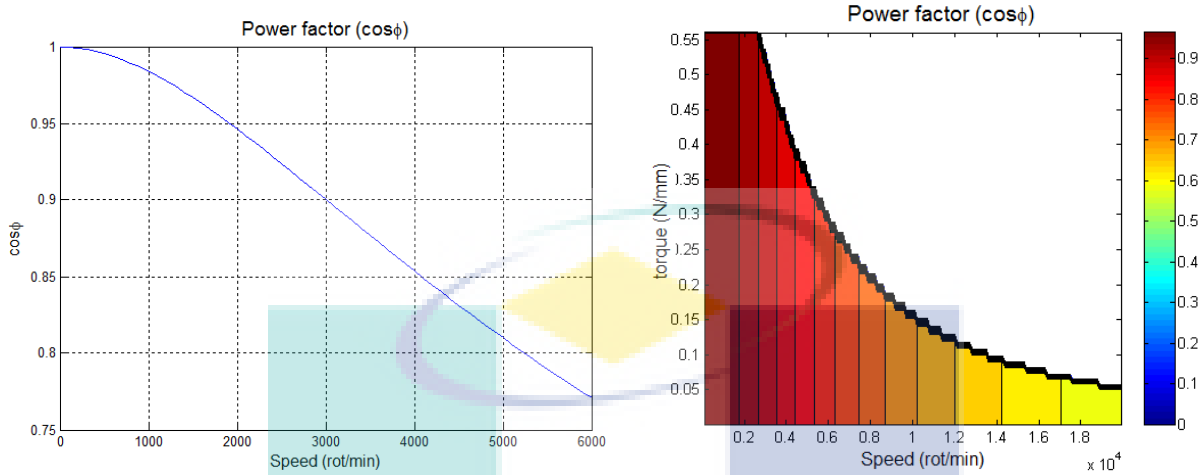

Figure 2.24: Left: Evolution of $cos(\varphi)$ computed in function of the motor speed at a given torque level. Right: Power factor computed on the motor operating area.

From the operating diagram, it can be clearly seen that the increase of speed at a fixed load angle increases in consequence the vectors $\omega.L_{q.}I_q.\vec{d}$ and $\omega.L_{d.}I_d.\vec{q}$, which in return bring the vector $\vec{V_s}$ farther away from the direction of $\vec{I_s}$. This bigger phase angle means a smaller $cos(\varphi)$. The resulting $cos(\varphi)$ in function of speed in continuous and extended speed range is presented in the left of Figure 2.24.

The power factor is constant at a given speed regardless the torque (Right of Figure 2.24) due to negligible impact of material non-linearity on power factor.

2.4.3 Influence of load angle β on $cos(\varphi)$

For a given motor design (given saliency ratio), the power factor varies in function of the control. Therefore, the load angle β can be used to optimize the power factor. As seen in subsubsection 2.3.3.2, the optimal load angle that maximize the torque is $\beta = 45°$. Whereas for power factor, our computation shows that it is maximum for a load angle between 70° and 80°, depending on speed (Figure 2.25). As a consequence, different load angles can be used at different operating points so as to keep an optimum power factor. This will be studied later in section 2.5, where different parameters will be optimized at the same time (e.g.: torque, power factor, speed range).

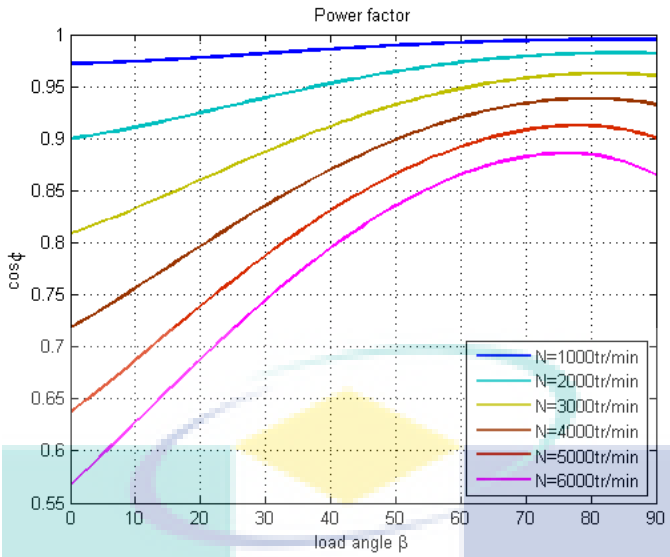

Figure 2.25: Evolution of $cos(\varphi)$ in function of β at different speed.

2.4.4 $cos(\varphi)$ variation due to winding's temperature variation.

The stator winding resistance R_s is the most trivial influencing parameter on power factor. At a constant complex component of impedance, higher resistance will in consequence bring the voltage vector closer to the current vector, thus reducing the phase shift. In practical, the resistance variation depends on the winding temperature variation, which is directly influenced by the winding copper losses. In an application where the temperature is particularly high, the influence of winding resistance variation on other performance figures cannot be neglected. To evaluate the winding resistance influence specifically on the power factor of our prototype motor, R_s was varied while all other parameters were left fixed. Figure 2.26 shows the influence of winding resistance variation on power factor at different speed. It can be seen that the power factor variation in function of speed is bigger for a lower winding resistance compared to the one with a higher winding resistance.

In case of usual practice where the winding resistance R_s is considered negligible, we can see that the power factor declines dramatically. In fact, at zero resistance, the power factor is found to be at 0.4 at all speed. On the contrary, in this approach where the winding resistance is not neglected and its variation taken into account, a better power factor is predicted. Therefore, in function of operating temperature (thus a corresponding winding resistance), a smaller power electronics component may be sufficient.

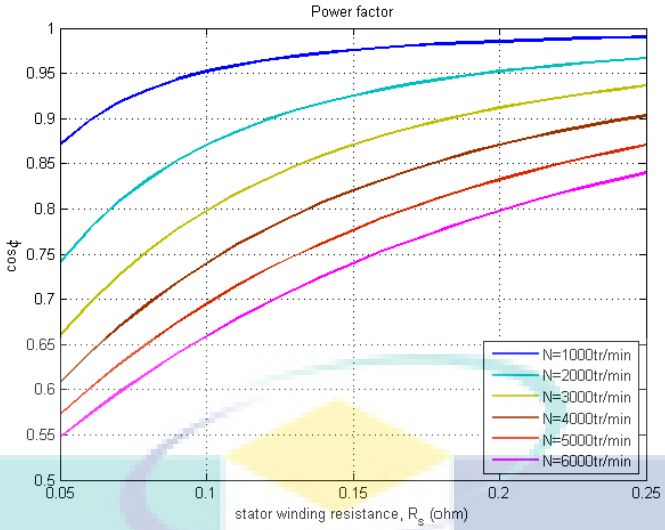

Figure 2.26: Evolution of $cos(\varphi)$ in function of R_s at different speed.

2.5 Interaction between different parameters

In previous sections, it has been shown that the power factor is influenced by speed, load angle, and winding resistance. At the same time, load angle and winding resistance also have direct influence on the torque-speed operating area. To help predictions of all these interconnected parameters, two abacus were constructed using analytical tools used previously. They are exposed in the following subsections.

2.5.1 Influence of load angle on power factor and torque

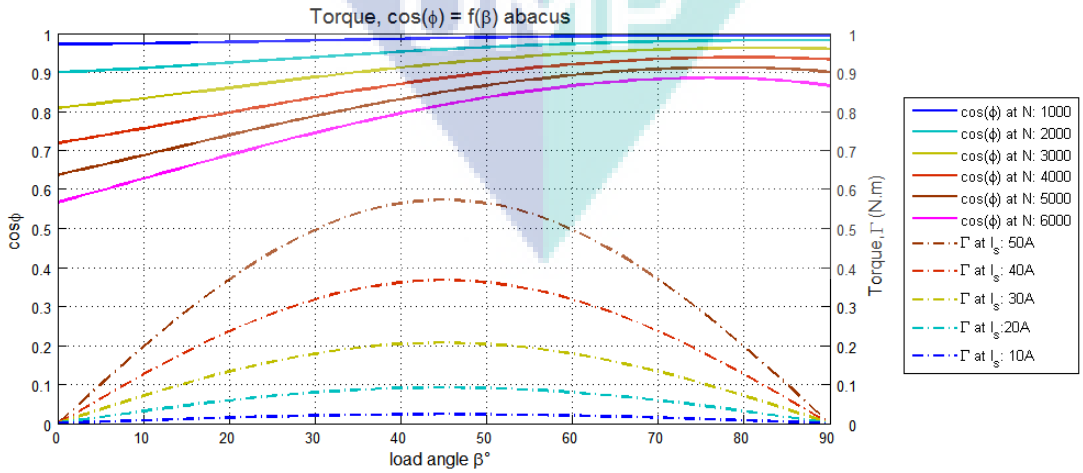

Figure 2.27: Abacus giving the torque at different current levesl and power factor at different speed in function of load angle. Both curves were computed for a nominal winding resistance (at ambient temperature).

The first abacus is an abacus giving the reading of torque at different currents and power factors at different speeds in function of the load angle (Figure 2.27). With this graphic tool, the choice of load angle can be modified to optimize the power factor in function of operating points. In an on-board system, high power factor means more autonomy and smaller power electronic to operate the motor. This can be useful especially for operating points requiring low load (lower current) and high speed. Instead of leaving the load angle at its default values (e.g. $\beta = 45°$ for maximum torque), intuitively, it may be better to increase the load angle (thus supply more current) in order to maximize the power factor.

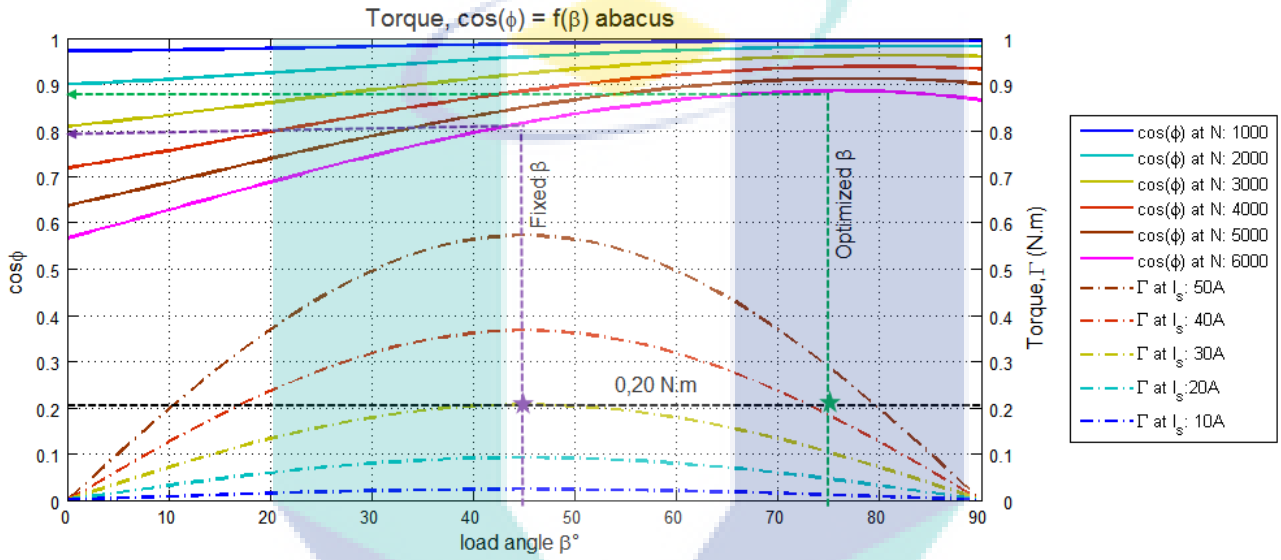

Figure 2.28: Example of power factor optimization on operating point (Γ, N)=(0.20N.m,6000rpm).

As practical example, take $(\Gamma, N) = (0.20N.m, 6000rpm)$ (Figure 2.28). By changing the load angle from 45° to 75°, a gain from 0.8 to 0.9 can be attained in power factor. However, this is attained at the cost of a higher current (42A instead of 30A). Due to this counter-effect, it is necessary to evaluate the overall apparent power that need to be supplied due to load angle modification before adopting it. For our Syncrel prototype motor, three potential operating points for power factor improvement were simulated for two different load angles: torque-maximizing load angle ($\beta_1 = 45°$), and power-factor-improvement load angle ($\beta* > 45°$).

Two main criteria are looked into to see the effect of improving the power factor: the efficiency comparison and the apparent power comparison. The efficiency comparison was done to evaluate the efficiency degradation due to current rise while the apparent power comparison was done to evaluate if there is reduction in apparent power as consequence of power factor increase. They are presented in Table 2.4.

(Γ, N) (N.m, rpm)	(0.20,6000)		(0.10,6000)		(0.10,7000)	
load angle β (°)	β_1	$\beta*$	β_1	$\beta*$	β_1	$\beta*$
	45	75	45	75	45	75
current, I_s (A)	30	42	21	30	21	30
voltage, V_s (V)	11.6	12.7	8.1	9.1	8.9	9.6
power factor, $cos(\phi)$	0.82	0.89	0.82	0.89	0.78	0.86
Absorbed power, P_{abs} (W)	417.6	720	204	369	302	372
$\eta_{\beta*} = n.\eta_{\beta_1}$	$\eta_{\beta*} = 0.58.\eta_{\beta_1}$		$\eta_{\beta*} = 0.55.\eta_{\beta_1}$		$\eta_{\beta*} = 0.81.\eta_{\beta_1}$	
Apparent power, P_s (V.A)	523	800	255	410	387	433

Table 2.4: Comparison between computation with $\beta = \beta_1$ and $\beta = \beta*$.

For efficiency comparison, at an operating point (Γ, N), the same mechanical power output is produced thus, the efficiency in each condition with different power factor can be written as:

$$\eta_{\beta_1} = \frac{P_{mecha}}{P_{abs\,\beta_1}} \tag{2.15}$$

$$\eta_{\beta*} = \frac{P_{mecha}}{P_{abs\,\beta*}} \tag{2.16}$$

Therefore, the efficiency comparison can be written as:

$$\eta_{\beta*} = \frac{P_{abs\,\beta_1}}{P_{abs\,\beta*}}.\eta_{\beta_1} \tag{2.17}$$

It can be seen in all three operating points, the efficiency have degraded as a cost of wanting to have a higher power factor.

As for the apparent power, all three operating points gave higher current and voltage thus, higher apparent power. Therefore, the power factor increase does not allow size and weight reduction on power electronic components, rather the opposite, it will require a bigger components. It shows that, for our Syncrel prototype motor, maintaining the load angle at the torque-maximizing position ($\beta_1 = 45°$) is favorable at all operating points. It can be concluded that the gain in power factor is unnecessary.

2.5.2 Degradation of speed limit in function of winding resistance and its effect on power factor

The second abacus is an abacus giving the maximum speed limit at different current levels and power factors at different speeds in function of winding resistance Figure 2.29. In func-

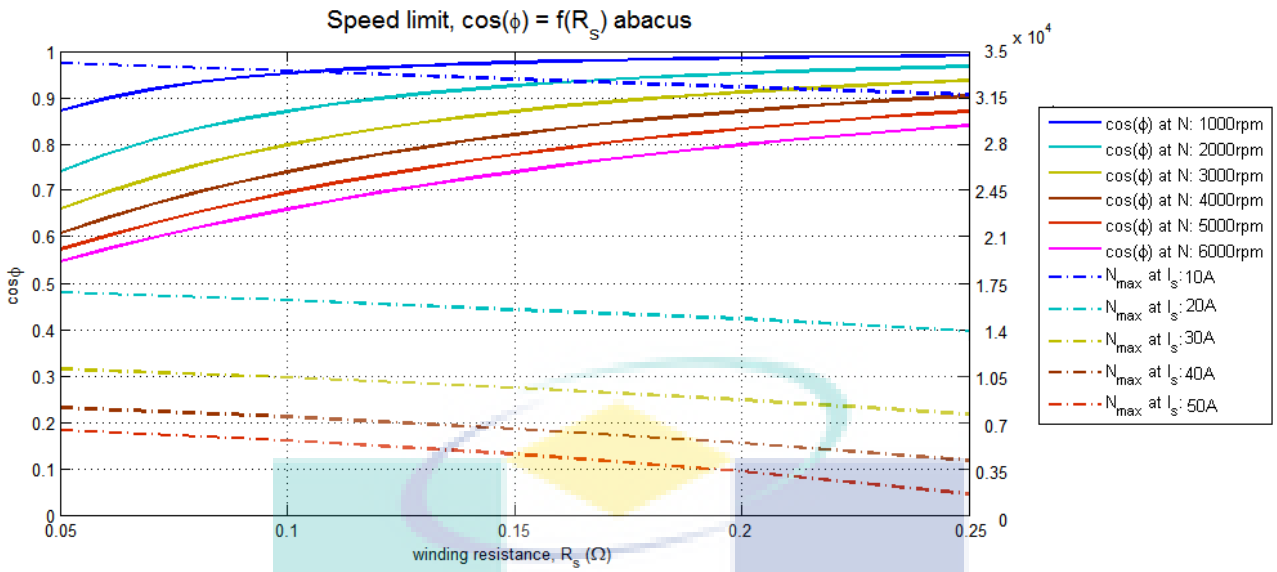

Figure 2.29: Abacus giving the speed limit at different current level and power factor at different speed in function of winding resistance. The maximum speed range was computed for a maximum voltage supply of 14V.

tion of winding resistance, the reading on the left axis gives the power factor at different speed levels. On the right axis, the maximum speed range for different currents (torque) can be found. The maximum speed range on the right axis represents the variation of torque-speeds area envelope (Figure 2.30) in function of winding resistance.

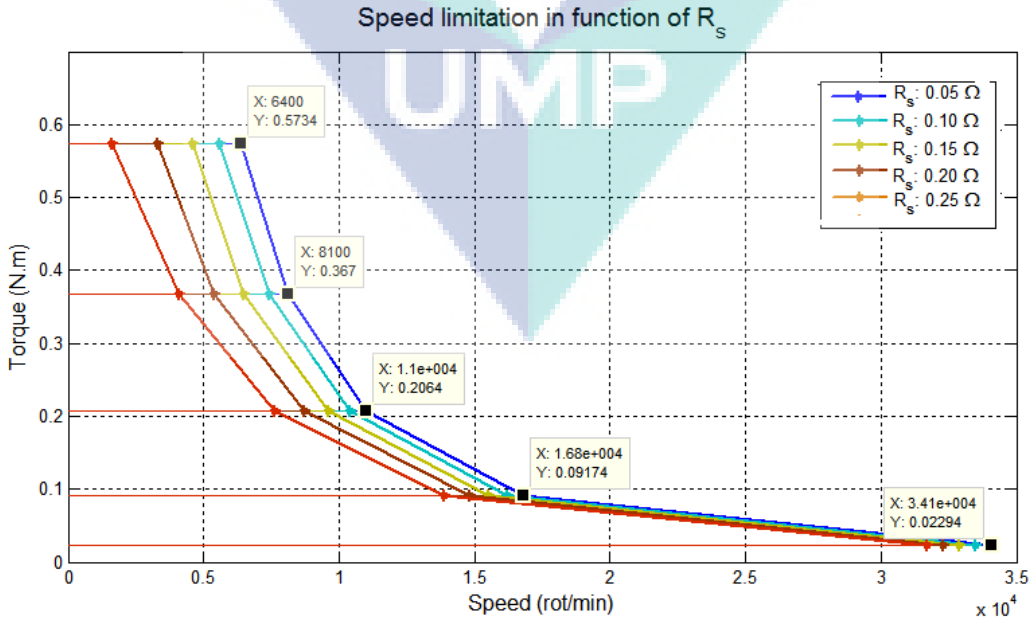

Figure 2.30: Variation of operating area in function of winding resistance R_s.

With this graphic tool, a simple measure of winding resistance in real-time will let us know the power factor and the operating area available for the motor. Furthermore, knowing that the resistance varies in function of temperature, a simple measure of winding temperature will be sufficient to deduce the power factor and the corresponding operating area. A development of an accurate thermal model (presented in chapter 3) and a coupling between the model and this abacus will further relate a motor utilization cycle to not only the winding temperature, but also power factor and operating area variation. This is important as the high temperature can modify the operating area severely and making certain operating points unattainable.

2.6 Efficiency

The efficiency η of a motor is determined by the ratio of mechanical output power over the electrical absorbed power. A better efficiency not only means less power consumption, but also lower losses. Especially for on-board system with high ambient temperature, an efficient motor helps to lower overheating risk with a simpler cooling system. Without over-heating, degradation of motor components can be prevented and the torque-speed area range can be maintained (subsection 2.5.2).

The absorbed electrical power in a phase can be computed using Equation 2.18.

$$P_{elec\,a,b,c} = 3.V_{eff}.I_{eff}.cos(\phi) \tag{2.18}$$

On the other hand, the output mechanical power is simply the product of speed and torque of the motor at a given operating points. By using torque-speed area and power factor computation tools developed previously (section 2.3 & subsection 2.4.1), the absorbed electrical power and the output mechanical power of the motor can be mapped on the torque-speed operating area (Figure 2.31).

Following the mapping of absorbed electrical power and mechanical output power, the theoretical efficiency, which is the ratio of mechanical output power over the electrical absorbed power is also mapped on the torque-speed area (Figure 2.32).

The theoretical efficiency map shows that in nominal configuration (load angle $\beta = 45°$, $R_s = 0.22\Omega$: at ambient temperature 20°C), the prototype motor has a low efficiency. It is relatively constant in function of torque, while improves as the speed increases. Several operating points have been validated using experimentation (the same experimental operating points used in subsubsection 2.3.2.2).

$$\eta = \frac{P_{mecha}}{P_{elec}} = \frac{\Gamma.\Omega}{3.V_{eff}.I_{eff}.cos(\phi)} \tag{2.19}$$

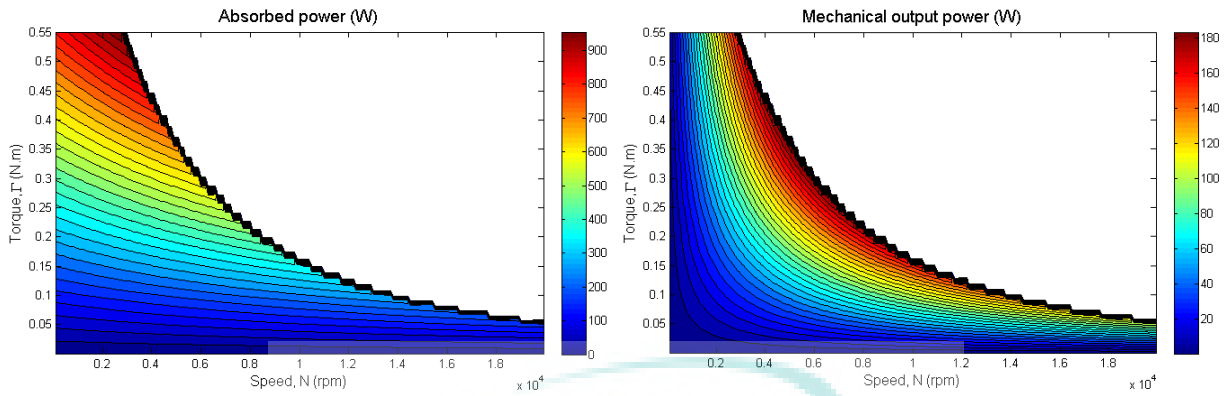

Figure 2.31: Left: Absorbed electrical power map for nominal configuration (load angle $\beta = 45°$, $R_s = 0.22\Omega$: at ambient temperature 20°C). Right: The corresponding output mechanical power.

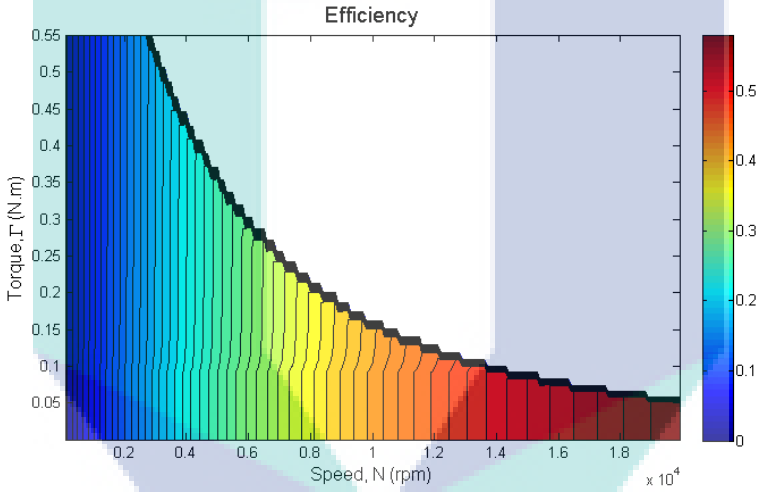

Figure 2.32: Theoretical efficiency η of the Syncrel prototype motor at nominal configuration (load angle $\beta = 45°$, $R_s = 0.22\Omega$: at ambient temperature 20°C).

The efficiency map traced is predictable with a closer look into the ratio η (Equation 2.19). The torque is proportional to current, thus, at constant speed, as the torque increases, the current increases as well. The small efficiency degradation as the torque increases starting at around $\Gamma = 0.1N.m$ is due to material non-linearity. On the other hand, the gradient of efficiency in function of speed is explained by the decrease of power factor as the speed increases (as shown in Figure 2.24).

In general, the efficiency of the Syncrel prototype motor is low.[8] At a fix saliency ratio, the efficiency of our prototype motor is particularly low due to the high winding resistance. The high winding resistance results in a high copper losses, which will be studied in the next

[8] As for e-Clutch application, the machine only actuated for several hundreds of milliseconds, which gives a relatively small total losses.

section. The efficiency can be easily improved by using a lower resistance winding (e;g;: low resistance conductors connected in parallel). For example, Doc in her initial study [1] has shown that it is possible to build the motor with a winding resistance $R_s = 0.05\Omega$. In that case, the efficiency map becomes as shown in Figure 2.33.

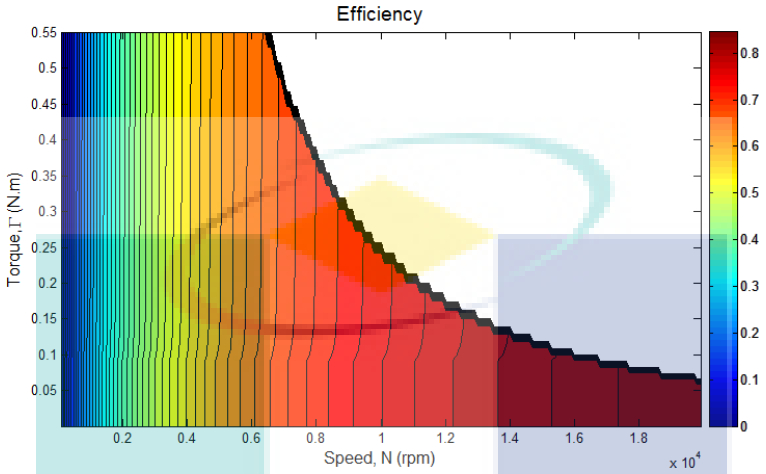

Figure 2.33: Theoretical efficiency η of the Syncrel prototype motor for an improved winding resistance (load angle $\beta = 45°$, $R_s = 0.05\Omega$: at ambient temperature 20°C).

At two critical operating points of the e-Clutch application, (Γ, N) at $(0.18, 7290)$ and $(0.54, 2050)$, the improvement of winding resistance increased the efficiency by 0.35 and 0.27. Furthermore, as seen in Figure 2.30, the winding resistance reduction has another advantage of extending the speed range of the motor.

At different operating points, experimental efficiency has been shown to be in agreement with the computed theoretical efficiency with a maximum difference $\eta_{comp} - \eta_{exp}$ equal to 0.054 points of efficiency at operating point $(\Gamma, N) = (0.12\text{N.m} , 2750\text{rpm})$. The difference can mainly be explained by the winding resistance increase due to the temperature during the test which has increased the copper losses in return.

The following section will cover the evaluation of each losses (copper losses and iron losses), their portions out of total losses and the map them on the motor torque-speed operating area. Their evaluation is important in order to build a thermal model that can be coupled with different tools developed in this chapter.

2.6.1 Copper losses

Copper losses, P_{Cu} in a motor is the heat produced by currents passing through conductors of its windings. The passive rotor in a Syncrel motor means that only stator winding produces copper losses. It can be quantified by experimentally measuring the current going through

the 3 windings of the motor and calculate using Equation 2.20:

$$P_{Cu} = 3.R_s.{I_{RMS}}^2 \tag{2.20}$$

where I_{RMS} is the winding RMS current (A), R_s the winding resistance(Ω).

The winding resistance is influenced by the current frequency and the temperature. Considering the conductors diameter and the frequency of the current fed to the motor, the skin effect does not appear in the motor operating speed range. Thus, the winding resistance which was measured using a direct current is considered constant in function of frequency, meaning at all speed range.

The winding temperature T increase results in a rise in copper resistivity $\rho_{Cu\,T}$ following Equation 2.21 [14]. The copper resistivity at 20°C, $Cu\,20$, is 1.73 x$10^{-8}\Omega m$ and temperature coefficient of resistivity α is 0.00393/°C. The motor's winding resistance at 20°C is, $R_{20^\circ} = 0.22\Omega$.

$$\rho_{Cu\,T} = \rho_{Cu\,20}.[1 + \alpha.(T - 20)] \tag{2.21}$$

As consequence, the rise of temperature will result in winding resistance increase and generation of more copper losses Figure 2.34.

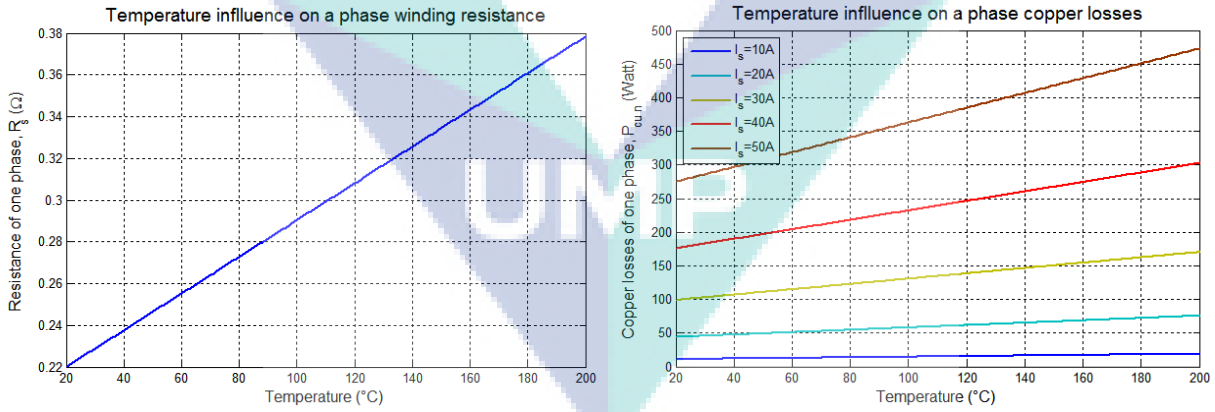

Figure 2.34: Temperature influence on a phase winding resistance (left) and copper losses (right).

Besides generation of more copper losses, the increase of winding resistance also affects the torque-speed area envelope (Figure 2.30). Two examples of copper losses mapped on torque-speed area at different temperature are shown in Figure 2.35.

Another inconvenient of high temperature is the dilation of the copper winding which can cause mechanical stress on the winding, resulting into motor fault [15]. The dilation

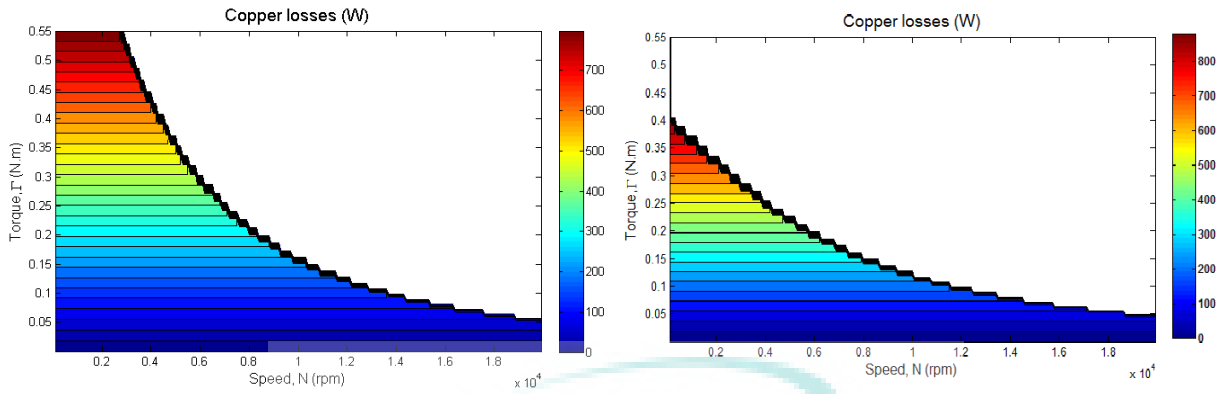

Figure 2.35: Copper losses on every points of the Syncrel motor operating points. Left: at ambient temperature (20°C). Right: at 150°C.

does not however affect the winding resistance.

$$R_s = \frac{\rho l}{S} \tag{2.22}$$

In fact, since the linear expansion coefficient and the superficial expansion coefficient of the material is related [13], the dilatation in the conductors length l does not increase the resistance (Equation 2.22) as it is compensated by the surface expansion S.

2.6.2 Iron losses

As in other electromagnetic devices, iron losses occurs in a Syncrel motor when its ferromagnetic components are subjected to changing magnetic field. The components in the Syncrel machine that is related to these losses are the stator structure and the rotor magnetic segments. The power that is ideally transformed into torque production is lost in the material, dissipated as heat and mechanical micro-vibration.

2.6.2.1 Generalities: iron losses modeling

There are 2 types of iron losses models: local and global. Local model calculates precisely the iron losses using fundamental equation of dissipated power density in the material locally Equation 2.23, provided that the relation between the magnetic field, the flux density and its derivative are known.

$$P_{iron} = \iiint_{\tau} \left(\frac{1}{T} \times \int_0^T \left(\oint_{cycle} H.dB \right) dt \right) d\tau \tag{2.23}$$

$d\tau$ represents the elementary volume. Therefore, it is necessary to take into account the hysteresis cycle of the machine precisely. This method is proven to be precise but relatively heavy, complex and time consuming to be integrated into a multiphysical model and optimization tool. It is suitable to be implanted into a finite elements tool as shown by the work of [16] who have developed the LS (Loss Surface) model that was implanted into FLUX software by Cedrat.

The global model in the other hand uses a frequency approach and usually with hypothesis that the evolution of the flux density in the material is purely sinusoidal. The first formulation on iron losses has been done by Steinmetz [17] who proposed a formulation of iron losses which depends on the frequency of the magnetization cycle f and the maximum flux density $\hat{B}$.

$$P_{iron} = C_{Stein}.f^{\alpha}.\hat{B}^{\beta} \tag{2.24}$$

when $C_{Steinmetz}$, α and β are coefficients determined from experiments. This model regroups numerous physical phenomena of different natures. Further development on the model lead to an improved formula Equation 2.25, separating the losses into the two primarily losses-contributors phenomenons: hysteresis and Eddy current.

$$P_{iron} = C_{hys}.f.\hat{B}^2 + C_{Eddy}.f^2.\hat{B}^2 \tag{2.25}$$

However, Equation 2.25 still neglects a certain number of losses that are minimal compared to hysteresis losses and Eddy current losses. They are added by Bertotti [18] in his equation (Equation 2.26) as excess losses.

$$P_{iron} = K_{hys}.f.\hat{B^{\alpha}} + \frac{(\pi d)^2}{6.\rho_t.m_v}.(f.\hat{B})^2 + K_{exc}.(f.\hat{B})^{\frac{3}{2}} \tag{2.26}$$

with d the steel sheet thickness, ρ_t the electrical resistivity of the material and m_v its density.

Other works such as [19] and [20] have lead to further improvements of estimation of hysteresis losses in order to take into account other small phenomena such as the deformation and enlargement of the hysteresis cycle area due to increase in magnetization frequency and hysteresis losses due to minor cycles.

The utilization of all the models cited are finally limited by the fact that they were formulated considering that the evolution of the flux density is purely sinusoidal whereas the flux density in a magnetic parts of a motor is not always perfectly sinusoidal, or even in some cases completely distorted when field-weakening is involved such as in [22].

A more general formulation (Equation 2.27) which is applicable for every form of flux density developed by [21] is the most commonly used in this case. The computation of this

formulation is however heavier than the previous ones.

$$P_{iron} = K_h.f.\hat{B}^{\alpha} + \frac{d^2}{12.\rho_t m_v}.\frac{1}{T}\int_0^T \left(\frac{\partial B}{\partial t}\right)^2 dt + K_{exc}.\frac{1}{T}\int_0^T \left|\frac{\partial B}{\partial t}\right|^{3/2} dt \qquad (2.27)$$

2.6.2.2 Application on Syncrel prototype machine

With different formulations, it is necessary to make hypothesis regarding the flux density wave form before start quantifying iron losses occurred in a motor so that the right formulation can be used for the right case. FE analysis was used to study the flux density waveforms across the ferromagnetic structure of the motor.

The study of iron losses are done for the stator part only. Iron losses on the rotor are neglected following the hypothesis that the flux density variation on the rotor of a synchronous machine in steady state is negligible. It is usually admitted that the flux density on the rotor is constant with some fluctuations originated from harmonics related to slot effect and inverter control. This has been proven by looking at the flux density in different points of the rotor segments using FE analysis (Figure 2.36).

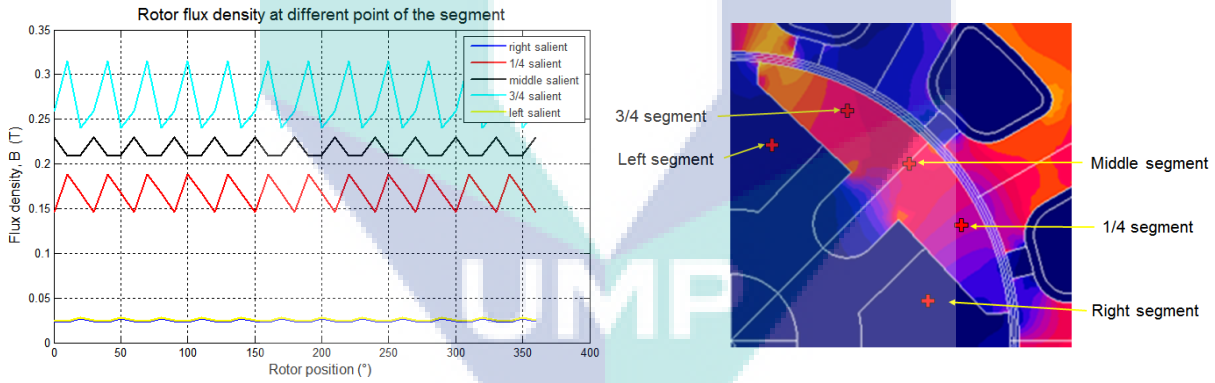

Figure 2.36: Flux density in the Syncrel rotor segment computed using Flux 2D for $I_s = 10A$. The flux density was measured at five different points of the rotor segment (shown in left)

The fluctuations observed are the slot harmonics that can be attributed to the slot opening crossings. (The number of the fluctuations peaks in a complete rotor rotation corresponds to the number of slot.)

FE analysis on the Syncrel prototype motor shows that the flux density waveform varies in function of load angle (Figure 2.37). The flux densities are not constant across the stator. At all load angles, its waveform in the stator yoke is in general close to sinusoidal while the waveform in the rotor is more distorted and higher, which can be explained by local

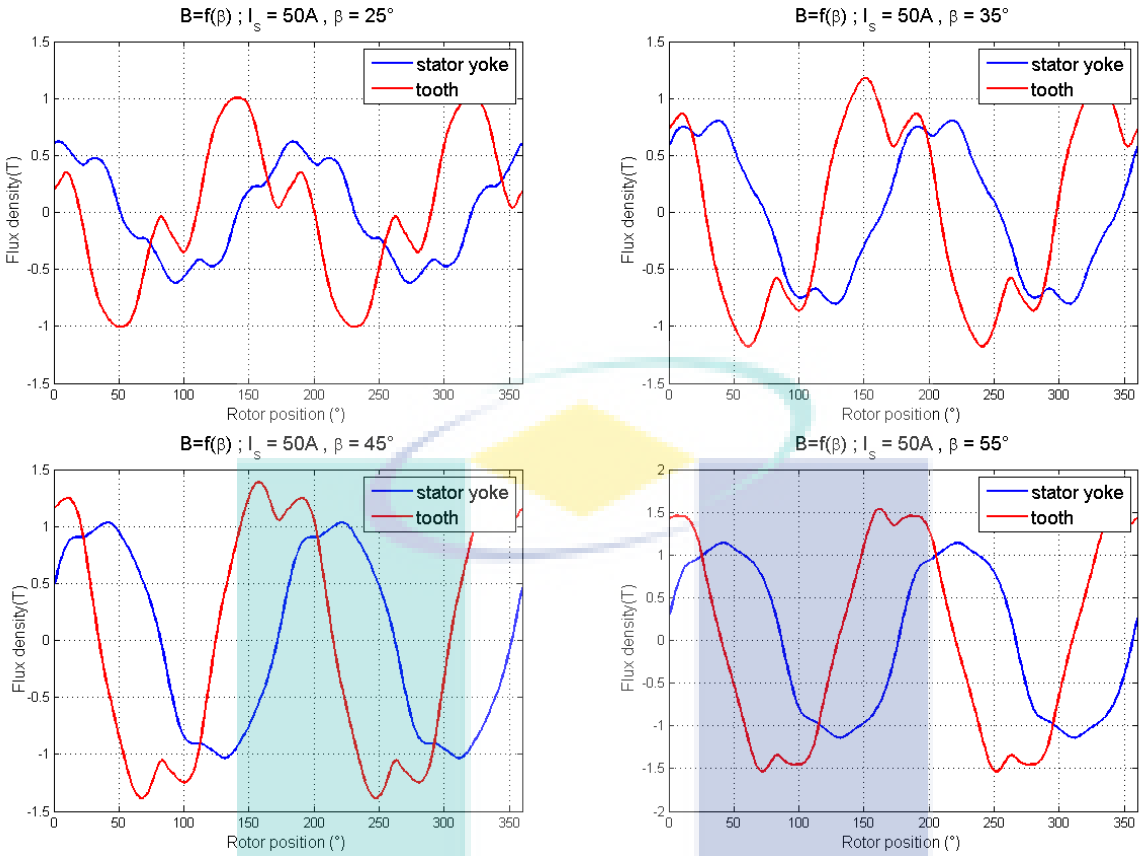

Figure 2.37: Flux density waveform in the middle of stator yoke and tooth at different load angle for a current $I_s = 50$A. (FE analysis)

saturation in teeth complex geometry. From literature, the most precise formulation to calculate iron losses in a non-sinusoidal flux density is by using Equation 2.27.

However, copper losses has been shown in previous section to counts for up 96% of the losses at minimum. Therefore, for initial estimation purpose, considering that iron losses will makes up to a maximum of 4% of the motor losses, a simpler formulation where the flux density is considered sinusoidal will be used (Equation 2.26). To do so, each signal (flux density in stator yoke in tooth) is decomposed into a Fourrier series (Figure 2.38), and the amplitude of the harmonic corresponding to the speed is used to compute iron losses.

With two different flux density amplitudes, the flux density in the whole stator is considered to be at the average of the stator yoke and the tooth flux densities. For example, in the case shown in Figure 2.38 where the motor is operating at $N = 1000$rpm for a load angle $\beta = 45$°and a current $I_s = 50$A (maximum torque), Equation 2.26 is computed with B takes the average value of $(B_{stat} + B_{tooth})/2$ and f is the electrical frequency of the rotational field[9].

[9]A volume weighted induction can also be done. An average is sufficient here as the volume of the teeth

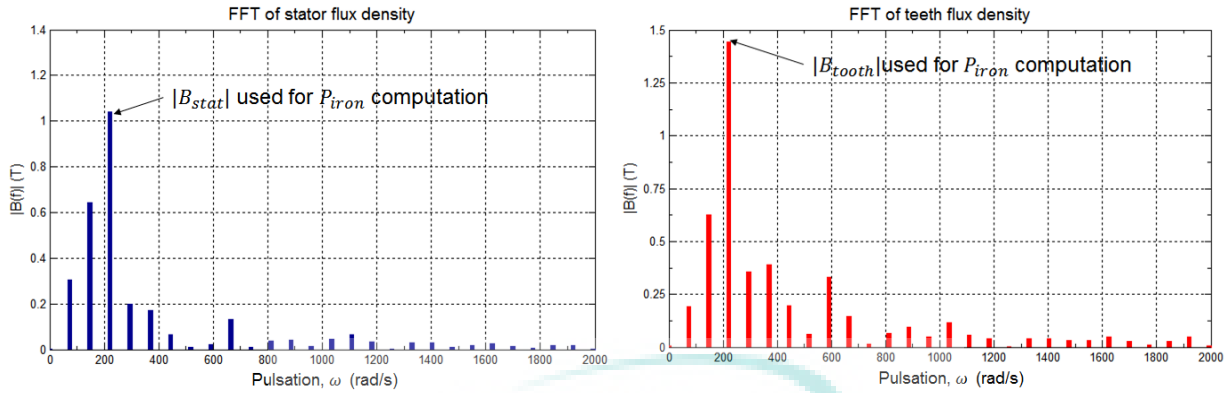

Figure 2.38: FFT done on stator yoke and tooth flux density waveforms at $N = 1000$rpm for a load angle $\beta = 45°$and a current $I_s = 50$A.

The remaining parameters needed to compute the iron losses can be divided into two categories: physical steel sheet properties and dimension (steel sheet thickness d, resistivity ρ_t, density m_v), and magnetic losses coefficients (hysteresis losses coefficient K_h and excess losses coefficient K_{exc}). The physical steel sheet properties and dimension are provided by manufacturer datasheet. Whereas for magnetic losses coefficients, they have to be deduced from an Epstein data provided by the manufacturer.

and the stator yoke are relatively equivalent

2.6.2.3 Determination of magnetic losses coefficients K_h and K_{exc}

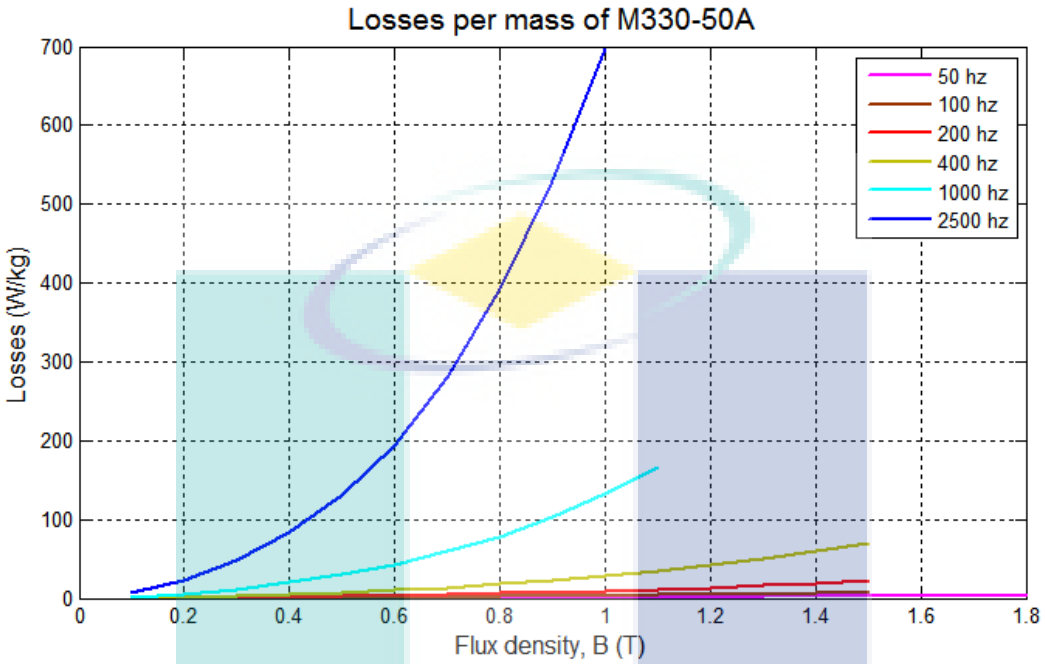

Figure 2.39: Epstein data of M330-50A steel provided by the manufacturer, Cogent.

K_h and K_{exc} are not given directly and they varies in function of material, thickness, frequency and flux density. They were deduced from an Epstein data of the material provided by the manufacturer, which is shown in Figure 2.39. The data gives an estimation of iron losses generated by polarization at different level of frequencies and flux densities.

In order to deduce K_h and K_{exc}, the losses given by the datasheet are going to be compared to the one calculated using Bertotti formulation (Equation 2.26). Equation 2.27 can be written in function of B as shown in Equation 2.28 .

$$P_{iron\,(datasheet)} = a.\hat{B}^2 + b.\hat{B}^{\frac{3}{2}} \tag{2.28}$$

with; $a = K_{.h}.f. + \frac{(\pi d)^2}{6.\rho_t.m_v}.f^2$ and $b = K_{exc}.f^{\frac{3}{2}}$.

By fitting the curves given by the material datasheet (Figure 2.39) to equation Equation 2.28 (Figure 2.40), a and b in the equation can be identified, hence K_h and K_{exc} for different frequencies. The results are shown inTable 2.5:

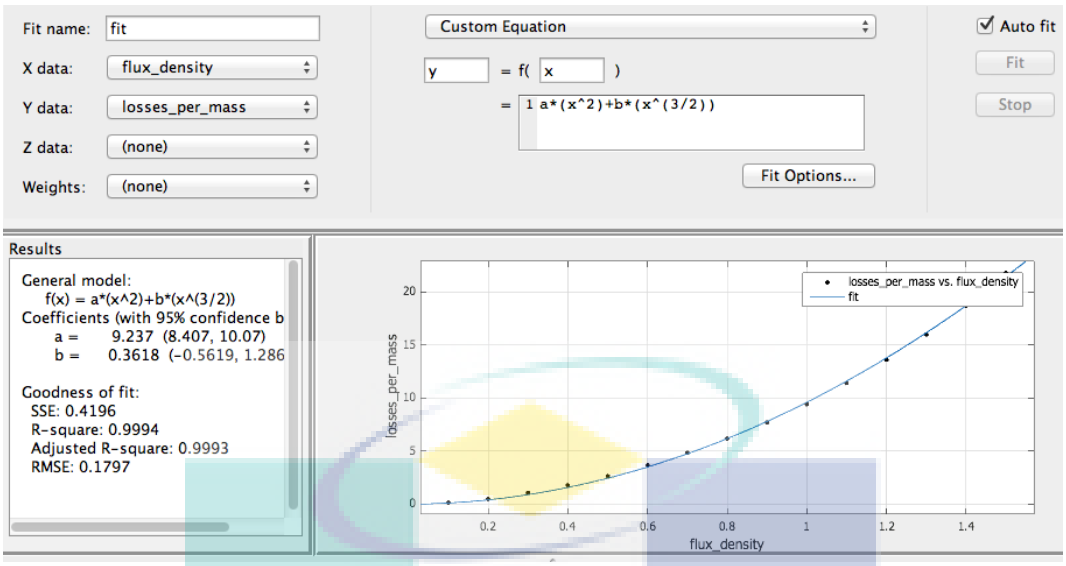

Figure 2.40: Curve fitting tools used to determine the losses coefficients at 200Hz.

frequency f	a	Hysteresis loss coefficient K_h	b	Excess loss coefficient K_{exc}
50 Hz	1.223	1.82 x 10^{-2} W/kg	0.112	3.17 x 10^{-4}W/kg
100 Hz	2.690	1.44 x 10^{-2} W/kg	0.801	8.01 x 10^{-4} W/kg
200 Hz	9.237	2.12 x 10^{-2} W/kg	0.362	1.12 x 10^{-4}W/kg

Table 2.5: K_h and K_{exec} values determined from curve fitting applied to manufacturer material curve data.

K_h and K_{exec} were shown to vary in unpredictable pattern. However, they reassuringly have the same order of magnitude (1×10^{-2} for K_h and 1×10^{-4} for K_{exec}). Therefore, for initial iron losses estimation, the average values from Table 2.5 are used to compute the iron losses, regardless the frequency.

With all the parameters of Equation 2.26 determined, a complete cartography of iron losses was mapped (Figure 2.41).

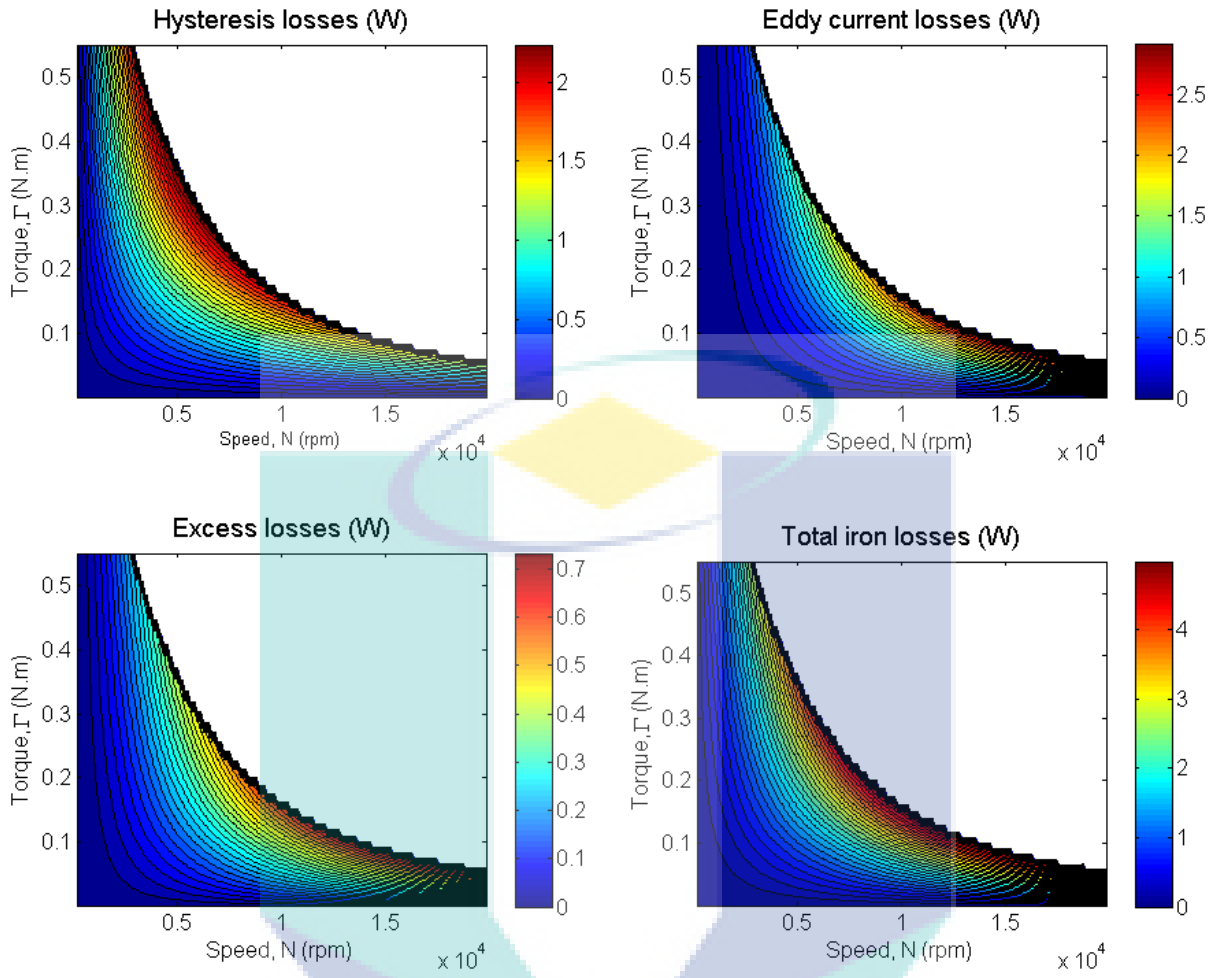

Figure 2.41: Cartography of iron losses in Syncrel motor for load angle $\beta = 45°$.

At load angle $\beta = 45°$ which will be the load angle used at all operating points of our prototype Syncrel motor, iron losses has been shown to be contributing at maximum 5W of losses. Compared to the copper losses, it is only 0.6% of total losses. It can be concluded that iron losses is negligible in our prototype motor.

2.6.3 Power balance check

In order evaluate the precision of both losses computation (iron and copper losses), a power balance evaluation on the computed power transformation in the motor was done. It is admitted that $P_{elec} = P_{mecha} + P_{losses}$, with $P_{losses} = P_{cu} + P_{iron}$. Figure 2.42 the power balance verification where the difference between absorbed electrical power and the sum of mechanical output and losses was computed.

It shows a maximum error of 4% of the mechanical output power. The increase of power balance error with speed can be explained with the usage of a constant iron losses coefficients

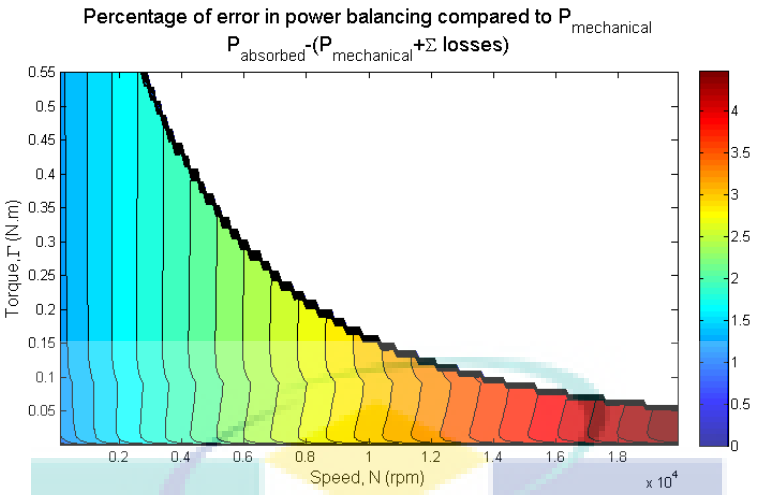

Figure 2.42: Power balance verification (analytical).

(K_h and K_{exec}). A more precise losses coefficients which vary in function of frequency will certainly give a better power balance. However, the error at 4% of mechanical power is considered negligible considering that it only occurs at an extremely high speed and that the maximum mechanical power is around 180W. The iron losses coefficients as well as the computation tools of losses are therefore validated.

2.7 Comparison with other motor

Following the evaluation of different electro-mechanical characteristics, we seek to position the Syncrel motor with segmented rotor among other motor that could satisfy the automotive application requirements. It was explained in the Introduction, other permanent magnet and rotor excited motors are considered too sensitive and vulnerable to high temperature environment. Therefore, the motor will only positioned among other Syncrel motor with passive rotor.

Among Syncrel motor, the study has been dominated by flux-barrier rotor (with and without magnet) due to the admitted superiority of flux-barriers $L_d - L_q$. Solid rotor has also been studied due to its structural simplicity. The segmented rotor which admittedly situated in the middle (in terms of performance and structural simplicity) is however not much studied. Therefore, a comparison of performance between these three rotor topologies is necessary to evaluate the gain of performance that can be obtained by adopting one rotor or another.

With all the computation tools validated and different electro-mechanical figures of the prototype motor evaluated, a comparison with other two rotors can be done. To do so, a

flux-barrier rotor and a solid rotor were designed (Figure 2.43) using FE tool and L_d and L_q were calculated afterward.

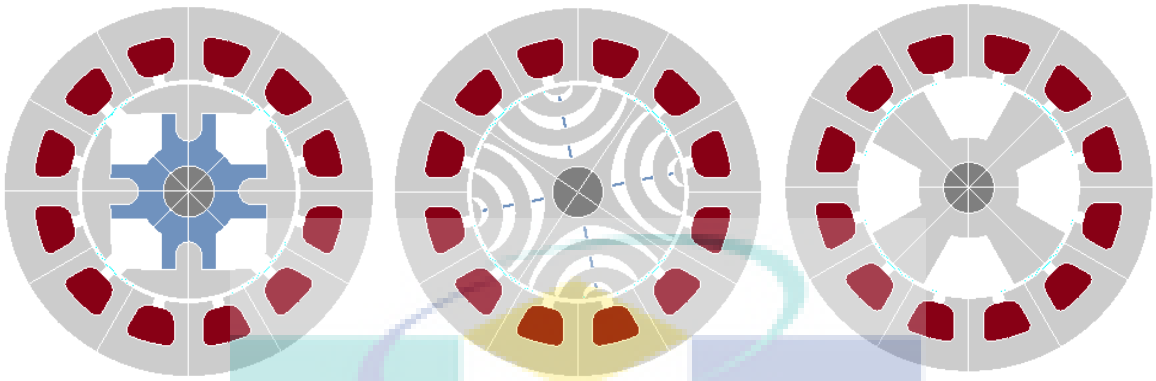

Figure 2.43: The three Syncrel motor compared. From left: the prototype Syncrel motor with segmented rotor, Syncrel motor with flux-barrier rotor and Syncrel motor with solid rotor.

The stator dimension, air gap, winding resistance, power supply and load angle are identical. It has to be noted that the design of the flux-barrier rotor and the solid rotor are not optimized. Comparison between the three motors are done with following configurations: power supply = 14V/50A, $\beta = 45°$, $R_s = 0.22\Omega$.The results of different characteristics computed using analytical tools developed earlier in this chapter is shown in Table 2.6.

	Segmented rotor	Flux-barrier rotor	Solid rotor
L_d : L_q (mH) (FEA)	0.254 : 0.102	0.244 : 0.088 [1]	0.236 : 0.113
L_d/L_q	2.49	2.77	2.09
Γ_{50A} (N.m) (analytical)	0.566	0.585	0.460
$cos(\phi)_{5000rpm}$ (analytical)	0.850	0.866	0.841
torque ripple (%) (FEA)	105	41	78

Table 2.6: Comparison of on magnetic characteristic and different electro-mechanical performance.(Power supply:14V/50A, $\beta = 45°$, $R_s = 0.22\Omega$)

[1] The value in the table is for inductances at maximum current (50A). The inductance values change in function of current. The difference of $(L_d - L_q)$ increases with the current. At lower current, the bridges are not saturated, hence a higher L_q.

Overall, the most competitive rotors are the flux-barrier rotor and the segmented rotor. The solid rotor falls behind these two rotors. Between them, the comparison has to be done with more details.

The saliency ratio of the segmented rotor is closer to the flux-barrier rotor than the solid rotor. It may be argue that the flux-barrier rotor is not optimized. However, considering the manufacturing constraints, with a rotor diameter of 25mm, it is very hard to build barriers

that can decrease L_q as well as being mechanically robust. In fact, a certain minimum size of barrier is required in order to prevent the flux from crossing the barrier. In the contrary, a too big barrier can be mechanically fragile. Therefore, for a small diameter motor, flux-barrier rotor can be impractical.

In terms of operating area range, Figure 2.44 shows that the flux-barrier rotor gives barely 0.1 N.m in torque and 300rpm in speed at maximum.

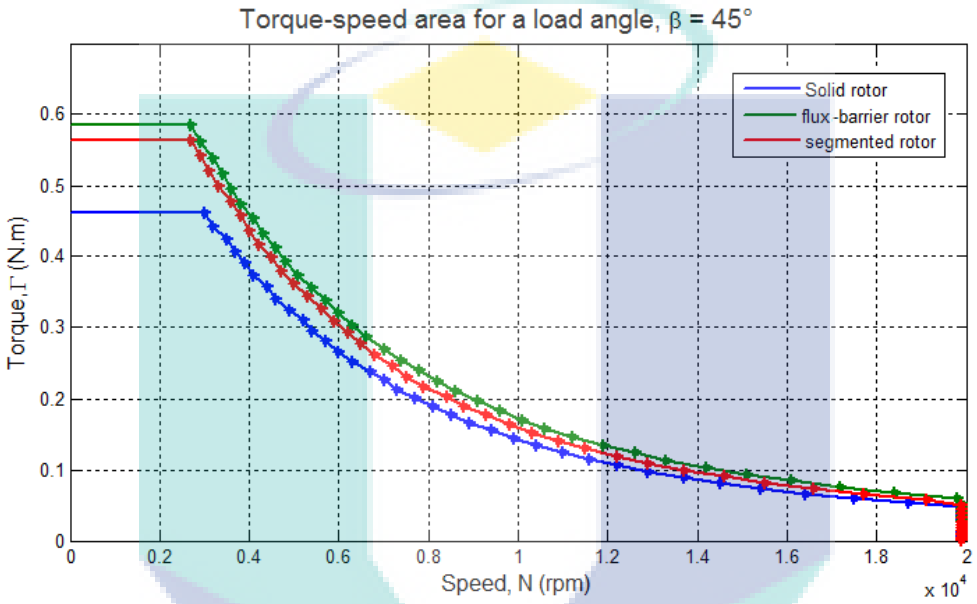

Figure 2.44: Comparison of torque-speed area range between the three Syncrel motor. (analytical tool)

However, by having a closer look into the torque at different current level Figure 2.45, the flux-barrier rotor has a lower torque at lower current. This is due to the non-saturated bridges at lower current that increase L_q in consequence. On the other hand, the segmented rotor gives better torque at lower current as it does not depend on saturation state of the material. Therefore, for an application where the operating points rarely attains the peak torque and operates majoritarily at lower torque, the segmented rotor is shown to be a better option. As for power factor, the higher saliency ratio of the flux-barrier rotor also means that it has a higher power factor.

In terms of torque quality, the torque ripple percentages were evaluated by comparing the peak to peak difference with the average value Figure 2.46. The segmented rotor torque ripple is twice as high as the flux-barrier torque ripple. The torque ripple evaluation and comparison will be done further in chapter 4.

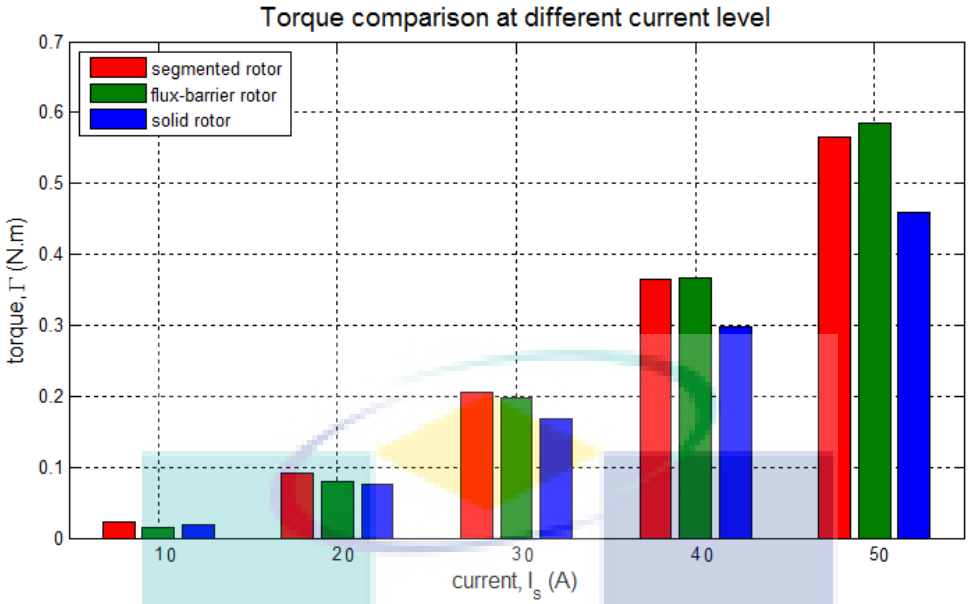

Figure 2.45: Mean torque comparison at different current level. (FEA analysis)

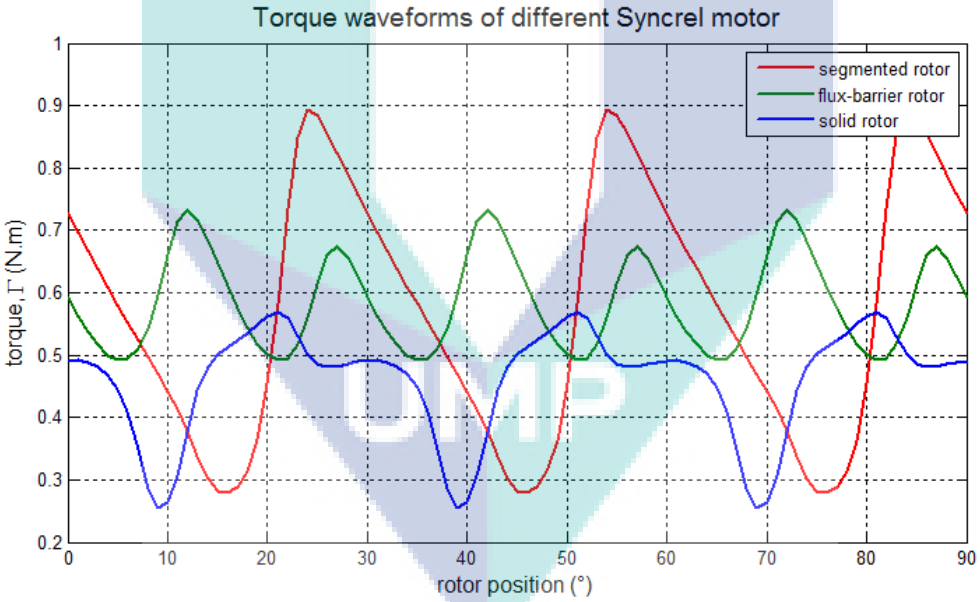

Figure 2.46: Torque comparison between the three Syncrel motor at maximum current $I_s = 50A$. (FE analysis)

2.8 Conclusion

In this chapter, different electro-mechanical characteristics of the segmented rotor Syncrel machine have been evaluated theoretically and validated experimentally.

An analytical tool was developed to map the operating areas attainable by the machine.

As opposed to other magnetically-active-rotor machine, the Syncrel has been shown to limited possibility to extend its operating area. We also have taken into account non-linearity of the material onto the operating area computation to produce a more precise prediction. It was shown that the linearity hypothesis made during the pre-design phase of the machine is acceptable for the application operating area range regarding the requirement demanded. Besides, the possibility of the machine to be operated to deliver static torque was also studied, resulting into understanding of instantaneous static torque and proposition of a tool allowing an optimum choice of flux and rotor position that maximizes the static torque.

Then, the power factor of the machine has been evaluated without neglecting the winding resistance as usually done in literature. This was important in a multiphysical approach as the winding resistance can increase importantly with temperature. Influence and interaction of different parameters such as resistance, load angle and speed on the power factor were studied. Two abacus helping to predict the interaction between these parameters were developed.

Later, the efficiency of the machine was studied. The copper losses has been shown to be major contributor to the machine losses. An increase of winding resistance due to heat generated by the losses has been shown to reduce the operating area heavily. With a high winding resistance in the prototype machine, the efficiency is low. In the meantime, the copper losses has also been briefly studied along with iron losses.

Finally, using the analytical tools developed previously, our prototype Syncrel machine was compared to two others Syncrel motor with different passive rotor topologies: flux-barrier and solid rotor. With a same stator size and same winding, the Syncrel with segmented rotor has been shown to be as nearly competitive as the flux-barrier rotor and far in front of the solid rotor in terms of torque, power factor and efficiency. Therefore, taking into account the industrial manufacturing feasibility and mechanical structure robustness, it can be concluded that Syncrel with segmented can be considered as the best machine for small space and high temperature application.

In perspective, the performance characteristics can be computed and tested with a better winding resistance, different inductances (following topology optimization) and power supply to extend the possibility of application of the Syncrel machine. The tools developed in this chapter can serve in the future as base to a coupled-multiphysical tool, including thermal and vibration model.

Bibliography

[1] Boldea I., “Reluctance Synchronous Machines and Drives”, Oxford Science Publications 1996, pp. 28, ISBN 0-19-859391-0. 30, 39, 43, 59

[2] Doc C., “Contribution à la Conception et au Dimensionnement d’un Actionneur d’Embrayage”, Ph.D. Thesis, Université de Technologie de Compiègne, 2010. 25, 40, 48

[3] T. A. Lipo "Synchronous Reluctance Machines: a Viable Alternative for A.C. Drives?", Electric Machines and Power System, pp.659 -671 1991

[4] Moghaddam, R.R.; Magnussen, F.; Sadarangani, C., "Theoretical and Experimental Reevaluation of Synchronous Reluctance Machine," Industrial Electronics, IEEE Transactions on , vol.57, no.1, pp.6,13, Jan. 2010 48

[5] Seth R. SANDERS Heath HOFMANN. Synchronous reluctance motor/alternator for wheel energy storage systems. Power Electronics in Transportation, pages 199206, 1996. 25, 48

[6] Nicola Bianchi. Electrical machine analysis using nite elements. CRC Press, 2005. 40

[7] Chiba, A.; Nakamura, F.; Fukao, T. & Azizur Rahman, M. Inductances of cageless reluctance-synchronous machines having nonsinusoidal space distributions Industry Applications, IEEE Transactions on, 1991, 27, 44-51 185

[8] Nicola Bianchi. Electrical machine analysis using finite elements. CRC Press, 2005. 185

[9] Raminosoa T., “Optimisation des performances des machines Synchro-reluctantes par reseaux de perméances”, Ph.D Thesis, Institut National Polytechnique de Lorraine (INPL), 2006. 48

[10] Vagati, A.; Fratta, A.; Franceschini, G. & Rosso, P., “AC motors for high-performance drives: a design-based comparison”, Industry Applications, IEEE Transactions on, 1996, 32, 1211-1219. 48

[11] Hamiti M. O., “Réduction des ondulations de couple d’une machine synchrone à réluctance variable: Approches par la structure et par la commande”, PhD thesis, Université Henri Poincaré, Nancy-I, Juin 2009. 48

[12] Fratta, A.; Troglia, G.; Vagati, A. & Villata, F. Evaluation of torque ripple in high performance synchronous reluctance machines Industry Applications Society Annual Meeting, 1993., Conference Record of the 1993 IEEE, 1993, 163-170 vol.1 45, 46

[13] J O Bird; A J C May (22 October 2013). Engineering Science 2 Checkbook. Elsevier. pp. 152. ISBN 978-1-4831-0539-0. 61

[14] Tildon H. Glisson (18 February 2011). Introduction to Circuit Analysis and Design. Springer Science & Business Media. pp. 32. ISBN 978-90-481-9443-8. 60

[15] Hamid A. Toliyat; Subhasis Nandi; Seungdeog Choi; Homayoun Meshgin-Kelk (30 October 2012). Electric Machines: Modeling, Condition Monitoring, and Fault Diagnosis. CRC Press. pp. 11–. ISBN 978-0-8493-7027-4. 60

[16] C. Cester, "Étude des pertes magnétiques supplémentaires dans les machines asynchrones alimentées par onduleur à modulation de largeur d’impulsion", PhD thesis, INPG, 1996. 62

[17] C. Steinmetz, "On the law of hysteresis", Proc. of the IEEE, vol. 72, no. 2, pp. 197-221, 1984 (originally published in 1892). 62

[18] G. Bertotti, "General Properties of Power Losses in Soft Ferromagnetic Materials", IEEE Trans. on Mag., vol. 24, no. 1, Jan. 1988. 62

[19] E. Hoang, "Études, modélisation et mesures des pertes magnétiques dans les moteurs à réluctance variable à double saillance." PhD thesis, SATIE Lab., 1995. 62

[20] Y. Chen and P. Pillay, "An improved formula for lamination core loss calculations in machines operating with high frequency and high flux density excitation." Ind. Appl. Conf., IAS Ann. Meeting, vol. 2, pp. 759-766, 2002. 62

[21] G. Bertotti, A. Boglietti, D. Chiampi, D. Chiarabaglio, F. Fiorillo, M. Lazzari, “An improved estimation of iron losses in rotating electrical machines”, IEEE Trans. Mag., vol. 27, no. 6, pages 5007-5009, nov. 1991. 62

[22] S. Kuttler, “Dimensionnement optimal de machines synchrones pour des applications de véhicules hybrides.” PhD dissertation, Université de Technologie de Compiègne, 2013.

62

Chapter 3

Thermal behavior

Prediction on heat transfer within an electric machine in operation is an important issue. This prediction will allow an evaluation of thermal class of the motor as well as the behavior of its components at the operating temperature. It can also help manufacturer to design a cooling system adapted to the machine in order to prevent a breakdown. The critical breakdown temperature can be set by any component (wire insulation impregnation, bearings, magnet, plastic cover, encoder, housing, etc.) and the temperature exerted on it during operation can have a very significant effect on the machine's lifespan. Temperature identification of these limiting components is therefore essential. More crucially, it has been shown in chapter 2 that the winding temperature will affect its electrical resistance thus, affects the operating area, power factor and the efficiency of the motor.

Syncrel machine has been mentioned as a thermally robust machine in various literature [1, 2, 3]. The passive rotor structure gives it two major thermal advantages: zero rotor losses (considering mechanical losses negligible) and less thermal sensitive components. However, the stator structure is nonetheless the structure like any other synchronous motor thus, an extreme temperature produced by copper losses in the stator slot still need to be observed carefully so as to avoid the critical insulation temperature. Depending on its thermal class, the critical temperature T_{max} over which it will be deteriorated can be situated from 150°C to 240°C [4]. Figure 3.1 shows an example of the effect of temperature on the durability of different types of winding insulation in a type of machine [5]. Thus, in the whole chapter, the temperature that is going to be observed in different studies is the in-slot winding temperature.

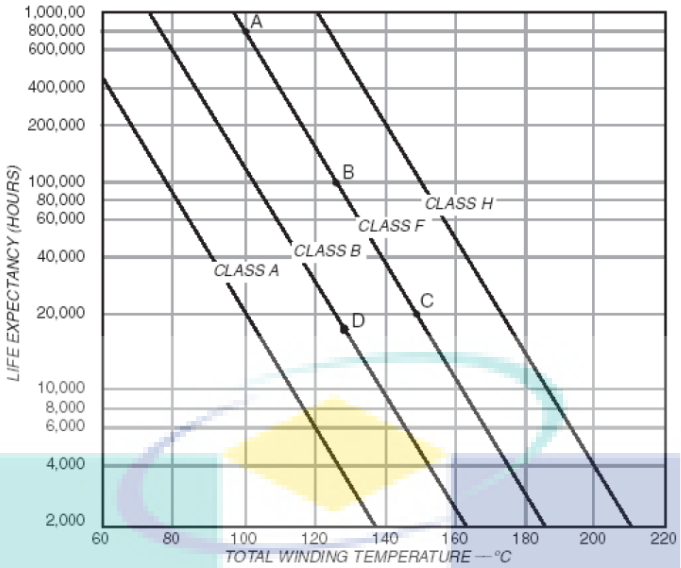

Figure 3.1: Temperature vs. life curves for insulation systems for different class of machine of the same type [5].

3.1 Modeling method

In order to assist engineers in designing a better machine that respect the thermal limitation, an appropriately accurate and robust thermal model is needed. A short development time and less computational resources are always preferable for industrial. The two major approaches that has been used to model thermal behavior in a machine structure has been lumped parameter (LP) model and numerical methods [6].

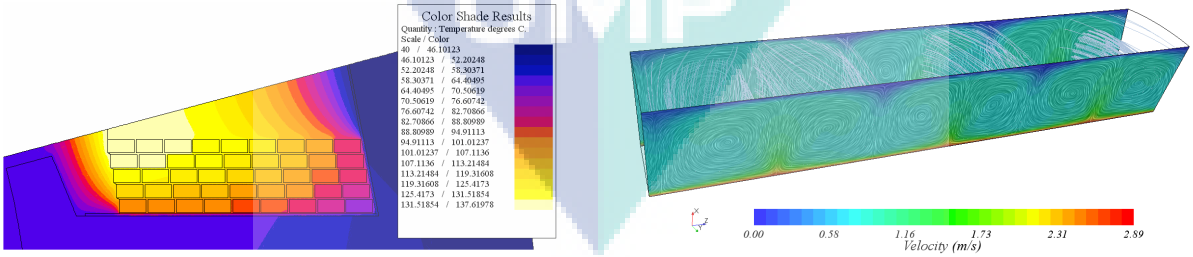

(a) An example of FEA analysis: steady state 2D finite element analysis of the temperature rise in a slot with rectangular copper conductors. [7]

(b) An example of CFD analysis: heated air flow pattern in airgap of a machine [8].

Figure 3.2: Two numerical methods used in electrical machine thermal analysis.

Finite element analysis (FEA) and computational fluid dynamics (CFD) are commonly numerical methods used for electrical machine thermal analysis [6]. FEA is used for solid structure while CFD, which usually use finite volume method is used for fluid areas (Figure 3.2).

It is commonly accepted that numerical method is more expensive method both in terms of development time and computational resources. It is mainly due to the significant time taken to define and calculate the solution for the problem. It requires an accurate geometrical representation, an appropriate discretization, a complete material data and a well-defined boundaries conditions in order to get the advantage of numerical methods. As consequence, utilization of numerical model can be costly for a complex structure such as an electrical machine.

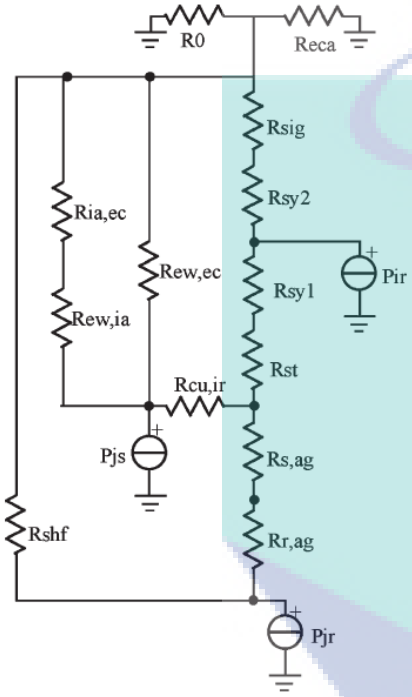

Name	Description
R_{eca}	Forced convection thermal resistance between external case and ambient
R_0	Natural convection thermal resistance between external case and ambient
$R_{ia,ec}$	Convection thermal resistance between internal air and endcaps
R_{sy1}	Radial conduction thermal resistance of the stator yoke lower half part
R_{sy2}	Radial conduction thermal resistance of the stator yoke upper half part
R_{st}	Radial conduction thermal resistance of the stator teeth
$R_{cu,ir}$	Conduction thermal resistance between stator copper and stator slot
$R_{ew,ec}$	Convection thermal resistance between stator winding external connections and external case
$R_{ew,ia}$	Convection thermal resistance between stator winding external connections and inner air
$R_{s,ag}$	Convection thermal resistance between stator teeth and airgap air
$R_{r,ag}$	Convection thermal resistance between rotor and airgap air
R_{sig}	Conduction resistance of the interface gap between the stator core and the external case
R_{shf}	Axial conduction thermal resistance of the shaft

Figure 3.3: An example of a LP thermal model for induction motor [7].

LP model in the other hand represents a simplification, where spatially distributed fields are approximated as a number of single scalars (Figure 3.3). Therefore, a thermal analysis can be carried out, providing fast results with reasonable accuracy provided that the network is chosen carefully. It should be mentioned however, that the calculation of lumped parameters, which are mainly based on dimensional data of the electrical machine and thermal properties of the materials used, can be difficult for complex parts such as the active part of the winding, and the exterior surface of the casing. LP model has been largely used for different machine architectures. Mellor, Kylander and Saari in[9, 10, 11] have applied the method on induction machines. Lindström[12] and Kolondovski [13] implemented LP thermal model of a permanent-magnet synchronous machines in their works. Even a more complex machine structure such as multibarrier interior permanent magnet machines has

also used LP model as presented by [14]. All of them have reported a good agreement between their model simulation and experiments at nominal speed and load. With all these arguments, LP method was chosen in this study.

3.2 LP model: generalities

In a LP model analysis, the machine is reduced to a number of discrete "lumps" and it is assumed that the temperature difference inside each lump is negligible [15]. This approximation allow a simplification of a complex differential heat equations. A mathematical analog of electrical circuit helps further in the ease of its development and utilization Table 3.1.

Electrical Parameter			Thermal Parameter		
Current	i	ampere, A	Heat flow rate	$\mathring{Q}$	Watt, W
Potential	E	volts, V	Potential	ΔT	°C
Resistance	R	ohms, Ω	Resistance	R_{th}	°C/W
Capacitance	C	farads, F	Capacitance	C_{th}	W.s/°C
Time constant	$R.C$	seconds, s	Time constant	$R_{th}.C_{th}$	seconds, s
Energy	$\int_0^t i.E.dt$	Joule, J	Energy	$\int_0^t q.dt$	Joule, J

Table 3.1: Formal analogy between thermal and electrical entities.

To built a LP thermal model, it is important to foremost identify all the losses in the machine, including losses in electrical circuits, in the magnetic circuits and mechanical losses.This requires quantifying, locating and separating the different sources of internal heat that generate the rise of temperature which are already treated in chapter 2. In this chapter, the next steps of thermal model construction are explained as follows:

1. Identification of heat transfer mechanism: The three basic mechanisms (conduction, convection and radiation) should be considered for a fine thermal analysis, but some mechanism may be paramount compared to others allowing certain simplifications.

2. Definition of thermal parameters of each part of the machine: Following certain hypothesis and simplification on the geometry of the machine, the thermal resistance and capacitance of each part will be calculated . It is necessary in this part to know absolutely all thermo-physical parameters specific to each part of the machine (densities, thermal capacity and conductivity of the components material).

3. Validation of the model and eventual fitting: Finally, the constructed model has to be validated by confronting it to a experiments using the prototype machine. The

simulation and the experiments need to be done in the exact same condition with as less as possible uncertainties in order to be comparable.

All three steps will be treated in following subsections.

3.2.1 Heat transfer mechanisms

The three main mechanisms of heat transfer in a motor are conduction, convection and radiation.

Conduction is the transfer of heat in a solid by means of molecular agitation within a material without any motion of the material as a whole. In general, conduction can be written in its integral form as in (Equation 3.1) according to Fourrier law.

$$\mathring{Q}_{cond} = \frac{\partial Q_{cond}}{\partial t} = -\lambda \oint_S \nabla T.\overrightarrow{dA} \tag{3.1}$$

Q_{cond} is the quantity of heat (J) and $\mathring{Q}_{cond} = \frac{\partial Q_{cond}}{\partial t}$ is the rate of heat transfer (in W), λ the material's conductivity ($W{\cdot}m^{-1}{\cdot}°C^{-1}$), ∇T is the temperature gradient ($°C{\cdot}m^{-1}$) and $\overrightarrow{dA}$ is an oriented surface area infinitesimal (m^2). In one dimensional form (in $\vec{x}$ direction) where homogeneity and isotropy are considered, the heat flow rate can be written as in (Equation 3.2) and the conduction thermal resistance R_{th} (W/m^2. K) can be written as (Equation 3.3).

$$\mathring{Q}_{cond} = \frac{dQ_{cond}}{dt} = -\lambda A \frac{dT}{dx} \tag{3.2}$$

$$R_{cond} = \frac{\Delta x}{\lambda} \tag{3.3}$$

R_{cond} calculation is strongly dependent on the thermal conductivity of the material. Most of motor construction material have a very well known thermal conductivity with minimal uncertainty which means a simple analytical calculation of R_{cond} for conduction is sufficient.

Convection is the heat transfer through fluids movements. The heat rate transfer can be written using Newton's cooling law as in (Equation 3.4).

$$\mathring{Q}_{conv} = \frac{dQ_{conv}}{dt} = h.A.\Delta T(t) \tag{3.4}$$

ΔT is the difference of temperature between the object's surface and the fluid and h is the convection heat transfer coefficient ($W/m^2.K$). h depends on various physical properties of the fluid and the physical situation in which convection occurs such as the temperature, the geometrical form, and external air flow influence. Different values were proposed for different

conditions [16, 17]. They are nonetheless empirical, thus may not completely suitable for a given system. It is therefore very difficult to calculate and must be derived or found by experimental identification.

Finally, radiation is the heat transfer process through electromagnetic waves from a surface [19]. The Stefan-Boltzmann's correlation in (Equation 3.5) defines the rate of heat transferred by radiation $\mathring{Q}_{rad}$ (J), where σ is the Stefan- Boltzmann constant ($5.67 \times 10 - 8$ $W/m^2/°C^4$), A is the area emitting the radiation (m^2) and T the surface temperature (°C) .

$$\mathring{Q}_{rad} = \sigma.A.T^4 \tag{3.5}$$

Radiation is difficult to compute as there are not just radiation emitted from the surface, but also radiation received by the surface from other exterior surface in its surroundings. The net radiation heat loss rate can be computed using (Equation 3.6).

$$\mathring{Q}_{rad} = \sigma.A.\varepsilon.F_{1-2}.(T_1^4 - T_2^4) \tag{3.6}$$

Where ε is the emissivity of the surface, a dimensionless quantity: 0 for absolute reflector such as a mirror, and 1 for absolute absorber such as a black body. F_{1-2} is the view factor of surface 2 with respect to surface 1 which means the proportion of the radiation which leaves surface 1 that strikes surface 2. In a setup where only two entities considered (the machine and its surrounding as a set), the view factor equal to one as result of energy conservation. T_1 is the temperature (°C) of the hot body and T_2 is the cold surrounding temperature (°C). Like convection coefficient h, ε is also difficult to be found and must be derived or found by experimental identification.

The three heat transfer mechanisms occur in a motor. Several hypothesis can however be made: Conduction occurs across every solid parts while convection and radiation occur in the airgap, interior cavity and on the exterior surface in contact with ambient air. Convection in a small airgap and cavity can be considered negligible compared to conduction when the Nusselt number which represents the ratio of convective to conductive heat transfer across the surface is very small [20]. Radiation in airgap and cavity can also be considered internally negligible especially for a compact motor and it can be explained by a low temperature gradient. For convection and radiation on exterior surface of the motor, both are going to be integrated into a single thermal resistance R_{ext} found by experimental identification.

3.2.2 Thermal parameters calculation

3.2.2.1 Thermal resistances

For conduction, there are several generic simple form on which the thermal resistance can be calculated easily: extruded profile form, cylindrical shells and spherical shells. Considering our application, only extruded profile and cylindrical shells are going to be used.

In a one direction heat transfer, Figure 3.4a illustrates the integration of a thermal resistance representing conduction heat transfer across an extruded profile form of a section S. The thermal resistance can be calculated as in Equation 3.7.

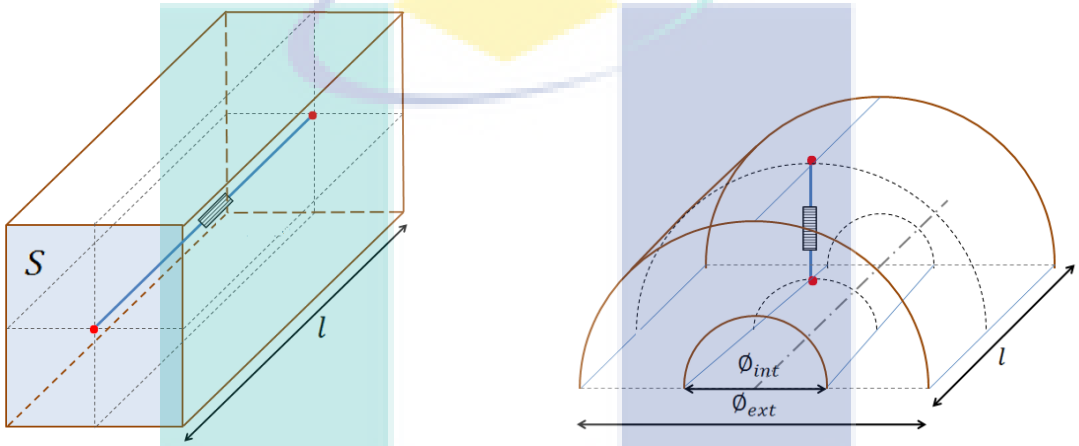

(a) The thermal resistance in an extruded profile form.

(b) The thermal resistance for a cylinder form body through which the heat passes. Only half of the cylinder is drawn here.

Figure 3.4: Thermal resistance representation in different generic form for a 1D heat transfer.

$$R_{cond\,extr} = \frac{1}{\lambda}\frac{l}{S} \tag{3.7}$$

Where l the length of the conductive path (m), λ is the thermal conductivity of the material (W/m/°C) and S is the cross-sectional heat transfer area (m^2). Figure 3.4b illustrates the integration of a thermal resistance representing conduction heat transfer across a cylinder section with the interior diameter of $\varnothing_{int}$ and the exterior diameter of $\varnothing_{ext}$. The conduction thermal resistance of cylindrical shell can be calculated as in Equation 3.8.

$$R_{cond\,cyl} = \frac{1}{\alpha\lambda l} ln(\frac{\varnothing_{ext}}{\varnothing_{int}}) \tag{3.8}$$

With α represents the angular section of the cylinder in which the heat is transferred.

However, application on electrical machine means that the heat transfer need to be

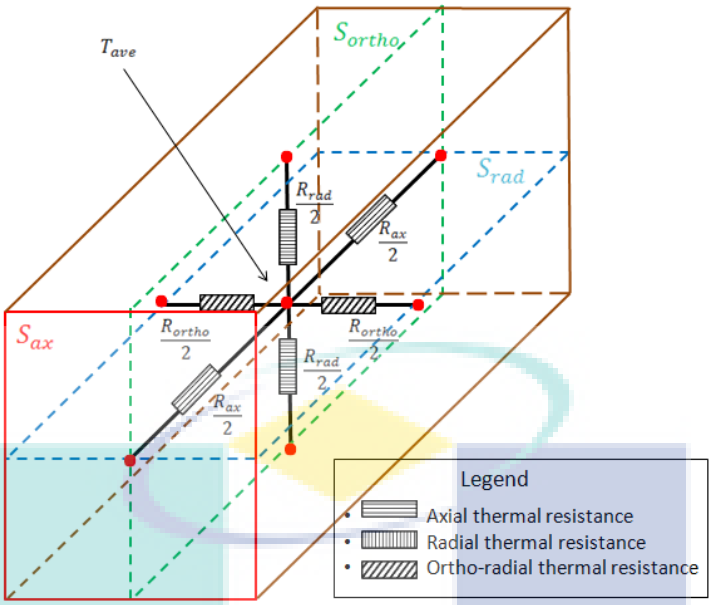

Figure 3.5: Connection between radial, axial and ortho-radial thermal resistance and the average temperature deduced from the model configuration.

modelized in more than one direction. There are usually three direction: radial, axial and ortho-radial. It is thus important to define the connection point and ensure that the right temperature can be deduced from the model. Figure 3.5 shows a simple cuboid element as example with all radial, axial and ortho-radial resistances being sectioned into half. Their thermal resistance (R_{rad},R_{ax} and R_{ortho}) are calculated regarding their respective perpendicular surfaces (S_{rad},S_{ax} and S_{ortho}) and the distances to the extremities of the surfaces using Equation 3.7. The middle point between the thermal resistance of each direction are connected together, giving access to the average temperature of the cuboid body, T_{ave}. The other points on the extremities of each direction give the surface temperature in the direction. They are also the points that are going to be connected with neighboring bodies.

For convection and radiation, regarding the difficulty of choosing a perfectly compatible empirical correlations (as mentioned in subsection 3.2.1), a more compatible procedure is use in order to have a thermal exterior resistance (radiation and convection effects combined). This procedure is based on experimental results and will be exposed later in subsubsection 3.3.5.1.

3.2.2.2 Thermal capacitance

In order to be able to evaluate the transient state, thermal capacity of each body C_{th} (J/K) are also integrated into the model. They are calculated using their material's specific heat

capacity c (J/kg.K), density ρ (kg/m^3) and volume V (m^3) (Equation 3.9).

$$C_{th} = \rho.V.c \tag{3.9}$$

In the lump body such in Figure 3.5, the capacity of the body will be connected to the center point, at the same point where T_{ave} can be found.

3.3 Thermal model of the Syncrel motor

In this section, the motor parts are discretized in function of generic forms (as presented in subsubsection 3.2.2.1) having a homogenous material characteristics. From a cross-sectional view (Figure 3.6), we can classify 7 elementary parts which are : casing, stator yoke, teeth, slot set, air gap, the rotor assembly and shaft. The radial and ortho-radial supposed heat flux presented by red arrows while the axial heat flux are in the direction perpendicular to the surface represented.

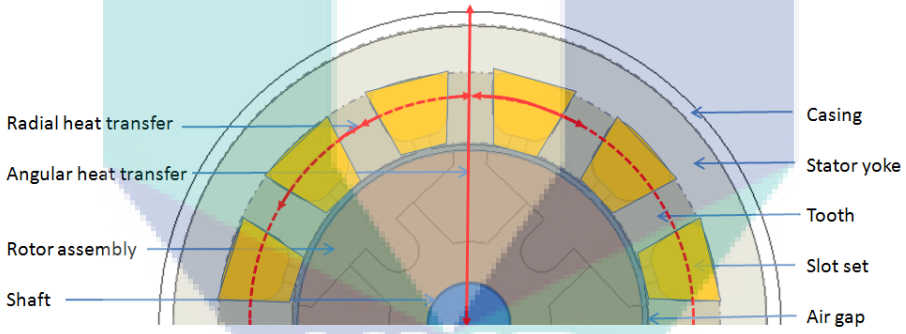

Figure 3.6: Elementary parts in simplified geometry form with the supposed heat flux. In each elementary part, a resistance representing the elements thermal resistance is calculated.

The rotor structure which is composed of ferromagnetic active segments, aluminum holder and air was homogenized into a single rotor assembly. The homogenized structure thermal resistance was calculated by taking into account each element ratio in the assembly. This was done because two major reason:

1. Being a synchronous motor and having a passive rotor, there will be no major losses to be injected on a specific point and the losses in the ferromagnetic segment are also supposed to be negligible.

2. With a passive rotor, there are also no critical elements in the rotor on which the temperature need to be looked into.

It is only useful in the model in quantifying the heat flux passing through the rotor compared to and towards other neighboring parts such as the shaft and the cavity.

In order to take into account the axial heat transfer, there are 3 other parts to be taken into account : end-winding, air cavity and flange-bearing set (Figure 3.7). With the same explanation as the rotor assembly set, the bearing and the flange were considered as a single set.

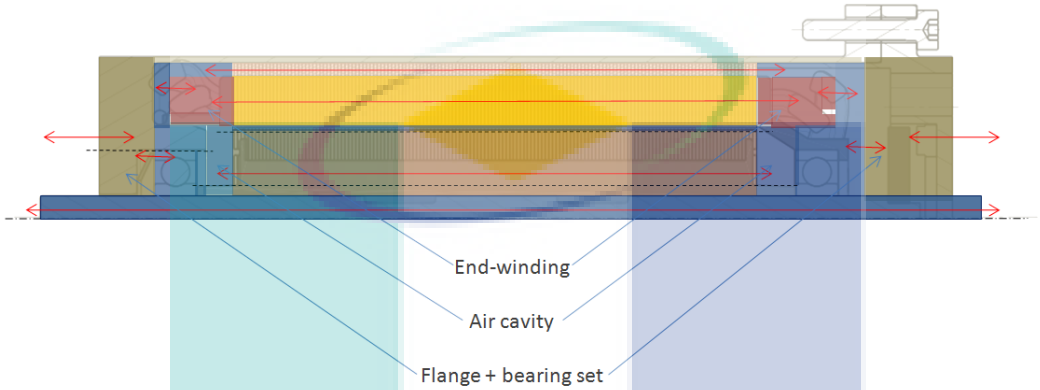

Figure 3.7: Axial heat transfer including the end-winding, air cavity and the flange and ball bearing set as elementary parts. In each elementary part, a resistance representing the elements thermal resistance is calculated (Table 3.2).

The summary of geometry simplification of each machine part and the conduction thermal resistance equation used are detailed in Table 3.2. The complete LP model can be seen as in Figure 3.8.

However, there are some other issues related to manufacturing and assembly process that can affect the heat transfer and make them more complex to determine. The conductivity λ of certain parts need to be found carefully before applying the equations in Table 3.2. These includes complex conduction within slot, conduction interference by gaps between components, as well as conduction interference across the stacked iron sheet. These issues are treated in next subsections (From subsection 3.3.1 to subsection 3.3.4).

3.3.1 Slot equivalent thermal resistance

The winding in the slot is the most crucial component in a machine. Due to its random wire disposition, it is also the area across which a fine and accurate temperature distribution is the hardest to determine. Choosing the most suitable method to find the thermal resistance within the stator slot of the machine is therefore very important. First, a clear objectives need to be made on what we are looking in the slot: the temperature distribution, the average

Bodies	Heat direction	Mode	Simplified form	Equation
Casing	Radial	Conduction	cylinder	(Equation 3.8)
Stator yoke	Radial	Conduction	cylinder	(Equation 3.8)
	Axial	Conduction	extruded profile	(Equation 3.7)
Teeth	Radial	Conduction	section of cylinder	(Equation 3.8)
	Axial	Conduction	extruded profile	(Equation 3.7)
	Ortho-radial	Conduction	cuboid	(Equation 3.7)
Slot set	Radial	Conduction	section of cylinder	(Equation 3.8)
	Ortho-radial	Conduction	cuboid	(Equation 3.7)
Air gap	Radial	Conduction	cylinder	(Equation 3.8)
Rotor assembly	Radial	Conduction	cylinder	(Equation 3.8)
Shaft	Axial	Conduction	extruded profile	(Equation 3.7)
End-winding	Axial	Conduction	extruded profile	(Equation 3.7)
Air gap	Radial	Conduction (convection negligible)	cylinder	(Equation 3.8)
Air cavity	Axial	Conduction (convection negligible)	extruded profile	(Equation 3.7)
Cap: Flange + ball bearing set	Axial	Conduction	extruded profile	(Equation 3.7)
Casing-ambient air contact	Axial and radial combined	Convection & Radiation	NA	by experimental identification (subsubsection 3.3.5.1)

Table 3.2: Thermal parameters calculation for each part of the model where conduction occur.

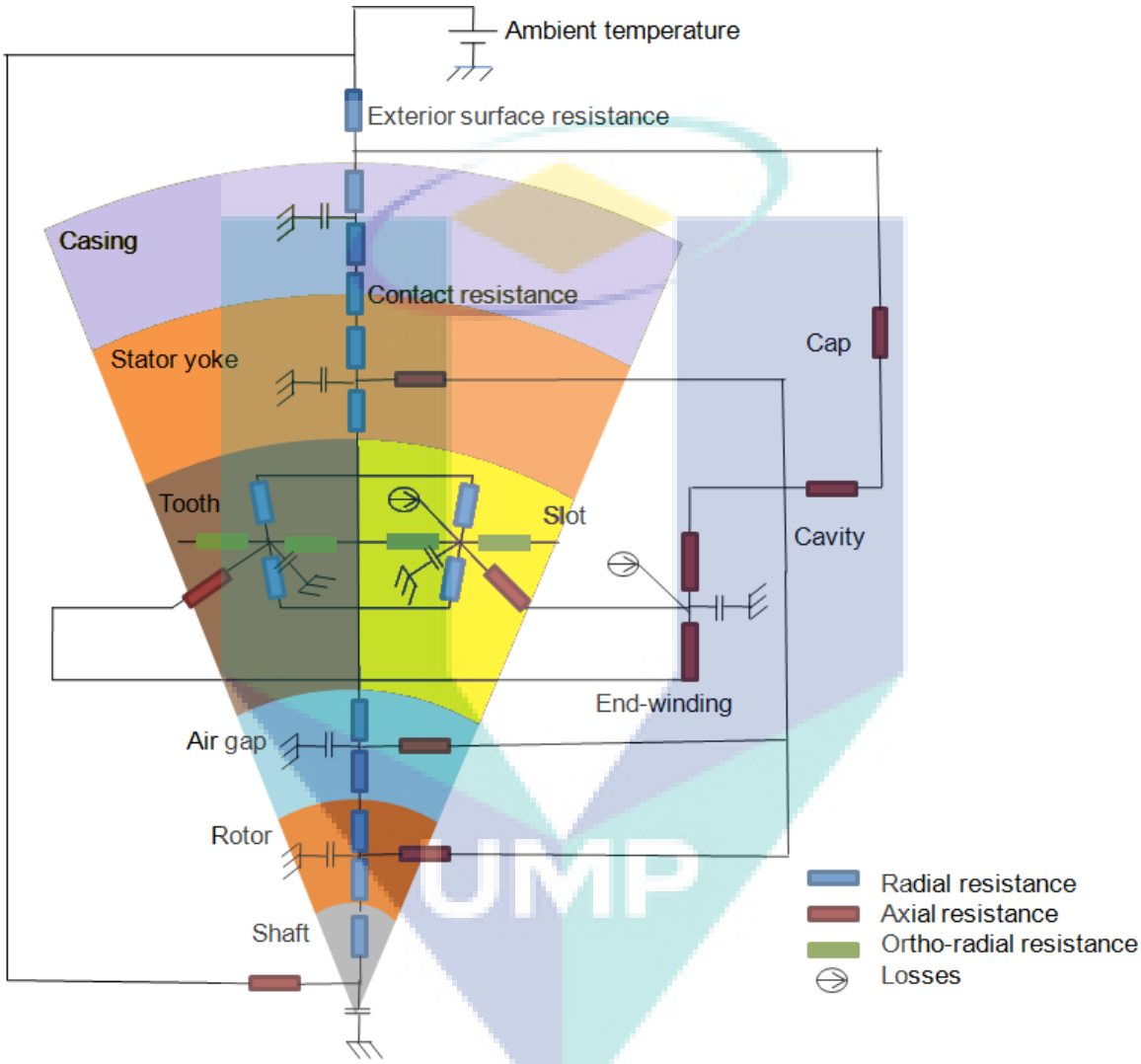

Figure 3.8: The complete LP model of the Syncrel motor. Only copper losses shown in this figure. Iron losses can be injected in the stator yoke and tooth middle point.
Remark: The model was reduced to one single pole radially and to the half of the axial dimension thanks to its symmetry and periodicity.

temperature, or the maximum temperature. Various method have been used to deduce the thermal resistance in a machine slot and they can be categorized as following:

1. Full numerical analysis: [21] has carried out a full numerical analysis in the beginning of his study to observe hot points in a machine slot. The difficulties regarding this method is that some assumptions must be made regarding the randomness of the conductor placement, the impregnation goodness, and any gaps between the slot liner and the stator lamination. However, if a good replication of the slot can be made, a good accuracy of temperature distribution can be achieved. Thus, the maximum temperature and its location in the slot can be accurately located.

2. Numerical-lumped element combination: There are mainly two approaches in this method:

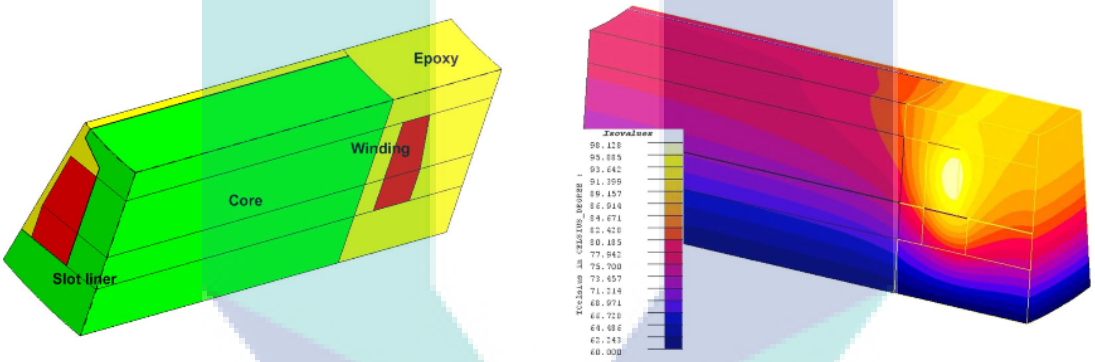

Figure 3.9: Section of wound stator segment showing the lumped regions used in FE thermal model and its results [22].

   (a) A homogenization of areas with the same thermal properties, just like in LP method Figure 3.9: Wrobel argued in [22] that the use of lumped regions in a 3D FE solver leads to a simpler model formulation and faster solution time. A composite lump region thermal properties such as the winding is very delicate to determine. He has experimentally derived its thermal properties using a custom built winding sample [23]. The thermal resistance of a sample of material also can now be easily measured with the appearance of thermal resistance measurement devices using Transient Plane Source Method [24]. However, with the utilization of this method, two questions can be arose: The first one is on the pertinence of using the thermal resistance deduced from an isolated sample in a slot, when we know that there are cases where winding in a slot does not correspond exactly to the winding sample. The second is on the advantages of this numerical-lumped

element combination method gained compared to a full LP model. We know that for solid area, LP approach is as good as FEA. The real advantages of FEA is in complex area such as the winding. However, here, this area has been reduced to a lumped area thus, just like in LP model, no accurate temperature distribution will be available in the FEA results.

(b) Equivalent LP model deduced from FEA: Another approach in this category is deduction of an equivalent LP model of a slot using a prior FEA analysis as proposed by [25]. Following an observation on the heat distribution pattern on a FEA, a LP model built of a n-layer isothermal components (copper and impregnation) in elliptical form is constructed. The accuracy of the temperature distribution compared to the FEA results is proportional to the layer number considered. In the example shown in Figure 3.10, $n = 5$. With this method, it can be argued that the accuracy of the LP model is good compared to experimental results if and only if the FE model represents the studied machine correctly. Furthermore, the method obliges a new FEA on new slot geometry and as shown in a) this can be costly in time.

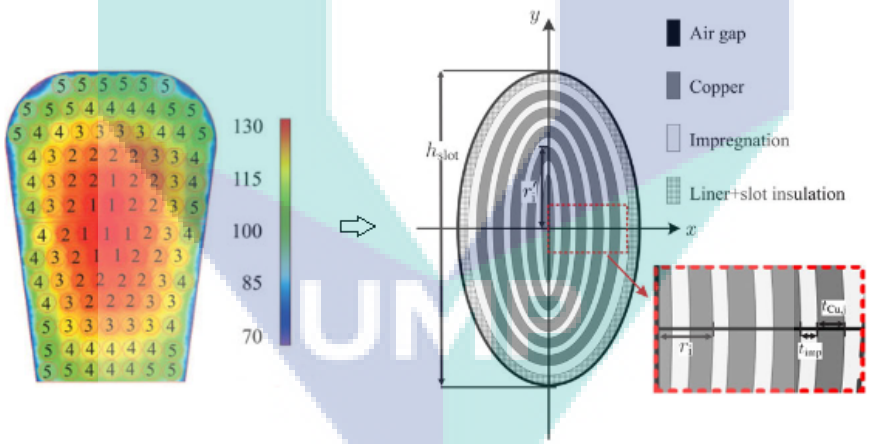

Figure 3.10: Proposed elliptical model of the active winding following observation on FEA [25].

3. Homogenization of slot into an isotropic single lump: Significant progress has long been made in domain of composite material engineering. Different characterization of composites materials in various aspects including heat distribution have been made. Studies on homogenization of composites materials include [26, 27, 28, 29]. They propose analytical equations allowing simplification of a complex structure such as an electrical winding into a single homogenized material with an equivalent thermal resistance. To summarize, homogenization method can be categorized according to

two characteristics: winding distribution (regular or random) and number of materials in the composite (2 or 3) Table 3.3.

Number of materials	Type of distribution	
	Regular	Random
2	Perrins [26]	Hashin & Shtrikman [27] Milton [28]
3	-	Mori & Tanaka [29]

Table 3.3: Different winding homogenization method.

Idoughi [21] has shown that the methods work in machine slot by validating them using FEA. In the other hand, Svensson [24] has also shown that the method works by validating them on a cuboid winding sample using a thermal sensor. The obvious advantage of using analytical equations proposed is that both the model development time and computation power can be reduced significantly.

With all the argument in the comparison, the third method (homogenization of slot into an isotropic single lump) was chosen. For in-slot winding, it is reasonable to adopt random distribution methods with three materials in order to replicate the slot as close as possible. The Mori & Tanaka method was then chosen. The three winding materials considered as example in Mori & Tanaka are copper wire, its insulation layer and the resin infiltration (Figure 3.11). The correlation used to calculate the equivalent thermal conductivity of the

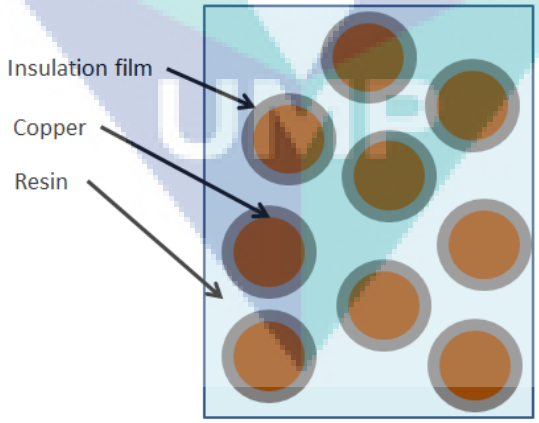

Figure 3.11: Three composites winding proposed by Mori and Tanaka (in axial cross section view).

slot homogenized material λ_{slot} is shown in (Equation 3.10).

$$\lambda_{re}.\frac{(2\lambda_{re}+\lambda_{copper}).(\tau_2(2\lambda_{re}+\lambda_{ins})+3\tau_3\lambda_{re})+3\tau_1\lambda_{copper}(2\lambda_{re}+\lambda_{ins})}{\tau_2(2\lambda_{re}+\lambda_{copper}).(2\lambda_{re}+\lambda_{ins})+3\lambda_{re}(\tau_1(2\lambda_{re}+\lambda_{ins})+\tau_3(2\lambda_{re}+\lambda_{copper}))} \tag{3.10}$$

τ_1,τ_2 and τ_3 represent the ratio of the volume occupied by the 3 materials (copper wire, resin and insulation film) to the total volume of the slot ($\tau_1 + \tau_2 + \tau_3 = 1$) while λ is each material thermal conductivity. τ_1 is also known as the slot filling factor. In our case, the resin infiltration was not used thus, the third material will be replaced by air instead of resin. The conductor used is a Grade 2[1] conductor with a diameter of 0.425mm. Surrounding the winding, there are also the slot linings. However, as the slot linings material (polyester) has a thermal conductivity very close to the conductor's insulation, the slot lining volume has been integrated into the insulation volume. The thermal conductivity of the homogenized material can be found using the curve presented in Figure 3.12

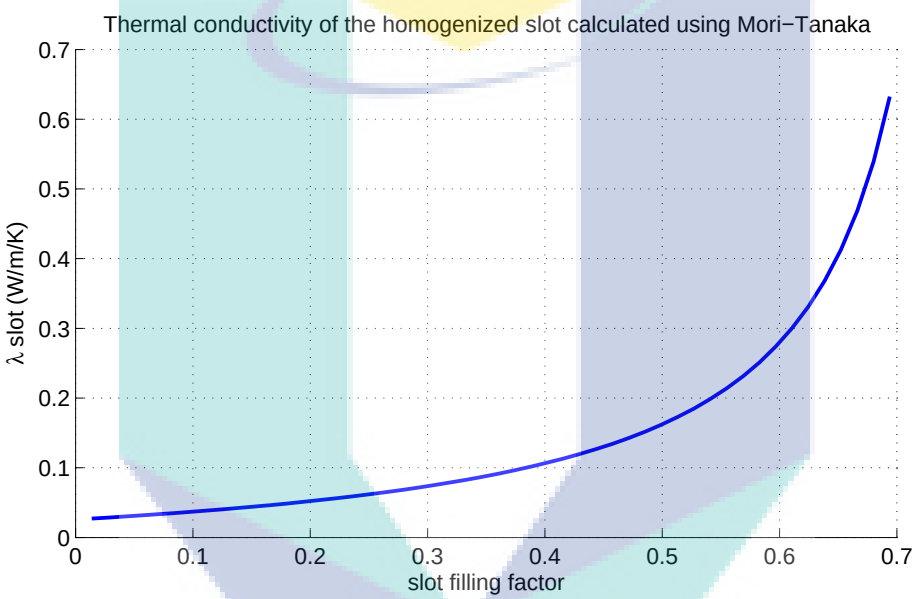

Figure 3.12: The homogenized slot thermal conductivity in function of filling factor τ_1, computed using Mori and Tanaka method Equation 3.10.

The homogenized material conductivity is later used to calculate the slot thermal resistance, taking into account its geometry as presented in Table 3.2.

3.3.2 End winding thermal resistance

The end-winding can be seen as a particular case of the slot because the structure is the same, except that the winding is in a much larger volume of air which is the cavity. Therefore, several hypothesis were admitted to make a discretization between the cavity and the end-winding:

[1] Classification of a conductor is made following its diameter, insulation class and temperature class. See IEC 60317 standard.

1. The conductors in the end-winding are bundled together and wounded tightly around the teeth forming a cylinder, adjacent to the slot area.
2. The air in the interstice between the conductors is considered negligible.
3. The cylinder representing the end-winding exchanges heat with the teeth and the cavity in the axial direction (as was presented in Figure 3.7).

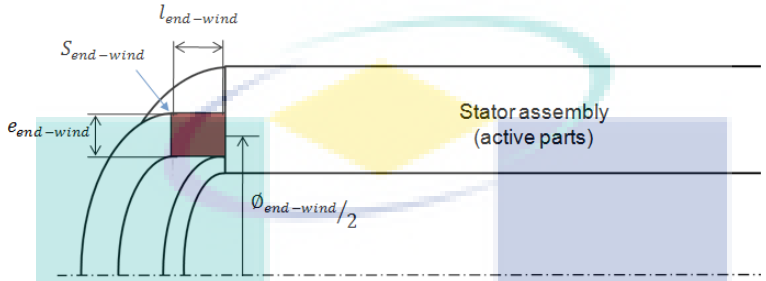

Figure 3.13: The dimension of the equivalent cylinder representing the end-winding.

For the dimension of the equivalent cylinder representing the end-winding, its cross section area as presented in Figure 3.13 is equal to the sum of the conductor's area. The cross section area $S_{end-wind}$ was considered as a square, thus the length $l_{end-wind}$ and the thickness $e_{end-wind}$ of the cylinder equal to Equation 3.11:

$$l_{end-wind} = e_{end-wind} = \sqrt{S_{end-wind}} = \sqrt{N_{cond}.(S_{cond} + S_{ins})} \tag{3.11}$$

The average diameter of the cylinder $\emptyset_{end-wind}$ is equal to the height of the center of the slot.

Following the hypothesis and the discretization explained, homogenization method was also used to deduce the equivalent thermal conductivity of the end-winding $\lambda_{end-winiding}$. Only two materials (copper wire and insulation film) within the same area was taken into account, thus Hashin & Shtrikman correlation as shown in equation (Equation 3.10) was used.

$$\lambda_{end-winiding} = \lambda_{ins}.\frac{(1+\tau_1).\lambda_{cu} + (1-\tau_1).\lambda_{ins}}{(1-\tau_1).\lambda_{cu} + (1+\tau_1).\lambda_{ins}} \tag{3.12}$$

It was found that without air, the conductivity of the end-winding is twice as big as the slot conductivity. The thermal resistance was calculated taking into account its geometry as a cylinder overhang.

It is also important to quantify the losses distribution between the end-winding and the active in-slot winding. It was found that up to 26% of the overall winding length is in the

end-winding parts. Therefore, in the LP model (Figure 3.8), 26% of the copper losses is going to be injected into the end-winding model while the rest 74% into the slot model.

3.3.3 Stacked iron sheet thermal resistance

Stator core assembly and rotor segments are made of stacked lamination steel, each 0.5mm thick. Both surfaces of the lamination are covered with insulation resin (usually at 1μm thickness) in order to reduce eddy current losses in the machine. The ratio between the total length of uninsulated lamination stack over the total length of the stator (or rotor) core assembly is called stacking factor. Depending on the stator core assembly method, the stacking factor varies from $0.85 - 0.98$. The assembly methods includes mechanical cleating, welding, bonding and loose stacking [30]. In function of these assembly methods, air or voids between laminations caused by burrs, flatness or too much coating or bonding adhesive between laminations will result in cores with a lower stacking factor. In our motor, the laminations was bonded using an epoxy adhesive properly, giving a high stacking factor of 0.95. Knowing the stacking factor, the sum of thickness of the resin insulation and the adhesive can be deduced knowing that the thickness of a lamination is 0.5mm.

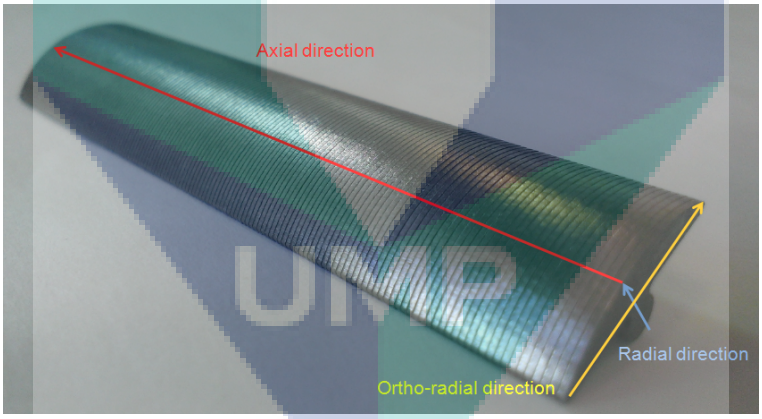

Figure 3.14: The lamination of the rotor segment. The thermal resistance direction are also shown by the arrows.

Besides direct effect on electromagnetic performance, the stacking factor can also influence the heat evacuation across the stacked laminations. According to [31], in axial direction, the heat flux goes through successions of laminations and insulation (plus adhesive) as can be seen in Figure 3.14. The axial equivalent thermal resistance can then be written as the sum of both elements (lamination and insulation) thermal resistances in series connection (Equation 3.13).

$$R_{eq\,ax} = n_{lam}.R_{lam\,ax} + n_{ins}.R_{ins\,ax} \tag{3.13}$$

With $R_{lam\,ax}$ and $R_{ins\,ax}$the thermal resistance in axial direction of a single piece lamination steel and insulation layer (adhesive layer included) respectively. For each part (stator yoke and teeth) they were calculated as presented in Table 3.2. $n_{lam}$and n_{ins} are the respective numbers of steel sheet and insulant resin constructing the final assembly. As for radial and ortho-radial equivalent thermal resistance, it can be written as sum of resistance in parallel connection Equation 3.14.

$$R_{eq\,ax} = \frac{R_{ins}.R_{lam\,rad}}{n_{lam}.R_{ins\,rad} + n_{ins}.R_{lam\,rad}} \tag{3.14}$$

With $R_{lam\,rad}$ and $R_{ins\,rad}$the thermal resistance in radial direction of a single piece lamination steel and insulation layer.

3.3.4 Surface contact thermal resistance

A contact resistance is due to imperfections in the contact surfaces and is a complex function of material hardness, interface pressure, smoothness of the surfaces and air pressure. Books on general heat transfer analysis such as Holman [33] and Mills [34] give typical values of surface thermal resistance (or conductance) in $m^2°C/W$ (or $W/m^2°C$) that can be expected between various materials for various root-mean-square (RMS) surface roughness. The RMS roughness values is defined as the deviations of a surface from the reference plane Figure 3.15 [35]. It was mentioned that it typically varies from 0.1pm for a mirror surface finish to 25.3μm for a rough finish.

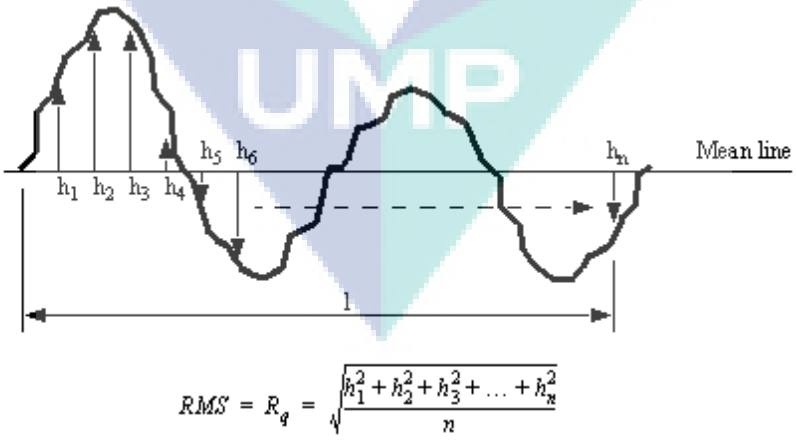

Figure 3.15: The definition of RMS roughness.

However, for application in electrical machine thermal analysis, there are other surface types involved besides plane, especially cylindrical. A simple uni-directional thermal resistance of the contact (independant of the surface type) is then preferable as it can be used

in any surface type. As solution, Staton [32] proposes converting the surface contact resistance (as given by Holman [33] and Mills [34]) to an equivalent effective airgap thickness as illustrated in Figure 3.16 by multiplying the surface contact resistance with the air thermal conductivity (0.026W/m/°C).

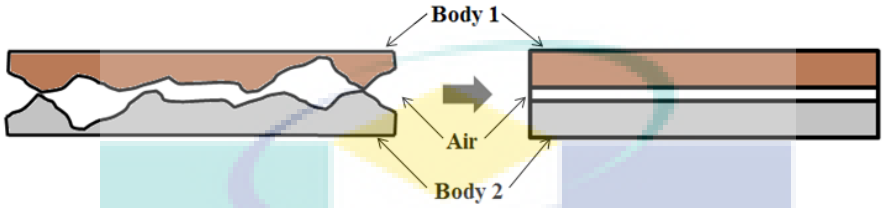

Figure 3.16: Converting the contact resistance in function of RMS roughness to an equivalent effective airgap as proposed by Staton.

The resulting effective airgaps are shown in the right column of each table in Table 3.4. Table 3.4a shows the conversion over the data given by Holman while Table 3.4b shows the conversion over the data given by Mills.

It can be observed that the softer and smoother the materials the smaller the effective gaps are. There is however a problem related to the machine construction method. For example, for a contact between stator-yoke and the casing, the stator yoke is built of stacked laminations. The gap in between is a function of how well the stack outer surface of the stator is prepared before inserting it into the casing. Further uncertainties can be introduced due to the fact that the thermal expansion rates between of the materials in contact can be different, leading to a constantly changing air gap. Staton [32] resolve the problem by identifying typical gaps in different sizes of machine and relate the gaps to manufacturing and material differences between machines. The gaps found are typically around 10 times greater than those found in Table 3.4.

In application to our motor, the contact resistance is recalculated in function of the contact surface type: cylindrical (Equation 3.8) or plane (Equation 3.7). Only the biggest surface contact in the Syncrel machine is considered, which is the contact between the stator yoke and the casing. The effective air gap value used is the one given by Mills for a stainless-aluminum contact (Table 3.4b) multiplied with the typical machine-construction-related coefficient found by Staton (0.007mm×10). Other surface contacts are negligible compared to it.

(a) Contact resistance between the same material by Holman [33] and the deduced effective air gap

Material	Contact Resistance ($m^2.°C/W$)	Effective Air Gap (mm)
416 ground stainless (3-25atm)	0.000264	0.0069
304 ground stainless (40-70atm)	0.000528	0.0137
ground aluminum (12-25atm)	0.000088	0.0023
ground aluminum (12-25atm)	0.000018	0.0005
ground copper (12-200atm)	0.000007	0.0002
milled copper (10-50atm)	0.000018	0.0005

(b) Contact resistance between two different materials with moderate contact pressure and usual finish by Mills [34]. The right column is the deduced effective air gap.

Interface contact	Interfacial Conductance ($W/m^2.°C$)	Effective Interface Air Gap (mm)
Ceramic-Ceramic	500-3000	0.0087 – 0.0052
Ceramic-Metal	1500-8500	0.0031 – 0.0173
Graphite-Metal	3000-6000	0.0043 – 0.0087
Stainless-Stainless	1700-3700	0.0070 – 0.0153
Aluminum-Aluminum	2200-12000	0.0022 – 0.0012
Stainless-Aluminum	3000-4500	0.0058 – 0.0087
Iron-Aluminum	4000-40000	0.0006 – 0.0060
Copper-Copper	10000-25000	0.0010 – 0.0026

Table 3.4: Effective interface air gap deduced from a) contact resistance by Holman and b) interfacial conductance by Mills.

3.3.5 Experiments

3.3.5.1 Identification of external surface thermal resistance R_{ext}

The only thermal parameter left to be determined in our model is R_{ext}. As it has been explained in subsection 3.2.1, R_{ext} comprises all the exterior element through which the heat is evacuated which include convection and radiation. Besides being difficult to calculate, it is important to remind that in a TENV (totally enclosed non-ventilated machine), the most important surface on which the heat will be evacuated is the exterior surface. Thus, any error on its value will cause a big error in the slot temperature prediction. It is therefore needed to be determined using experimental identification.

Theoretically, when the machine has a stable temperature (steady state), it is supposed that the heat input (generated internally) is equal to the heat output (evacuated by convection and radiation through the outer surface of the machine). The temperature on the

surface can also be considered homogenous due to two reasons:

1. The outer surface is made of aluminum casing with a very high thermal conductivity.
2. The dimension (diameter and length) of the machine is relatively small (Ø×l =45mm×100mm).

Therefore a one node model can be applied over the entire surface and can be modelized by equation Equation 3.15.

$$T_{surface}(t) - T_{ambient}(t) = \mathring{Q}_{th}.R_{ext}.(1 - e^{-t/\tau}) \tag{3.15}$$

with $\tau = R_{ext}.C_{total}$; C_{total} is the thermal capacity of the complete machine assembly.

As it attains steady state ($t \to \infty$), the temperature difference between the machine surface and the ambient air at steady state is the product of machine exterior convection thermal resistance R_{ext} and the heat input $\mathring{Q}_{th}$. It is important to note that for R_{ext} identification, the first degree equation is properly used here as the interface between the exterior surface and ambient air is only one node.

Losses, $\mathring{Q}_{th}$ (W)	$T_{surface\ steady\ state}$(°C)	$T_{ambient}$(°C)	R_{ext}(°C/W)
1.3	25.5	23.0	1.5
5.2	32.5	24.0	1.4
10.9	42.0	25.0	1.4

Table 3.5: Deduction of R_{ext} using experimental identification at steady state.

Practically, copper losses were generated by means of injecting direct current into the winding and the machine is left heating until it reaches the steady state. The temperature on the surface of the machine is registered via a thermocouple installed on its surface while the ambient temperature is the same thermocouple reading before the experiment started ($t = 0$). Knowing the winding resistance and the current injected, thus the copper losses generated $\mathring{Q}_{th}$, R_{ext} is then deduced (Table 3.5). To ensure the robustness of the method in obtaining R_{ext}, the experiments are done on three different current levels and R_{ext} was found to be around 1.6 and 1.5 for our test bench set-up. $R_{ext} = 1.5$°K/W is used in the LP model.

3.3.5.2 Validation of the complete LP model

In order to validate the model in both transient and steady state, both total thermal resistance and total thermal capacity need to be verified and validated. Therefore this validation step comprises two separate validations: the total thermal capacity validation and the complete model validation in copper losses configuration.

Verification of the total thermal capacity of the machine The total thermal capacity C_{total} of the motor and its test bed has been verified using an experimental identification and fitting method. This was done by fitting the curve of temperature rise on the surface $T_{surface}$ of the machine to a first degree equation (Equation 3.15) so as to identify C_{total} of the machine set. Like in subsubsection 3.3.5.1, this method considering one node is also valid as the identified capacity is C_{total} , which is the sum of capacity of all the motor components. The identified C_{total} has been compared to the calculated capacities and it shows good agreement with C_{total} equal to approximately 500 J/K.

Validation of the complete model in copper losses configuration Losses in a motor originate from different sources: copper losses, magnetic losses and mechanical losses among others. Apart from copper losses, accurate estimation of other losses are difficult, thus can introduces uncertainties in model validation process. By having a copper losses experimentation, losses estimation uncertainties can be reduced. As explained at the beginning of the chapter, the most important part to be observed is the winding, thus the validation is done on the slot temperature and it will be compared to the LP model simulation in similar condition.

To do so, an experiment set-up where losses generated from direct current step was injected into the three phase of the stator winding. The temperature rise is registered until the steady state is attained. To ensure the robustness of the model, the test was done on 3 different operating points defined by three different losses. The losses account up to nearly 10% of the machine maximum power deliverable.

The results of comparisons between the simulation and experimental results are shown in Figure 3.17. The precision of the K-junction thermocouple used is at ±1°C and the current measurement by the shunt is at ±0.25%. A remark on the losses level chosen for validation test can be made: It is certainly better to use a higher losses for validation test, however, it has been observed that at $\mathring{Q}_{th} = 20W$, the slot temperature goes beyond 100°C before reaching the steady state and it was decided that the prototype machine will not be subjected to a temperature exceeding 100°C[2]. With all the consideration on measures made and the comparison shown in Figure 3.17, it was concluded that the LP model is accurate and robust for copper losses configuration in both transient and steady state.

[2]Extra careful measure considering that it is the only prototype that the lab possesses

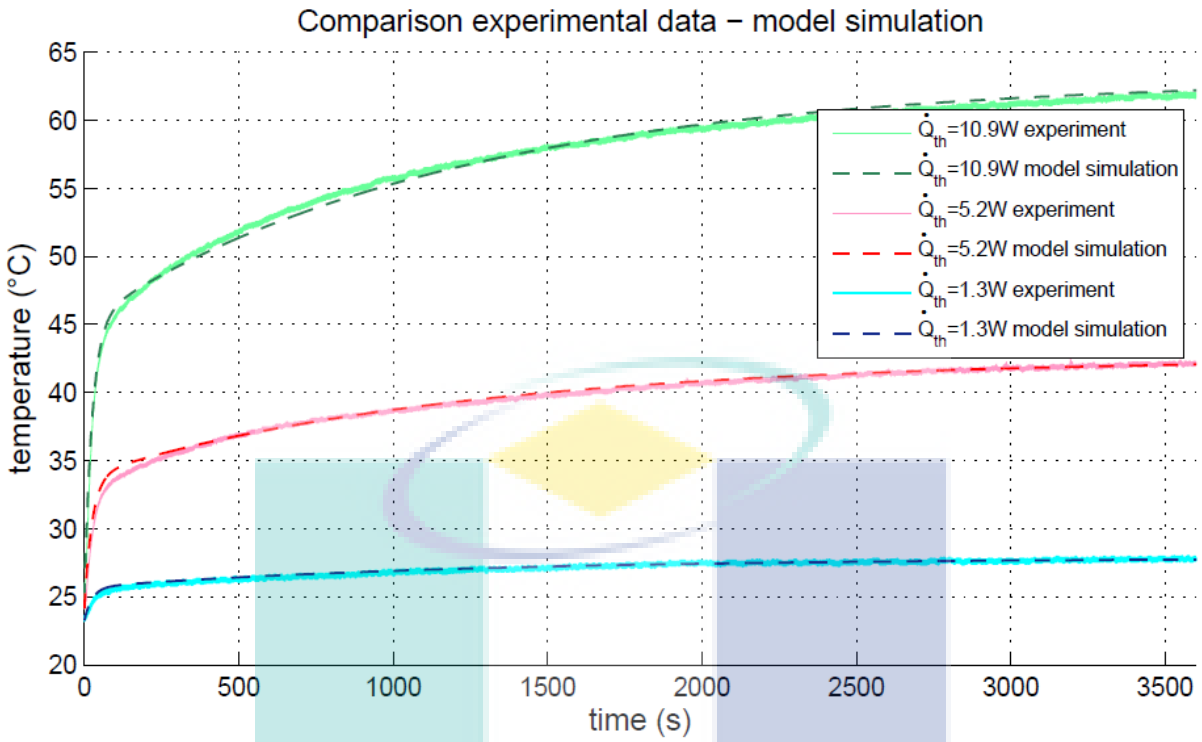

Figure 3.17: Model simulation and experimental winding temperature comparison on different losses injected .

3.4 Sensitivity study of the thermal model

Following the good agreement of the model and experimental results in previous section, a sensitivity study using the model can be done. The temperature rise (ΔT) in the slot depends on various thermal parameters ($R_{th\,1}, C_{th\,1}, \ldots, R_{th\,n}, C_{th\,n}$) and the heat source input $\mathring{Q}_{th}$, thus

$$\Delta T = f(R_{th\,1}, C_{th\,1}, \ldots, R_{th\,n}, C_{th\,n}, Q_{th}). \tag{3.16}$$

Conceptually, the simplest method to carry out a sensitivity analysis is to repeatedly vary one parameter at a time while holding the others fixed, which is called local sensitivity [36]. It is done by partially differentiating the function ΔT ($\frac{\partial \Delta T}{\partial R_{th\,i}}$). By doing so, a sensitivity ranking can be obtained quickly by increasing each parameter by a given percentage while leaving all others constant, and quantifying the change in model output. In this study, each thermal resistance found previously will be varied from 50% to 200% of its initially-calculated value. Similar study on bigger TEFC (totaly enclosed forced cooled) machine has been done regarding the effect on steady state temperature response [37].

The slot temperature T_{slot} variations shown in Table 3.6 are comparisons done with the steady state temperature of the model simulated using initially-calculated thermal resis-

tances. The graphique showing the temperature variation is shown in Figure 3.18 and the deviation in percentage compared to the nominal temperature is shown in Figure 3.19.

Thermal parameter	Parameter variation (max/min ($W/m^2.K$))	T_{slot} deviation (+/-(°C))	Deviation % over experimental temperature
R_{slot}	487.88/121.97	$+7.02/-7.02$	22.59 %
R_{teeth}	0.96/0.24	$+2.16/-2.16$	6.96 %
R_{rotor}	5.92/1.48	$+0.16/-0.16$	0.52 %
$R_{stator\ yoke}$	$16 \times 10^{-3}/4 \times 10^{-3}$	$+0.97/-0.97$	3.14 %
R_{shaft}	55.68/13.92	$+0.33/-0.33$	1.05 %
R_{airgap}	10.92/2.73	$+2.21/-2.21$	7.12 %
R_{casing}	$19.44 \times 10^{-4}/4.86 \times 10^{-4}$	$+0.21/-0.21$	0.66 %
$R_{contact}$	$29.96 \times 10^{-6}/7.49 \times 10^{-6}$	$+0.20/-0.20$	0.65 %
$R_{endwinding}$	39.08/9.77	$+4.04/-3.43$	19.36 %
R_{cap}	0.04/0.01	$+0.20/-0.20$	0.65 %
$R_{air\ cavity}$	330.76/82.69	$+0.26/-0.26$	0.83 %
R_{ext}	2.80/0.70	$+7.30/-7.30$	23.51 %

Table 3.6: Variation of each parameters and the effect on the slot temperature. For elements with radial, axial or ortho-radial heat transfer direction, only the radial resistance is presented here. The variation was made on all the thermal resistance in all direction.

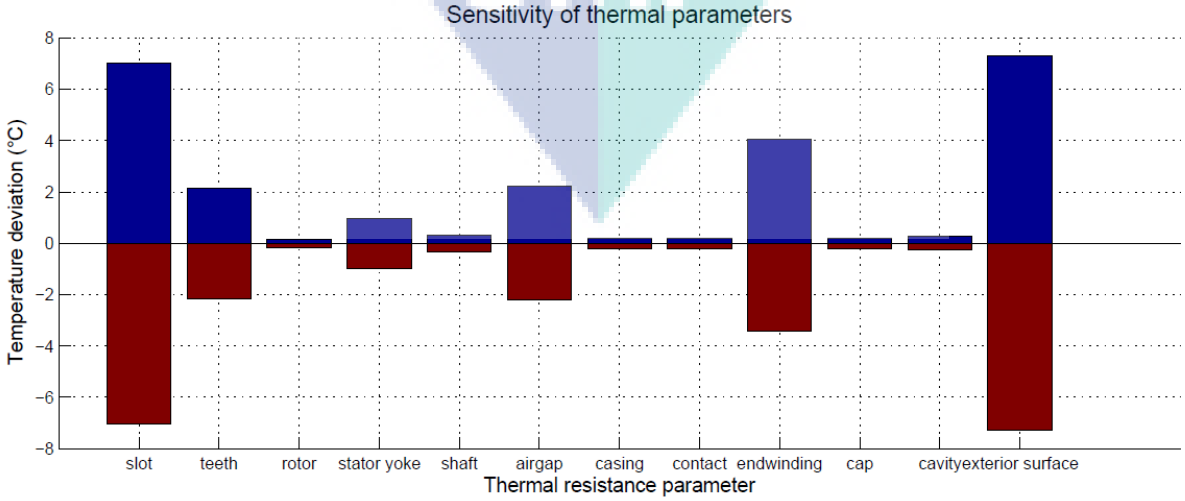

Figure 3.18: The slot temperature deviation following the thermal parameters variation.

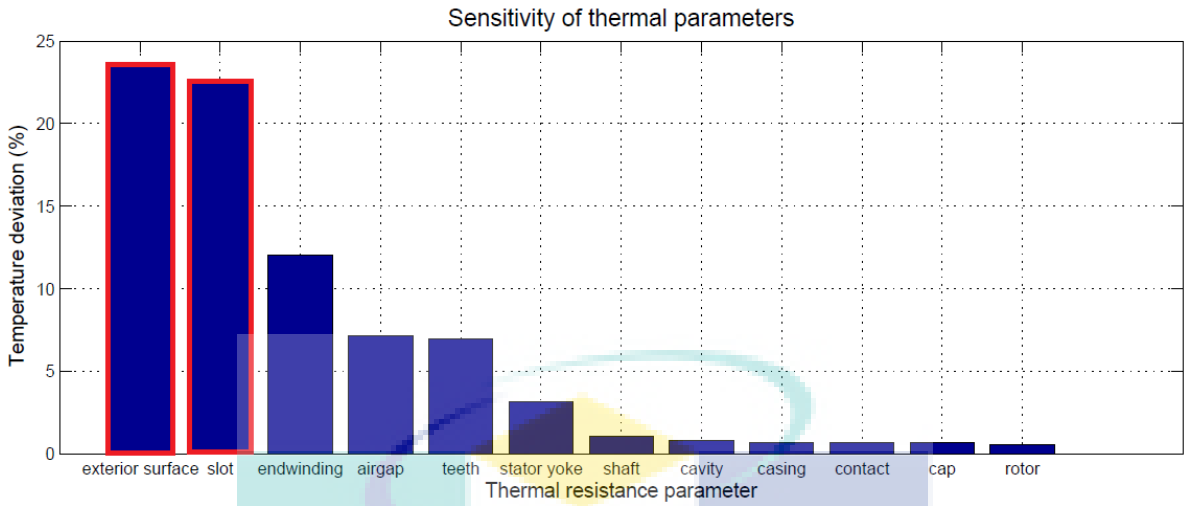

Figure 3.19: The effect of thermal parameter variation on the slot temperature in decreasing order.

As can be clearly seen in both graphs, there are two most influential thermal resistances in the model which can alter the way the temperature rises in the slot: the exterior surface thermal resistance R_{ext} and the slot equivalent thermal resistance R_{slot}. Apart from the steady state variation, the way R_{ext} and R_{slot} variations modify the slot temperature curve are interestingly different. More specific studies on how R_{ext} and R_{slot} effect the slot temperature and influencing parameters that can practically modify R_{ext} and R_{slot} , are detailed in the next subsections.

3.4.1 Influence of exterior surface thermal resistance, R_{ext}

From the simulation shown in Figure 3.20, we can observe that R_{ext} plays major role in definition of slot temperature in steady state. Primarily, by adding R_{ext}, the time constant rises, thus delays the steady state. In the case of theoretical adiabatic exterior surface (red dotted line), the temperature continue to rise and never attain the steady state. In the other way, by reducing R_{ext}, the time constant decreases thus, reducing the time to attain the steady state and the steady state temperature becomes lower.

Secondly, it is also interesting to observe that the R_{ext} variation does not affect the slot temperature in the early portion of transient state ($t < 100$s). The variations in time constant can only be observed after this time point. For a R_{ext} that correspond to a perfect conductor (blue dotted line), the last portion disappears completely and the steady state was attained right at $t = 100$s.

An experiment configuration providing another value of R_{ext} was prepared to validate the observation made in the sensitivity study of the model (Figure 3.21a). The motor was

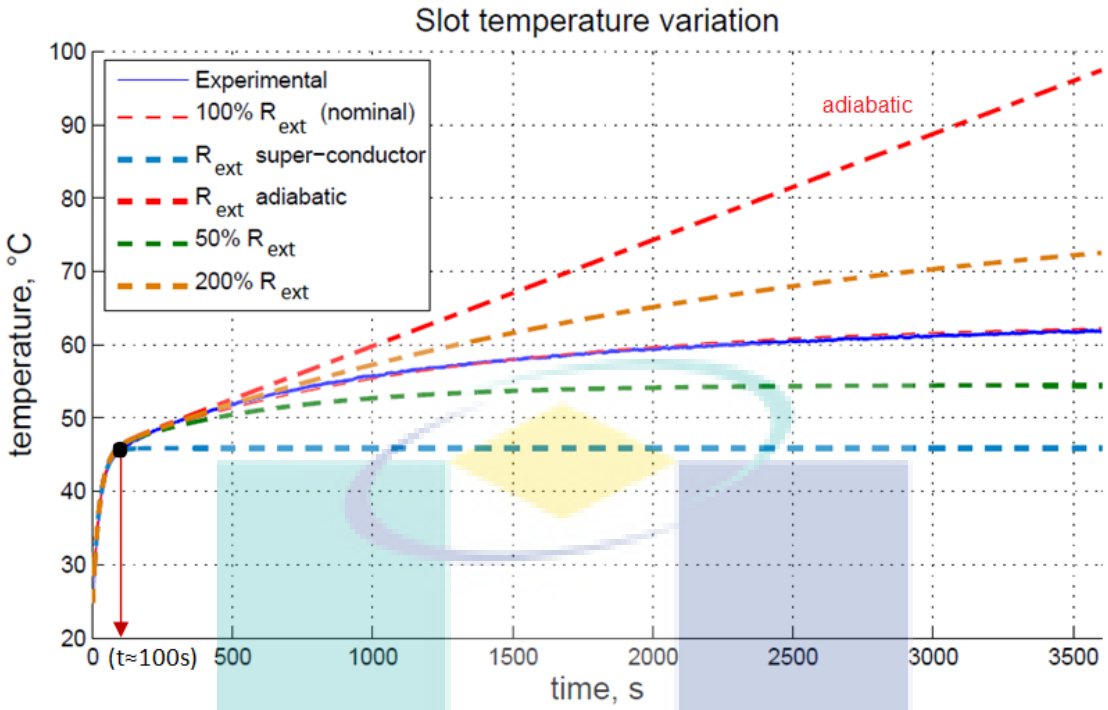

Figure 3.20: Simulation of the slot temperature variation in function of R_{ext} variation.

in fact hanged in the air using a rope. The results (Figure 3.21b) validate the prediction by the model simulation in Figure 3.20. The rise of R_{ext} has delayed and increases the steady state temperature but does not affect the early transient state at $t < 100$s.

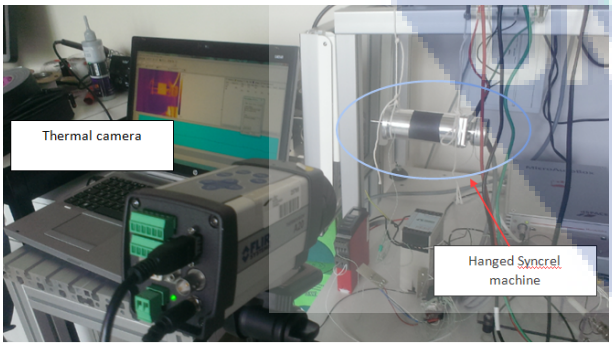

(a) The experiments set up with a thermal camera to double check the measurement given by the thermocouple.

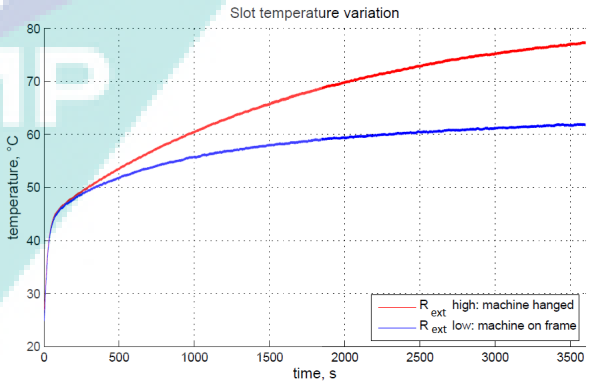

(b) Experimental results for different R_{ext}.

Figure 3.21: Experimentation with the Syncrel machine hanged so as to have a different R_{ext} (higher) and its results to validate the simulation Figure 3.20.

This result let us suggest that the last portion (starting from $t = 100$s) corresponds to

a first degree response of the exterior surface node. To confirm the proposition, a one node model (with the thermal resistance being R_{ext} and the capacity being C_{total}) was simulated and compared to the last portion ($t > 100$s) of the experimental slot temperature and the experimental casing surface temperature (Figure 3.22).The result of the one node model simulation (crossed orange line) shows good agreement with the casing surface temperature (black line). When it is translated (dotted yellow line) to the same temperature level of the slot (blue and red line) at $t = 100$s, we found that the slot temperature rise is equal to a first order response of the casing surface of the machine.

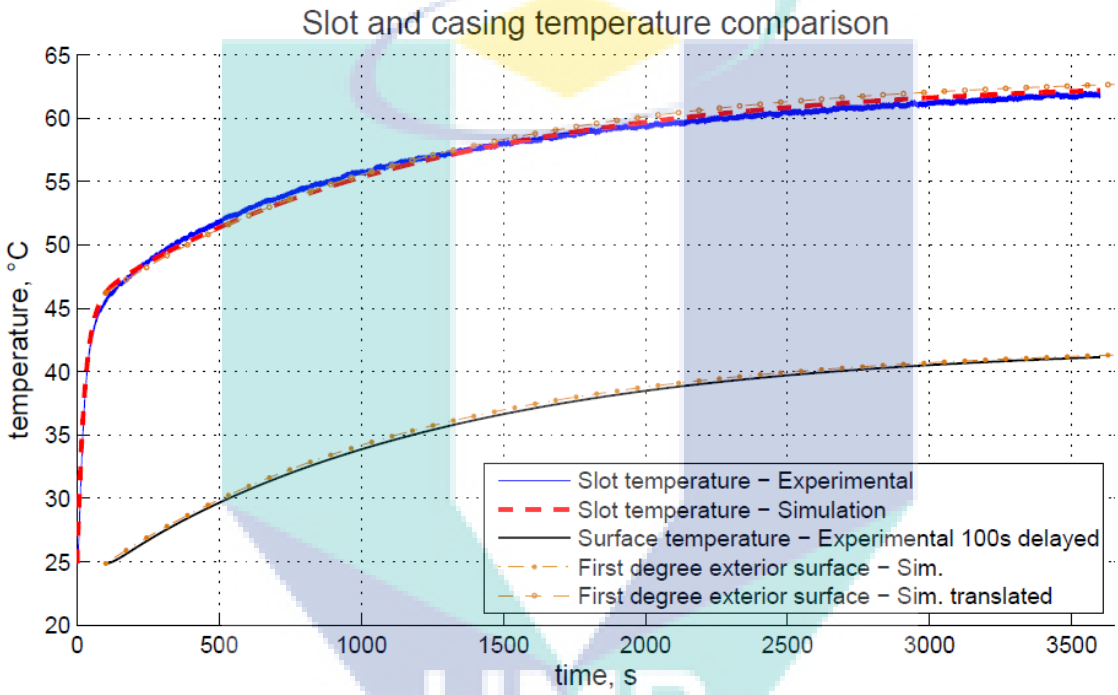

Figure 3.22: Exterior surface single node model simulation compared to experimental casing surface temperature and tranaslated to the last portion (starting at $t = 100s$) of the slot temperature curve.

In conclusion, R_{ext} variation affects only the last portion of the slot temperature response in our motor. Using a local sensitivity study on R_{ext}, the last portion of the temperature rise that corresponds to a first degree response of the exterior surface can be found. Following this conclusion, further remark and practical proposition can be made. In the perspective of relevant thermal model construction, an accurate calculation or identification of R_{ext} is unnecessary for thermal prediction of a similar type of motor if it is used in a short and intermittent utilization cycle. In a more practical perspective for a similar motor working in short and intermittent cycle, solutions for heat evacuation at the casing level is unnecessary as the effect will not appear immediately in the early transient state. For example, the

addition of fins and exterior ventilation are not effective in this case. In this case, the important factors affecting the slot temperature rise that need to be highlighted is in the slot, which will be treated in the next sub-section.

3.4.2 Influence of slot equivalent thermal resistance, R_{slot}

The slot equivalent thermal resistance R_{slot} is another parameter that has been found to influence the temperature rise in the slot. Unlike R_{ext}, R_{slot} affects the slot temperature prediction in the machine from the beginning of the transient state ($t < 100$s) (Figure 3.23).

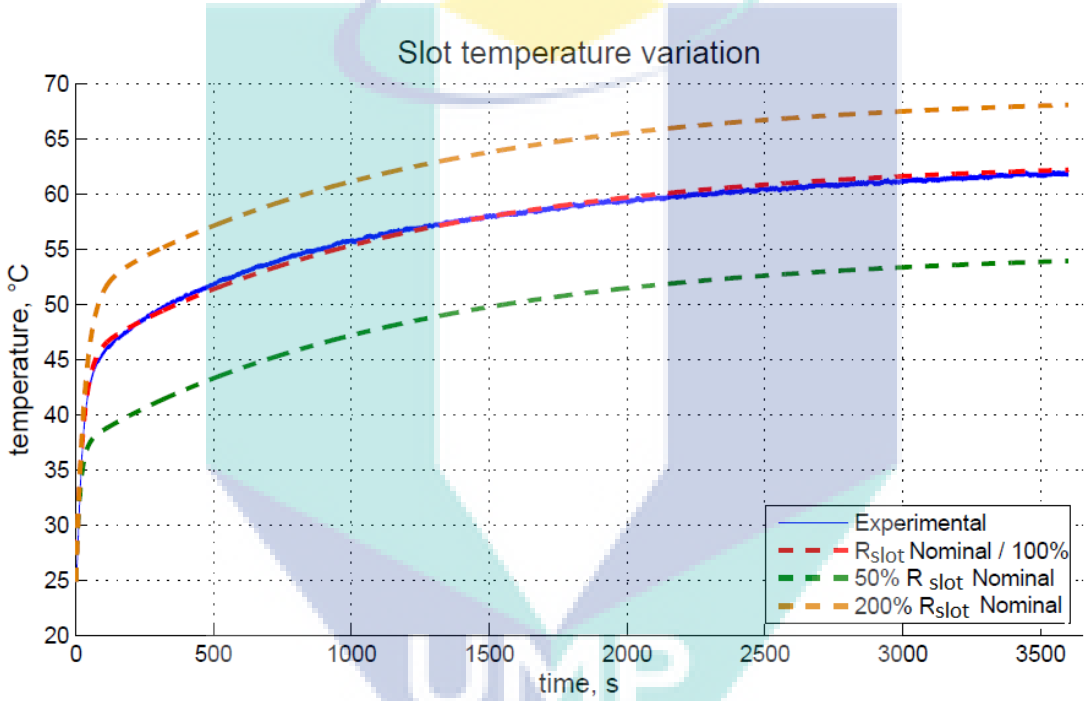

Figure 3.23: The slot temperature variation in function of R_{slot} variation.

In order to look at the possible influence of R_{slot} on the final slot temperature, a closer look into its definition is necessary. It was calculated in subsection 3.3.1 using equation Equation 3.10. From the equation, we can see that R_{slot} can be influenced by 2 major factor:

1. Slot infiltration. Infiltration is the fact that the slot is filled with potting material such as resin or left with air.

2. Slot filling factor. Filling factor is the ratio of the copper winding over the total volume of the slot.

Besides being used to seal motor critical components from solvent and moisture ingress, potting can also protect from mechanical damage and degradation caused by thermal cycling, vibration, and impact [38]. Having a higher thermal conductance compared to air, infiltrating the slot with potting material is known to be an easy means to increase the slot thermal conductivity as proven in Figure 3.24.

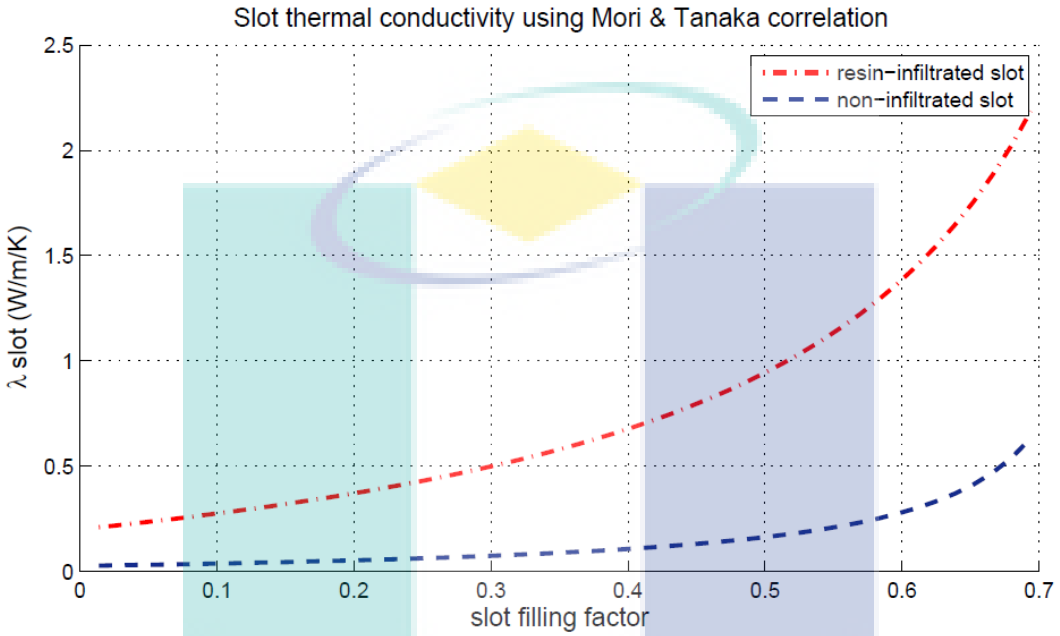

Figure 3.24: The equivalent thermal conductivity (inverse of R_{slot}) variation in function of filling factor and infiltration.

However, the right potting material that can withstand the machine operating temperature has to be selected among available options . It can be seen from Figure 3.25 that the maximum temperature resistance for the best potting material is about 200°C which is not far from our application operating temperature. Other consideration such as the cost and manufacturing process means that the potting need to give a sufficient amount of temperature reduction in order to justify its utilization.

Unlike the effect of infiltration alone, the simultaneous influence of both infiltration and filling factor is however less predictable. In Figure 3.26, it can be clearly seen that in both resin infiltrated (dotted lines) and non-infiltrated (continuous lines) slot, increase on the filling factor lead to a better heat evacuation. It is more interesting to see that by infiltrating the slot, the temperature drop massively without changing the filling factor. In purely thermal point of view, having a mediocre filling factor (0.3) with resin-infiltrated slot appears to be a better option compared to the effort of increasing the filling factor up to the double (0.6) with non-infiltrated slot. This is not suprising as the thermal conductivity of the

TABLE 4. COMPARISON OF ADHESIVE TYPES FOR POTTING

ATTRIBUTE		ACRYLIC, LIGHT CURE	EPOXY, ONE-PART HEAT CURE	EPOXY, TWO-PART	SILICONE, LIGHT CURE	URETHANE, TWO-PART
PERFORMANCE						
Adhesive to Substrates	Metals	Good	Excellent	Excellent	Good	Good
	Plastics	Excellent	Good	Good	Fair	Very Good
	Paper	Excellent	Excellent	Excellent	Good	Good
Gap Fill	Ideal	0.020 - 0.125"	0.050 - 0.25"	0.050 - 0.25"	0.020 - 0.125"	0.050 - 0.25"
	Maximum	0.250"	>0.50"	>0.50"	0.250"	>0.50"
Tg		30 - 80°C	50 - 90°C	50 - 90°C	< -40°C	-10 - 50°C
Temp. Resistance	Typical Range	-65 to 300°F	-65 to 300°F	-65 to 300°F	-65 to 350°F	-65 to 250°F
	Maximum	350°F	400°F	400°F	400°F	300°F

Figure 3.25: Examples of different potting material with their temperature resistance [38].

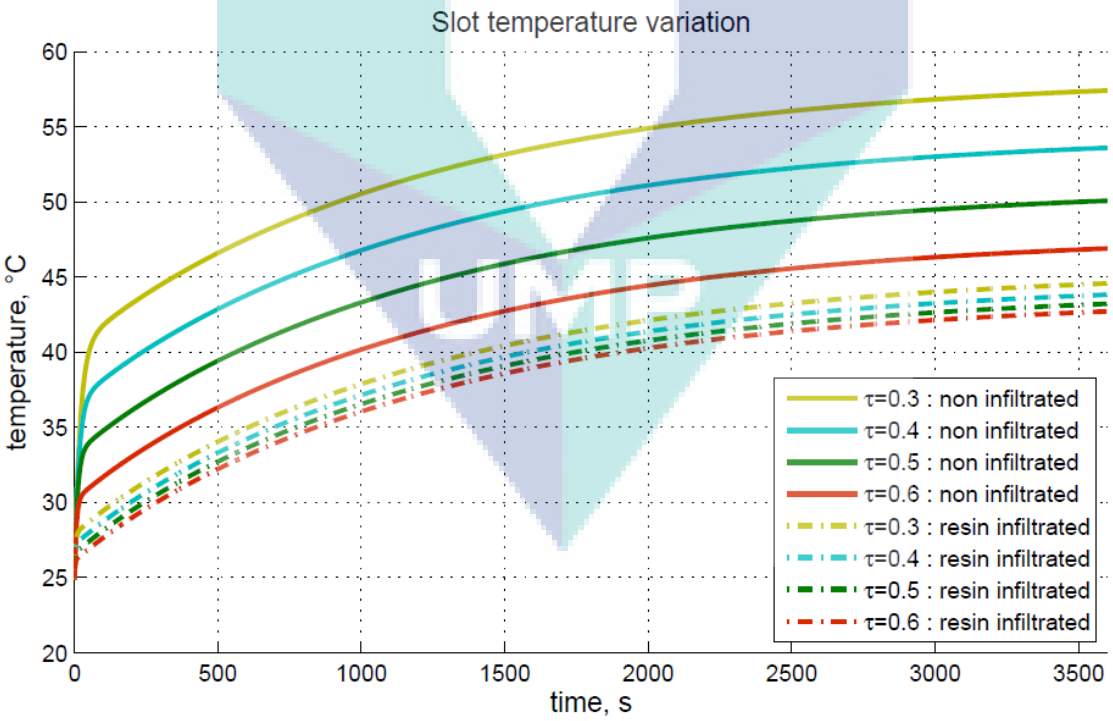

Figure 3.26: The slot temperature variation in function of filling factor and slot infiltration.

infiltrated resin (epoxy) is around 0.2W/m.K while the conductivity of air is 10 times less at about 0.02W/m.K (both at 20°C). However, it is known that filling factor has effects on other electromechanical characteristics of a motor and its choice can be constrained by these characteristics. Nonetheless, in thermal aspect, increasing the filling factor is not as efficient as filling the slot with resin in order to reduce slot temperature. More importantly, with the filling factor and infiltration function integrated in the model, we have now a tool permitting the estimation of temperature reduction in function of these two slot-related parameters.

In parallel, the same reasoning can be made for end-winding. By potting the endwinding, it will reduce the air around it leading to a higher overall thermal conductivity. A better option would be to make direct contact between the end-winding and the lateral caps in order to increase the conduction axially. All these propositions can be treated in future perspective.

3.4.3 Conclusion on sensitivity study

A local sensitivity study has shown that the parameters that play major roles in rising the temperature in the slot are the exterior surface (casing-ambient air contact) thermal resistance R_{ext} and the slot thermal resistance R_{slot} itself. It has been shown that the slot temperature rise can be separated and attributed to these two parameters as function of time range. For early transient state, it is R_{slot} that influence the temperature rise. Next, a local sensitivity study on the effect R_{ext} on the slot temperature rise can help to find the time point starting from which only R_{ext} influence the slot temperature rise.

Following these findings, for similar type of motor used in short utilization cycle such as S2 duty cycle [42], we conclude that efforts need to be done on reducing the slot thermal resistance R_{slot} to reduce the temperature. The thermal model combined with slot filling factor and slot infiltration functions is a complete tool permitting a temperature reduction estimation in function of the filling factor and slot infiltration. It can be used by industrials as early as in the design phase to predict the slot temperature in function of the filling factor chosen (filling factor can be constrained by other electromechanical performances characteristics). The tools can also help to estimate the profitability of injecting resin into the slot in function of possible temperature reduction that can be gained in return.

3.5 Simulation on different duty cycle

3.5.1 Model accuracy on short time range

In previous subchapters, the model has been proven to be accurate and robust in a time magnitude of order of a hundreds. However, a motor can also be use intermittently in a much smaller time range (e.g: milliseconds).

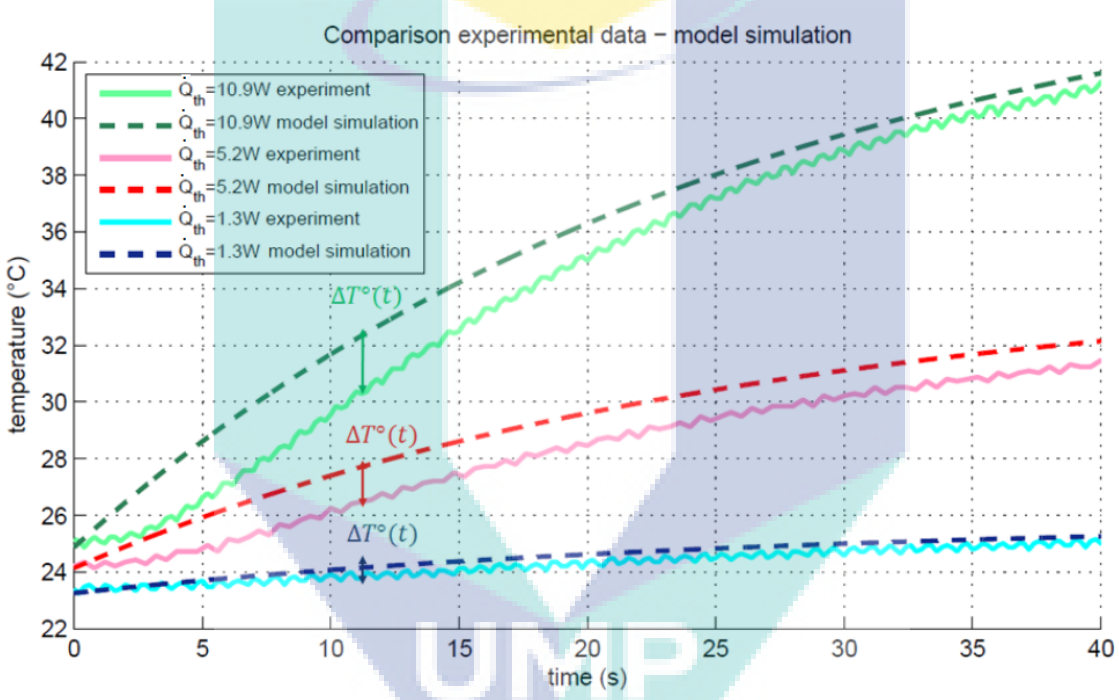

Figure 3.27: A zoom on Figure 3.17 to observe the model accuracy on short time range.

In Figure 3.27, the experimental results shown were measured using the thermocouple installed in the slot. It can be observed that there is an apparent horizontal asymptote at the $t = 0$s, whereas for the simulation, the temperature rises instantaneously with a certain slope which depends on the losses injected. The temperature difference between simulation and experimental results $\Delta T(t)$ increases at the begining and decreases rapidly as it approaches the steady state. It can also be seen that $\Delta T(t)$ is proportional with the losses.

The discrepancy between the simulation and experimental results can be explained by two phenomenon:

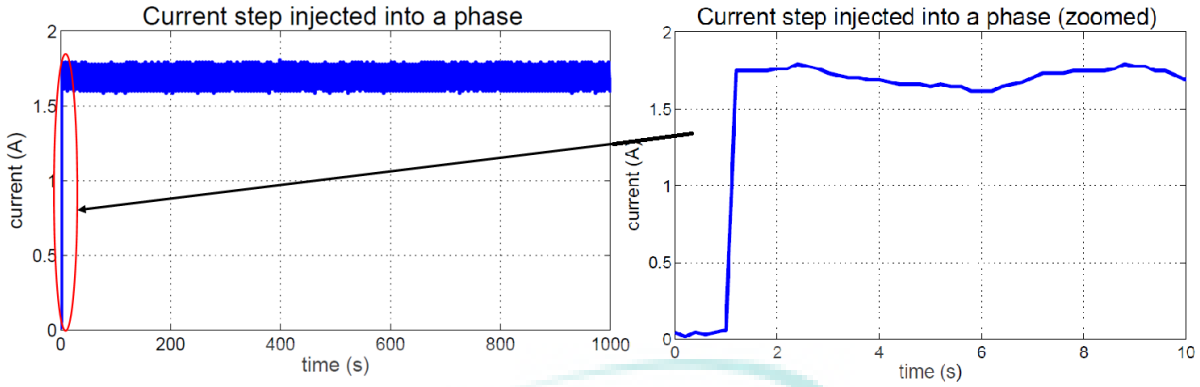

Figure 3.28: The current step injected into a phase of the Syncrel winding.

1. The delay in losses injected itself: The model was simulated for a step losses that is injected at $t = 0$s. Any delay in losses injection and error in the step form can affect the temperature rise. Observation on the injected current Figure 3.28 using a shunt shows that the current was actually injected with a 1 second delay after the temperature recording. Furthermore, the current rises from zero to the demanded step value takes another 0.2 seconds. To resolve the error caused by this practical constraints, the simulation can be easily corrected by delaying the losses step injection in the simulation by 1.2 seconds.

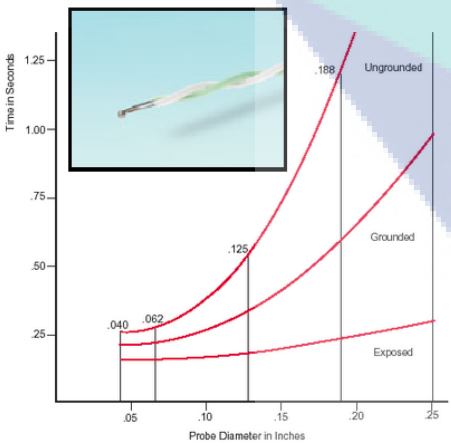

IEC Tolerance Class EN 60584-2; JIS C 1602

IEC Code		Class 1	Class 2	Class 3††
J	Temp Range Tolerance Value Temp. Range Tolerance Value	-40 to 375°C ±1.5°C 375 to 750°C ±0.4% Reading	-40 to 333°C ±2.5°C 333 to 750°C ±0.75% Reading	Not Established
K N	Temp Range Tolerance Value Temp. Range Tolerance Value	-40 to 375°C ±1.5°C 375 to 1000°C ±0.4%	-40 to 333°C ±2.5°C 333 to 1200°C ±0.75% Reading	-167 to 40°C ±2.5°C -200 to -167°C ±1.5% Reading
T	Temp Range Tolerance Value Temp. Range Tolerance Value	-40 to 125°C ±0.5°C 125 to 350°C ±0.4% Reading	-40 to 133°C ±1°C 133 to 350°C ±0.75% Reading	-67 to 40°C ±1°C -200 to -67°C ±1.5% Reading
E	Temp Range Tolerance Value Temp. Range Tolerance Value	-40 to 375°C ±1.5°C 375 to 800°C ±0.4% Reading	-40 to 333°C ±2.5°C 333 to 900°C ±0.75% Reading	-167 to 40°C ±2.5°C -200 to -167°C ±1.5% Reading
R S	Temp Range Tolerance Value Temp. Range Tolerance Value	0 to 1100°C ±1°C 1100 to 1600°C ±[1 + 0.3% x (Rdg-1100)]°C	0 to 600°C ±1.5°C 600 to 1600°C ±0.25% Reading	Not Established
B	Temp Range Tolerance Value Temp. Range Tolerance Value	Not Established	600 to 1700°C ±0.25% Reading	600 to 800°C ±4°C 800 to 1700°C ±0.5% Reading

Figure 3.29: The thermocouple used for the test bench with its indicative time constant (0.3s) and tolerance.

2. The thermocouple time constant $\tau_{thermocouple}$: The thermocouple used is a class 1 K type junction with a 0.2mm diameter conductor, ungrounded and coated with PFA. It has a time constant of 0.3s given by the manufacturer Figure 3.29. The time constant varies in function of different parameters (the junction type, the conductors material,

its length, grounding etc.). Once installed onto the solid on which the temperature want to be measured, extra time constant can appear due to the attachment method [39]. In our case, the thermocouple was sticked in between the winding in a slot using a thermal paste. Therefore, it is in contact not only with the winding, but also the thermal paste and the air in the slot. Furthermore, the measured temperature is not directly the copper wire temperature, but the insulation covering the wire. Various methods exists in order to compensate the delay caused by the time constant directly on the test bench, during the test [39]. It has also been theorically modeled [41] and has been shown to be not as simple as a first order response if a very accurate prediction is required.

Following the observation and the possible causes mentioned above, a model with better accuracy in the short time range was developed. The main objective of the model is to identify the thermocouple equivalent time constant of our experimental set up and verify if $\Delta T(t)$ can really be attributed to the thermocouple time constant.

Initially, the simulation temperature was measured at the center of the homogenized slot (on the connection point between the radial and ortho-radial thermal resistance). In order to build the accurate model, a method we call "thermocouple delay compensation" was used. It consists of addition of a RC circuit replicating the thermocouple time constant before the temperature measurement (Figure 3.30).

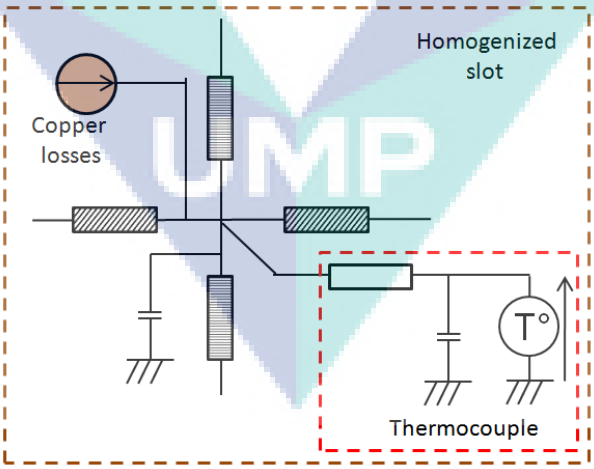

Figure 3.30: The temperature measurement in the simulation with $\tau_{thermocouple}$ compensation.

The values of these $R_{thermocouple}$ and $C_{thermocouple}$ were found by fitting the simulation curve to the experimental result. Finally, the values of $R_{thermocouple}$ and $C_{thermocouple}$ found (Figure 3.31) gave a time constant of $\tau_{thermocouple} = 1.5$ seconds. The thermocouple time

constant given by the manufacturer was 0.3 seconds. This means that the extra 1.2 seconds is due to the attachment method and its positioning in the slot, which is reasonable regarding the slot filling factor and the fact that the slot is filled with air (non-potted).

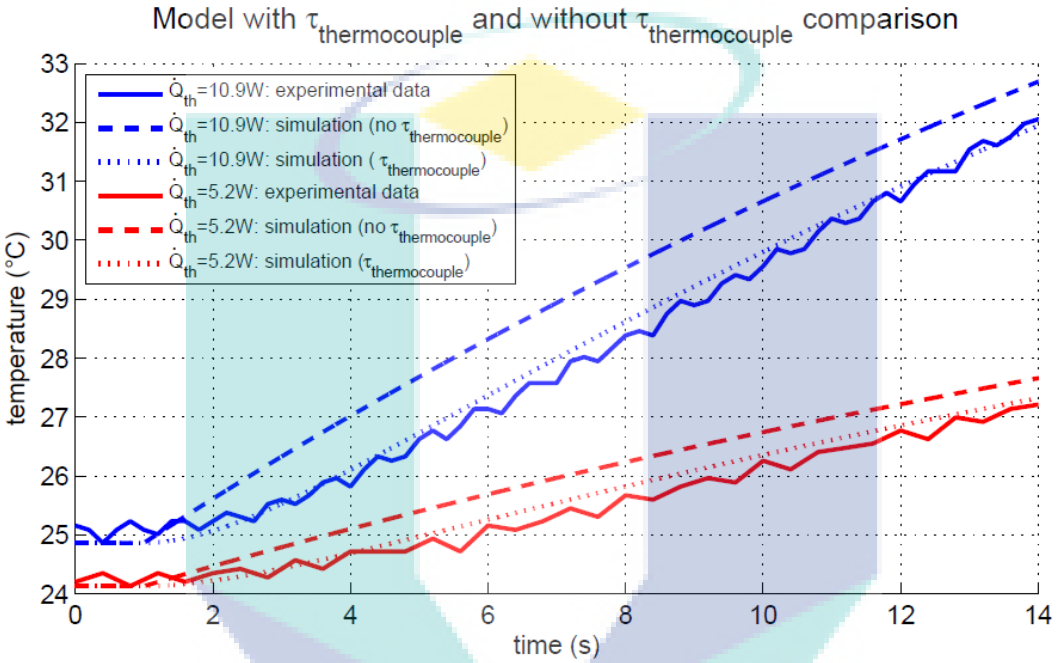

Figure 3.31: The model response compared to experimental results after model correction using $\tau_{thermocouple}$ compensation. Case for $Q_{th} = 10W$.

From the simulation in Figure 3.31, it shows that if we are able to measure directly to the center on the copper wire without having the thermocouple time constant delaying the temperature rise, the temperature in the winding would rise immediately as the dashed lines. It can then be concluded that there are risk of underestimating the copper winding temperature if we depend solely on the thermocouple measure. The risk is furthermore important in case of a higher losses as we know that the error is proportional to the losses. To demonstrate the variation of $\Delta T(t)$ in function of losses, simulations were done for different level of losses and $\Delta T(t)$ was calculated (Table 3.7 and Figure 3.32).

Losses (W)	10				50				100			
t(s)	2	5	100	3600	2	5	100	3600	2	5	100	3600
T_1(°C)	25.8	28.3	50.8	69.2	29.5	42.2	154.6	252	34.0	59.3	284.3	480
T_2 (°C)	25.1	27.2	50.7	69.2	26.1	36.3	154.3	252	27.4	47.8	283.7	480
ΔT (°C)	0.7	1.1	0.1	0	3.4	5.9	0.3	0	6.6	11.5	0.6	0

Table 3.7: Error between the thermocouple reading with and without $\tau_{thermocouple}$ compensation in function of time for a step losses simulation.

T_1: T without thermocouple compensation
T_2: T with thermocouple compensation
Remark: Certain temperature in a higher time range are far too high for a real Syncrel motor application. The simulation and comparison were done to demonstrate the risk of underestimating the winding temperature at a low time range (e.g.: $t < 30$ seconds)

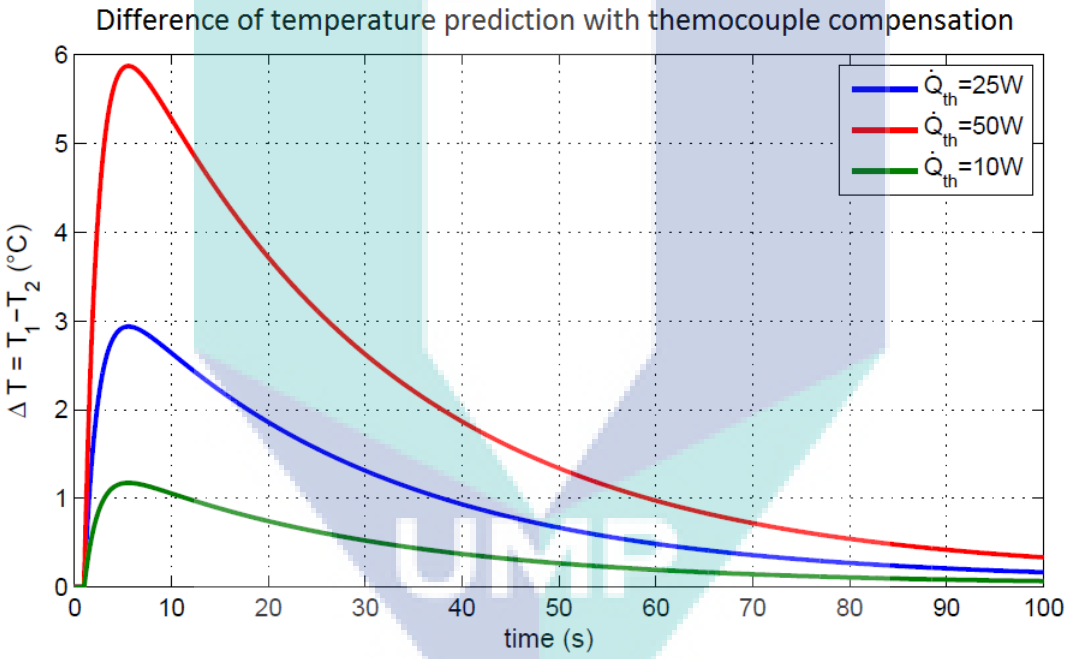

Figure 3.32: The variation of temperature prediction difference between a simulation with $\tau_{thermocouple}$ (T_2) and without $\tau_{thermocouple}$ compensation (T_1).

It shows that for a step losses, the error increases rapidly in the begining and peak at $t = 5$ seconds, and later decreases exponentially towards zero as the time approaches the steady state. The error is also more important as the losses increases.

As the motor will usually be used in different cycles, it is also interesting to see how a winding temperature could be under-estimated or over-estimated in a cycle if the thermocouple time constant was not taken into account. To do so, a square wave cycle with a period and duty cycle related to the critical time range found in Figure 3.32 ($T_{square\,cycle} = 10$

seconds and $\tau_{square\,cycle} = 0.5$ seconds) was simulated for different losses and the results are shown in Figure 3.33.

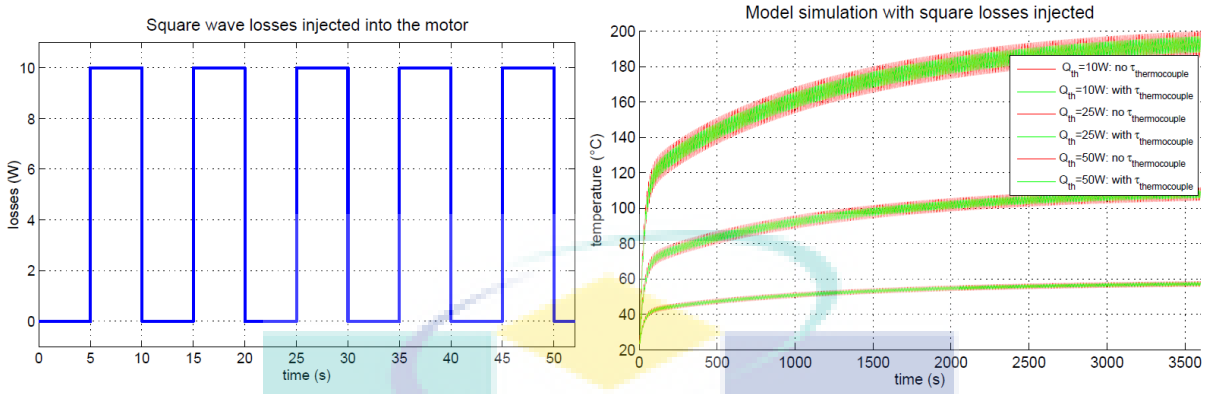

Figure 3.33: Square losses injected with a particularly chosen frequency for a square wave duty cycle $\tau_{square\,cycle} = 0.5$.

It can be observed that the simulation without $\tau_{thermocouple}$ compensation rises and falls rapidly during a period of the square waves, giving a bigger temperature variation (red curves). Thus it can attain a much higher maximum as well as a much lower minimum temperature at a given time compared to the simulation with $\tau_{thermocouple}$ compensation. However, their average temperatures are the same when the simulation are observed in a much larger time range. The same observation can be made for simulations with different duty cycle as shown in Figure 3.34. Again, the average temperature for the simulation using $\tau_{thermocouple}$ compensation and simulation without $\tau_{thermocouple}$ compensation give the same average temperature. The temperature difference at a given time is maximum when the duty cycle is at 5 seconds (which is the time at which the maximum difference was found) and lower at other duty cyle values.

As conclusion, in general, a thermocouple delay estimation of every new thermocouple installation is then important and should be done to estimate the real winding temperature. To do so, the 'thermocouple delay compensation' method can be used with a condition: this method is only applicable onto a model which is already proven to be accurate in the steady state and a longer transient time range such as ours (Figure 3.17). Its purpose is only to correct the discrepancy at the begining of the temperature rise caused by thermocouple time constant, as been used in our case.

In practical, the necessities of doing the thermocouple delay estimation is in function of two general cases:

1. Case where the average temperature can be accepted. The components can resist a higher temperature due to underestimation for a short time range: it is not impor-

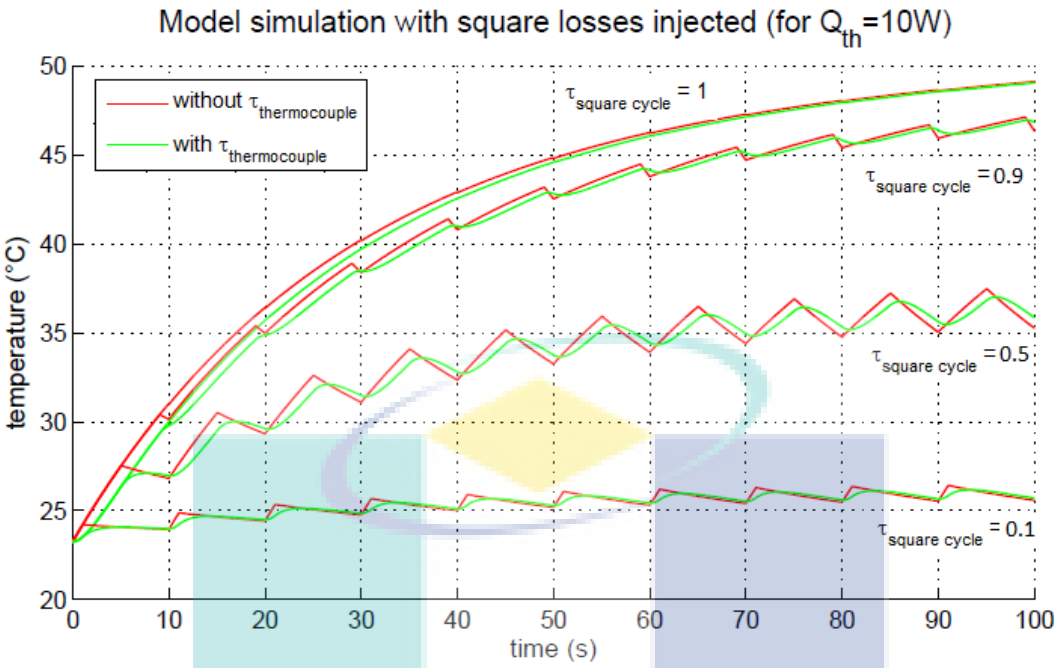

Figure 3.34: Thermocouple compensation effect comparison with different square losses duty cycle $\tau_{square\,cycle}$.

tant to compensate the delay caused by the thermocouple as the average temperature finally corresponds to the simulation without thermocouple delay compensation. Furthermore the thermocouple time constant is very short. As soon as the losses stops, the temperature will drop converges to the temperature predicted by the model without thermocouple delay compensation.

2. Case where the exact temperature for a given time is absolutely necessary: The thermocouple installation time constant need to be found using the 'thermocouple delay compensation' method in order to avoid the error of underestimating the real temperature.

In following subsections, all simulations will be presented with curves of both thermocouple delay compensated and non compensated temperature.

3.5.2 Standard duty cycle

Having an accurate and robust thermal model, we can subsequently make an observation of the motor thermal behavior under different utilization conditions. This can help us in proposing the best utilization of this type of motor in the future.

Following the International Electrotechnical Comission (IEC) [42], there are 8 duty cycle designations to describe an electrical motors operating conditions as described in Table 3.8.

S1	Continuous duty	The motor works at a constant load for enough time to reach temperature equilibrium.
S2	Short-time duty	The motor works at a constant load, but not long enough to reach temperature equilibrium. The rest periods are long enough for the motor to reach ambient temperature.
S3	Intermittent periodic duty	Sequential, identical run and rest cycles with constant load. Temperature equilibrium is never reached. Starting current has little effect on temperature rise.
S4	Intermittent periodic duty with starting	Sequential, identical start, run and rest cycles with constant load. Temperature equilibrium is not reached, but starting current affects temperature rise.
S5	Intermittent periodic duty with electric braking	Sequential, identical cycles of starting, running at constant load and running with no load. No rest periods.
S6	Continuous operation with intermittent load	Sequential, identical cycles of running with constant load and running with no load. No rest periods.
S7	Continuous operation with electric braking	Sequential identical cycles of starting, running at constant load and electric braking. No rest periods.
S8	Continuous operation with periodic changes in load and speed	Sequential, identical duty cycles run at constant load and given speed, then run at other constant loads and speeds. No rest periods.

Table 3.8: Description of eight IEC standard duty cycles.

After taking the standard definition into account, all the cycles above (Table 3.8) were simulated using losses profiles with parameters shown in Table 3.9. In order to make a comparison, they are all simulated at the same load level, producing losses $\mathring{Q}_{th\,run}$ at 10W for the whole motor when its running with the load. $\mathring{Q}_{th\,start}$ represents the losses produces during the starting and it lasts for 2 seconds. $\mathring{Q}_{th\,run\,2}$ represents losses generated at another load level. It represents the no-load run for S5 and S6, rheostatic breaking for S7 and a different load level for S8.

S7 depends on the type of braking. There are in general 3 types of electric breaking: regenerative braking, dynamic or rheostatic braking and reverse current braking. Thermally speaking regenerative breaking and dynamic or rheostatic breaking make S7 a trapezoidal

	$\dot{Q}_{th\,start}$ (W)	$\dot{Q}_{th\,run}$ (W)	$\dot{Q}_{th\,run\,2}$ (W)	$\dot{Q}_{th\,rest}$ (W)	cycle
S1	$\dot{Q}_{th\,run}$	10	NA	NA	Step
S2	$\dot{Q}_{th\,run}$	10	NA	0	Square wave
S3	$\dot{Q}_{th\,run}$	10	NA	0	Square wave
S4	$2.\dot{Q}_{th\,run}$	10	NA	0	Square wave
S5	$2.\dot{Q}_{th\,run}$	10	$\dot{Q}_{th\,no\,load} = 0.2Q_{th\,run}$	NA	Square wave
S6	$\dot{Q}_{th\,run}$	10	$Q_{th\,no\,load} = 0.2Q_{th\,run}$	NA	Square wave
S7	$2.\dot{Q}_{th\,run}$	10	slope until zero	NA	Trapezoidal
S8	$\dot{Q}_{th\,run}$	10	$Q_{th\,run\,2} = 0.8Q_{th\,run}$	NA	Square wave

Table 3.9: Parameters for IEC standard cycle simulation at identical load (identical $Q_{th\,run}$).

losses cycle with a downward slope during braking as the current flows in the opposite direction and decreases in time until the motor stops. It is the profile that is used here.

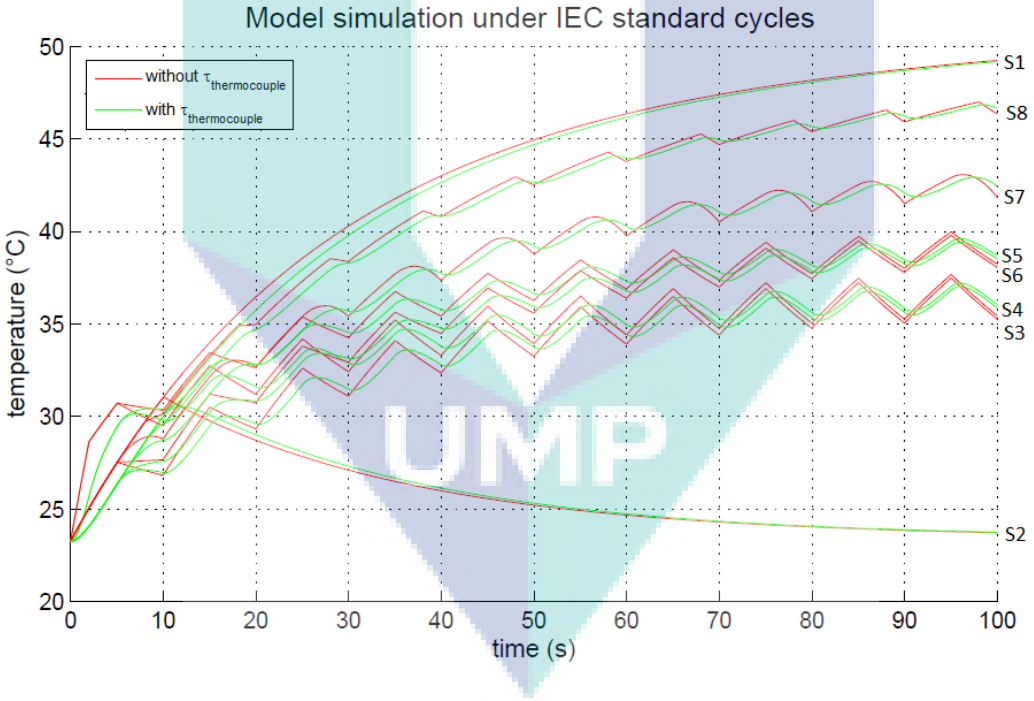

Figure 3.35: The model simulation under IEC standard cycles.

The temperature rise in function of different IEC standard cycle are presented in Figure 3.35.

3.5.3 E-Clutch duty cycle.

It is in the upmost interest to test the machine using a realistic cycles which represent the motor intended utilization. Depending on the application, these cycles cannot be presented

by IEC standard equivalent. There are therefore different test cycles for different application that has been used worlwide. In case of an automobile clutch, simulations can be done using a cycle representing the actual clutch actuating operation deduced form a standardized automotive driving cycle.

Cycle	Acronym	Region	Update
New European Driving Cycle	NEDC	Europe	1990
EPA Federal Test Procedure	FTP-75	U.S.A.	2008
Japanese Cycle	JC08	Japan	2008
World Light Test Procedure	WLTP	Global	2015

Table 3.10: Different automotive driving cycles.

In general, standardized driving cycles are cycles produced by different organizations with an objective to assesses the performance of a vehicle in various aspects especially in fuel consumption and polluting emissions. There have been 3 major standard (Table 3.10) and the latest global standard has recently been finalized by United Nation Economic Commission for Europe (UNECE) which is called WLTP cycles [43]. In order to be as representative and up to date as possible, the WLTP cycle were chosen. The WLTP procedure includes three test cycles applicable to vehicle categories of different power-to-mass ratio as shown in Figure 3.36.

Table 1
WLTP Test Cycles

Category	PMR	Speed Phases	Comments
Class 3	PMR > 34	Low, Middle, High, Extra-High	If v_max < 135 km/h, phase 'extra-high' is replaced by a repetition of phase 'low'.
Class 2	34 ≥ PMR > 22	Low, Middle, High	If v_max < 90 km/h, phase 'high' is replaced by a repetition of phase 'low'.
Class 1	PMR ≤ 22	Low, Middle	If v_max ≥ 70 km/h, phase 'low' is repeated after phase 'middle'. If v_max < 70 km/h, phase 'middle' is replaced by a repetition of phase 'low'.

Figure 3.36: WLTP Test cycles descriptions.

The prototype machine is intended to be used as a clutch actuator thus, the machine can be used for all 3 class of automobile cycles. All of them will be then simulated. To begin, certain information linked to the clutch actuation need to be extracted from the cycles above. There are 3 main information needed to make the simulation:

1. The moment when the clutch is actually actuated.

2. The operating period of the machine to actuate the clutch in order to make gear change.

3. The current intensity fed into the machine in order to actuate the clutch.

For Syncrel machine operating moment, it can be easily extracted from the cycle. Each car has an optimal speed for each gear change. Table (a) in Figure 3.38 provides a general guide for the speed on which the gear would be changed up or down. Despite that different automobile would have different optimum gear changing, the table is used as approximation to deduce the moment when the Syncrel is turned on. The number of gear changes in each cycle is shown in Table (b) of the figure. The speed profiles and the moment the Syncrel motor actuates the clutch in all three WLTP cycles are shown next to the tables in Figure 3.38.

As for the operating period of the clutch actuator, Doc [44] has mentioned that the final design of the machine allows it to deliver torque in operating period as shown in Figure 3.37. The summary of critical points including the maximum torque delivrable are shown in Table 3.11:

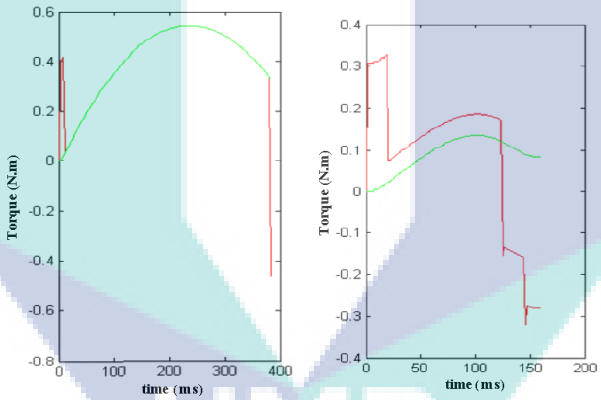

Figure 3.37: The Syncrel machine torque profile in non-assisted (left) and assisted (right) mode in function of time for clutch engagement [44].

Operating mode	Engaging clutch			Disengaging clutch		
	time (ms)	speed (rot/min)	torque (N.m)	time (ms)	speed (rot/min)	torque (N.m)
		critical points			critical points	
assisted	160	7290	0.18	400	1800	0.28
non-assisted	385	2050	0.54	400	1800	0.28
		at maximum torque			at maximum torque	
assisted	160	3990	0.33	400	1800	0.28
non-assisted	**385**	2050	**0.54**	**400**	1800	**0.28**

Table 3.11: Torque and operating time specifications for e-Clutch application.

(a)

Speed (km/h)	Gear change
0	First
10	Second
30	Third
50	Fourth
70	Fifth

(b)

Cycle	Number of gear changes
C1	37
C2	92
C3	99

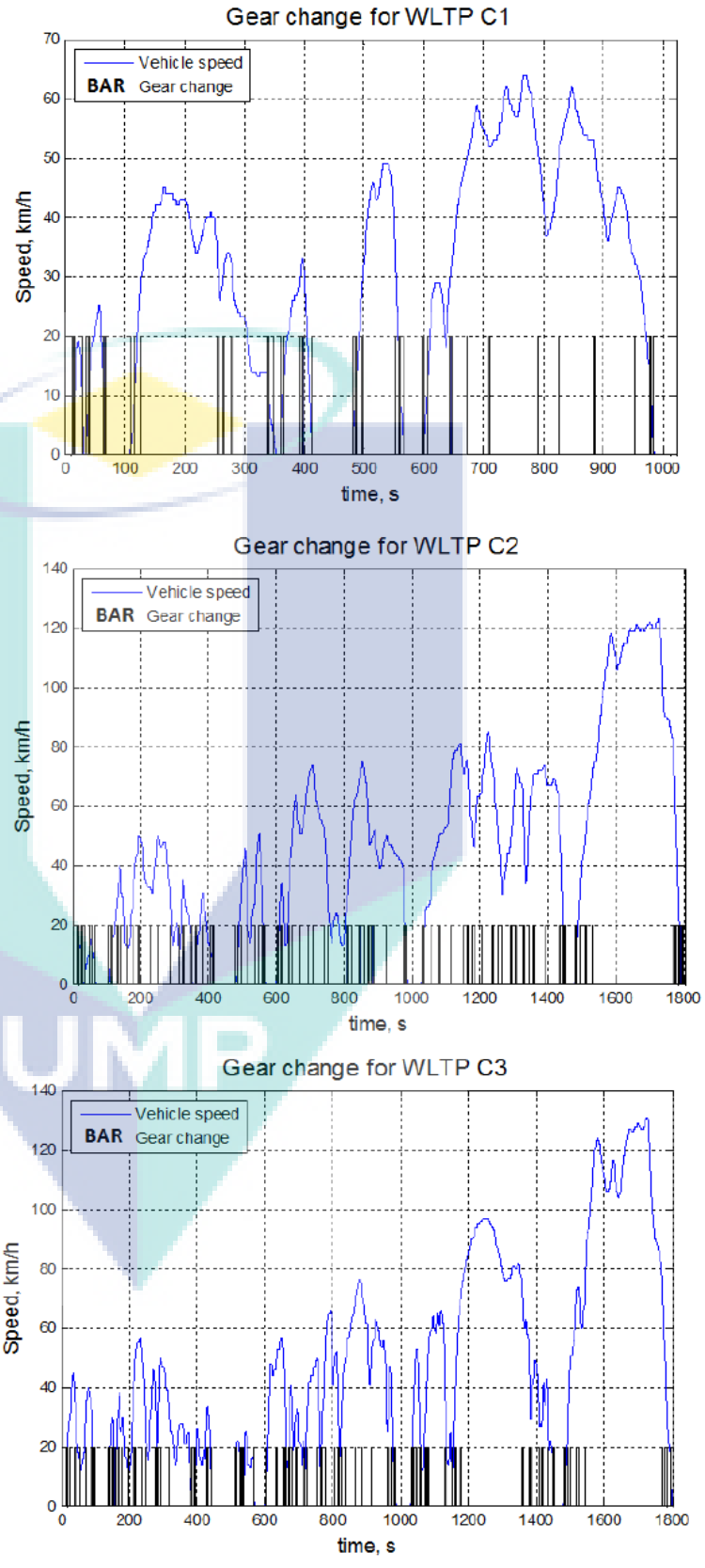

Figure 3.38: The vehicle speed and the gear changes for all three WLTP driving cycles.

It can be seen that the torque profile defined is non linear and they are due to frictions and inertia of the system. In order to simplify the heating simulation, a simplified linear torque profile set at the maximum torque value will be used as input in order to make sure that the simulated heat rise is not underestimated. The most critical case that will push the temperature of the winding to the highest point is the non-assisted mode with maximum torque (highlighted in red for engaging clutch and in green for disengaging clutch Table 3.11). This gives us a linear torque profile as following Figure 3.39:

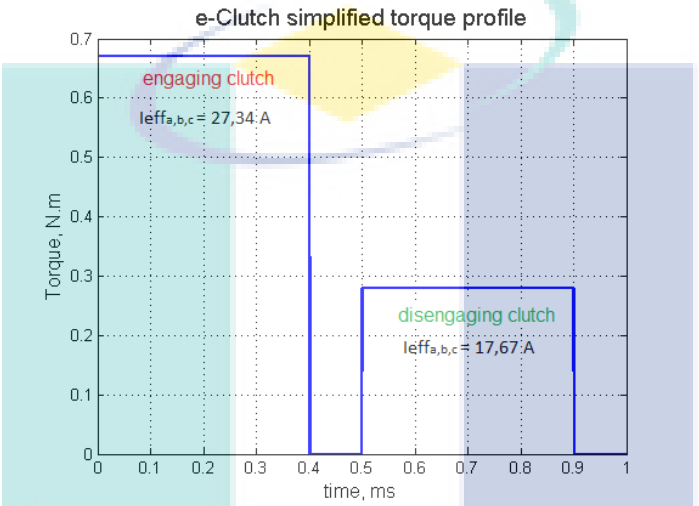

Figure 3.39: The simplified linear torque profile with the deduced current for a load angle $\beta = 45°$.

With all the information mentioned, the heating of the machine in the condition of clutch utilization under WLTP cycles can be done. Several hypothesis were done regarding the iron losses. The iron are not taken into account as it accounts a negligeable portion of losses as shown in chapter 2.

As consequence, only copper losses are going to be taken into account in order to estimate the machine temperature rise. Using the torque equation Equation 3.17, the intensity of the current delivered into each phase of the winding can be deduced (also shown in Figure 3.39).

$$\Gamma = \frac{3}{2} p(L_d - L_q) I_d I_q \tag{3.17}$$

The deduced current intensity are injected into parts in the model which generate copper losses (winding and end-winding) at each moment when the clutch is actuated, as found in Figure 3.38. The machine heating resulting from the clutch actuation in different WLTP cycles are shown in (Figure 3.40).

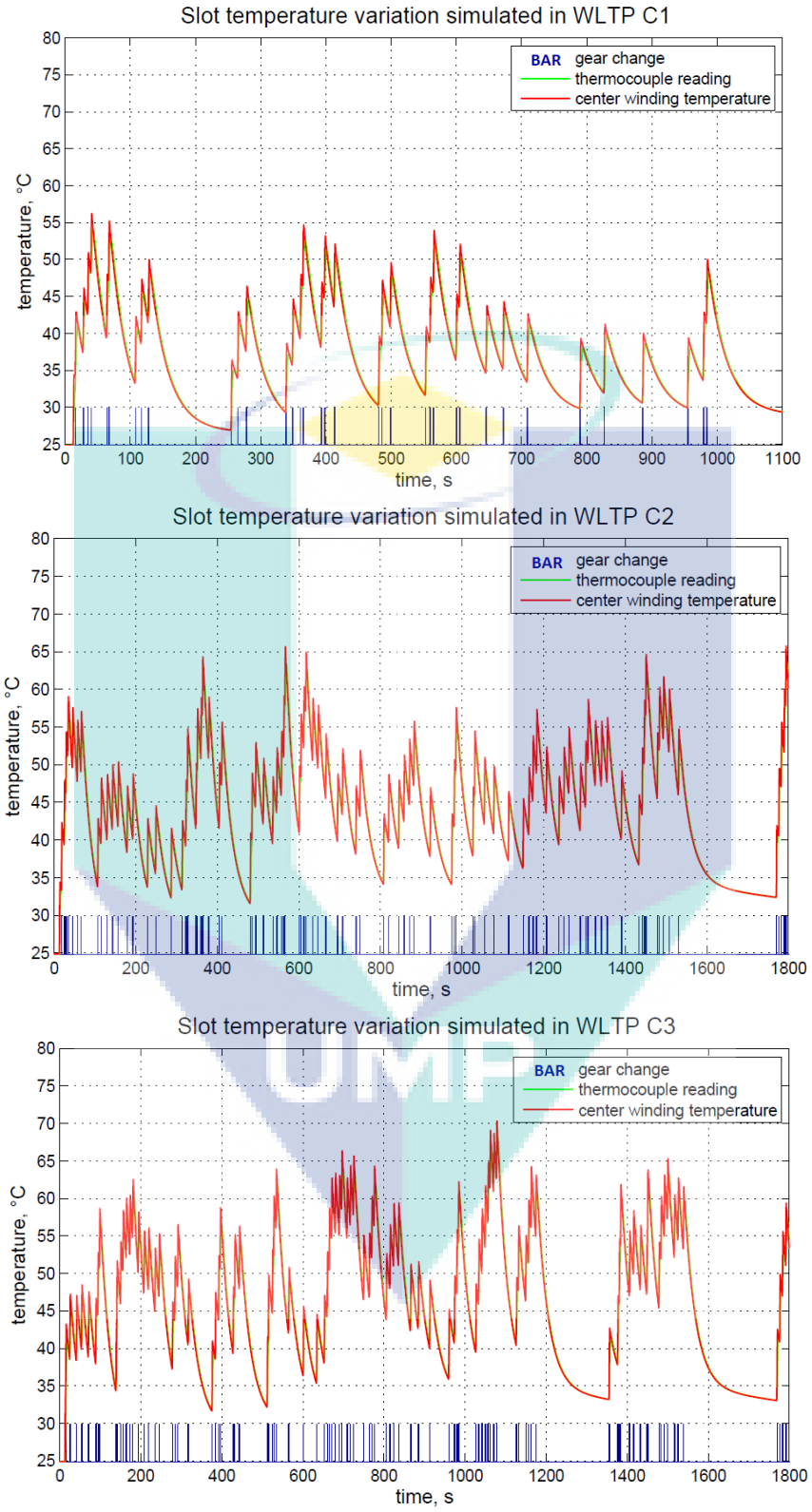

Figure 3.40: The temperature rise in the winding of the syncrel motor due to clutch operation for all three WLTP driving cycles.

It can be seen that, as the gear changes rapidly at the moment of acceleration or deceleration, the winding temperature rises instantaneously as the heat does not have time to be evacuated, thus a higher temperature peak can be observed. This can be especially observed in the cycle where the vehicle is able to accelerate and speed up to the fifth gear (WLTP C2 and C3). Whereas for WLTP C1, the low speed profile limit the sequential gear changes.The maximum temperature rise observed is in C3 with $\triangle T = 45$°C. However, it is important to note that the simulation was done with an ambient temperature of 25°C. In practical, as explained in Chapter 2, the motor will be connected to the clutch and installed in the clutch casing itself. The clutch assembly is then placed between the engine and the gear box.

By taking into account the ambient temperature of the clutch environment at 140°C (as stated by requirements. See section 1.3), the temperature rise in the machine winding was found for C3 cycle (Figure 3.41). The maximum temperature reaches 198°C.

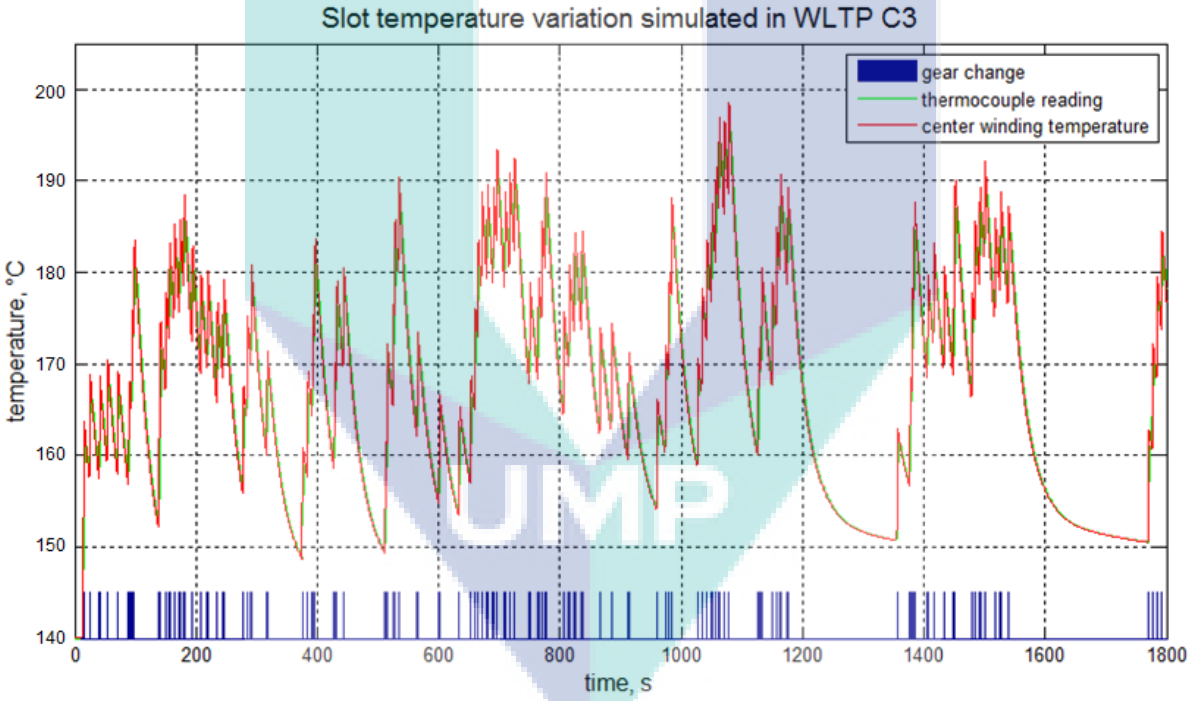

Figure 3.41: The winding temperature rise in clutch environment with a C3 cycle.

The insulation used in the motor's conductor was rated at a temperature index of 220°C (thermal class H). According to [5], the temperature index was obtained using an extrapolation of the Arrhenius plot of life versus temperature to 20000 hours. It means that the insulation can withstand a continuous 180°C temperature for 20000 hours. In usual utilization condition as been simulated, the peak temperature of 198°C in the winding is attained only once in the cycle. Besides, it is stil far below the maximum temperature index of 220°C.

Other than that even 180°C is only attained intermittently. The Syncrel motor is then shown to be a thermally capable and suitable motor for this particular application. It is therefore also relevant for other applications with similar thermal constraints.

3.6 Conclusion

At the beginning of the model construction, it was acknowledged that R_{ext} is difficult to be found accurately using analytical and empirical corelations. With the practical problematic of the motor mounting to the system (holder or test bed), experimental identification was used to find R_{ext}. Furthermore, in the case of a prototype availability, this solution will reduce the model development time massively and an accurate result related to the chosen mounting system can be found. After having calculated all other thermal parameters using relevant analytical equations find in litteratures, validation of the LP model was done using copper losses configuration.

Following the validation of the LP model in accuracy and robustness, a local sensitivity study shows that the temperature rise can be mainly attributed to two parts: the exterior surface thermal resistance and the slot thermal resistance. A very interesting observation is that, each of them contributes to elevation in different portion of the temperature curve: the exterior surface thermal resistance affects the last portion of the curve while the slot thermal resistance affects the early transient phase.

Following the results of sensitivity study, it was shown that the effort in reducing the temperature need to be done by taking into account the duty cycle: Effort of heat evacuation need to be done in the slot and end-winding structure for short duty cycle. Adding a resin infiltration is an easy mean to make the heat evacuation a lot more efficient, with a condition: the resin used can withstand the environment high temperature. In case of a long duty cycle, the adding of exterior heat evacuator such as fins or water cooling coat is very beneficial.

The thermal model combined with slot filling factor and slot infiltration functions forms a complete set of tools permitting a temperature reduction estimation in function of the filling factor and slot infiltration. This proposed tool can be used by industrial as early as in the design phase to predict the slot temperature in function of the filling factor chosen and estimate the profitability of injecting resin into the slot in function of possible temperature reduction that can be gained in return.

A concern regarding measurement has also been studied. In a short transient cycle, a thermocouple delay of every new thermocouple installation is important to be find and estimated. It is necessary to avoid under-estimating the real winding temperature. To do so, the thermocouple delay compensation method can be used with a condition: this method is

only applicable onto a model which is already proven to be accurate in the steady state and a longer transient time range.

Finally, the Syncrel motor temperature rise was simulated under standard standard IEC duty cycles and WLTP cycles in the context of clutch actuator. The Syncrel motor in its current state (as our prototype machine) has been shown to be capable and suitable for the clutch actuator application in particular and a high ambient temperature applications in general due to its lack of magnet components and passive rotor.

In perspective, with another few prototypes with better winding insulation, the machine can be tested in operating condition, operated using the WLTP cycles and placed in a high ambient temperature to validate furthermore our simulation. The proposed method of pertinent heat evacuation using slot potting and outer surface cooling can also be appplied and tested.

Bibliography

[1] Moghaddam, R.R.; Magnussen, F.; Sadarangani, C., "Theoretical and Experimental Reevaluation of Synchronous Reluctance Machine," Industrial Electronics, IEEE Transactions on , vol.57, no.1, pp.6,13, Jan. 2010 76

[2] Boldea, I.; Tutelea, L.; Parsa, L.; Dorrell, D., "Automotive Electric Propulsion Systems with Reduced or No Permanent Magnets: an Overview," Industrial Electronics, IEEE Transactions on , vol.PP, no.99, pp.1,1 76

[3] Boglietti, A.; Cavagnino, A.; Pastorelli, M.; Staton, D.; Vagati, A., "Thermal analysis of induction and synchronous reluctance motors," Industry Applications, IEEE Transactions on , vol.42, no.3, pp.675,680, May-June 2006 76

[4] H. Rosen, R. Mayschak. UL1446-A practical Electrical Insulation Standard. Electrical Insulation Magazine, IEEE. Sept. 1985. 76

[5] Emerson Motor Technologies, Product data sheet, Horizontal A.C. Motors, Unimount 125®, Totally enclosed fan cooled, 2003. 76, 77, 122

[6] A. Boglietti, A. Cavagnino, D. Staton, M. Shanel, M. Mueller, and C. Mejuto, "Evolution and modern approaches for thermal analysis of electrical machines," IEEE Trans. Ind. Electron., vol. 56, no. 3, pp. 871– 882, Mar. 2009. 77

[7] Boglietti, A.; Cavagnino, A.; Staton, D., "Determination of Critical Parameters in Electrical Machine Thermal Models", Industry Applications, IEEE Transactions on , vol.44, no.4, pp.1150,1159, July-Aug. 2008. 77, 78

[8] Romanazzi P.; Howe D. A., "Air-Gap Convection in a Switched Reluctance Machine", International Conference on Ecological Vehicles and Renewable Energies (EVER), 2015. 77

[9] P. H. Mellor, D. Roberts, and D. R. Turner, "Lumped parameter thermal model for electrical machines of TEFC design," IEE Proc. Elect. Power Appl. B, vol. 138, no. 5, pp. 205–218, Sep. 1991. 78

[10] G. Kylander, "Thermal modelling of small cage induction motors," Ph.D. dissertation, Dept. Electr. Mach. Power Electron., Chalmers Univ. Technol., G¨oteborg, Sweden, 1995. 78

[11] J. Saari, "Thermal analysis of high-speed induction machines" Ph.D. dissertation, Lab. Electromagnet.,Helsinki Univ. Technol., Helsinki, Finland, 1998. 78

[12] J. Lindström, "Development of an experimental permanent-magnet motor drive" Licentiate Thesis, Dept. Electr. Power Eng., Chalmers Univ. Technol., Göteborg, Sweden, Apr. 1999. 78

[13] Z.Kolondzovski, A. Belahcen, and A. Arkkio, "Comparative thermal analysis of different rotor types for a high-speed permanent-magnet electrical machine," IET Electr. Power Appl., vol. 3, no. 4, pp. 279–288, Jul. 2008. 78

[14] A. M. El-Refaie, N. C. Harris, T. M. Jahns, and K. M. Rahman, "Thermal analysis of multibarrier interior PM synchronous machine using lumped parameter model," IEEE Trans. Energy Convers., vol. 19, no. 2, pp. 303– 309, Jun. 2004. 79

[15] Incropera; DeWitt, Bergman, Lavine (2007). Fundamentals of Heat and Mass Transfer (6th edition ed.). John Wiley & Sons. pp. 260–261. ISBN 978-0-471-45728-2. 79

[16] Cavagnino, A.; Staton, D., "Convection heat transfer and flow calculations suitable for analytical modelling of electric machines," presented at 32nd Conference of the IEEE Industrial Electronics Society (IECON), Page(s): 4841-4846, November 2006. 81

[17] K&K Associates for National Aeronautics and Space Administration, "Thermal Network Modeling Handbook", Version 97.003, 1999-2000. 81

[18] Doc C., "Contribution à la Conception et au Dimensionnement d'un Actionneur d'Embrayage". Ph.D. Thesis, Université de Technologie de Compiègne. 2010.

[19] Blundell S.; Blundell K., "Concepts in Modern Physics", Oxford University Press. p. 247. ISBN 978-0-19-856769-1, 2006. 81

[20] Bouafia M.; BertinY.; SaulnierJ.B.; Robert P., "Analyse expérimentale des transferts de chaleur en espace annulaire étroit et rainuré avec cylindre intérieur tournant", International Journal of Heat and Mass Transfer, 41, n° 10, p. 1279-91, 1998. 81

[21] Idoughi, L.; Mininger, X.; Bouillault, F.; Bernard, L.; Hoang, E., "Thermal Model With Winding Homogenization and FIT Discretization for Stator Slot," Magnetics, IEEE Transactions on , vol.47, no.12, pp.4822,4826, Dec. 2011 88, 90

[22] Wrobel, R.; Mellor, P.H.; Holliday, D., "Thermal Modeling of a Segmented Stator Winding Design," Industry Applications, IEEE Transactions on , vol.47, no.5, pp.2023,2030, Sept.-Oct. 2011. 88

[23] Simpson, N.; Wrobel, R.; Mellor, P.H., "Estimation of Equivalent Thermal Parameters of Impregnated Electrical Windings," Industry Applications, IEEE Transactions on , vol.49, no.6, pp.2505,2515, Nov.-Dec. 2013 88

[24] Svensson, L., Andersson, M., Reinap, A., Alaküla, M. (2014), "Thermal properties on high fill factor electrical windings: Infiltrated vs non infiltrated". International Conference on Electrical Machines (ICEM14), Berlin, Germany, 2-5 September, 2014. 88, 90

[25] Nategh, S.; Wallmark, O.; Leksell, M.; Shuang Zhao, "Thermal Analysis of a PMaSRM Using Partial FEA and Lumped Parameter Modeling," Energy Conversion, IEEE Transactions on , vol.27, no.2, pp.477,488, June 2012 89

[26] Perrins W. T.; McKenzie D. R.; McPhedran R. C., "Transport properties of regular arrays of cylinders", Pro. R. Soc. Lond A 369, pp. 207-225, 1979. 89, 90

[27] Hashin Z. ; Shtrikman S. , "A variational approach to the theory of the effective magnetic permeability of multiphase materials", J. Appl. Phys., 33(10), pp. 3125, 1962. 89, 90

[28] Milton Z.G.W. , "A complete characterization of invariant jointly rank-r convex quadratic forms and applications to composite materials", J. Appl. Phys., 52, pp. 5294-5304, 1981. 89, 90

[29] Mori T.; Tanaka K. , "Average stress in matrix and average elastic energy of materials with misfitting inclusions", Pro. R. Soc. Lond A 417, pp. 59-80, 1988. 89, 90

[30] Crow A., "Stator and Rotor Laminations from Prtotype to Volume Production", UK-MAG Advance in Manufacture Seminar, 19 June 2013. 93

[31] B. Renard, "Etude expérimentale et modélisation du comportement thermique d'une machine électrique multi-fonctions. Applications à un alterno-démarreur intégré", Ph.D. dissertation, Université de Poitiers, 2003. 93

[32] Staton, D.; Boglietti, A.; Cavagnino, A., "Solving the More Difficult Aspects of Electric Motor Thermal Analysis in Small and Medium Size Industrial Induction Motors," Energy Conversion, IEEE Transactions on , vol.20, no.3, pp.620,628, Sept. 2005 95

[33] Holman, J.P., Heat Transfer, McGraw-Hill, New York, 1997. 94, 95, 96

[34] A.F. Mills, Heat Transfer, Prentice Hall, 1999. 94, 95, 96

[35] W. S. Janna, Engineering Heat Transfer . New York: Van Nostrand, 1988. 94

[36] Hamby, D. M. 1994. "A review of techniques for parameter sensitivity analysis of environmental models. Environ. Monitoring and Assessment", 32(2): 135-154. 99

[37] Boglietti, A.; Cavagnino, A.; Staton, D.A., "TEFC induction motors thermal models: a parameter sensitivity analysis," Industry Applications Conference, 2004. 39th IAS Annual Meeting. Conference Record of the 2004 IEEE , vol.4, no., pp.2469,2476 vol.4, 3-7 Oct. 2004 99

[38] "Design Guide for Electrical Motors and Generators," Loctite, Henkel Corporation, October 2005. 105, 106

[39] Shaukatullah, H.; Claassen, A., "Effect of thermocouple wire size and attachment method on measurement of thermal characteristics of electronic packages," Semiconductor Thermal Measurement and Management Symposium, 2003. Ninteenth Annual IEEE , vol., no., pp.97,105, 11-13 March 2003. 110

[40] J.P. Holman, Experimental Methods for Engineers, 7th Ed., McGraw-hill, New York, 2001: First-order systems, p. 19-23; Thermocouples p. 368-377.

[41] Rabin, Y. & Rittel, D. A model for the time response of solid-embedded thermocouples Experimental Mechanics, Kluwer Academic Publishers, 1999, 39, 132-136 110

[42] Duty cycle, IEC Standard, Section 151-16-02: Operating conditions and testing. 107, 115

[43] Tutuianu M., Marotta A., Steven H., Aricsson E., Haniu T., Ichikawa N., Ishii H., "Development of a World-wide Worldwide Harmonized Light Duty Driving Test Cycle (WLTC)," technical report, 68 th GRPE, 7-10 January 201 4. 117

[44] Doc C., "Contribution à la conception et au dimensionnement d'un actionneur d'embrayage". Ph.D. dissertation, Université de Technologie de Compiègne, 2010. 118

[45] "Standard Test Method for Thermal Endurance of Film-Insulated Round Magnet Wire", ASTM International, D2307-1.

Chapter 4

Torque ripple and vibro-acoustic behavior

4.1 Torque ripple of segmented-rotor Syncrel

Like any other salient pole and permanent magnet assisted machine such as the SRM and IPMSM, the Syncrel machine produces a relatively important torque ripple [1, 7]. With the absence of a rotor cage, the torque pulsation cannot be reduced by damping effect produced by the cage[5]. It is also important to know that torque ripple can usually be related to important vibration and acoustic noise.

The torque ripple is mainly due to interaction between the stator and the rotor geometry which has variable reluctance accross the airgap. This variable reluctance results in variation of flux path during the machine operation, therefore emergeance of torque ripple. Knowing the principle of reluctance machine that insists on having important reluctance variation, the torque ripple of the machine is therefore inevitably important. In a sinusoidal-current-fed machine, the harmonic content of the torque can takes origin from different source: slot harmonics, and winding-configuration-related harmonics (also called belt harmonics).

The first harmonic which is caused by the slots opening has been studied in [5, 6], where extensive analytical studies on the torque ripple of Syncrel machine have been made. They resulted in simplified analytical model of flux oscillations due to stator-rotor interactions. In brief, the usual torque analytical equation Equation 4.1 uses a single value for each inductances L_d and L_q, which were measured or calculated when the magnetic field position and the rotor positions are as shown in Figure 4.1 [9, 10] .

$$\Gamma = \frac{3}{2} p (L_d - L_q) I_d I_q \tag{4.1}$$

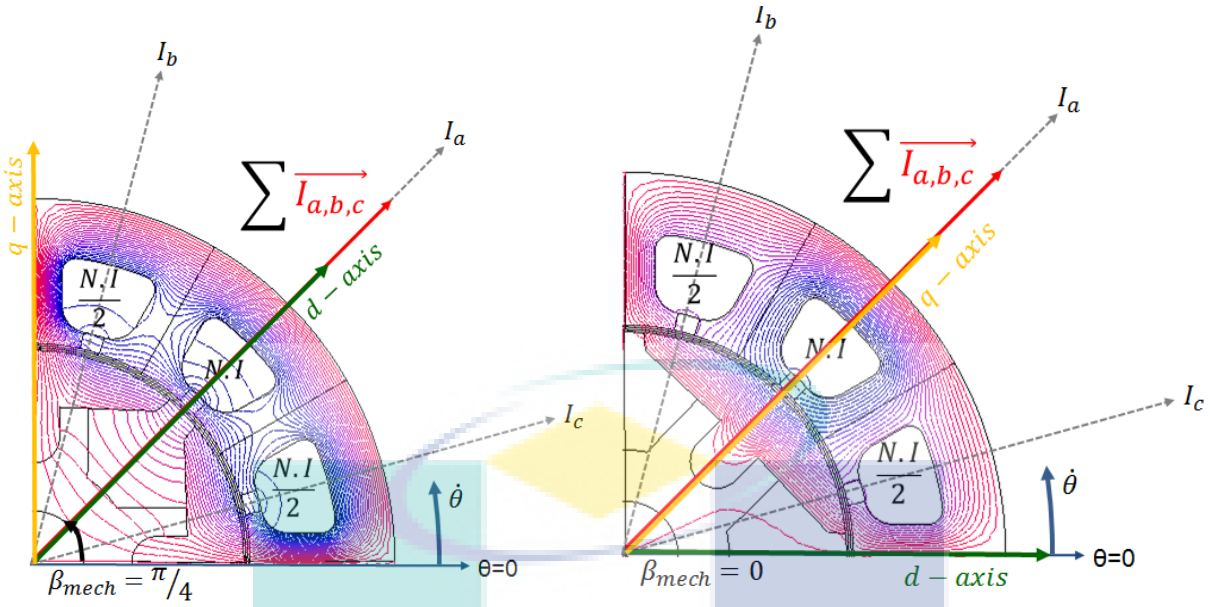

Figure 4.1: Quadrature (left) and direct (right) position on which L_d and L_q have been calculated.

The torque calculated using equation Equation 4.1 and L_d, L_q values found as such will gives an average torque and the torque ripple cannot be deduced unless the inductances variation in function of the magnetic field position θ is taken into account. Rather than having a single value for each L_d and L_q, the inductance matrix depending on the rotation angle θ such in Equation 4.2 is more precise.

$$\begin{bmatrix} \lambda_d \\ \lambda_q \end{bmatrix} = \begin{bmatrix} L_d(\theta) & L_{dq}(\theta) \\ L_{dq}(\theta) & L_q(\theta) \end{bmatrix} \begin{bmatrix} i_d \\ i_q \end{bmatrix} \tag{4.2}$$

Following the inductance variation, [5] proposes the inductances to be written in forms shown in Equation 4.3, Equation 4.4, and Equation 4.5:

$$L_d(\theta) \cong L_{do} + \Delta L_d.cosN_{slot}\theta \tag{4.3}$$

$$L_q(\theta) \cong L_{qo} - \Delta L_q.cosN_{slot}\theta \tag{4.4}$$

$$L_{dq}(\theta) \cong -\Delta L_{dq}.sinN_{slot}\theta \tag{4.5}$$

Parameters ΔL_d, ΔL_q and ΔL_{dq} values were identified experimentally in [5] and these parameters help defining the flux and torque ripple behavior of the machine. Consequently,

instead of having the torque equation as in Equation 4.1 which only gives an average torque, the torque equation will look like Equation 4.6:

$$\frac{\Gamma(\theta)}{p} = \frac{3}{2}(L_d - L_q)i_d i_q + a + b \tag{4.6}$$

with a and b being:

$$a = (\frac{\Delta L_d + \Delta L_q}{2} - \frac{N_{slot}/p}{2}\Delta L_{dq})2i_d i_q cos N_{slot}\theta \tag{4.7}$$

$$b = \left[\frac{N_{slot}/p}{2}(\Delta L_q i_q^2 - \Delta L_d i_d^2) - \Delta L_{dq}(i_q^2 - i_d^2)\right] sin N_{slot}\theta \tag{4.8}$$

From Equation 4.6, instantaneous torque can be calculated at any position θ where the main torque and the ripple component are shown. Fratta pointed out that in a constant-current, torque control, a gives a ripple proportional to the average torque while b is always present even in no-load condition ($i_q = 0$ or $i_d = 0$). [5] also note that the ripple decreases with N_{slot} because all $\triangle L$ decrease reasonably with N_{slot}.

Having established briefly the theoretical background, the objective of our studies in the following section is to evaluate the torque ripple of our Syncrel with segmented rotor prototype machine and observe the ripple phenomena as shown in Equation 4.6. Later, a comparison of the torque ripple between three different rotor topologies with the same stator configuration will be done qualitatively and quantitatively in order to highlight the origin of the torque ripple in the design of the machine. Finally, a review on usual torque ripple reduction techniques and its possibility to be done on our machine will be looked into.

4.1.1 Torque ripple characteristics evaluation using FE analysis

In this section, the torque ripple of our prototype machine will be evaluated using FE analysis and later validated experimentally. Identification of the origin of the ripple will be explained thereafter. For reminder, our prototype machine is a 2 pair pole p, 12 slots, and full-pitch winding machine. The evaluation of the torque ripple is done using a FE model that was validated in chapter 2.

4.1.1.1 Torque ripple in function of current I_s, at fixed load angle β

We begin the study with an observation of the torque ripple variation in function of current I_s, with the load angle being fixed the maximum torque position ($\beta = \pi/4$). A perfect sinusoidal current is fed to the stator and the load angle is set to the maximum torque position ($\beta = \pi/4$). The result of the torque ripple form is shown in Figure 4.2. The torque

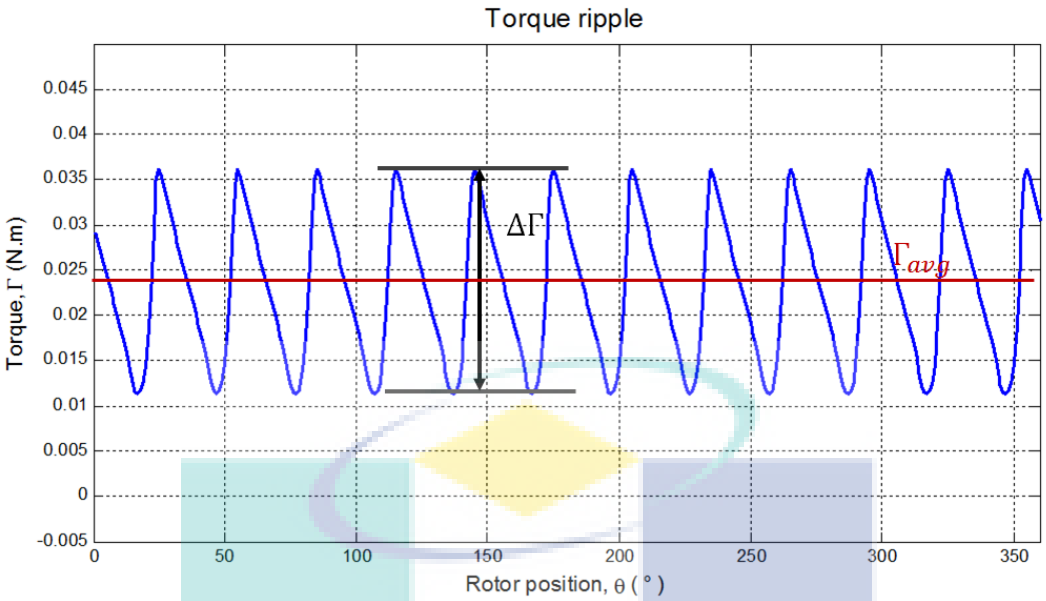

Figure 4.2: Torque ripple in segmented-rotor Syncrel at $I_s = 10A$, $\beta = \pi/4$.

ripple was calculated by measuring the ratio of maximum variance (peak to peak) to the average torque ratio Equation 4.9.

$$ripple = \frac{\Delta\Gamma}{\Gamma_{avg}} \tag{4.9}$$

At five different current level, $I_s = [10A, 20A, 30A, 40A, 50A]$, the torque ripples were found to be at 105%, thus it suggests that the torque ripple is constant at all current level (thus torque developed by the machine) for a fixed load angle. The ripples are relatively high, with a sawtooth waveform. In a complete rotation, 12 periods of the sawtooth can be observed which corresponds to the number of slots of the machine. A closer look into the rotor positions in relation to the ripple waveform is provided in Figure 4.3.

The minimum torque is observed when the non-magnetic part of the rotor is positioned in front of the slot opening. In this position, the magnetic flux (left side of the second tooth of the bottom Figure 4.3) has to go through larger airgap (which in this case includes: non-magnetic rotor part, airgap and slot opening) to get to the rotor segment. The discontinuity and higher reluctance in this path due to larger airgap lead to a drop in torque delivered. On the other hand, it can be seen that the maximum torque is attained (top Figure 4.3) when the flux start to have a better crossing to the rotor segment through the machine airgap, not through the non-magnetic rotor part and slot opening. It is also the position in which the flux linkages are the shortest. In reference to [5] which has been briefly presented in previous section (section 4.1), the discontinuity of reluctances faced by a flux linkage in function of rotor position are taken into account analytically by the introduction of ΔL_d,

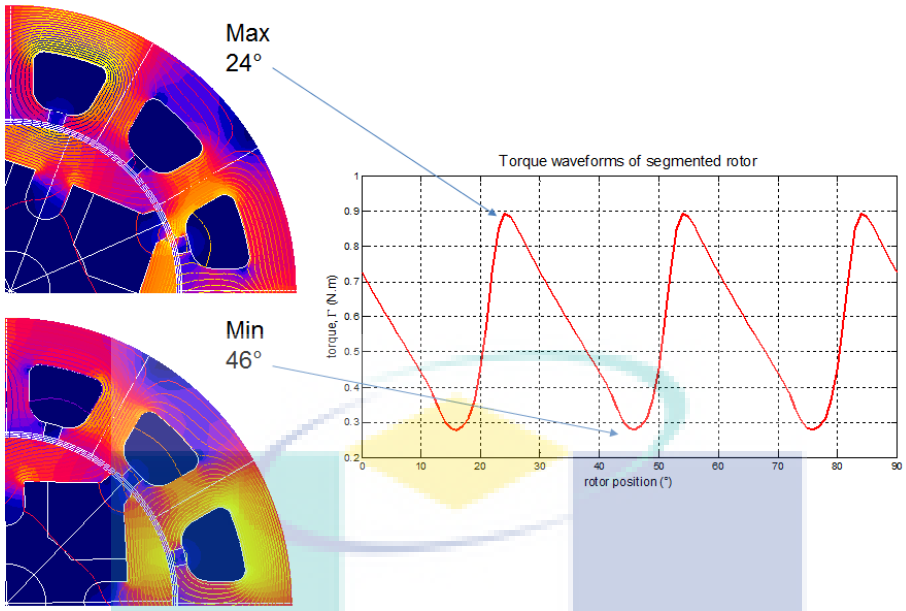

Figure 4.3: Identification of rotor position in relation to the torque waveforms in segmented rotor.

ΔL_q and ΔL_{dq}.

In brief, the interaction between the slot openings and the non-magnetic parts of the rotor plays major role in defining the torque ripple (form and amplitude). Therefore, influencing parameters on the torque ripple in this type of machines include the slot numbers N_{slot} , the length of slot openings $l_{slot\,opening}$ and the length of the non-magnetic rotor segments $l_{non\,mag}$. The parameters are recalled in Figure 4.4. The possible improvements will be treated later in subsection 4.1.4.

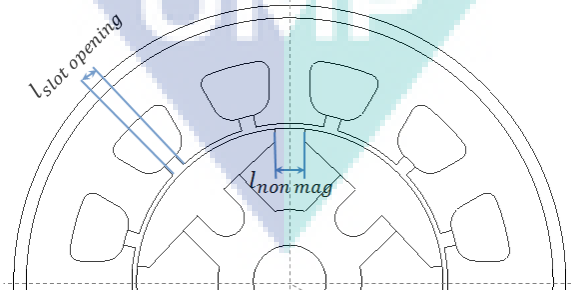

Figure 4.4: The parameter $l_{non\,mag}$ and $l_{slot\,opening}$.

4.1.1.2 Torque ripple in function of load angle β, at fixed current I_s

In previous paragraph, the torque ripple has been studied for a constant load angle control ($\beta = \pi/4$) at different current intensities I_s. We are now going to evaluate the influence of

the load angle control β, (by consequent dictate i_d and i_q) at a constant current I_s on the torque ripple. In function of the load angle a simulation was done by maintaining the speed and the current level of the machine at $N = 1500rpm$ and $I_s = 50A$. The machine is rotated for during a quarter of electrical period which is sufficient to observe the torque ripple. The results is shown in Figure 4.5.

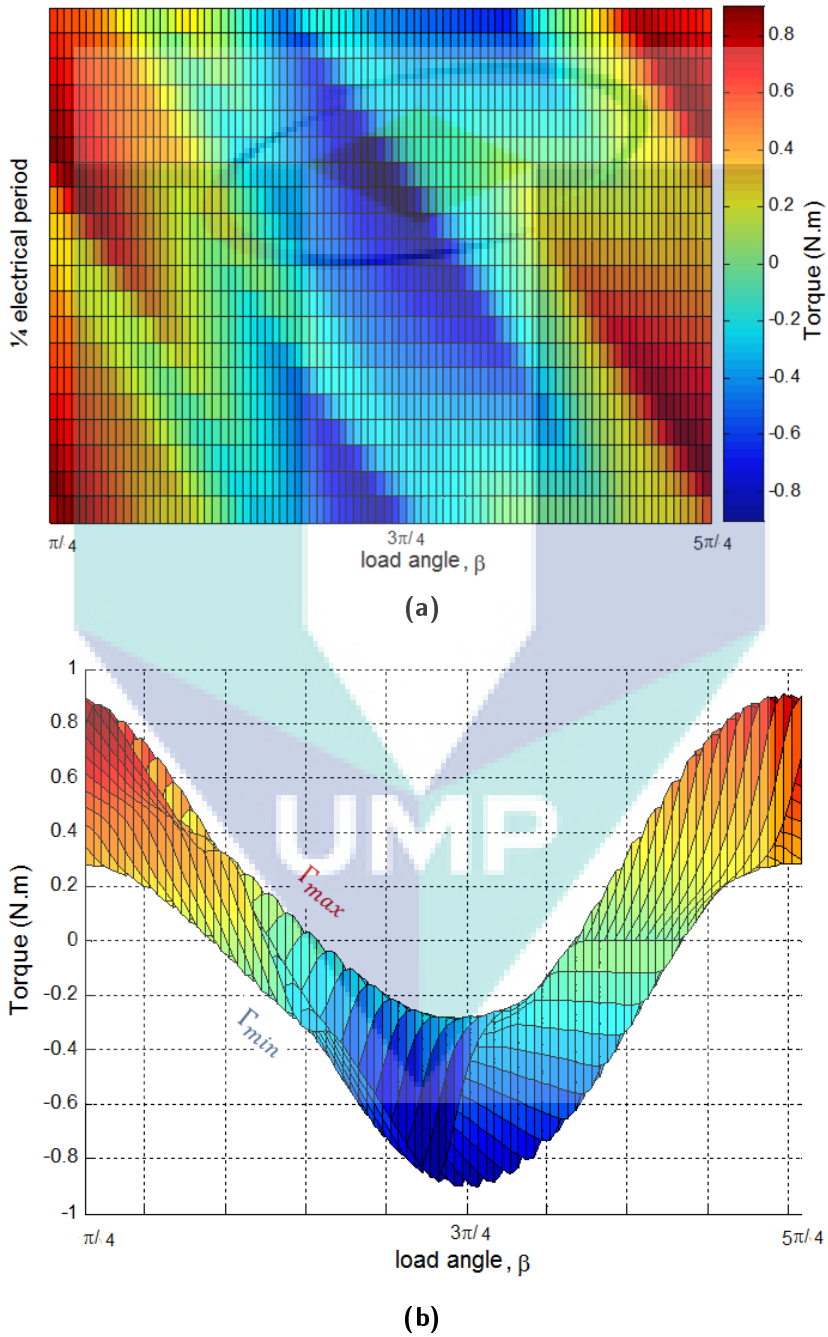

Figure 4.5: Torque ripples variation in function of load angle for 1/8 rotation at constant current of I_s=50A.

We can observe the torque ripple that varies (waveforms and amplitude) in function of the load angle. In Figure 4.5a, we can see one and a half period of the torque ripple along the time axis as the rotor passes in front of one and a half slots in a quarter electrical period. In the same figure, as the load angle varies from $\pi/4$ to $5\pi/4$, the average torque makes a full range variation from maximum average torque, to minimum average torque and back to maximum average torque. In Figure 4.5b, the maximum and the minimum torque at every load angle can be seen. From these data, the average torque, the peak-to-peak torque range and the torque ripple in percentage have been deduced, and put together in a graph Figure 4.6.

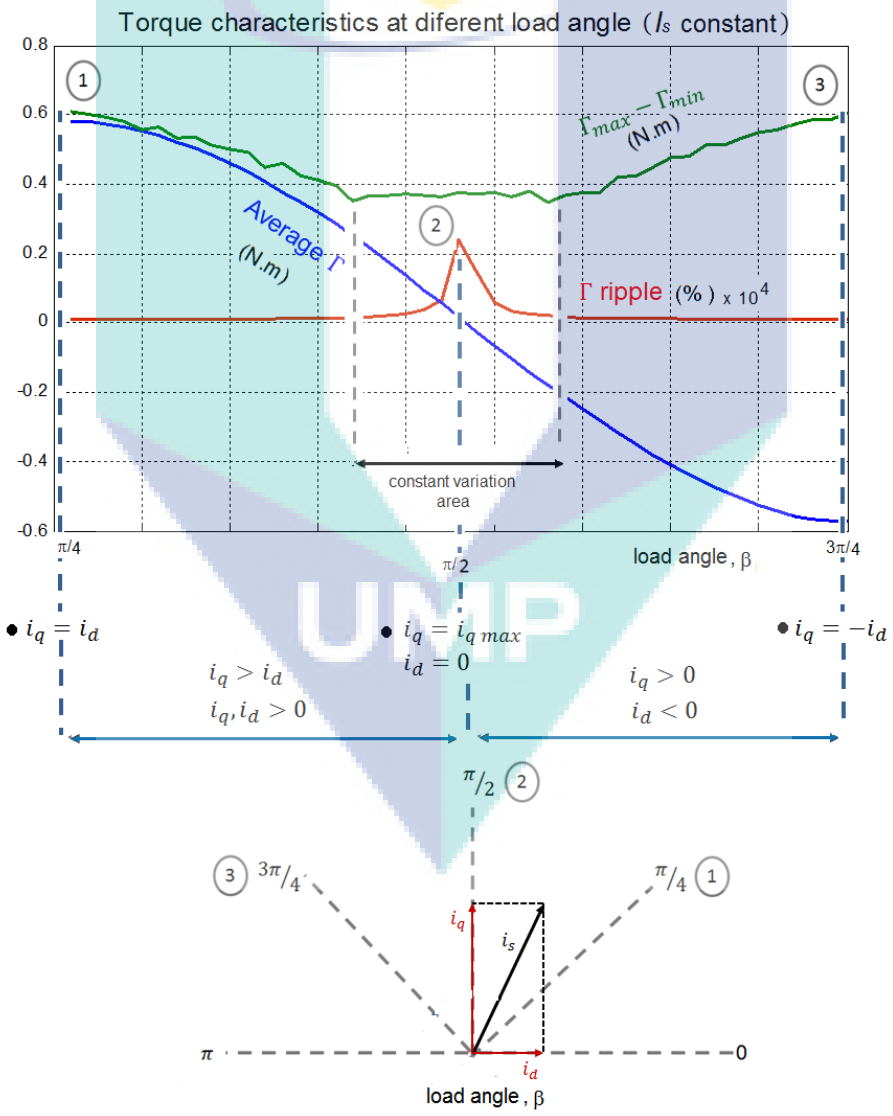

Figure 4.6: Average torque (blue), peak-to-peak torque difference (green) and the torque ripple (red) in function of mechanical load angle and electrical load angle (i_d, i_q).

The average torque oscillates with the load angle, reaches maximum when the $\beta = \pi/4$, and becomes zero when it reaches $\pi/2$ (which is also the quadrature position) as expected. The curves in Figure 4.6 only represents half of the period of average torque oscillation, and there are four average torque oscillations in one complete rotor rotation.

The most important torque ripple characteristic to be noted is that the peak-to-peak torque difference at each load angle varies in the same pattern as the average torque, but stay nearly constant as the average torque approaches zero, (note constant variation area in Figure 4.6). The torque ripple variation can be represented by a Gaussian curve (Figure 4.7).

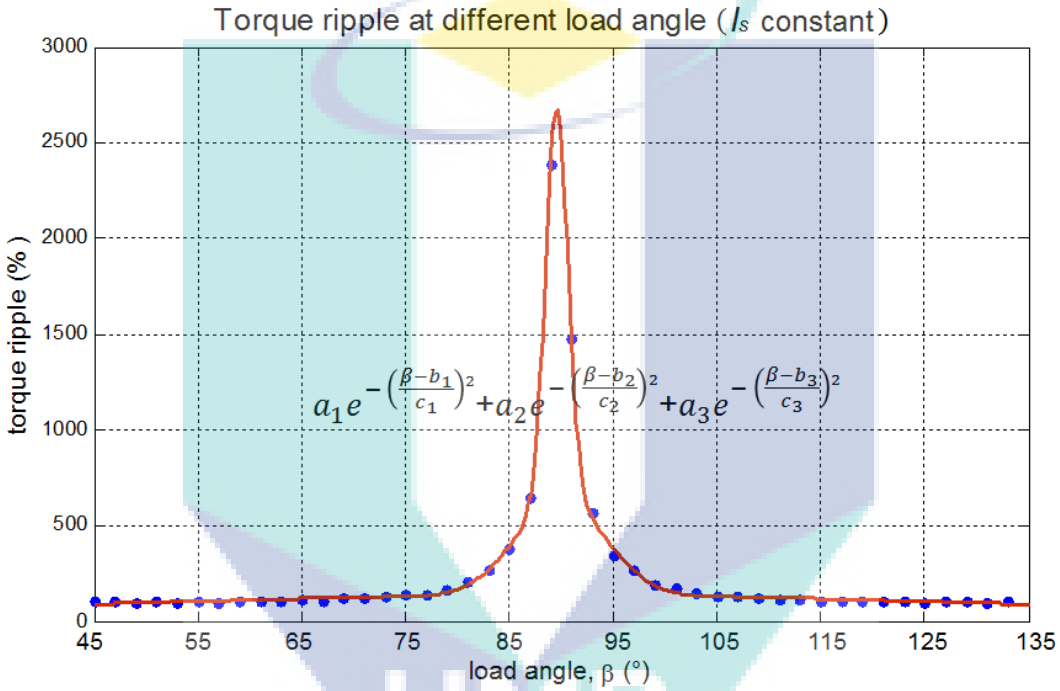

Figure 4.7: The torque ripple of the machine in function of electrical load angle, fitted to a Gaussian function.

From Figure 4.7, we can see that at 45°, the ripple is constant at around 105%. It increases slowly and gradually up to 75° and spikes as the average torque approaches zero (when the load angle is at 90°, which is also the quadrature position). It has been shown that the torque ripple can be fitted to a Gaussian function centered at quadrature or direct position and there are 4 period of the torque ripple function in a complete electric angle rotation. In reference to Fratta [5], the torque ripple spike area represents the term b in Equation 4.6 which produces ripple even if the machine is operated in no-load condition.

In terms of application, we have seen in chapter 2 that higher torque or speed operating points can be attained by changing the load angle. In case of load angle modification, this observation tells us that the torque ripple can increase importantly. The torque ripple curve

presented in Figure 4.7 can therefore be very helpful for user to predict the torque ripple in function of operating points of the machine.

4.1.2 Experimental observation

To validate the torque ripple characteristics (values and pattern) observed in FE analysis, the torque ripple was quantified experimentally using the prototype machine. The machine was connected to the torque-meter and the brake load. The torque measured by the torque-meter is displayed using an oscilloscope and recorded. The machine was operated using speed control so as to maintain the machine at a constant speed for a given load. As the machine will be used at a fixed load angle of $\beta = \pi/4$ most of the time, the experiments were done for such load angle.

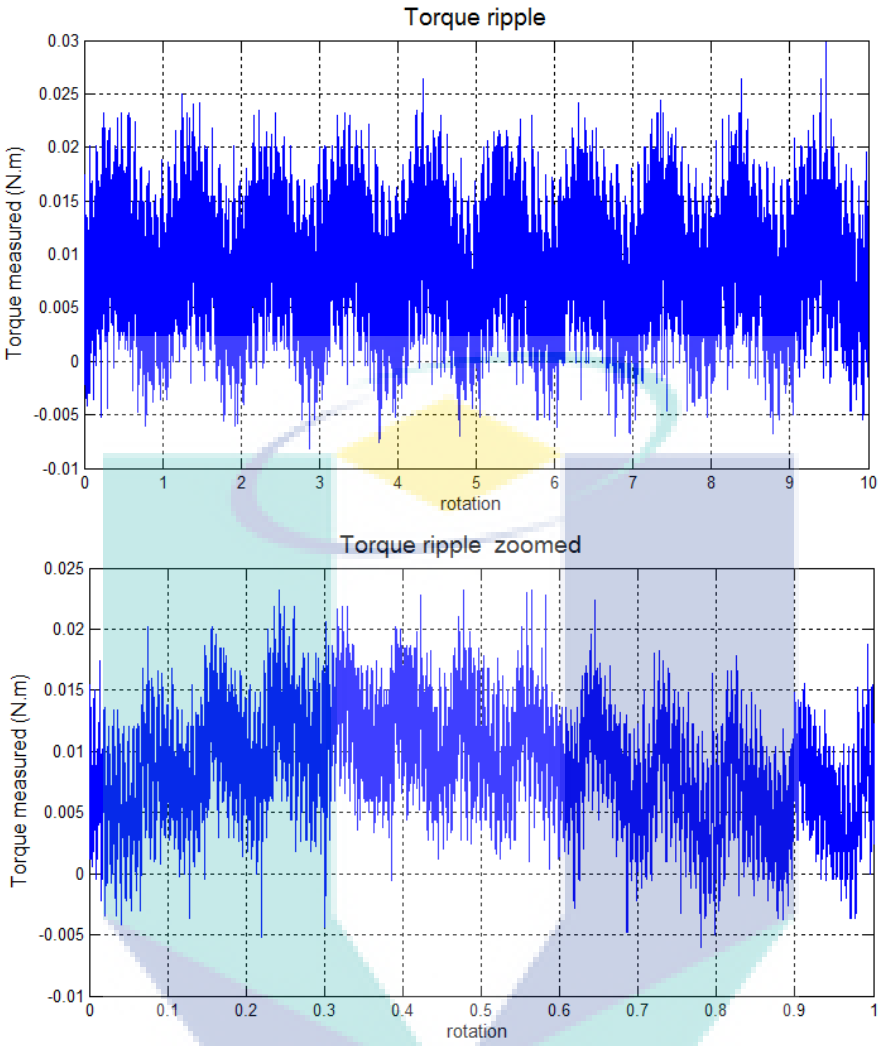

Figure 4.8: Top: Experimental torque ripple measured using the torque-meter, recorded for 10 rotation. Bottom: Zoomed torque on one rotation, showing 12 period sawtooth waveforms.

An example of experimental data is shown in Figure 4.8 where the speed was set at $N = 60rpm$ (1 revolution per second). The low speed was used to make sure that the ripple frequency is within the bandwidth of the torque-meter to make it observable. It would also help us distinguish the pattern coming from the machine electromagnetic torque ripple and lower frequency mechanical harmonics. It can be seen in top Figure 4.8 where 10 rotations have been recorded, that the largest ondulation with a frequency of 1 revolution per second (1Hz) modulate the torque signal. This ondulation can be attributed to friction caused by imperfection of the alignments between the shafts of the machine, torque-meter and brake load. The overall ripple observed in top Figure 4.8 is then the sum of the misalignment ripple added to the machine's ripple. What we are interested in is the ripple produce by the

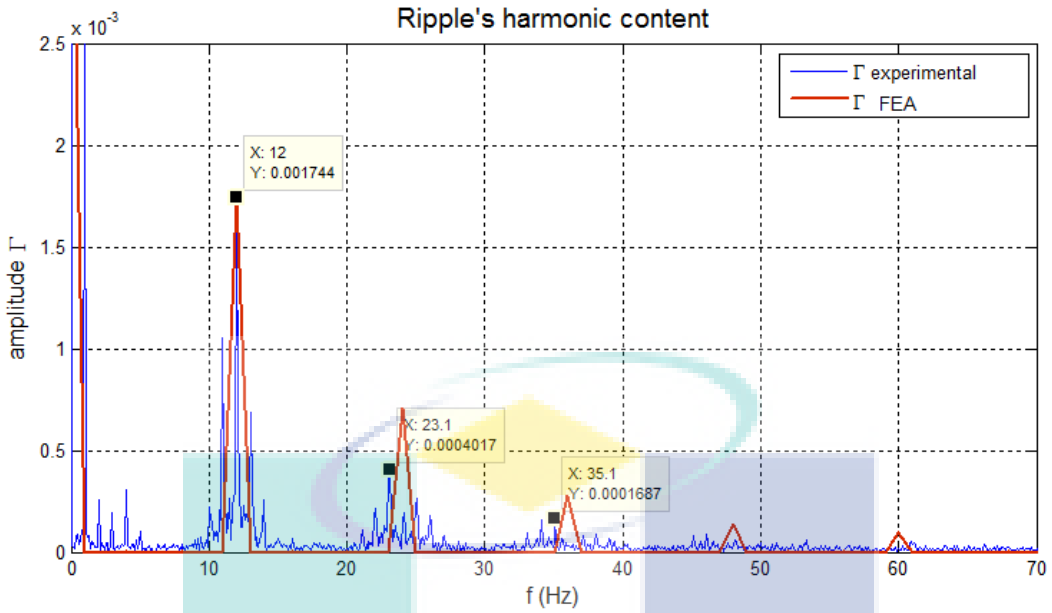

Figure 4.9: Comparison of the torque ripples harmonic content for a speed of $N = 60rpm$ (f_{mech}= 1Hz) between experimental and FE results.

machine alone. Therefore, the torque ripple of the machine cannot be simply deduced by Equation 4.9 applied on curve in Figure 4.8.

When the torque in top Figure 4.8 is zoomed to a single rotor revolution, a clearer view on the torque ripple can be seen on the bottom. The same sawtooth pattern of the torque that was found in the FE results can be recognized in the zoomed view. As the ripple is directly related to the relative position of the non-magnetic part of the rotor to the slot opening, 12 sawtooth can be observed, which are related to 12 slots (and slot openings) of the machine in one rotation. It can be seen that the peak-to-peak torque difference ($\Gamma_{max} - \Gamma_{min}$) across the modulated torque is nearly constant. After filtering the 1Hz frequency, we get the torque waveform on which the torque ripple can be computed using Equation 4.9.At different operating torques, the ripple computation resulted in a torque ripple of around 110%, which is very close to the one found in subsubsection 4.1.1.1 previously.

After having validated the amplitude of the torque ripple, we also want to validate the pattern of the torque ripple. To do so, the harmonic content of the experimental torque ripple was compared to the FEA torque ripple at the same load level. The comparison harmonic content comparison is shown in Figure 4.9.

In general, it can be said that the two torque ripple forms correspond with some minor and particular difference in the experimental harmonic content. The content at 0Hz is the offset of the pulsating torque signal which corresponds to the average torque. There is an important line at 1Hz for the experimental torque ripple which does not exist in FEA. This

can be explained by the modulation originated from the test bench resistance torque, as explained earlier in Figure 4.8. We can observe that the experimental and FE harmonics content of the torque fits very well as for the first harmonic at 12Hz. This is the harmonic that originated from the slot opening, called slot harmonics that can be observed at $k.N_{slot}$. For example, in Figure 4.9, at a speed of 60rpm (f_{mech}= 1Hz), the harmonics are at around 12Hz, 24Hz, 36 Hz and so forth. Particular to experimental harmonic content, instead of having a single line at each slot harmonic frequency, we observe a family of lines around the main line. These lines can have origins from mechanical eccentricity and friction.

Following comparison of the experimental torque ripple with the FEA, both in terms of amplitude, and harmonic content, it has been shown that the waveform of the torque ripple matches, thus validate the torque estimated.

4.1.3 Comparison with other rotor topologies

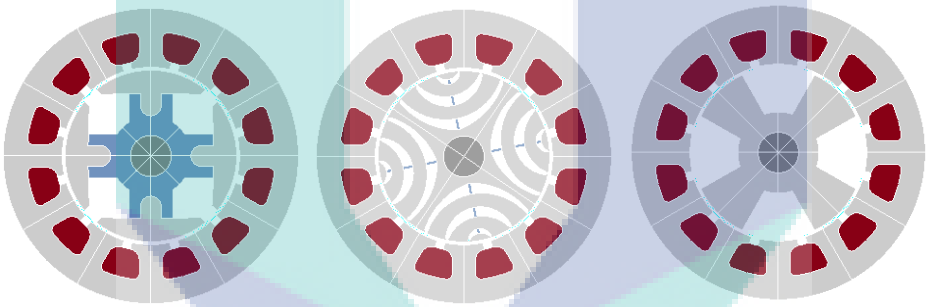

Figure 4.10: The three Syncrel motor compared. From left: the prototype Syncrel motor with segmented rotor, Syncrel motor with flux-barrier rotor and Syncrel motor with solid rotor.

As in chapter 2, the rotor topologies that will be put into comparison are the flux barrier rotor and the solid rotor (Figure 4.10). To do so, FE model of the other two rotor topologies were used to deduce their torque ripples. Considering that the other two rotor topologies are not highly optimized[1], the comparison is only to evaluate the order of magnitude of the torque ripple.

The comparison is done at the highest torque operating point of our prototype machine. This corresponds to a maximum current supply of $I_s = 50A$. The load angle was set at $\beta = \pi/4$. The comparison between their torque ripples forms is shown in Figure 4.11, and the value in Table 4.1.

[1]However, considering the small diameter constraints, all rotor topologies have very little margin for modifications. Therefore, the comparison on the order of magnitude is reasonable.

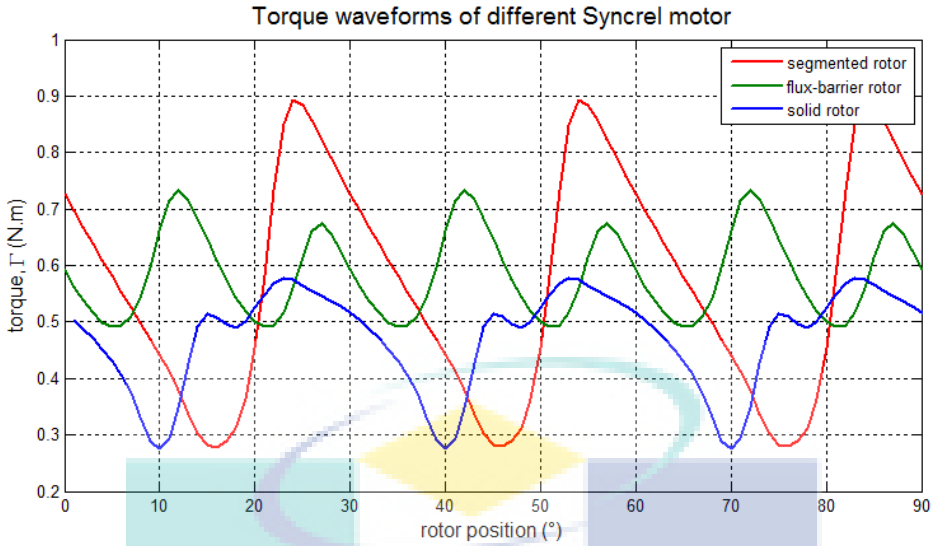

Figure 4.11: Torque comparison between the three Syncrel rotor topologies at maximum current $I_s = 50A$. (FE analysis).

Rotor topology	segmented	flux barrier	solid
Torque ripple (%)	105	41-48	78

Table 4.1: Torque ripple comparison between the three Syncrel rotor topologies. (for I_s varying from 10A to 50A)

The torque ripple is the highest for the segmented rotor and the lowest for the flux-barrier rotor. The segmented rotor torque ripple is twice as big as the flux-barrier rotor while the average torques are comparable (see Figure 2.45 in chapter 2). Compared to the literature, it has been reported that the flux barrier rotor with regular symmetrical similar to the one we modelized produces torque ripple around 50% to 60% for a load angle of $\beta = \pi/4$ [1]. [2] The solid and segmented rotor being less studied, no information on their torque ripple values have been found. Some torque ripple of similar segmented rotor can however be found for SRM which is not the same type of machine regarding the stator field commutation. In this case, the torque ripple has been reported to varies from around 60% to 110% for different winding method [11].

In terms of the ripple waveforms, it was observed qualitatively that the segmented rotor waveforms has three peaks per quarter machine. The flux-barrier and solid rotor torque on the other hand have six peaks (three global peaks and three local peaks) (Figure 4.12 and Figure 4.13).

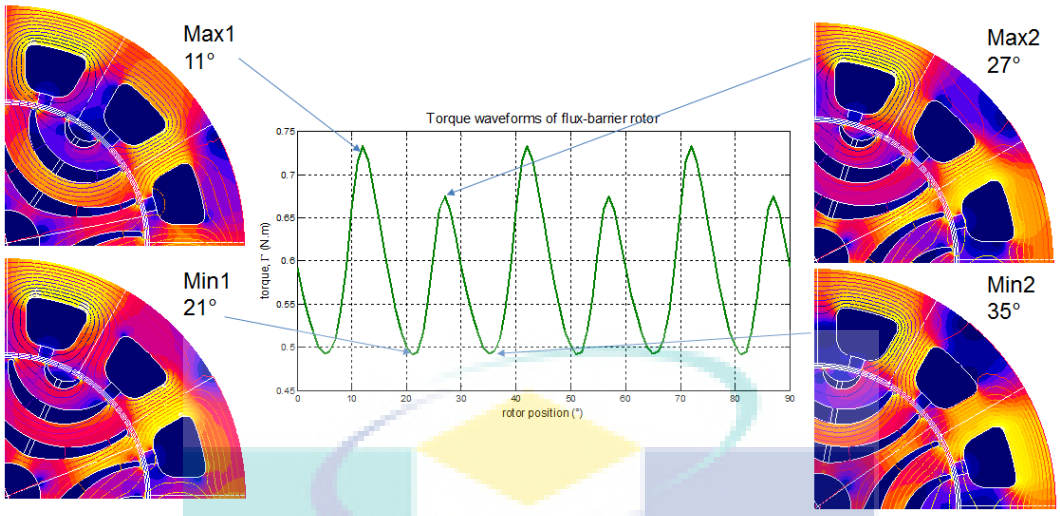

Figure 4.12: Identification of rotor position in relation to the torque waveforms in flux-barrier rotor.

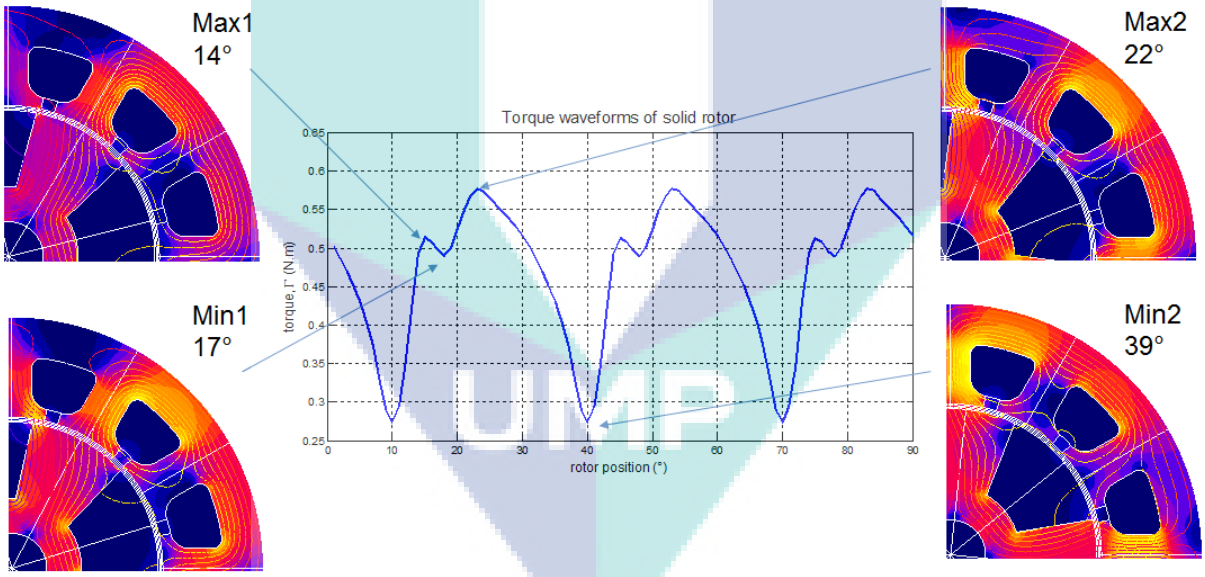

Figure 4.13: Identification of rotor position in relation to the torque waveforms in three different Syncrel rotor topologies solid rotor.

The local and global peaks in flux-barrier rotor look alike and they are both followed by a minimum torque of the same amplitude. In solid rotor, the local peak occurs near the global peak and the local minimum torque following the local peak is far higher than the global minimum (which arrives after the global peak). The flux-barrier has the advantage of repartitioning the non-magnetic segments of the rotor into multiple saturated bridges, resulting in less interaction between slot-opening and the non magnetic segment at a time.

This leads to a low torque ripple. As for the solid rotor, the flux linkage pattern is totaly different from the previous two. The flux linkage enters and exits the rotor from different rotor tooth. Observation on the relationship between the rotor position and the torque waveforms in each rotor topology is consistent to what have been observed for segmented rotor previously. The more the flux linkage variation occcurs while the rotor moves, the more torque pulsation observed.

Another comparison can be made by comparing the harmonic content of the three machines torque waveforms Figure 4.14.

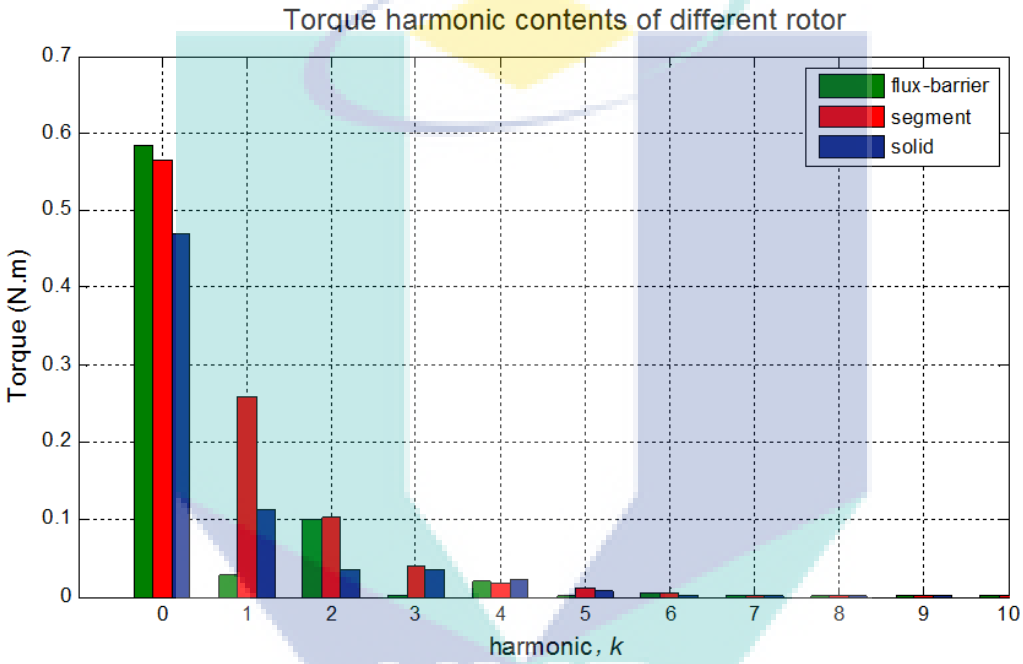

Figure 4.14: Ripples harmonics comparison between the three rotor topologies presented in harmonic order, k. (FE analysis)

The frequency of each line can be found at $k \times f_{mech} \times N_{slot}$. The order zero represents the average torque of each machine which has already been presented in chapter 3. The harmonic content generating torque ripple is clearly higher for segmented rotor compared to other two rotors topologies. The flux-barrier rotor has the most advantageous torque quality where its harmonic content is the lowest in all order except for the second order.

Following these comparisons, we deduce that it is important reduce the discontinuity in flux passing between the stator and the rotor to the maximum. To do so, the most obvious way is to make the non-magnetic part of the rotor as small as possible relative to the size of the slot opening. As result, the flux-barrier rotor has shown the lowest ripple among the three topologies compared. The solid rotor the second and the segmented rotor

in last position. However, as mentioned in chapter 2, considering the compromise between manufacturing feasibility and average torque delivered, the segmented rotor is still the best option for our application.

4.1.4 Perspective on torque ripple reduction

For a fixed stator, we have seen that by reducing the non-magnetic segment of the rotor and multiplying its number, the torque ripple can be smoothed while maintaining the L_d/L_q ratio, which is easily done by adopting the flux-barrier rotor. This has also been proven in literature such as in [2, 3] where they have demonstrate the importance of having many small flux-barriers compared to the slot opening (in their studies called slits). Many other studies has been done in the path of flux-barrier rotor improvement such as in [7, 8].

However in regard to the cost and manufacturing constraints, flux-barrier solution is unfeasible and the segmented rotor is the best solution to be used for our application. Therefore, for our machine and it's intended application, the torque ripple can only be reduced by finding an optimized length for $l_{slot\,opening}$ and $l_{non\,mag}$ Figure 4.15.

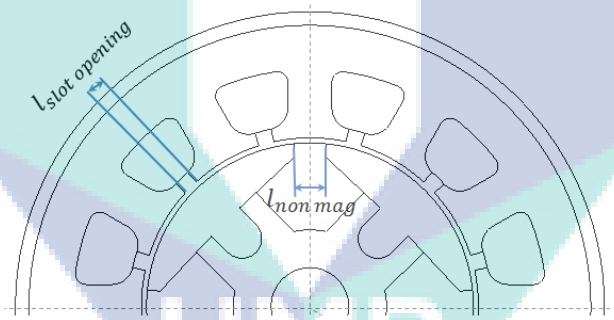

Figure 4.15: The parameter $l_{non\,mag}$.

Therefore, the parametrized FE model of the machine can be used coupled with a multi-objective optimization algorithm where the problem can be formulated as:

$$min(f_1(x,y),\ f_2(x,y)) \tag{4.10}$$

$s.t. x \in X,\ y \in Y$, where f_1 and f_2 is the average torque and torque ripple function, depending on x and y, the two influencing parameters shown in Figure 4.15 which are limited X and Y, the possible and acceptable values for both parameters. Another geometry parameter that may help in improving the torque ripple which is less trivial is the form of rotor segment corner. This optimization study will be subject of nearest future studies.

Other design parameters that were not studied here, such as the winding method can

also impact the torque ripple. This has been studied in [4, 6] and interesting results have been shown. This will also be tested for our segmented rotor Syncrel machine in order to find the best winding configuration optimizing both average torque and torque ripple.

A more classic method of stator chording and rotor skewing is generally known to reduce torque ripple in an AC motor. However, it adds complexity to manufacturing process though the skew is effective in the torque ripple decrease. Moreover, the average output torque can decrease [4]. In addition, there is a problem that the copper loss increases as the length's of the armature winding becomes longer. Therefore, this torque ripple reduction method will not be considered.

4.2 Vibro-acoustic behavior

In automotive industry, the problematic of vibration and noise in electrical machine has been seen as important and crucial especially for a big traction motor. From physio-acoustic point of view, electrical machines creates relatively unpleasant high frequencies acoustic noises compared to internal combustion engine and other automobile noise sources (e^{2}xhaust, intake and tires) [13, 14]. Electrical machines are subject to the International Electrotechnical Commission standard IEC 60034-9 (Rotating electrical machines - Part 9: Noise limits) [12]. For each power category of machine and ventilation, it specifies a total sound power level (SWL) limit in dBA depending on speed. An example of the noise limit is shown in Figure 4.16.

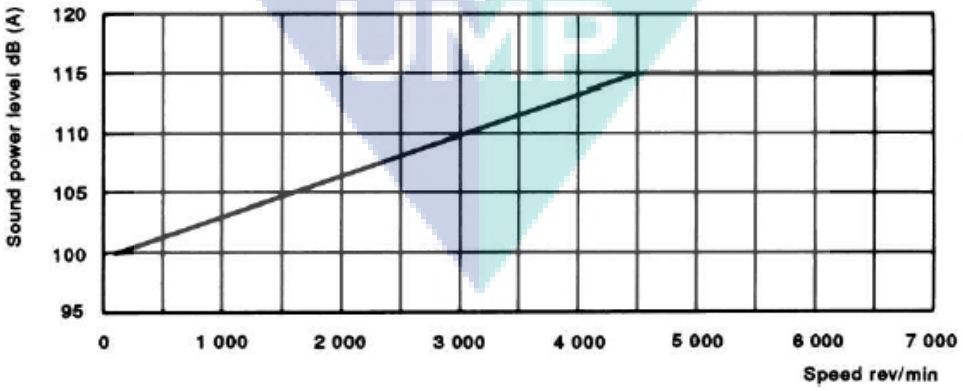

Figure 4.16: EC 60034-9 norm for noise limit.

Thanks to severe standards and clients requirements, advance progress has been made in pure mechanical noise reduction. As consequence, electromagnetic noises that were before masked by the mechanical noise can now be heard, especially of higher frequency. There-

fore, vibro-acoustic study on electrical system in automotive industry becomes nowadays necessary.

The primary objective and intended contribution of this study is to evaluate the vibro-acoustic behavior of the segmented-rotor Syncrel prototype machine. A validated internal-developed numerical tool will also be used in parallel to deduce the spectrograms and vibration spectrum, in order to see correlation despite several hypothesis made in the model.

4.2.1 Vibro-acoustic of electric machine: generalities

The noise in electro-mechanical system originates from three major sources:

1. Mechanical components noises, which are related to contact and friction between different pieces in an assembly. For example, whistling noises from ball bearing and power transmission gears.

2. Aerodynamic noises, which are related to turbulence in the air flow in the cavity of the machine such as motor cooling ventilation.

3. Noises caused by electromagnetic forces in the electric machine. These noises are directly related to the deformation of parts that are submitted to electromagnetic forces such as the stator core and the rotor segment. Electromagnetic forces can be further divided into three categories: Maxwell forces, Laplace forces, and magnetostrictive forces.

The magnetostrictive vibration is neglected as it has been shown to be negligible compared to the Maxwell force in multiple studies [15, 16, 17]. Acoustic noise coming from Laplace force is also usually neglected considering that the stator flux density in the winding is too low to produce significant vibrations to be transmitted to the stator yoke. Furthermore, the conductors are usually wedged into slots with a certain filling factor, leaving void spaces in the slot [14]. Therefore, we are only interested in the noises originated from electromagnetic forces, specifically the Maxwell forces.

With the forces originating from electromagnetic source and transmitted to the mechanical structure in forms of vibration and acoustic radiation, the two physics need to be coupled. In following sections, we will present the generalities of each physics, electromagnetic forces modeling and the vibro-acoustic modeling before exposing the coupling tool that link the magnetic force computation and the structure vibration computation.

4.2.1.1 Electromagnetic forces modeling

A several number of method exist to compute the magnetic pressures in an electric machine. Among them are: equivalent source method [18], derivation of magnetic energy [19], virtual work method [20], and Maxwell stress tensor [21]. The Maxwell stress tensor method has been seen as the most adapted method which provide us with the best compromise between the ease of implementation in a numerical tool and adequate precision [22].

Therefore here, a brief presentation on how the magnetic pressure is obtained using the Maxwell stress tensor will be done. Consider an elementary volume subjected to a magnetic field B Figure 4.17.

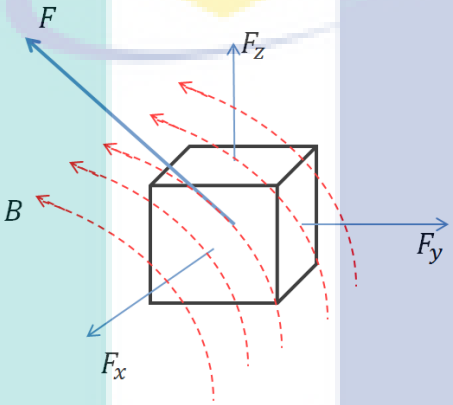

Figure 4.17: Elementary volume subjected to a magnetic field B.

The resulting force on the volume can be computed using the divergence of the Maxwell tensor Equation 4.11.

$$\overrightarrow{F} = div(\boldsymbol{T}) \tag{4.11}$$

For example, in direction x, the force can be written as:

$$F_x = \frac{\partial T_{xx}}{\partial x} + \frac{\partial T_{xy}}{\partial y} + \frac{\partial T_{xz}}{\partial z} \tag{4.12}$$

In order to construct the Maxwell tensor, several relation between different electrical quantities need to be established. The first one is the relation between the source electric field and the electrostatic charges which state that the flux $\overrightarrow{D}$ across a closed surface is proportional to the electrical charge it contains Equation 4.13:

$$div(\overrightarrow{D}) = \rho \tag{4.13}$$

The second relation is the one relating the electric field and the flux density (Equation 4.14)

which states that the induced electromotive force in any closed circuit is equal to the negative of the time rate of change of the magnetic flux enclosed by the circuit. This is known as Faraday-Lenz law.

$$rot(\overrightarrow{E}) = -\frac{\partial \overrightarrow{B}}{\partial t} \tag{4.14}$$

The third relation is the conservation of the magnetic flux Equation 4.15:

$$div(\overrightarrow{B}) = 0 \tag{4.15}$$

Finally the last relation is the conservation of electric charges Equation 4.16:

$$rot(\overrightarrow{H}) = \overrightarrow{J} + \frac{\partial \overrightarrow{D}}{\partial t} \tag{4.16}$$

We note that the Maxwell tensor also introduces the Lorentz force which represents the the effects of the magnetic field on electric charges Equation 4.17, and by consequence the Laplace force in a conductor Equation 4.18.

$$\overrightarrow{F} = q\overrightarrow{v} \wedge \overrightarrow{B} \tag{4.17}$$

$$\overrightarrow{F} = \overrightarrow{J} \wedge \overrightarrow{B} \tag{4.18}$$

To simplify further development, we write Equation 4.18 on one direction x and becomes Equation 4.19:

$$F_x = J_y.B_z - J_z.B_y \tag{4.19}$$

Considering that only static aspect is studied, $\frac{\partial \overrightarrow{D}}{\partial t}$ of Equation 4.16 becomes zero, and $\overrightarrow{J}$ can be written as a composition of partial derivative of $\overrightarrow{H}$. Therefore, Equation 4.19 can be written as Equation 4.20:

$$F_x = \left(\frac{\partial H_x}{\partial z} - \frac{\partial H_z}{\partial x}\right).\mu.H_z - \left(\frac{\partial H_y}{\partial x} - \frac{\partial H_x}{\partial y}\right).\mu.H_y \tag{4.20}$$

A zero quantity (Equation 4.21) resulting from the conservation of magnetic flux (Equation 4.15) is later added to the equation, making Equation 4.20 into Equation 4.22.

$$H_x.div(\overrightarrow{B}) = \mu H_x \left(\frac{\partial H_x}{\partial x} + \frac{\partial H_y}{\partial y} + \frac{\partial H_z}{\partial z}\right) \tag{4.21}$$

$$F_x = \mu\left(H_x\frac{\partial H_x}{\partial x} - H_y\frac{\partial H_y}{\partial x} - H_z\frac{\partial H_z}{\partial x}\right) + \mu\left(H_y\frac{\partial H_x}{\partial y} - H_x\frac{\partial H_y}{\partial y}\right) + \mu\left(H_z\frac{\partial H_x}{\partial z} - H_x\frac{\partial H_z}{\partial z}\right) \tag{4.22}$$

With x, y and z the spatial coordinates, δ_{ij} the Kronecker symbols ($\delta_{ij} = 1$ if i=j, $\delta_{ij} = 0$ if $i \neq j$), the components of Maxwell tensor T can then be written as Equation 4.23:

$$T_{ij} = \mu\left(H_iH_j - \frac{1}{2}\delta_{ij}H^2\right) \tag{4.23}$$

By taking into account the material behavior,

$$T_{ij} = \frac{1}{\mu}\left(B_iB_j - \frac{1}{2}\delta_{ij}|\boldsymbol{B}|^2\right) \tag{4.24}$$

the Maxwell tensor can be written in the following form:

$$\boldsymbol{T} = \mu\begin{pmatrix} H_x^2 - \frac{1}{2}H^2 & H_xH_y & H_xH_z \\ H_yH_x & H_y^2 - \frac{1}{2}H^2 & H_yH_z \\ H_zH_x & H_zH_y & H_z^2 - \frac{1}{2}H^2 \end{pmatrix} \tag{4.25}$$

Using the Ostrogradski theorem (Equation 4.26), the force on a volume can be found by integrating the force in Equation 4.11 of the elementary volume over the total volume (Equation 4.27),

$$\int_V div(\overrightarrow{F}).dv = \int_S \overrightarrow{F}.\overrightarrow{ds} \tag{4.26}$$

$$\overrightarrow{F} = \int_V \overrightarrow{f_v}dv = \int_V div(\boldsymbol{T})dv \tag{4.27}$$

and later reduced to an integration over a surface :

$$\int_V div(\boldsymbol{T})dv = \int_S n\boldsymbol{T}ds \tag{4.28}$$

Based on methodology of mechanical studies, where the local distribution of the stress in a material is usually done using a tensor, the Maxwell tensor can be used to find the local magnetic pressure. The Maxwell tensor can be written in normal and tangential reference frame as:

$$\boldsymbol{T} = \mu\begin{pmatrix} H_nH_n - \frac{1}{2}H^2 & H_nH_t & 0 \\ H_tH_n & H_tH_t - \frac{1}{2}H^2 & 0 \\ 0 & 0 & -\frac{1}{2}H^2 \end{pmatrix} \tag{4.29}$$

By expressing H^2 in the form of $H_n^2 + H_t^2$ and taking into account the magnetic properties

of the material, the normal and tangential magnetic pressure can be written as:

$$\sigma_n = \frac{B_n^2}{2\mu} - \frac{\mu H_t^2}{2} \tag{4.30}$$

$$\sigma_t = B_n H_t \tag{4.31}$$

With the magnetic permeability of airgap equal to μ_0, Equation 4.30 and Equation 4.31 becomes:

$$\sigma_n = \frac{\mu_0}{2}\left(H_n^2 - H_t^2\right) = \frac{(B_n^2 - B_t^2)}{2\mu_0} \tag{4.32}$$

$$\sigma_t = \mu_0(H_n H_t) = \frac{B_n B_t}{\mu_0} \tag{4.33}$$

By supposing that the magnetic field mostly cross the airgap in radial direction, the tangential components can be then neglected for a first estimation. In function of the angular position θ and time, the magnetic pressure can then be approximated to:

$$\sigma_n(\theta, t) \backsimeq \frac{B_n(\theta, t)^2}{2\mu_0} = \frac{\left(B_s(\theta, t) + B_r(\theta, t)\right)^2}{2\mu_0} \tag{4.34}$$

According to [23], the harmonic content of the magnetic pressure can be generalized by the following expression:

$$\sigma_{r,t}(\theta, t) = \sum_{m=0, n=-\infty}^{+\infty} \sigma_{m,n}^{r,t} cos(m\theta + n\Omega t + \varphi_{m,n}^{r,t}) \tag{4.35}$$

where r and t are the radial and tangential component of the pressure in the airgap, m is the space harmonic order of the pressure related to the angular position θ, n the rank of the time harmonic related to the mechanical frequency Ω, and $\varphi_{m,n}^{r,t}$ the phase shift associated to each harmonic.

These pressures in the airgap are directly transmitted to stator core through the teeth and by extension the casing. In a vibro-acoustic modeling of electric machine, these pressures will be affected on the mechanical structure of the stator core in order to deduce the vibration response. This will results in radiation of possibly audible sound power level.

4.2.1.2 Vibration modeling

In mechanical vibration point of view, a structure is characterized by its natural modes of vibration. Mathematically, they are eigenvalues that diagonalized the FE matrix of mass

and elasticity. Physically, they are vibration stationary waves that are naturally produced when the structure is excited at specific frequencies. These natural modes are determined by the mass, elasticity and boundary conditions. The study of the mode and its shape of a structure is called modal analysis. After knowing the modal characteristics of a structure, it can be submitted to excitation where its vibration response can be analyzed. The study of vibration response is called frequency response analysis, where it is usually studied by deducing the frequency response function of the structure, called FRF.

We are now going to look at an example of vibro-acoustic modeling, where it is usually illustrated in its simplest form using a one-end-fixed beam. The beam is excited at its free extremities by an oscillating force (Figure 4.18).

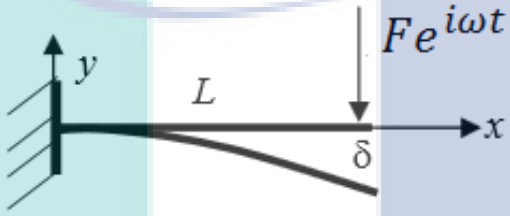

Figure 4.18: One-end-fixed beam, excited at its free extremities by an oscillating force.

At different frequency of excitation, different natural modes appears as a stationary wave forms of different frequencies (Figure 4.19), called mode.

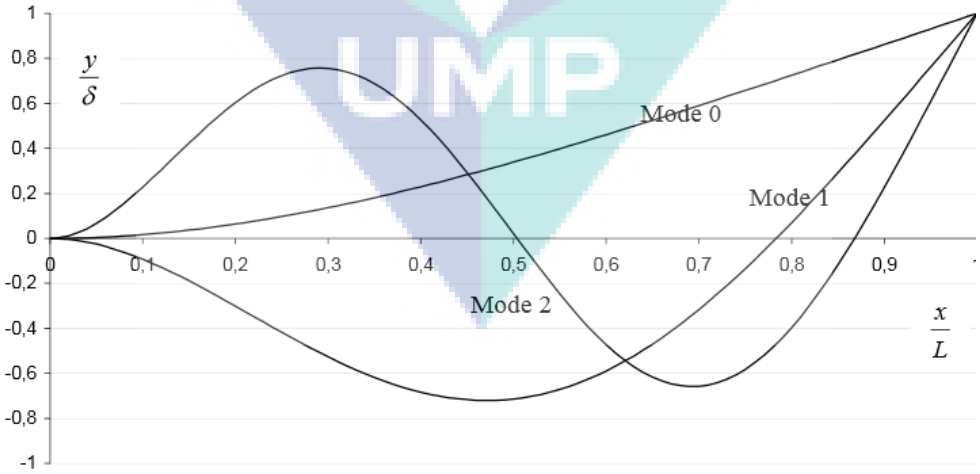

Figure 4.19: The first three natural modes of a simple beam.

A structure has in theory infinite number of natural modes. The vibration response can in fact be a superposition of response of different modes close to the excitation frequency.

In case of multiple pulsation excitation, the vibration response is the sum of the response of each excitation pulsation. In an assembly of pieces, the natural modes of the system is the result of complex coupling between all its sub-system.

Each mode behaves like a mass-spring system with one degree of freedom (DOF) Figure 4.20. Consider the mass spring system with m the mass, k the spring stiffness and c the structural

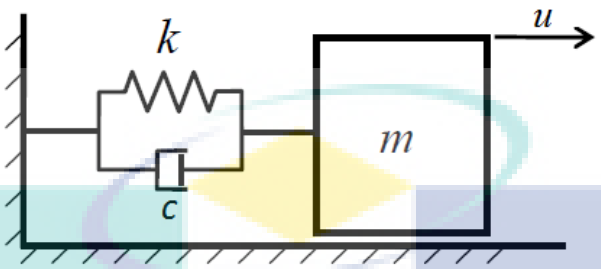

Figure 4.20: Vibration system with one degree of freedom.

damping, excited by a harmonic oscillator with the force $F = F_0 e^{j\omega t}$ in the direction $\vec{u}$. According to the Newton second law, the dynamic of the system can be written as:

$$m\ddot{u} + c\dot{u} + ku = F_0 e^{j\omega t} \tag{4.36}$$

With $u = Ue^{(j\omega t - \varphi)}$ the displacement, $\omega_0 = \sqrt{\frac{k}{m}}$ the natural pulsation of the system, $\varepsilon = \frac{c}{c_c}$ the reduced damping, $c_c = 2\sqrt{km}$ the critical damping, $\xi = \frac{\omega}{\omega_0}$ the reduced pulsation, and by resolving the above equation (Equation 4.36), we obtain the transfer function of the system relating the displacement and the excitation force:

$$H(\omega) = \frac{1}{1 - \xi^2 + 2j\varepsilon\xi} \tag{4.37}$$

Using the function Equation 4.37, the dynamic deflection can be obtained. The resonance occurs if and only if the spatial order of the force oscillation and the modal number of the structure match.

We have now seen the basic of modal and frequency response analysis. By extension, the vibro-acoustic study of a machine has the same steps, except the mechanical structure is more complex than a beam. The structure studied for vibration is mainly the stator core. The mode shapes are therefore bi-dimensional, with a circumferential and axial modes similar to a hollow cylinder. These modes are usually noted as the pair (i, j) and the first modes are shown in Figure 4.21.

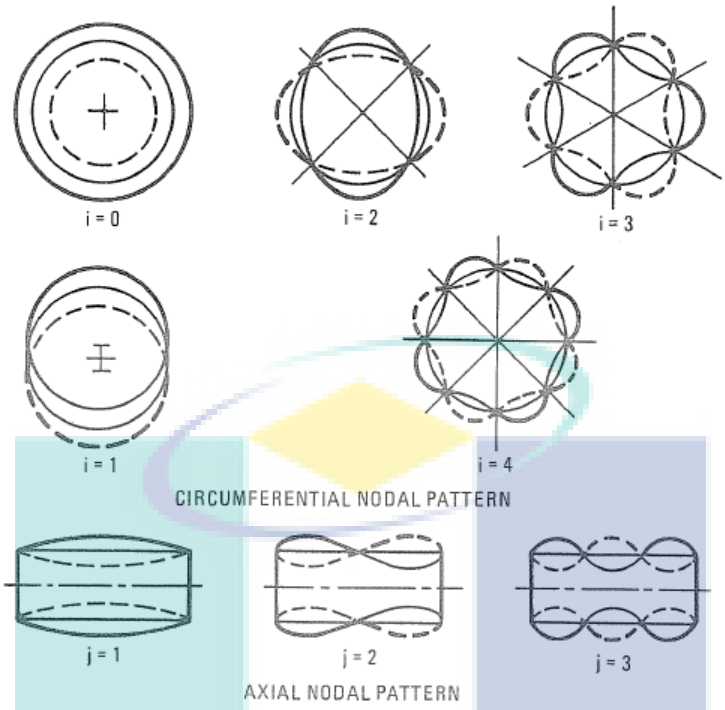

Figure 4.21: Natural mode shape pattern for a hollow cylinder structure [24].

In modal theory and free-free condition, having an electromagnetic forces excitation originated from a rotating magnetic field, the resonance in an electric machine structure occurs in two conditions, if and only if:

1. The spatial order of the magnetic pressure oscillation and the mode order of the structure match ($m = i$).

2. The electrical frequency and the natural frequency of the structure's mode match ($f_{elec} = f_i$).

In practical, the presence of excentricity can produce different results. A force with a specific spatial order can excite a resonance with different spatial order [30].

We can note that in case of non-skewed machine, as the magnetic pressure is usually considered independent of the machine axial direction , therefore deformations in axial direction are hardly observable. Therefore, many has adopted a 2D-ring structure studies in the case of such electric machine. We have however adopted a 3D structure as it offers a possibilty of studying the effect of forces at the extremities of the core in the future.

4.2.2 Vibro-acoustic evaluation of the Syncrel motor

In order to evaluate the vibro-acoustic behavior of our prototype Syncrel machine, a numerical tool that was developed internally and validated will be primarily used, followed by comparison with experimental results.

The magnetic-mechanical-coupled numerical tool was developed by Hallal under the project AVELEC with the collaboration of various industrial partners (Cedrat, Renault and Vibratec) [22]. Diagram in Figure 4.22 shows the magnetic-mechanical coupling tool. The magnetic model uses the Cedrat's FLUX2D [25], mechanical model uses MSC-Nastran

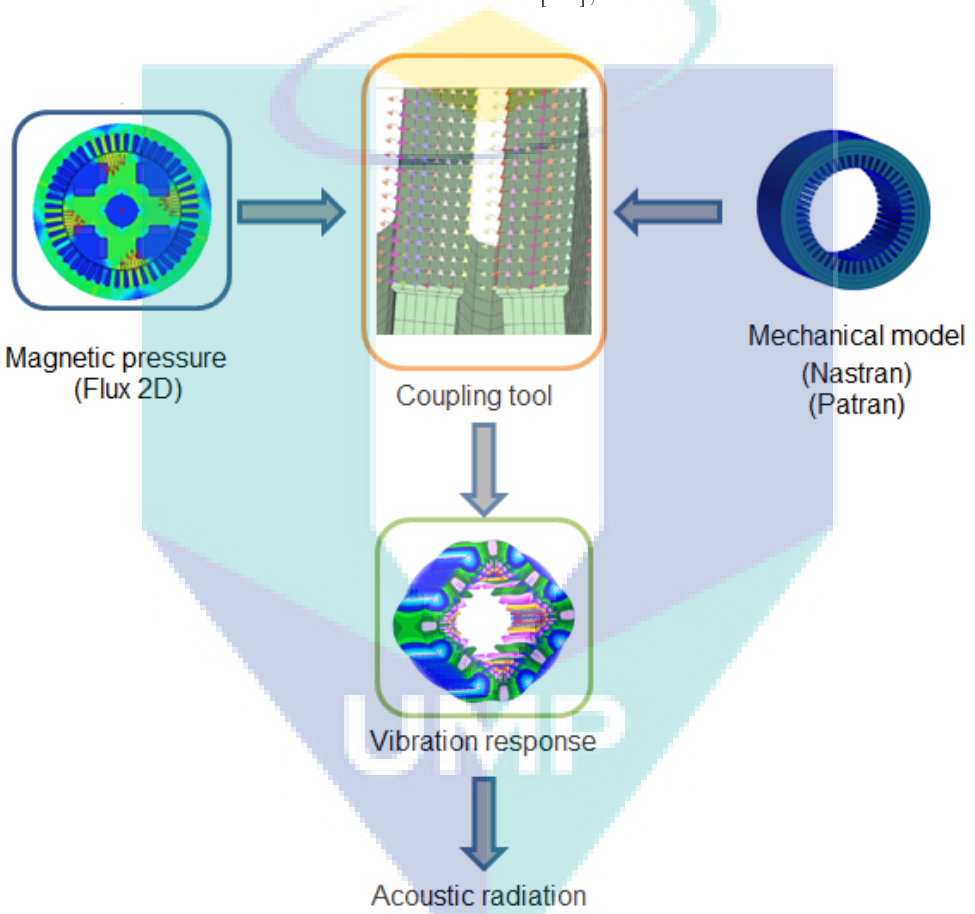

Figure 4.22: The magnetic-mechanical-coupled numerical tool developed by Pellerey and Hallal in [22, 23].

[26] and the coupling tool was developed using Matlab [27]. It is a weak-coupling tool which means that the mechanical deformation is considered to be small that it does not affect the magnetic behavior of the machine [2]. The magnetic model exploited is the same model that was used in previous studies (left of Figure 4.23). The mechanical model is a

[2]This hypothesis is acceptable because the deformation order of magnitude of 10^{-6}m accounts for less then 1% of the airgap. The magnetic behavior (flux linkage and saturation) can be considered unchanged.

3D finite element model representing the whole stator core with 38880 H8 elements (right of Figure 4.23).

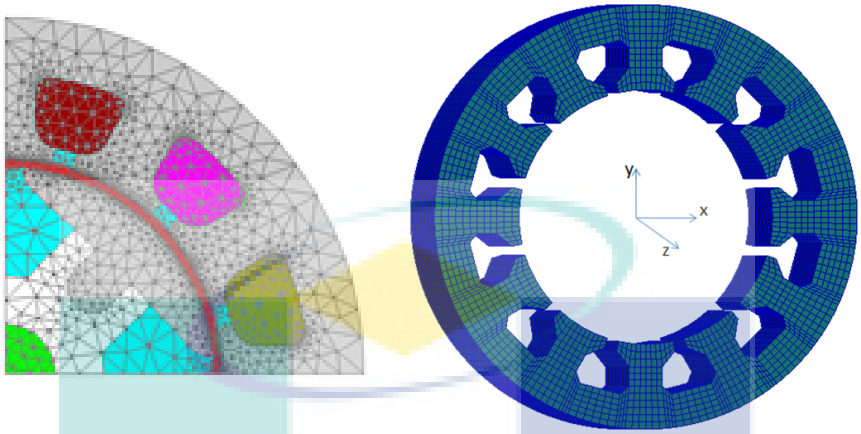

Figure 4.23: Left: The magnetic model ; Right: The mechanical model.

Several hypothesis were made in construction and utilization of both models. For the magnetic model, the current fed is purely sinusoidal. The magnetic pressure is computed in the middle of the airgap. Due to symmetry, only one pole of the machine is modeled. For mechanical model, the winding is not considered for first estimation. This is a reasonable approach regarding the fact that the winding is hanging loose in the slot, the filling factor is low and the slot is not filled with resin infiltration. Consequently, the winding would have very little impact on the overall structure natural frequency. The teeth and the stator yoke are considered as one solid piece making the stator core (the lamination stacking is not considered).

The resulting vibrations in acceleration computed by the numerical tools are going to be compared to acoustic experimental results. The vibration and the acoustic radiation are certainly two different physical quantities. However, knowing that what interests us is the acoustic aspect of the machine assembly, validation using the experimental acoustic spectrum on the basis of frequency comparison is sufficient. This validation using frequency comparison is valid because the frequency should be identical in both cases (vibration and acoustic). The amplitude of the noise can differ depending on the medium of transmission, but no new frequency are created [28].

4.2.2.1 Magnetic pressure computation

With all the hypothesis mentioned previously, the magnetic model is run with the machine following a certain torque-speed profile. Here is an example presented in Figure 4.24, the

radial and tangential magnetic pressures in the airgap were computed at a constant speed and constant torque.

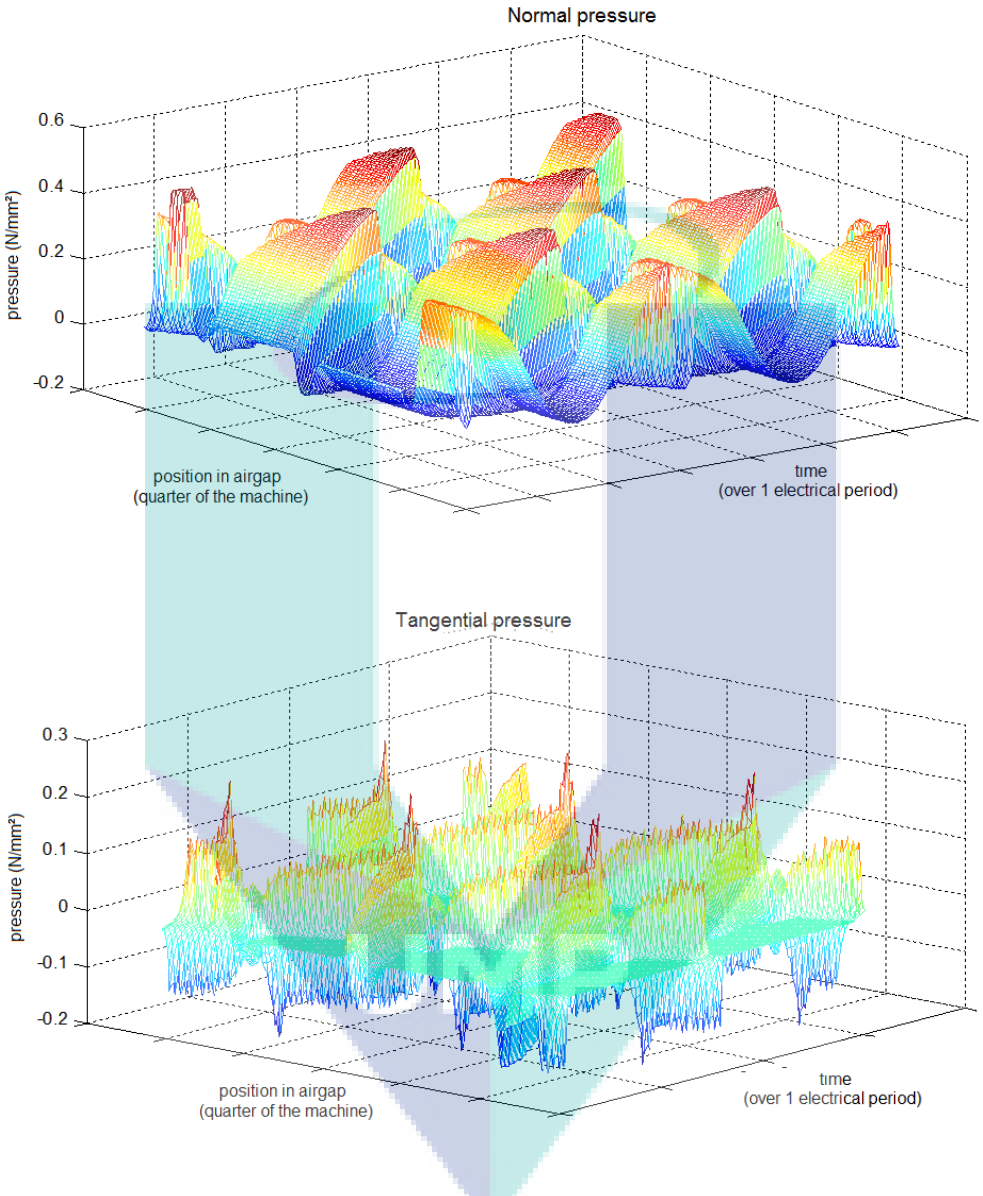

Figure 4.24: The radial (top) and tangential (bottom) magnetic pressures in function of angular position in the airgap and time. They are computed for a speed of 1000rpm and at maximum application current, 50A.

In comparison to usual synchronous machine such as the wounded-rotor synchronous machine (WRSM) studied by Pellerey and Hallal in [22, 23] (Figure 4.25), the general pattern of the pressure repartition is similar as it repeats along a diagonal. The differences are only on the number of teeth per pole and the detail of pressure repartition on each tooth.

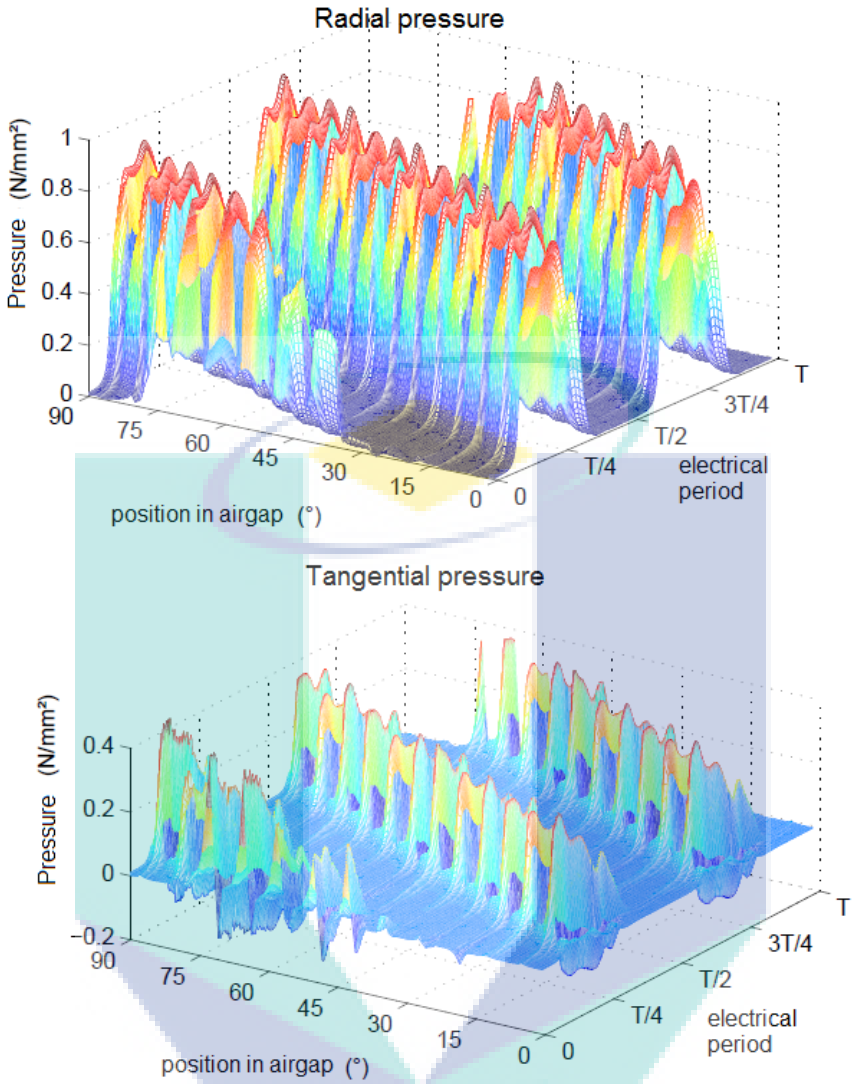

Figure 4.25: Magnetic pressure in WRSM studied by Pellerey and Hallal in [22, 23].

With the hypothesis that the saturation effect is minor, the same form of magnetic pressure surface should be observed at all operating points $\{\Gamma, N\}$. From a 2D-plane-projected surface (Figure 4.26), if we look at the pressure along the position in the airgap, we can note the effect of three stator teeth in one pole, on both radial and tangential pressure. Also, if we look at the electrical period axis, we can note two rotor poles effect on the pressure. Additionally a constant zone of low pressure independent of time that can be attributed to the slot opening can also be observed. Higher pressure zones appear on the side of rotor segments where high flux density occurs. The tangential pressure occurs mainly on the extremities of the teeth and it is less important than the radial pressure.

With the pressure surface obtained, harmonic content of the magnetic pressure can be studied, both in terms of spatial harmonic and time harmonic (spatio-temporal). To do so,

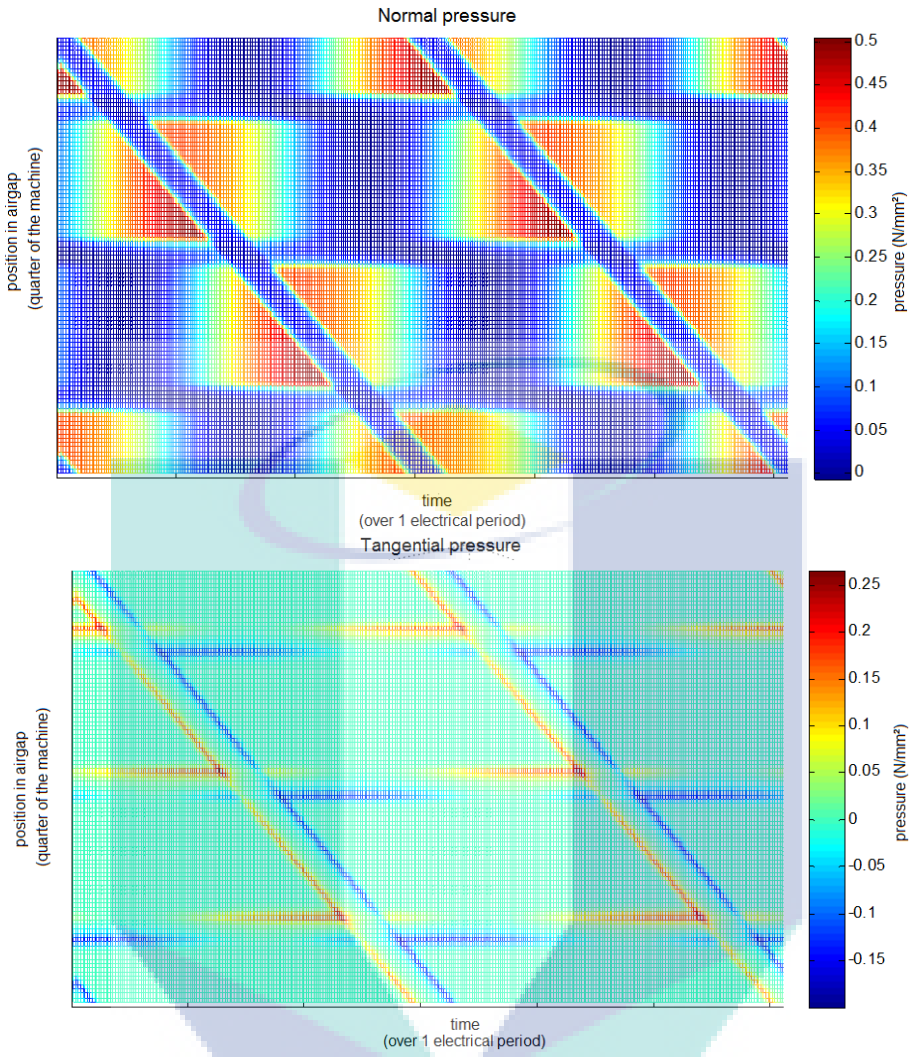

Figure 4.26: The radial (top) and tangential (bottom) magnetic pressure in a 2D plane view.

the spatio-temporal bi-dimensional harmonic content analysis can be done using the Fourier transformation on the magnetic pressure presented in Figure 4.24. We obtained as result the pressure spectrum on the spatio-temporal as shown in Figure 4.27. $\{m, n\}$ represent the pair of space order and time rank of the pressure. Every square represents a harmonic component of $\{m, n\}$ coordinate of the spatio-temporal plane.

In reference to theory (Pellerey formulation [23]), it represents the values $\sigma_{m,n}^{r,t}$ of the Equation 4.35 presented earlier in theoretical generalities. Time harmonic is related to the current supply generating the rotating field, therefore the time harmonic rank n of the magnetic pressure is a multiple of the electric frequency (which is also a multiple of mechanical

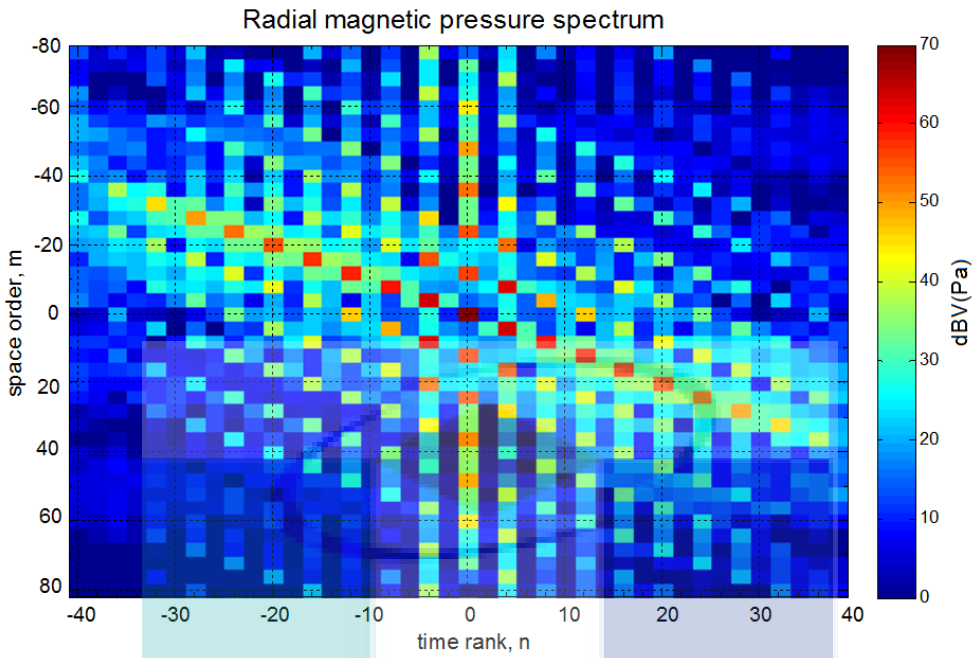

Figure 4.27: The radial magnetic pressure bi-dimensional harmonic content analysis.

speed Ω with a coefficient p). It can be written as Equation 4.38 [13].

$$n.\Omega = 2.k.p\Omega, \ k \in \mathbb{N} \tag{4.38}$$

The spatial harmonic rank m on the other hand is a multiple of the pole number $2p$ and also modulated around the number of stator teeth Z_s at the same time. This harmonic is also called as slotting harmonics as it is related to the teeth and slot number. It can be written as Equation 4.39 [13].

$$m\theta = (l.Z_s \pm 2k.p).\theta, \ \{k, l\} \in \mathbb{N} \tag{4.39}$$

By taking into account both harmonic content, the pair of rank $\{m, n\}$ where high magnetic pressure occur can be positioned at:

$$\{m, n\} = \{l.Z_s \pm 2k.p, \ 2.kp\} \tag{4.40}$$

As $Z_s = 12$, we can note in Equation 4.40 that regardless the values taken for k and l, all ranks time and space are multiples of $2p$.

On our computed pressure spectrum (Figure 4.27), $\{m, n\}$ pairs in Equation 4.40 can be found and verified to generate high pressure. We can remark that the patterns are symmetrical where $\sigma^{r,t}_{-m,-n} = \sigma^{r,t}_{m,n}$. The pressure is especially high for lower m and n. The diagonal formation shows that there are modulations between the space and time harmonics

related to the number of poles and the number of teeth. This is expressed in Equation 4.40 by the dependance of both ranks m and n on the same coefficient k. Pellerey in [13] called this the 'teeth modulation harmonics'. Besides, we can see that a time rank can have different space order that generate high pressure. Table 4.2 shows the first important spatio-temporal ranks of our Syncrel machine deduced from Equation 4.40.

l	0			1		
k	0	1	2	0	1	2
m	0	± 4	± 8	12	12 ± 4	24 ± 8
n	0	± 4	± 8	0	± 4	± 8

Table 4.2: First $\{m, n\}$ ranks that produce important magnetic pressure. They are calculated using Equation 4.40 with $p = 2$ and $Z_s = 12$

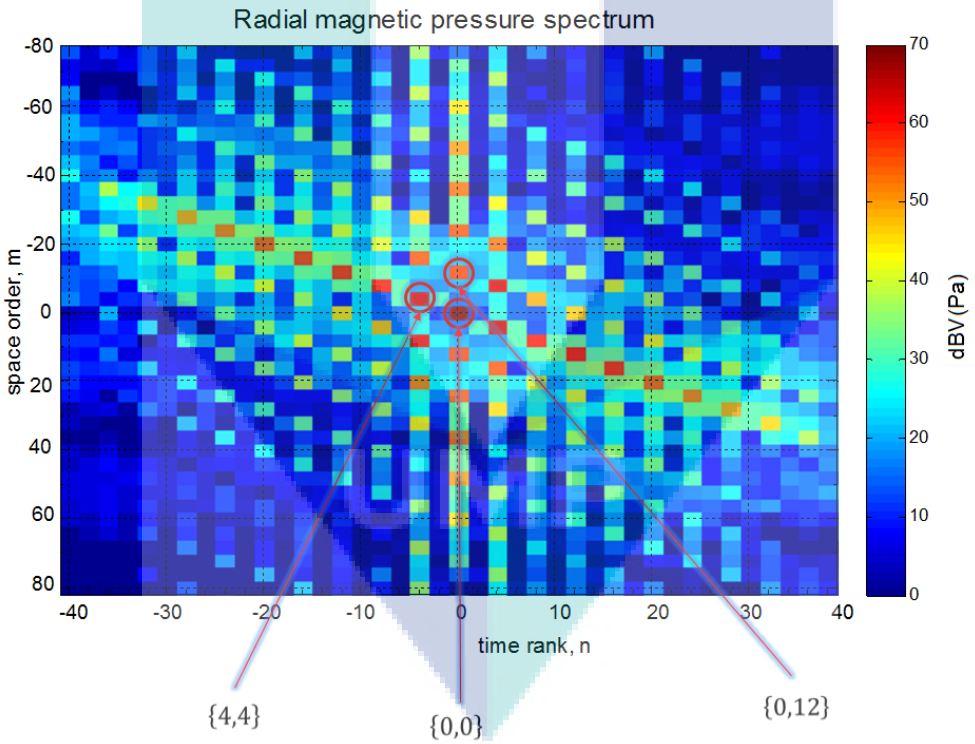

Figure 4.28: $\{m, n\}$=$\{0, 0\}, \{4, 4\}$ identified on a quarter of the radial magnetic pressure spectrum.

Among these $\{m, n\}$ pairs, we can easily identify the $\{m, n\}$=$\{0, 0\}, \{4, 4\}$ the influence of the stator teeth at $\{m, n\}$=$\{12, 0\}$ on Figure 4.28.

The computed pressure is going to be affected later onto the stator mechanical structure to deduce the vibration response. We remind that resonance will be observed when the time

rank of an important pressure coincides with the structure natural frequency, and the space order also coincides with the deformation mode.

4.2.2.2 Modal analysis

In the meantime, for the mechanical structure characterization, the modal analysis using the FE model gives the natural mode shape and frequency of the nine first mode shown in Figure 4.29. An impact test was done on the stator core alone. The trend on the natural frequencies has been validated.

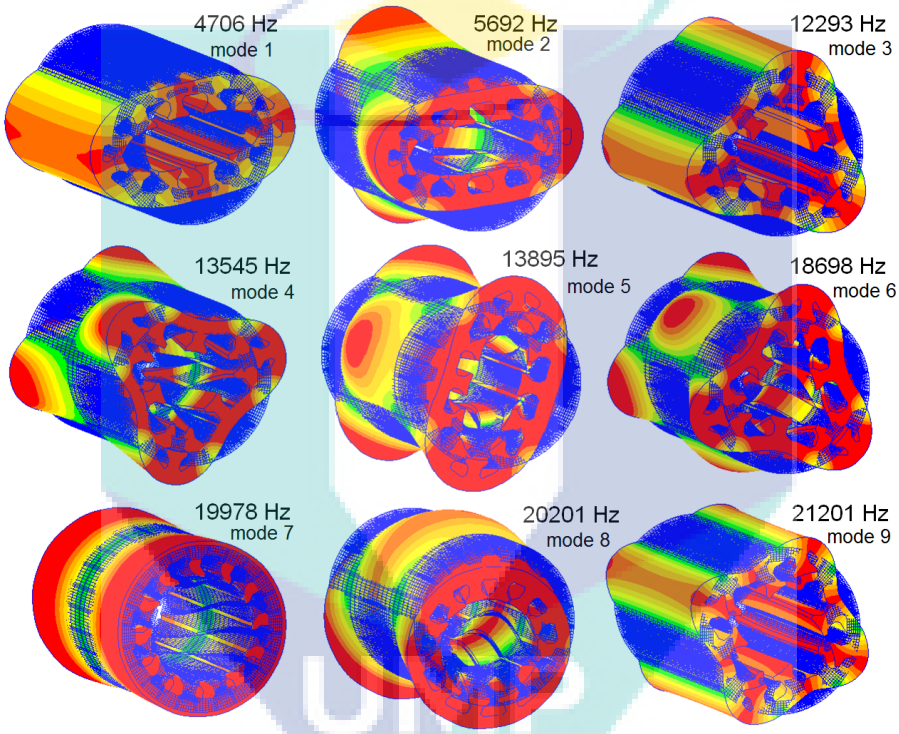

Figure 4.29: The first natural mode of the stator found using FE analysis.

Taking into account the magnetic pressure analysis previously, the ranks m that are very likely to be solicited are 0 and multiples of $2p$. Among the mode presented in Figure 4.29, the seventh and ninth mode which are radial order 0 and 4 are likely to be solicited. In a non-skewed machine, the independence of the magnetic pressure from the machine axial direction means that deflection may not be observed theoretically. Nonetheless, as the seventh, eighth and ninth mode are very close, mode appropriation can occur. Mode appropriation means the operational deformation shape can take the form of the three deformation modes when an excitation force is close the natural frequencies of the three natural mode.

The modal analysis results in this section will be used later to explain the computed vibration response (and the acoustic experimental results).

4.2.2.3 Response in operational condition

Following the magnetic pressure computation and modal analysis of the stator core structure, the magnetic pressures are later applied to the mechanical model and the acceleration spectrum can be computed. The mechanical structure was loaded with both radial and tangential magnetic pressures.

A simulation of the machine on the test bench accelerating with no load on (with only test bench resistance torque = 0.01N.m) was done. The current fed to the machine is purely sinusoidal. A spectrogram response of the machine acceleration was traced from the simulation results in Figure 4.30.

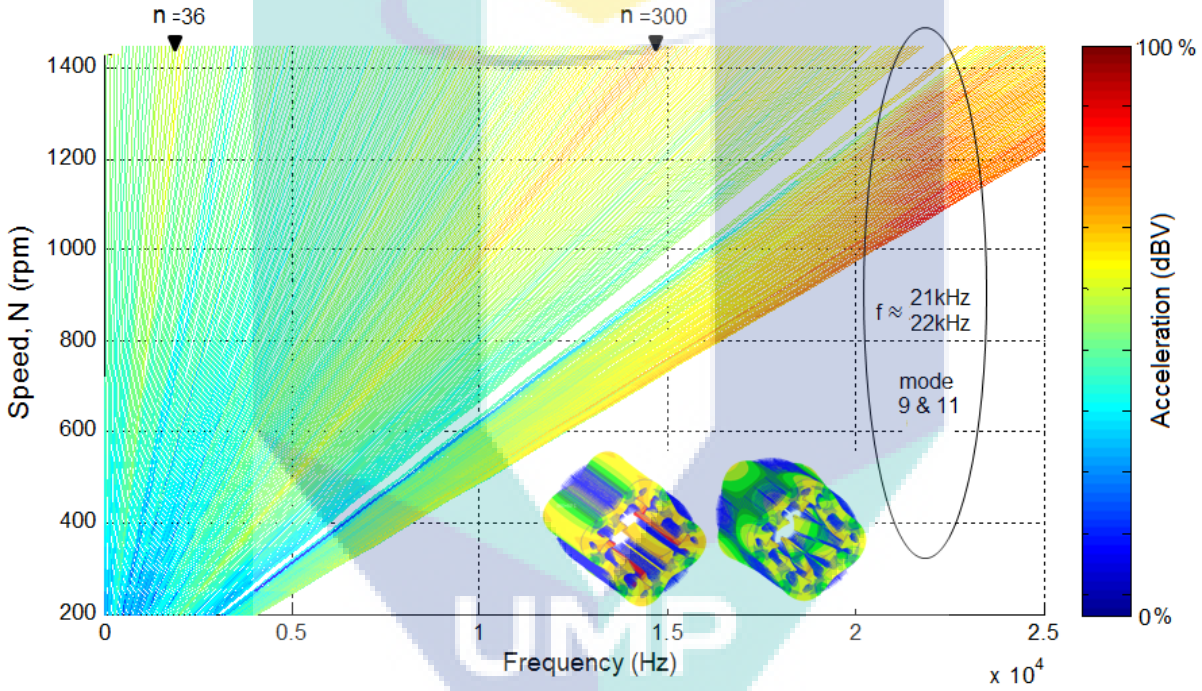

Figure 4.30: Simulated spectrogram of acceleration using FE tools.

We observe a high vibration between 21kHz and 23kHz which means that natural modes were excited. There are in fact the ninth and eleventh mode which are of order 4 at 21.2kHz and 22.4kHz. Otherwise, in general that excitation lines becomes more and more important in intensity as the speed increases. Certain excitation lines such as $n = (36, 300)$ are slightly more highlighted in their areas. At a higher speed, having the excitations $n = (36, 300)$ at around 21kHz and 22kHz can produce resonance, if and only if they can excite the same radial 4 spatial mode. For a resonance to occur, the time rank 36 and 300 need to have a spatial mode of either 0 or 4. For example, using Equation 4.38 and Equation 4.38:

For $n = 36$

$2kp = 36 \Rightarrow k = 9$

Thus, knowing that $m = l.Z_s \pm 2kp$

$\Rightarrow m = 12l \pm 36$

We can see that for $l = 3$, m can takes the value of 0. Therefore, the pair $\{m, n\}$=$\{0, 36\}$ can generates resonance if it attains the frequency around 22kHz. However, this resonance will only occur at an extremly high speed, around 18,000rpm which is not in our operating area. As for the time rank $n = 300$, it cannot have a spatial mode of neither 0 nor 4.

After having seen main operating vibration phenomena at variable speed, we now want evaluate the impact of the magnetic pressure intensity variation on the vibration. For that, two simulation were done where the motor was operated at two different current levels (one with a current corresponding to the test-bench no-load operating current, and another one with maximum operating current), at a single speed of 1000rpm. The resulting spectrum is traced in Figure 4.31.

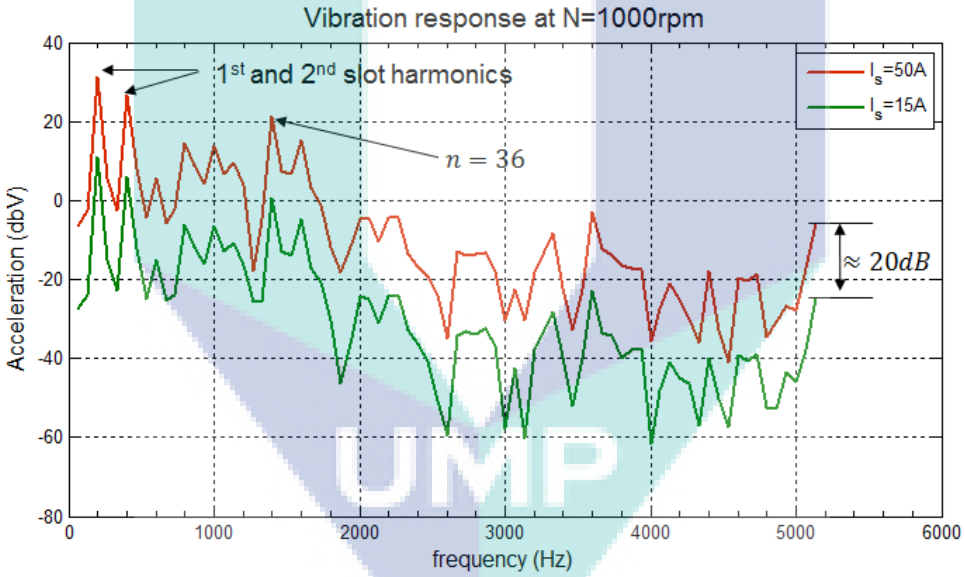

Figure 4.31: Vibration spectrum simulated at a speed of 1000rpm, at two current levels.

It was traced only up to 5kHz just to observe the trend. The observation on line $n = 36$ made previously for spectogramm in Figure 4.30 can be identified. With a smaller frequency scale, we can also see the vibration generated by first and second ranks of slot harmonics. With a magnetic pressure increase thanks to the currrent rise from 15A to 50A, the vibration has increased by nearly 20dB, which is considerable. By taking into account the acoustic propagation, the same increase in sound pressure can be expected up to some extent. Therefore, as the fundamental current increases, high intensity noise can be expected in the machine.

4.2.2.4 Experimental validations and discussion

In order to validate the operational vibration response computed, a series of experiments were done. The sound pressure of the prototype machine is registered using a setup of microphone and its conditioning amplifier, connected to an oscilloscope for data visualization and data logging Figure 4.32.

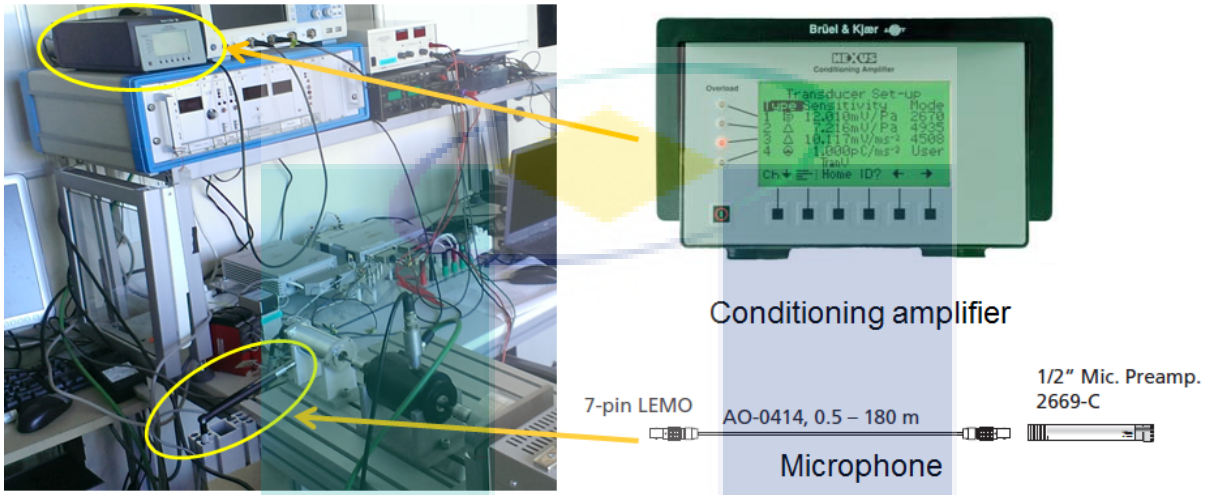

Figure 4.32: The microphone installed on the test bench with it's conditioning amplifier.

The microphone is positioned in a very close field. An enclosure with a microphone insert, built using acoustic foam is placed around the machine during the test to reduce ambient noises. We are aware that the standard acoustic measurement positions the microphone at 1 meter from the vibration source in an anechoic chamber. However, here, we are not interested in doing a standard acoustic measurement. What we want is a spectrum that allows a qualitative comparison between computed vibration and experimental acoustic spectrum.

The first experiments were done on constant single speed. The objectif is to observe the major lines found in computation results (Figure 4.30, done at 1000rpm). For comparison, one experiment with no-load and another experiment with load were done. The spectrums can be seen in Figure 4.33.

Several observations can be made on the spectrum comparison between Figure 4.31 and Figure 4.33:

1. We can remark the same family lines generated by the PWM around the chopping frequency of 20kHz in Figure 4.33 independant of the fundamental stator current. These lines do not exist in a motor sinusoidally fed (such as in simulations). The PWM harmonics can play important role in vibration of a machine as its have a spatial order of 0 or $2p$, or combination between slotting and PWM harmonics [14, 31]. Knowing

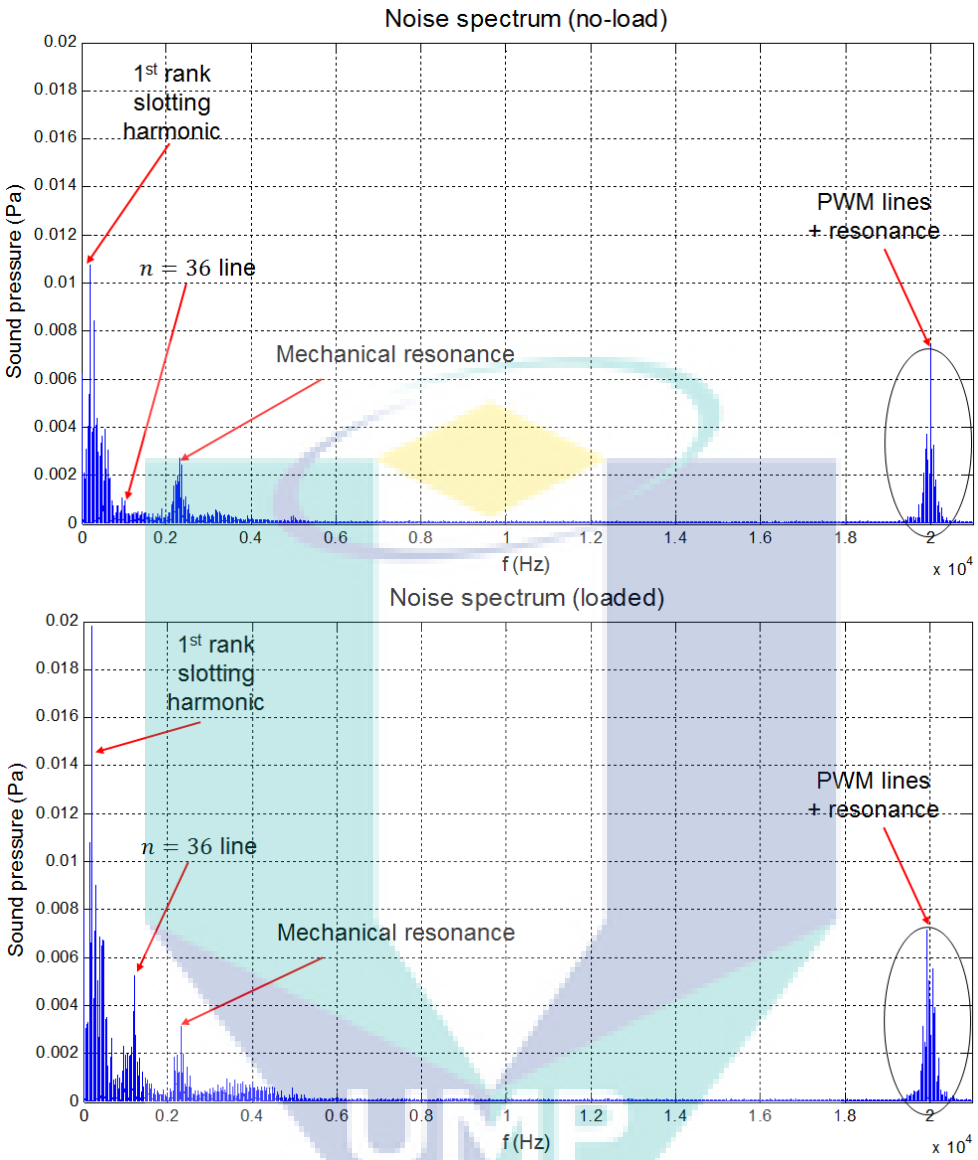

Figure 4.33: The acoustic spectrums at N=1000rpm. Top: no-load (stator phase current $I_s = 9.5A$). Bottom: loaded by the brake (stator phase current $I_s = 13.3A$)

that three natural modes of the spatial order of 0 and 4 are situated around 20kHz (seventh, ninth and eleventh mode), we deduce that the high sound pressure around the chopping frequency is caused by mechanical resonance, excited by the PWM lines. This can be confirmed later.

2. The highest line in both experiments is situated at 12 times the mechanical frequency ($f = 12 \times f_{mech}$) . This corresponds to the slotting harmonics. As the current increases, the lines intensity increases accordingly. In both spectrum, there are multiples lines with the frequency of $n \pm k_{ecc}$, $k_{ecc} \in \mathbb{N}$ forming a family of lines around the major line

which can be explained by the eccentricity in the machine.[14].

3. The $n = 36$ excitation line that was identified in simulation results can be clearly seen in Figure 4.33. An increase on current results in important magnetic pressure increase, thus sound pressure. It is the principal excitation line observed in our machine.

4. A mechanical resonance was observed in both non-loaded and loaded experimental spectrums at a frequency of 2.266 kHz, excited by $n = 68$ line (Figure 4.33). This natural frequency was not found in modal analysis on stator alone done previously. In terms of acoustic intensity, we can observe that despite the current increase when the machine was loaded, the intensity of the line barely increases. This can be explained by the high rank excitation that has low magnetic pressure.

Later, the acoustic variation is evaluated at variable speed. A speed-up operational sound pressure were registered with no load. The spectrogram of the noise registered can be seen in Figure 4.34. The spectrogram is comparable to the computed spectrogram in Figure 4.30.

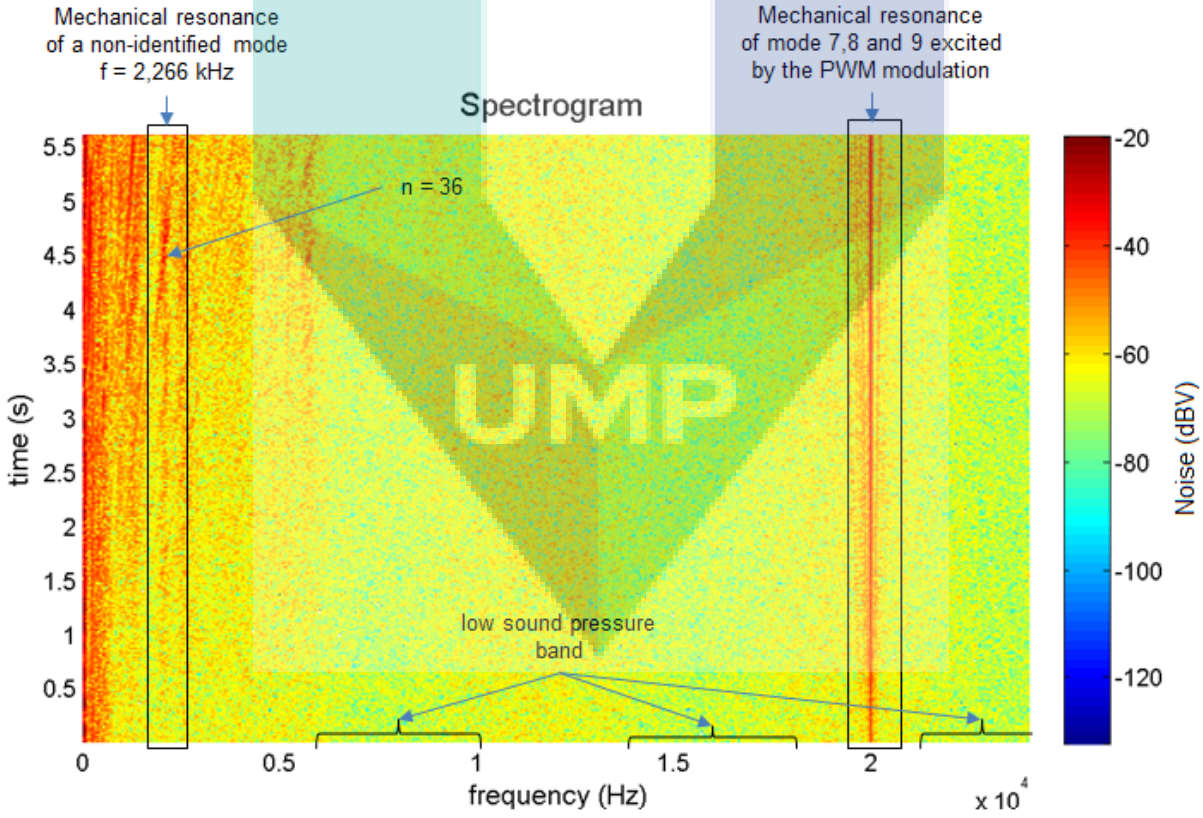

Figure 4.34: The experimental spectrogram of noise for the machine in constant acceleration.

First of all, we observe a high level of sound pressure independent of the machine's

speed at lower frequency, less than 6kHz. Like in previous explanation for Figure 4.33, among the lines, there are the first ranks of slotting harmonics. Others can be attributed to mechanical vibration of the different sources on the test bench (mechanical and magnetic due to excentricity). The excitation lines of $n = 36$ that have been identified in simulation results in Figure 4.30 can be seen exciting the non-identified mode, producing a localized resonance. The resonance is relatively localized at a speed around 1890rpm. We also observe zones of lower sound pressure in green band which can be identified as zones with no natural mode was identified (Figure 4.29).

We can note that due to PWM current harmonics, very important lines appear centered around $f = 20$kHz . In fact, the current harmonics does not excite new modes, but only adds new forces [29]. This results in lines modulated by the PWM chopping frequency and the current fundamental frequency. Particularly for a saw-tooth carrier, the PWM current harmonics are centered around the switching frequencies at $f_c \pm f_{elec}$ and $f_c \pm 3f_{elec}$. These harmonics can be seen as lines originating from f_c at zero speed and diverge as the speed increase.

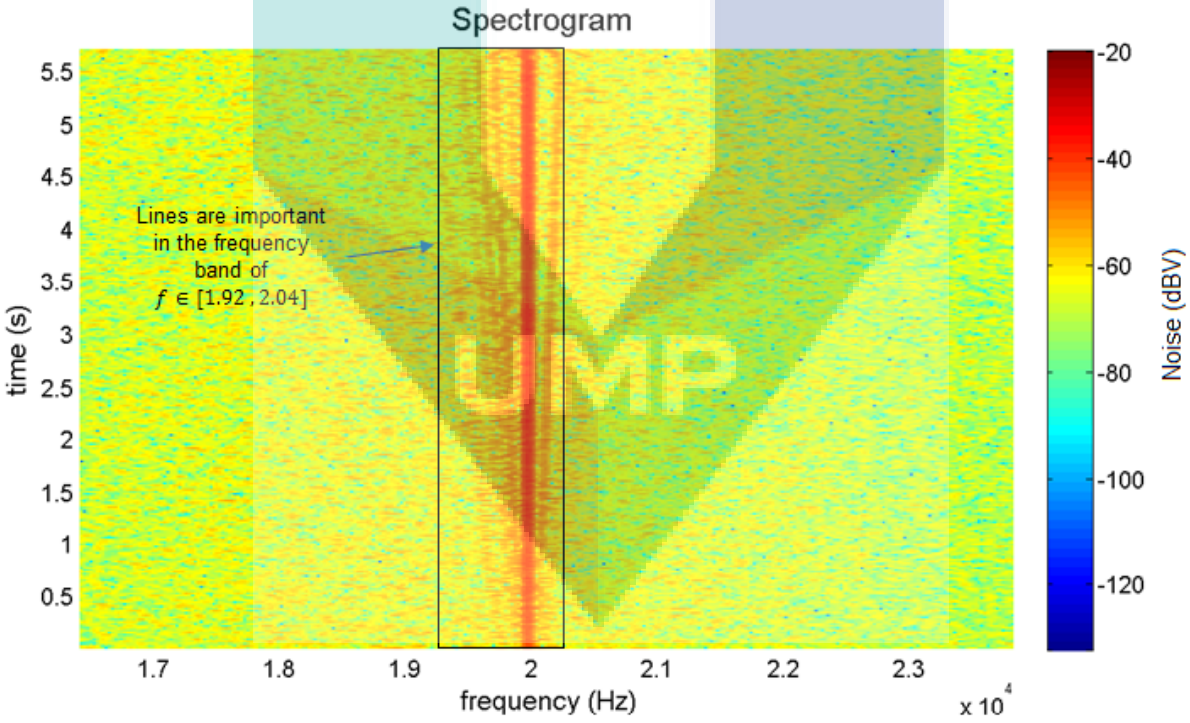

Figure 4.35: The zoom of Figure 4.34 around the PWM chopping frequency.

Interestingly, we remark that in the zoomed experimental spectrogram (Figure 4.35), the line at 20kHz is extremely important and there are slightly more noise in the lower side of the PWM frequency. It can be deduced that resonance not only occur at 20kHz, but also

in the frequency band ranging form $f \in [1.92, 2.04]$kHz. Consequently, we can say that several natural modes such as the seventh, eighth, ninth, and eleventh modes are located in that frequency band and modes appropriation could occur. In comparison to modal analysis results found in Figure 4.29, the natural frequencies of these experimental are a little lower. This can be explained by higher mass and lower rigidity of the prototype structure.

To confirm that the resonances really in fact happened, the PWM chopping frequency was changed into different values to observe the sound pressure variation. Figure 4.36 shows two spectrogram of the machine operating at the same condition as before except for the PWM switching frequency that has been changed. In both $f_c = 19$kHz and $f_c = 21$kHz, the PWM

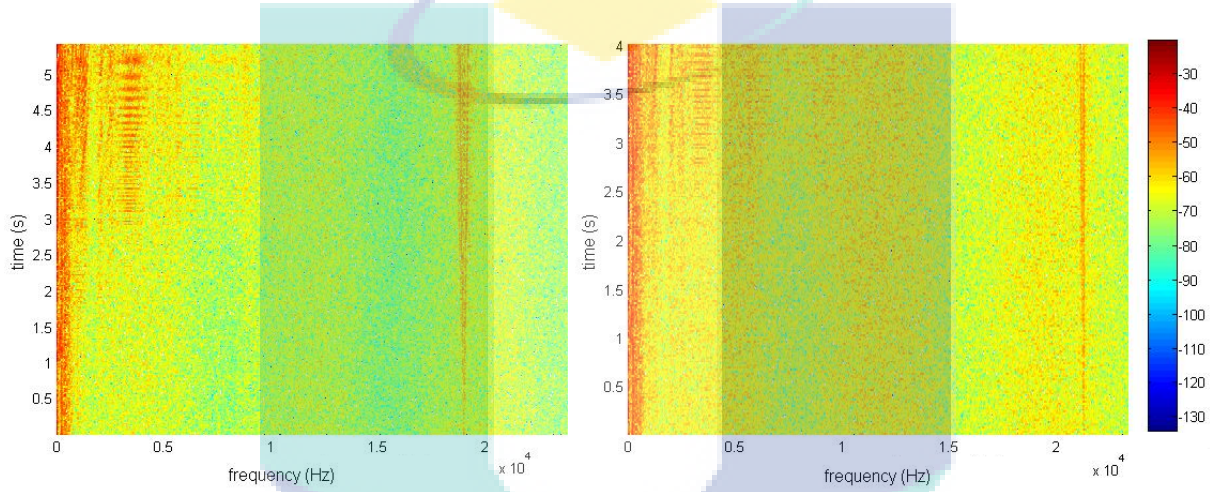

Figure 4.36: Two spectrogram with different PWM switching frequency. Left: $f_c = 19$kHz, Right: $f_c = 21$kHz.

lines has far less intensity of noises compared to the one with $f_c = 20$kHz. This confirms that resonance has effectively occured very close to the switching frequency of 20kHz. It can then be concluded that a natural mode of order either 0 or 4 is located very close to 20kHz.

Having observed all these phenomena, the FE analysis of the vibro-acoustic behavior of the machine can be validated. Resonances have been observed in simulation and identified experimentally to occur at higher frequency (around 20kHz) at lower current. At this high frequency, the resonance is excited by the PMW. This high natural frequencies are expected for a small machine as the natural frequency is proportional to $\sqrt{\frac{k}{m}}$.

Even if the resonance was shown to occcur around 20kHz which is a non-audible frequency, it is important to remind that an increase of vibration around 20dB between no-load and maximum current operation was predicted by simulation. Therefore, as the fundamental current increases, the machine can generates high intensity noise accross the audible frequency bandwith.

4.2.3 Conclusion and perspectives

The concern of physio-acoustic comfort for automotive application has lead us to evaluate the vibro-acoustic behavior of the Syncrel machine. Only electromagnetic originated forces were studied. The theoretical generalities on electromagnetic forces modeling and vibration modeling of electrical machine were presented at the begining of this chapter.

In this study, the magnetic-mechanical-coupled numerical tool developed by Pellerey and Hallal in [22, 23] were used. The magnetic pressure was computed and was shown to have classic pattern as in other synchronous machines.

Experimentally, independent of the fundamental stator current, important pressure has been observed originating from the PWM chopping harmonics around 20kHz. At the same time, it happened that several natural modes of order of zero and four close to 20kHz were shown in modal analysis. This results in confirmation of resonances. They are however physio-acousticly harmless as it is out of the audible bandwidth. If needed though, the chopping frequency can be moved away from the natural modes frequency. Operating vibration response simulation has been shown to be coherent with the experimental observation. Meanwhile, an increase of vibration around 20dB between no-load and maximum current operation was also predicted. Therefore, as the fundamental current increases, high intensity noise can be observed in the machine, which is usually expected in this type of motor.

In near perspective, a more realistic speed-torque profile that corresponds to the application can be simulated and experimentally done to evaluate the application-operating noise. In farther perspective, in terms of multiphysical interaction with the machine thermal behavior, the influence of temperature on the vibration can be studied by coupling the thermal model and the vibro-acoustic model. In reference to literature, Tan-Kim in [32] has shown that temperature increase results in noise reduction. He observed the increase of modal damping as well as a slight decrease of natural frequencies. These were mainly explained by the decrease of the windings rigidity (Young modulus). However, regarding our prototype machine, as the filling factor is low, variation in the winding rigidity would unlikely change the stator modal characteristic. Besides, we have shown that the vibrational behavior of the Syncrel machine can be modeled without taking into account the windings.

Bibliography

[1] Sanada, M.; Hiramoto, K.; Morimoto, S. & Takeda, Y. Torque ripple improvement for synchronous reluctance motor using an asymmetric flux barrier arrangement Industry Applications, IEEE Transactions on, 2004, 40, 1076-1082 130, 142

[2] Nashiki, M.; Satake, A.; Kawai, Y.; Yokochi, T. & Okuma, S. A new flux-barrier-type reluctance motor with a slit rotor Industrial Electronics, IEEE Transactions on, 1999, 46, 1199-1206 142, 145

[3] Nashiki, M.; Satake, A.; Kawai, Y.; Yokochi, T. & Okuma, S. Torque Ripple Reduction of Reluctance Motor with Slit Rotor IEEJ Transactions on Industry Applications, 1997, 117, 1008-1014 145

[4] Bomela, X. & Kamper, M. Effect of stator chording and rotor skewing on performance of reluctance synchronous machine Industry Applications, IEEE Transactions on, 2002, 38, 91-100 146

[5] Fratta, A.; Troglia, G.; Vagati, A. & Villata, F. Evaluation of torque ripple in high performance synchronous reluctance machines Industry Applications Society Annual Meeting, 1993., Conference Record of the 1993 IEEE, 1993, 163-170 vol.1 130, 131, 132, 133, 137

[6] Vagati, A.; Pastorelli, M.; Francheschini, G. & Petrache, S. Design of low-torque-ripple synchronous reluctance motors Industry Applications, IEEE Transactions on, 1998, 34, 758-765 130, 146

[7] Bianchi, N.; Degano, M. & Fornasiero, E. Sensitivity Analysis of Torque Ripple Reduction of Synchronous Reluctance and Interior PM Motors Industry Applications, IEEE Transactions on, 2015, 51, 187-195 130, 145

[8] Bianchi, N.; Bolognani, S.; Bon, D. & Dai Pre, M. Torque Harmonic Compensation in a Synchronous Reluctance Motor Energy Conversion, IEEE Transactions on, 2008, 23, 466-473 145

[9] Chiba, A.; Nakamura, F.; Fukao, T. & Azizur Rahman, M. Inductances of cageless reluctance-synchronous machines having nonsinusoidal space distributions, Industry Applications, IEEE Transactions on, 1991, 27, 44-51 130

[10] Nicola Bianchi. Electrical machine analysis using finite elements. CRC Press, 2005. 130

[11] Sun, J.; Wang, S.; Kuang, Z. & Wu, H. Torque ripple comparison of short-pitched and fully-pitched winding switched reluctance machine Electrical Machines and Systems (ICEMS), 2012 15th International Conference on, 2012, 1-6 142

[12] International Electrotechnical Commission standard IEC 60034-9 (Rotating electrical machines - Part 9: Noise limits), Fourth edition, 2003 146

[13] Pellerey, P.; Lanfranchi, V. & Friedrich, G. Coupled Numerical Simulation Between Electromagnetic and Structural Models. Influence of the Supply Harmonics for Synchronous Machine Vibrations Magnetics, IEEE Transactions on, 2012, 48, 983-986 146, 160, 161

[14] Le Besnerais J. "Reduction of magnetic noise in PWM-supplied induction machines" , Ph.D. Thesis, Ecole Centrale de Lille, 2008. 146, 147, 165, 167

[15] Belmans, R., Verdyk, Geysen, and Findlay. Electro-mechanical analysis of the audible noise of an inverter-fed squirrel cage induction motor. IEEE Trans. on Ind. Appl. 27, 3 (May/June 1991). 147

[16] Garvey, S., and Glew, G. Magnetostrictive excitation of vibration in machines - a modal approach. In Proceedings of the 9th Int. Conf. Electrical Machines and Drives (1999). 147

[17] Delaere, K., Heylen, W., Belmans, R., and Hameyer, K. Comparison of induction machine stator vibration spectra induced by reluctance forces and magnetostriction. IEEE Trans. on Magnetics 38, 2 (Mar. 2002). 147

[18] Bobbio, S.; Delfino, F.; Girdinio, P.; Molfino, P., "Equivalent sources methods for the numerical evaluation of magnetic force with extension to nonlinear materials," in Magnetics, IEEE Transactions on , vol.36, no.4, pp.663-666, Jul 2000 148

[19] Ren, Z.; Cendes, Z., "Shell elements for the computation of magnetic forces," in Magnetics, IEEE Transactions on , vol.37, no.5, pp.3171-3174, Sep 2001 148

[20] Coulomb, J.l.; Meunier, G., "Finite element implementation of virtual work principle for magnetic or electric force and torque computation," in Magnetics, IEEE Transactions on , vol.20, no.5, pp.1894-1896, Sep 1984 148

[21] Amrhein, M.; Krein, P.T., "Force Calculation in 3-D Magnetic Equivalent Circuit 148

[22] Hallal J., “Études des vibrations d’origine électromagnétique d’une machine électrique : conception optimisée et variabilité du comportement vibratoire”, Ph.D. Thesis, Université de Technologie de Compiègne, 2014. 148, 155, 157, 158, 170

[23] P. Pellerey, “ Etude et optimisation du comportement vibro-acoustique des machines électriques, application au domaine automobile”, Ph.D. Thesis, Université de Technologie de Compiègne, 2012. 151, 155, 157, 158, 159, 170

[24] Blevins, R. D., “Formulas for Natural Frequency and Mode Shape” , Robert E. Kieger Publishing Company, New York, 1979. 154

[25] Cedrat, Guide d’utilisation Flux 11, Juillet 2012. 155

[26] MSC Nastran, Quick Reference Guide, 2012. 155

[27] MATLAB and Statistics Toolbox Release 2011b, The MathWorks, Inc., Natick, Massachusetts, Unites States. 155

[28] Norton, M. P. and D. G. Karczub. Fundamentals of Noise and Vibration Analysis for Engineers. 2nd ed. Cambridge: Cambridge University Press, 2003. 156

[29] Maliti, K. Modelling and analysis of magnetic noise in squirrel-cage induction motors. PhD thesis, Stockholm, 2000. 168

[30] Tan-Kim, A.; Lanfranchi, V.; Vivier, S.; Legranger, J.; Palleschi, F., "Vibro-acoustic simulation and optimization of a claw-pole alternator," in Energy Conversion Congress and Exposition (ECCE), 2015 IEEE, vol., no., pp.5227-5232, 20-24 Sept. 2015 154

[31] Lo, W., Chan, C., Zhu, Z., Xu, L., Howe, D., and Chau, K. Acoustic noise radiated by PWM- controlled induction machine drives. IEEE Trans. on Industrial Electronics 47, 4 (Aug. 2000). 165

[32] Tan-Kim, A.; Lanfranchi, V.; Legranger, J.; Palleschi, F.; Redon, M., "Influence of temperature on the vibro-acoustic behavior of claw-pole alternators," in Electrical Machines (ICEM), 2014 International Conference on , vol., no., pp.1628-1634, 2-5 Sept. 2014

170

Conclusion and perspectives

Conclusion

In an effort to electrify more functions in automotive application, severe requirements were set by manufacturers for electric motor candidates. The most constraining requirements include torque to volume ratio, thermal robustness and noise level without neglecting the cost and manufacturing feasibility. In previous study on electrical clutch actuator, the synchronous reluctance machine (Syncrel) with segmented rotor was selected, designed and a prototype was provided. In continuity to the study, this thesis aims to contribute to multiphysical evaluation of the Syncrel machine. The physics studied includes usual electro-mechanical performance, thermal and vibro-acoustic behavior.

The principles of operation of Syncrel machine has been presented at the beginning of second chapter. An analytical model capable of computing the operating area of a Syncrel machine in function of its power supply, direct and quadrature inductances and the control load angle was developed and validated experimentally. The operating area in function of load angle evaluation of the Syncrel machine shows that the machine has limited possibility of operating area extension due to its passive rotor. The influence of material non-linearity on the operating area was also studied. Besides, static torque delivery of the machine was evaluated, explained and a tool was proposed to help user attain optimum static torque. The next performance criteria studied was the power factor. Knowing the importance of temperature influence on the winding resistance, it was therefore not neglected as usually done in literature in power factor computation and evaluation. Influence and interaction between different parameters such as resistance, load angle and speed on the power factor were studied. Two abacus helping to predict the interaction between these parameters were developed. At the end, all the developed tools were used to compare three Syncrel machines with different rotor topologies. The comparison lead us to conclude that Syncrel with segmented rotor can be the best solution for such application.

The thermal behavior of the machine was studied and evaluated in the third chapter. A lumped parameter model of the machine was developed and validated experimentally.

Following the validation in accuracy and robustness of the model, a local sensitivity study was done. The result shows that in a small and compact machine as ours, the temperature rise can be mainly attributed to two parts: the exterior surface thermal resistance and the slot thermal resistance . A very interesting conclusion is that each of them contributes to elevation in different portion of the temperature curve: the exterior surface thermal resistance affects the last portion of the curve while the slot thermal resistance affects the early transient phase. This observation has lead to proposition of pertinent heat evacuation improvement and a gain evaluation tool following the proposed improvement. Finally, the model was used to evaluate the temperature rise of the machine in different cycles including the standard WLTP cycle in the context of electric clutch application. The prototype machine has been shown to be capable and suitable for this application in particular.

Finally, in the last chapter, the torque ripple and vibro-acoustic evaluation of the machine was done. The Syncrel machine with segmented rotor has been shown to have a high torque ripple. Two geometrical major parameters that affect the torque ripple identified were the length of slot opening and the non-magnetic segment of the rotor. The torque ripple improvement concentrated on these two parameters can therefore be done in the future. For vibro-acoustic evaluation, the magnetic-vibration-coupled numerical tool developed internally was used alongside experiments. Experimentally, independent of the fundamental stator current, important pressure has been observed originating from the PWM chopping harmonics around 20kHz. At the same time, it happened that the machine has several natural modes of order of zero and four close to 20kHz, which generates important resonances in consequence. These resonances are harmless physio-acousticly as it is out of the audible bandwidth. If needed though, the chopping frequency can be moved away from the natural modes frequency. Operating vibration response simulation has been shown to be coherent with the experimental observation. An increase of vibration around 20dB between no-load and maximum current operation was also predicted. Therefore, as the fundamental current increases, high intensity noise is expected in the machine.

At the end of this thesis, the Syncrel machine was not only evaluated multiphysically, but several propositions of improvement have also been made in each physic. A complete test bench was built and exploited for validation of models developed in this thesis. It is an important asset to the laboratory and should continue to serve for different test in the future. Most importantly, multiple tools were developed and tested. Their utilization can be extended to different machines for different applications and environment.

Perspectives

This thesis has contributed to a very large evaluation of the Syncrel machine. There are nonetheless research works that can be suggested to be carried out in the future to complete the presented studies. They can be grouped in following points:

1. Coupling the magnetic, electro-mechanical, thermal and vibro-acoustic model Figure 4.37: In this thesis, analytical model of electro-mechanical and thermal along with numerical model of magnetic and vibration was exploited. In chapter 2, the influence of temperature on the operating area and power factor was indirectly evaluated by means of resistance variation. An automated coupling tool between the electro-mechanical and thermal model will be made in near future. The influence of temperature on the vibrational behavior is also interesting too look into. This coupling will allow a better understanding of interactions between them, hence providing us with a more global view on modification that might occur in different physics following a variation of a parameter.

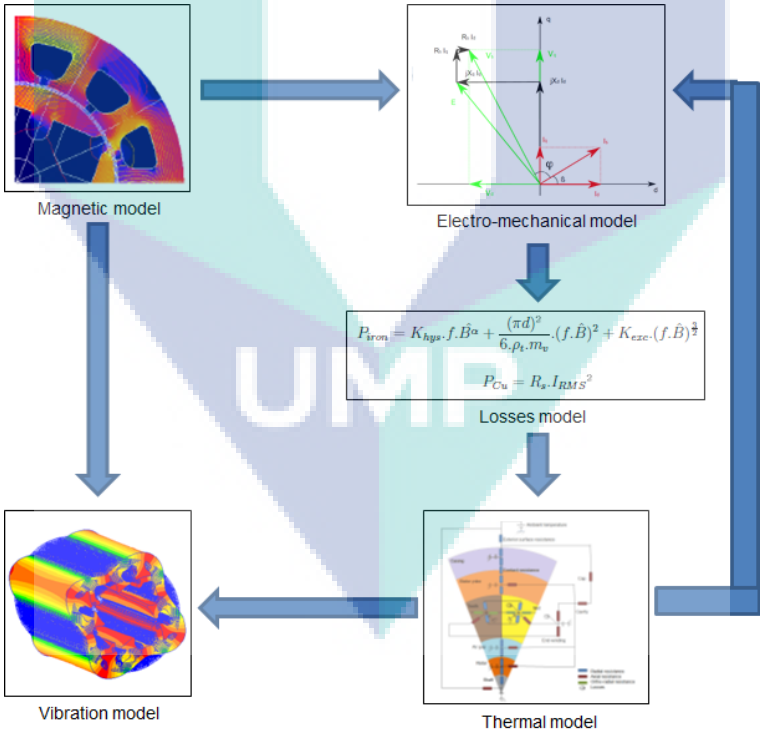

Figure 4.37: Coupling between different physic model will allow a better understanding of interactions between them.

2. Improvements of the test bench: The test bench has served well in different model validations. There were nonetheless several limitations pointed out in the thesis. For

example, the power electronic is not capable of delivering the maximum intended operating current for the machine which means that saturation effect on the operating area cannot be totally verified. Therefore, a more capable power electronic can be very beneficial.

3. Application of models and tools to evaluate different Syncrel machines: With validated models, we have theoretically evaluated two other Syncrel machines with solid rotor and flux-barrier rotor. More type of Syncrel machine with different environment constraints can now on be evaluated. Along the same spirit, different interchangeable rotor prototypes can be built to make more validation and comparisons experimentally. Even before that, the winding of the current prototype machine can be redone and improved before reevaluating its new electro-mechanical and thermal performance.

4. Optimization of the machine: Finally, all the models can be exploited for optimization purpose separately for now, and maybe together as coupled multi-physical model in the future.

Publications

1. Détermination Rapide d'un Modèle Thermique de Machine à Synchro Réluctance

Revue 3EI-SEE, No. 74, pp. 67-72, Octobre 2013 / Journées des Jeunes Chercheurs en Génie Electrique 2013 (JCGE 2013) June 5, 2013

Authors: Mohd Azri Hizami RASID

Abstract: La construction d'un modèle thermique d'une machine électrique devient aujourd'hui souvent nécessaire pour pouvoir intégrer le comportement thermique dès la phase de conception. Dans les applications pour accessoires automobiles où sont réalisées plusieurs prototypes un vue de grande série, cette étude propose l'utilisation d'un premier prototype combiné avec une méthode de calage expérimental afin de permettre une réalisation d'un modèle thermique rapide et suffisamment précis.

2. Simple Lumped Parameter Thermal Model with Practical Experimental Fitting Method for Synchronous Reluctance Machine

Power Electronics and Applications (EPE), 2013 15th European Conference on , vol., no., pp.1,10, 2-6 Sept. 2013; published by IEEE Xplore September 2, 2013

Authors: Mohd Azri Hizami RASID, Lanfranchi Vincent, Khadija El Kadri, Alejandro Ospina

Abstract: With the ever increasing pressures in automotive industries to develop smaller and more efficient electrical motors for their applications, it becomes necessary to have a thermal model at the design stage. This study proposes a fast, precise and practical thermal model construction that requires minimal development time for a synchronous reluctance machine which is to be used in automotive applications. It uses a method we call "practical experimental fitting method" which corrects a basic and simple thermal model by adding corrector coefficients into the model in order to fit it to experimental results obtained from the first machine prototype.

3. Thermal Model of Stator Slot for Small Synchronous Reluctance Machine

Electrical Machines (ICEM), 2014 International Conference on , vol., no., pp.2199,2204, 2-5 Sept. 2014; published by IEEE Xplore September 2, 2014

Authors: Mohd Azri Hizami RASID, Alejandro Ospina, Khadija EL Kadri, Lanfranchi Vincent

Abstract: Machine slot thermal behavior is one of the most complex issues in electrical machine thermal modeling. It may however take advantages of various studies on composite winding homogenization to make the slot modeling less complex. In order to reduce computation time of winding, many has developed and adopted Page3 winding homogenization method. The composite windings are assimilated to a single homogenous body with an equivalent thermal conductivity, using either analytical or numerical approach. A direct application of these winding homogenization methods on the slot of an electrical machine thermal model has however several limitations. In this paper, a winding homogenization method are chosen and applied on a Syncrel machine stator slot model. Experimental results obtained using the machine prototype submitted to direct current test has shown that modifications have to be made to the homogenized slot model. The proposed modifications on the slot model are presented and the model was tested with different thermal operating points so as to validate the modifications.

4. Experimental investigation of contact resistances for small TENV electrical machine

Sensors & Transducers Journal, March/April 2016, International Frequency Sensor Association (IFSA) Publishing

Authors: Olfa Meksi, Mohd Azri Hizami RASID, Alejandro Ospina, Lanfranchi Vincent

Abstract: In this paper, a thermal study of Synchronous Reluctant motor is proposed. A specific experimental method is applied in order to identify the thermal parameters, this method focus on the study of contact resistances and total thermal capacity. Generally, in the classical thermal modeling, the thermal contact resistance (TCR) is estimated by empirical values and the thermal capacities are calculated by analytical solutions. The originality of the proposed model is based on the complementarity between experimental procedure (machine at rest), thermal modeling and model reduction technique in order to determine these important parameters and validate results (thermal contact resistances and capacities).

Appendix

UMP

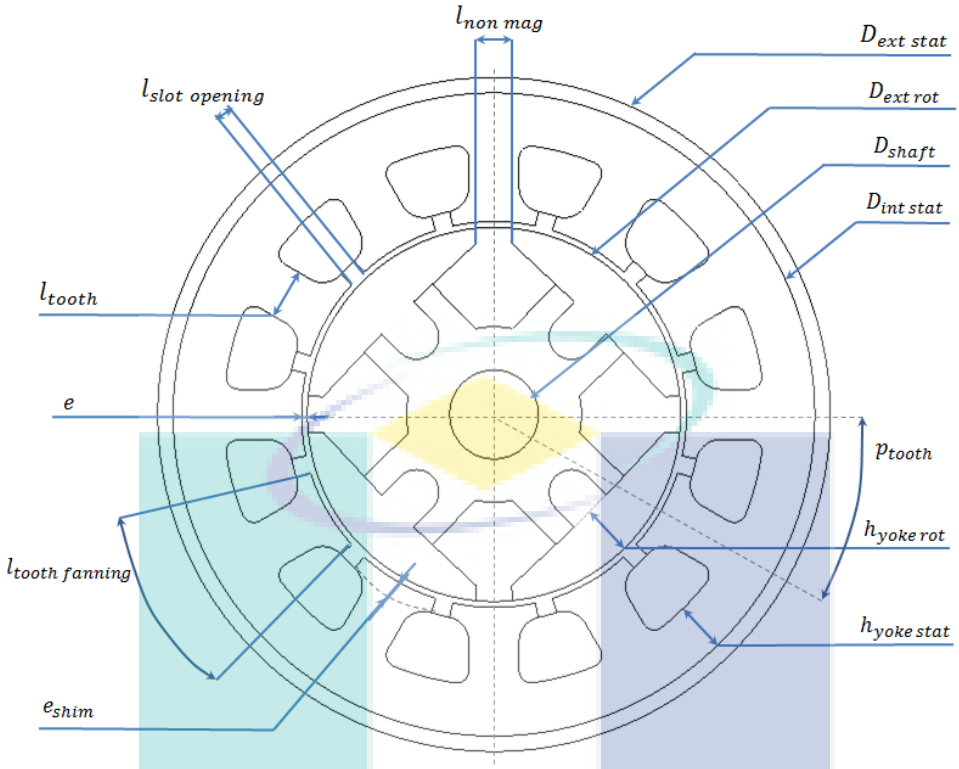

Figure 38: Syncrel machine dimensions.

	Dimension parameters	values
D_{shaft}	Rotor shaft diameter	6.00 mm
$D_{ext\ rot}$	Rotor exterior diameter	25.24 mm
$D_{ext\ stat}$	Stator exterior diameter	43.40 mm
D_{wire}	Wire diameter	0.60 mm
$D_{int\ stat}$	Stator interior diameter	26.04 mm
e	Air gap thickness	0.40 mm
e_{shim}	Slot shim thickness	1.00 mm
e_{casing}	Casing thickness	0.80 mm
$h_{stat\ yoke}$	Stator yoke height	3.40 mm
$h_{rot\ yoke}$	Rotor yoke height	3.40 mm
l_{tooth}	Tooth width	3.40 mm
$l_{non\ mag}$	Rotor's non-magnetic part width	2.21 mm
l_{fan}	Teeth fanning width	5.62 mm
$l_{slot\ opening}$	Slot opening width	1.19 mm
l_u	Active length	70.00 mm
N_{wire}	Number of wire	7
N_{teeth}	Number of teeth	12
p	Number of pole pair	2

Table 3: Syncrel machine dimension parameters.

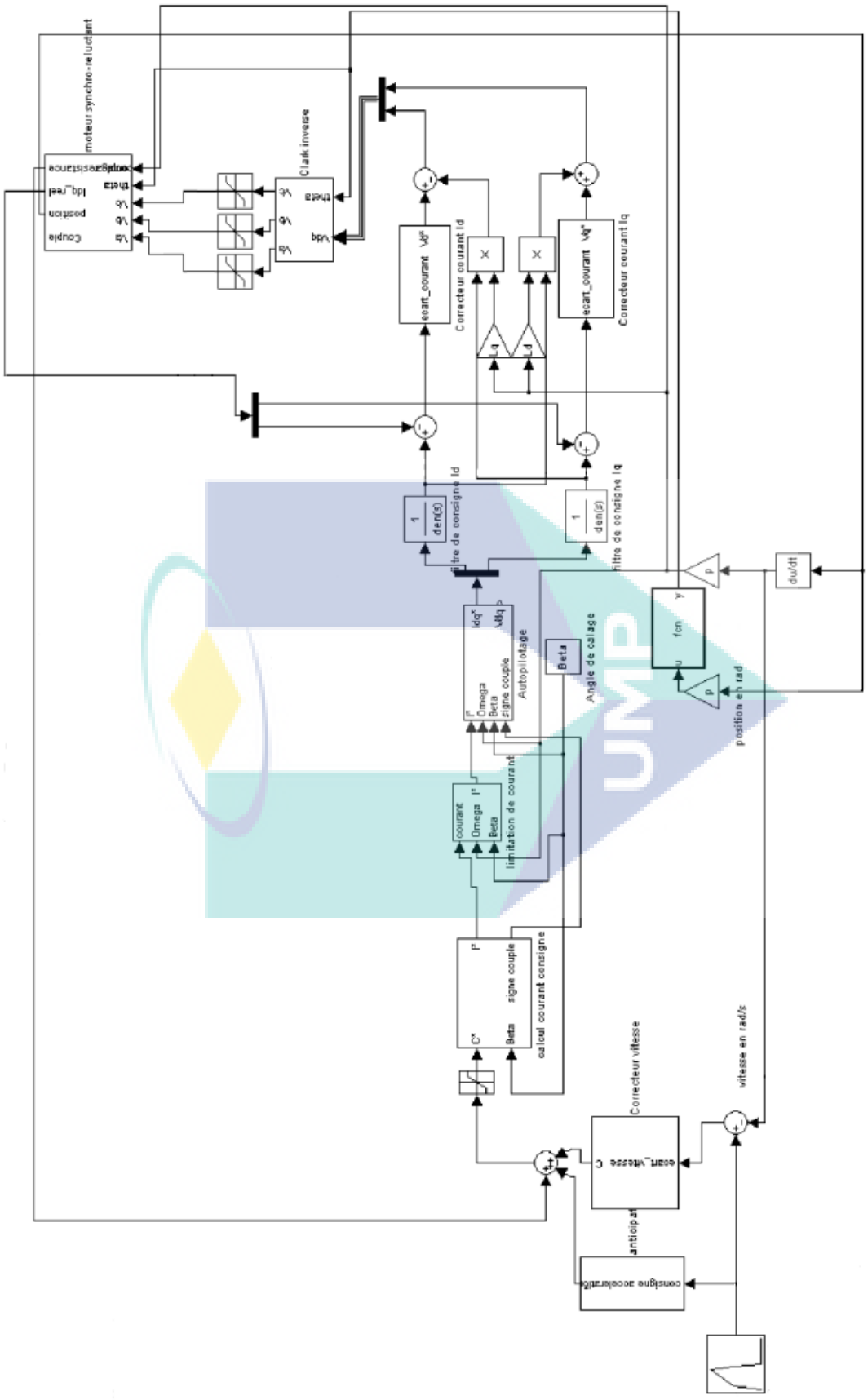

Figure 39: Diagram of the speed control in Simulink.

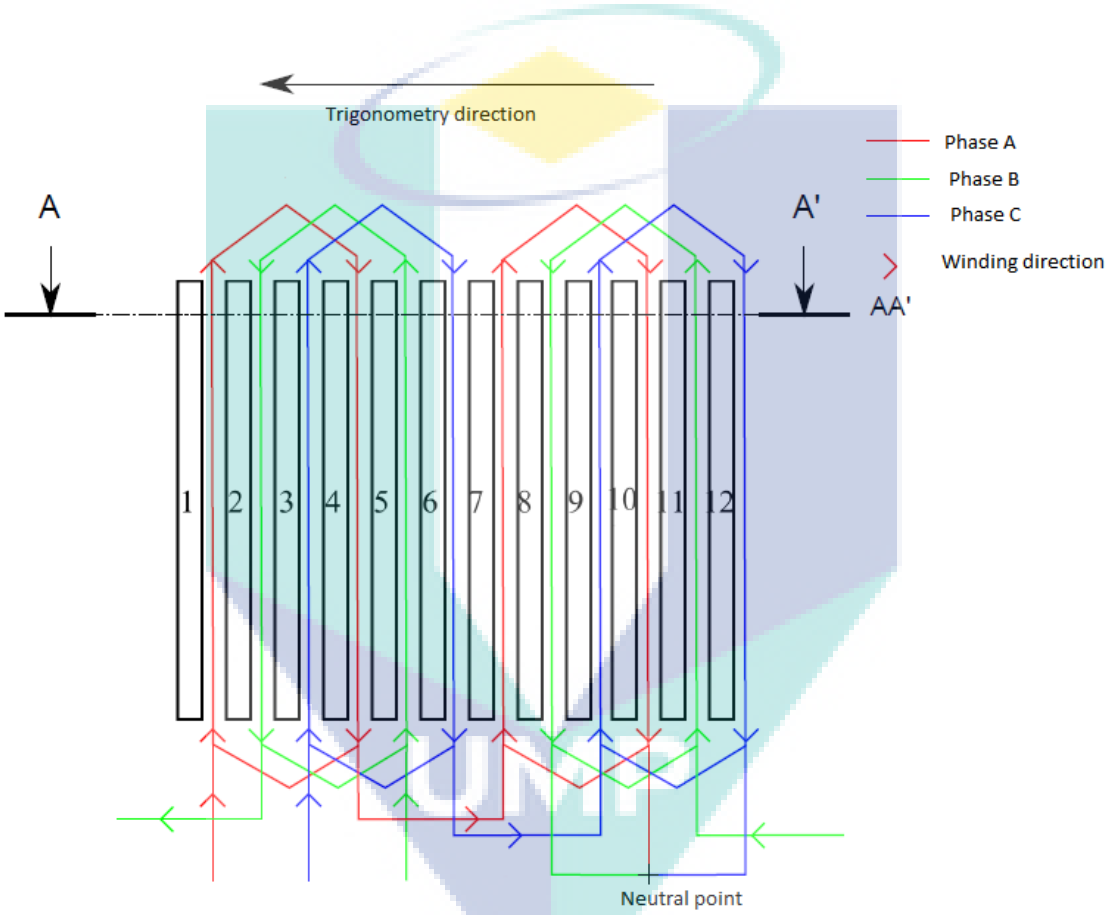

Figure 40: The stator winding was done in full-pitch winding configuretion.

Before developping subsubsection 2.3.3.2 further, it is necesary to remind and reclarify several terminologies and symbols that are going to be used.

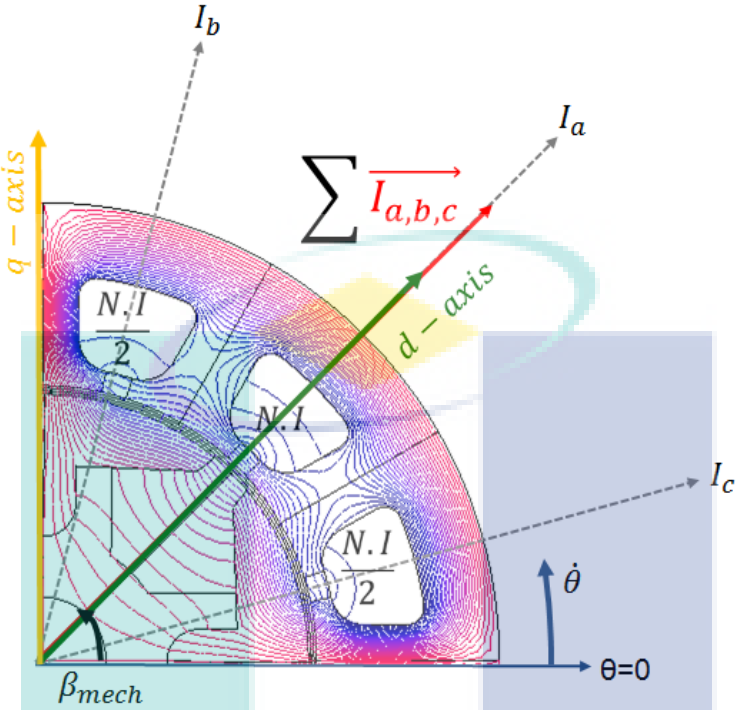

Figure 41: The definition of the magnetic field position θ and the load angle β shown on one pole. In this figure, the load angle shown is mechanical load angle β_{mech}.

First, the stator magnetic field position θ. θ is defined as an electrical angular position of the flux axis. Consequently, it is always electrically perpendicular to the resultant current vector $\sum \overrightarrow{I_{a,b,c}}$ (Figure 41). We remind that the mechanical and electrical angle are related by a factor of p, the number of pair pole ($p.\beta_{mech} = \beta$).The magnetic field rotates at the speed of $\dot{\theta}$ and θ is independant of the rotor position. The position $\theta = 0$ is defined at position shown in Figure 41.

The second terminology is the load angle β. β is the relative angular position of the rotor's $d-axis$ to the magnetic field position θ. For example, in Figure 41, the $d-axis$ is $\pi/4$ away from the flux axis θ in mechanical angle, making $\beta = \pi/2°$. As the motor operates in normal condition, β will have one value chosen and defined in the control program (Appendix C). For example, it is theoretically admitted that the load angle that gives the maximum torque at a given stator current is $\beta = \pi/4$. Therefore, the rotor rotates synchronously with the stator magnetic field at the speed of $\dot{\theta}$, but angularly shifted by $\beta = \pi/4$ relative to θ.

Finally, the direct and quadrature position. The method used to locate the direct axis position was by applying a DC curent to the machine using the connection shown in Figure 42a [7, 8]. Consequently, the rotor d-axis will align with theflux axis, giving us the direct position

shown in left Figure 42b. The quadrature position can then be deduced as it is 90° electrical degrees away from the direct position which is shown in right Figure 42b.

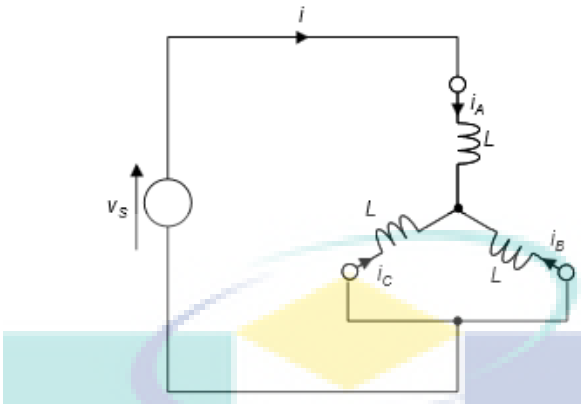

(a) The circuit connection to find direct position.

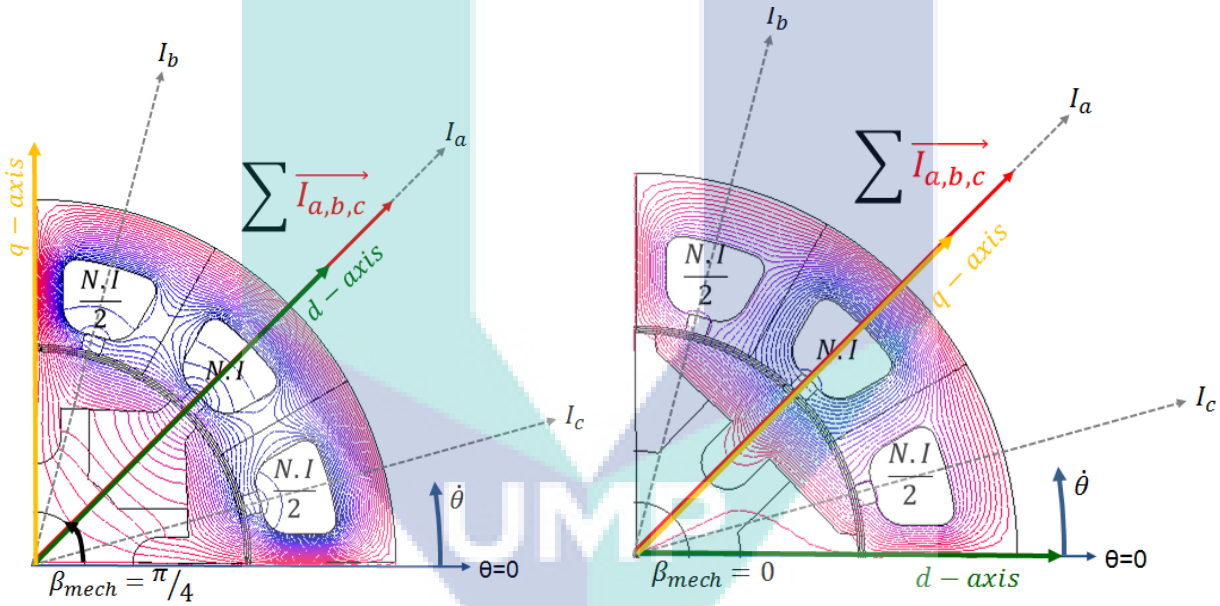

(b) Left: The quadrature position. Right: The direct position.

Figure 42: The definition of direct and quadrature position.